



TECHNICAL REPORT 94-02E

Grimsel Test Site

FRACTURE SYSTEM FLOW TEST Experimental and Numerical Investigations of Mass Transport in Fractured Rock

March 1994

L. Liedtke, A. Götschenberg, M. Jobmann,
W. Siemering

Federal Institute for Geoscience and Natural
Resources, Hannover, Federal Republic of Germany

GRIMSEL TEST SITE / SWITZERLAND
A JOINT RESEARCH PROGRAM BY

- NAGRA - National Cooperative for the Disposal of Radioactive Waste, Wettingen, Switzerland
- BGR - Federal Institute for Geoscience and Natural Resources, Hannover, Federal Republic of Germany
- GSF - Research Centre for Environmental Sciences, Munich, Federal Republic of Germany

TECHNICAL REPORT 94-02E

Grimsel Test Site

FRACTURE SYSTEM FLOW TEST Experimental and Numerical Investigations of Mass Transport in Fractured Rock

March 1994

L. Liedtke, A. Götschenberg, M. Jobmann,
W. Siemering

Federal Institute for Geoscience and Natural
Resources, Hannover, Federal Republic of Germany

GRIMSEL TEST SITE / SWITZERLAND
A JOINT RESEARCH PROGRAM BY

- NAGRA - National Cooperative for the Disposal
of Radioactive Waste, Wettingen, Switzerland
- BGR - Federal Institute for Geoscience and Natural
Resources, Hannover, Federal Republic of Germany
- GSF - Research Centre for Environmental Sciences,
Munich, Federal Republic of Germany

"Copyright © 1994 by Nagra, Wettingen (Switzerland) / All rights reserved.

All parts of this work are protected by copyright. Any utilisation outwith the remit of the copyright law is unlawful and liable to prosecution. This applies in particular to translations, storage and processing in electronic systems and programs, microfilms, reproductions, etc. "

FOREWORD

Concepts for the disposal of radioactive waste in geological formations place a significant emphasis on acquiring extensive knowledge of the proposed host rock and the surrounding strata. For this reason Nagra has, since May 1984, been operating **the Grimsel Test Site (GTS)** which is located at a depth of 450 m in the crystalline rock of the Aare Massif of the Central Swiss Alps. The general objectives of the research being carried out in this underground laboratory include

- the build-up of know-how in planning, performing and interpreting field experiments in various scientific and technical disciplines and
- the acquisition of practical experience in the development of investigation methodologies, measuring techniques and test equipment that will be of use during actual repository site explorations.

On the basis of a collaborative agreement various experimental activities started 1984 by Nagra and its two German partners, the Federal Institute for Geoscience and Natural Resources (BGR) and the Research Center for Environmental Sciences (GSF). The Grimsel projects of both GSF and BGR have been supported by the German Federal Ministry for Research and Technology (BMFT). International cooperation was continuously extended with partners from USA (DOE), Japan (PNC), Sweden (SKB), and France (ANDRA). In addition various foreign and Swiss organisations, research institutes or universities participate in many Grimsel projects or independently carry out their own investigations at the underground facility.

This report was produced in accordance with the cooperation agreements mentioned above. The authors have presented their own opinions and conclusions which do not necessarily coincide with those of Nagra or its participating partners.

VORWORT

Bei Konzepten, welche die Endlagerung radioaktiver Abfälle in geologischen Formationen vorsehen, ist die Kenntnis des Wirtgesteins und der angrenzenden Gesteinsschichten von grundlegender Bedeutung. Die Nagra betreibt deshalb seit Mai 1984 **das Felslabor Grimsel (FLG)** in 450 m Tiefe im Kristallin des Aarmassivs. Die generelle Zielsetzung für die Arbeiten in diesem System von Versuchsstollen umfasst

- den Aufbau von Know-how in der Planung, Ausführung und Interpretation von Untergrundversuchen in verschiedenen wissenschaftlichen und technischen Fachgebieten, und
- den Erwerb praktischer Erfahrung in der Entwicklung und der Anwendung von Untersuchungsmethoden, Messverfahren und Messgeräten, die für die Erkundung von potentiellen Endlagerstandorten in Frage kommen.

Auf der Basis eines deutsch-schweizerischen Zusammenarbeitsvertrages begannen 1984 verschiedene Versuche der Nagra und der beiden deutschen Partnern, Bundesanstalt für Geowissenschaften und Rohstoffe, Hannover (BGR) und Forschungszentrum für Umwelt und Gesundheit GmbH, München (GSF). Das Deutsche Bundesministerium für Forschung und Technologie (BMFT) hat dabei die Arbeiten der BGR und der GSF im FLG gefördert. Die internationale Zusammenarbeit wurde im Verlauf der Jahre ausgeweitet mit Partnern aus USA (DOE), Japan (PNC), Schweden (SKB) und Frankreich (ANDRA). Für ausgewählte Projekte im Felslabor Grimsel ergab sich eine zusätzliche Zusammenarbeit mit verschiedenen in- und ausländischen Organisationen, Forschungsinstituten oder Universitäten, wobei vereinzelte Untersuchungen auch eigenständig durchgeführt werden.

Der vorliegende Bericht wurde im Rahmen der erwähnten Zusammenarbeitsverträge erstellt. Die Autoren haben ihre eigenen Ansichten und Schlussfolgerungen dargelegt. Diese müssen nicht unbedingt mit denjenigen der Nagra oder des beteiligten Partner übereinstimmen.

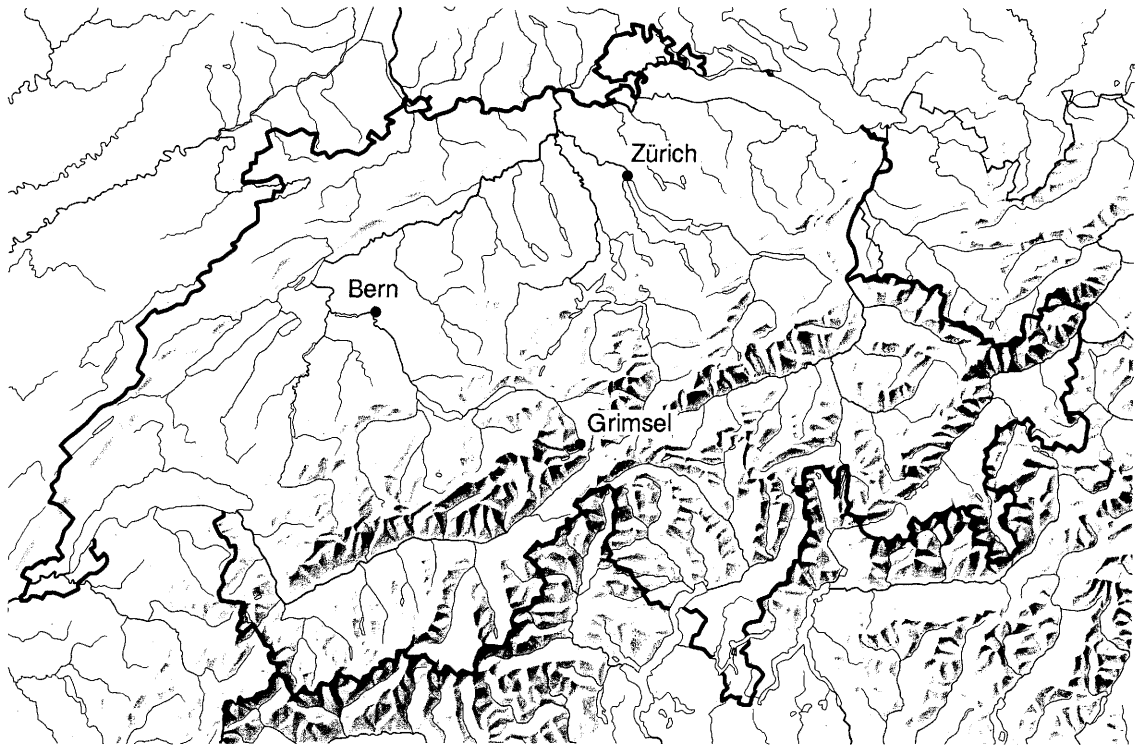
AVANT - PROPOS

Lors d'études de concepts de stockage de déchets radioactifs dans des formations géologiques, on attache une grande importance à l'acquisition d'informations étendues sur la roche d'accueil et les formations rocheuses environnantes. C'est pour cette raison que la Cédra exploite depuis mai 1984 son **Laboratoire souterrain du Grimsel (LSG)** situé à 450 m de profondeur dans le cristallin du massif de l'Aar, au coeur des Alpes centrales. Les principaux objectifs des recherches effectuées dans ce réseau de galeries comprennent:

- l'acquisition de savoir-faire dans diverses disciplines techniques et scientifiques en ce qui concerne la conception, la réalisation et l'interprétation d'expériences in situ, ainsi que
- l'accumulation d'expériences pratiques dans la mise au point et l'application de méthodes d'investigation, de techniques et d'appareillages de mesure, qui pourraient être utilisés lors de l'exploration de sites potentiels de dépôts finals.

Le LSG est exploité par la Cédra et diverses expériences y sont réalisées à partir de 1984 par celle-ci et deux institutions allemandes, la "Bundesanstalt für Geowissenschaften und Rohstoffe, Hanovre" (BGR) et le "Forschungszentrum für Umwelt und Gesundheit GmbH, Munich" (GSF), dans le cadre d'un traité de collaboration germano-suisse. Les projets menés au Grimsel par la BGR et le GSF sont financés par le Ministère fédéral allemand de la recherche et de la technologie (BMFT). La coopération internationale s'est accrue au fil des années, avec des partenaires des USA (DOE), du Japon (PNC), de la Suède (SKB) et de la France (Andra). Des instituts de recherche, des universités et des organisations étrangères et suisses ont participé à de nombreux projets au Grimsel, certains y ont mené leurs propres recherches.

Le présent rapport a été élaboré dans le cadre des accord de collaboration mentionnés. Les auteurs ont présenté leurs vues et conclusions personnelles. Celles-ci ne doivent pas forcément correspondre à celles de Nagra ou ses partenaires participants.



Reproduziert mit Bewilligung des Bundesamtes für Landestopographie vom 19.6.1991

Location of Nagra's underground test facility at the Grimsel Pass in the Central Alps (Bernese Alps) of Switzerland (approximate scale 1 cm = 25 km).

Geographische Lage des Nagra Felslabors am Grimselpass (Berner Oberland) in den schweizerischen Zentralalpen (Massstab: 1 cm = ca. 25 km)



GRIMSEL-GEBIET

Blick nach Westen

- 1 Felslabor
- 2 Juchlistock
- 3 Räterichsbodensee
- 4 Grimselsee
- 5 Rhonetal

GRIMSEL AREA

View looking West

- 1 Test Site
- 2 Juchlistock
- 3 Lake Raeterichsboden
- 4 Lake Grimsel
- 5 Rhone Valley

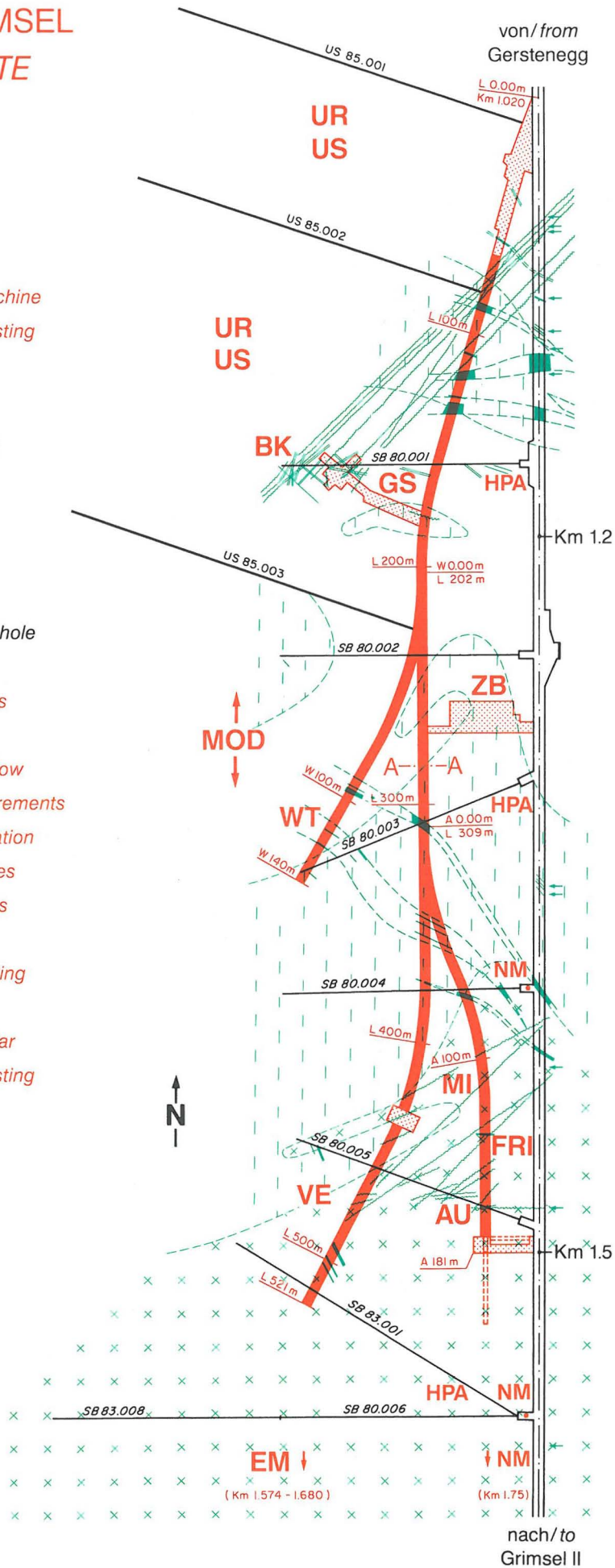
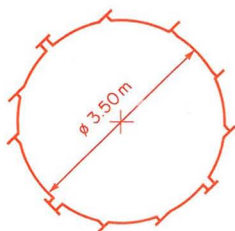
FLG FELSLABOR GRIMSEL
GTS GRIMSEL TEST SITE

Situation



- Zugangsstollen/ Access tunnel
- Fräsvortrieb/ by tunnel boring machine
- Sprengvortrieb/ excavated by blasting
- Zentraler Aaregranit ZAGR
Central Aaregranite CAGR
- Biotitreicher ZAGR
CAGR with high content of biotite
- Grimsel-Granodiorit
Grimsel-Granodiorite
- Scherzone/ Shear zone
- Lamprophyr/ Lamprophyre
- Wasserzutritt/ Water inflow
- Sondierbohrung/ Exploratory borehole
- US Bohrung/ US borehole
- ZB Zentraler Bereich/ Central facilities
- AU Auflockerung/ Excavation effects
- BK Bohrlochkranz/ Fracture system flow
- EM El.magn. HF-Messungen/ -measurements
- FRI Kluftzone/ Fracture zone investigation
- GS Gebirgsspannungen/ Rock stresses
- HPA Hydr. Parameter/ Hydr. parameters
- MI Migration/ Migration
- MOD Hydrodyn. Modellierung/ H. modeling
- NM Neigungsmesser/ Tiltmeters
- UR Untertageradar/ Underground radar
- US Seismik/ Underground seismic testing
- VE Ventilationstest/ Ventilation test
- WT Wärmeversuch/ Heat test

A — A Schnitt/ Section



SUMMARY

Investigation of the effectiveness of the host rock as a geological barrier and hydraulic studies are important for the safety analysis of a potential final repository for radioactive or toxic wastes. The flow patterns of water in the rock and the capacity of the water for transporting dissolved substances are studied using conservative (salt) and non-conservative (heat) tracers to assess the potential migration of contaminants and toxic substances in the rock.

Within the scope of the German-Swiss cooperation in the field of final disposal, the Rock Mechanics and Civil Engineering section of the Federal Institute for Geosciences and Natural Resources (BGR) was engaged in the third phase of the "Fracture System Flow Test" project from 1991 to 1993. As in the preceding phases, interest was focused on the development of methods and techniques. In the present report, the further development of the equipment and numerical methods used for evaluation of the data are described in detail. The findings of the in-situ tests at the NAGRA Grimsel Test Site are summarised and the results of the simulation of flow and transport processes using both numerical (DURST) and analytical methods are presented. The basics of the DURST (DURchströmung and STofftransport) finite element program system were developed during the first two phases of the project, together with the Institute for Flow Mechanics and Computing of Hannover University.

Newly developed multipacker combined probes were tested during the several-month tracer tests. The computer program developed for this type of equipment proved to be reliable.

The speed of the DURST/ROCKFLOW finite element program was increased by implementing faster algorithms. Introducing the possibility of selecting the initial boundary conditions improves the adaption of the program to complex model structures. The simulation of multiphase flow was theoretically prepared.

The tests during Phase III of the fracture system flow test were also focused on in-situ hydraulic testing in the BK section of the Test Site. Experiments to determine the permeability of fractured rock as a function of stress were carried out in the peripheral area of the laboratory tunnel. The objective of the tracer tests was to determine the transport velocity of toxic substances in fractured rock.

ZUSAMMENFASSUNG

Die Untersuchung der Barrierenwirkung des Wirtgesteins um ein potentielles Endlager für radioaktive oder toxische Stoffe und die Bestimmung des hydraulischen Potentialfeldes sind wesentliche Grundlagen für die sicherheitstechnische Bewertung. Zur Beurteilung von Ausbreitungsvorgängen kontaminierter und toxischer Stoffe im Gebirge sind felshydraulische Untersuchungen notwendig, in denen das Strömungsverhalten von Wasser und sein Transportvermögen hinsichtlich konservativer (Salz) und nicht konservativer (Temperatur) Tracer festgestellt wird.

Im Rahmen der deutsch-schweizerischen Zusammenarbeit auf dem Gebiet der Endlagerung hat die Bundesanstalt für Geowissenschaften und Rohstoffe, Referat B2.11 (Felsmechanik und Baugeologie) in den Jahren 1991 - 1993 das Forschungsprojekt "Bohrlochkranzversuch" in seiner dritten Förderungsphase bearbeitet. Die Entwicklung von Methoden und Verfahren stand, wie in den vorangegangenen Förderungsphasen, im Mittelpunkt des Interesses. Im vorliegenden Bericht werden die Weiterentwicklung der verwendeten Meßeinrichtung und die eingesetzten numerischen Verfahren ausführlich beschrieben. Die Erkenntnisse aus den in-situ Versuchen, die im Felslabor Grimsel der Nagra durchgeführt wurden, werden zusammengefaßt und Ergebnisse der Simulation von Strömungs- und Transportprozessen sowohl mit einem numerischen Verfahren (DURST) als auch mit einem analytischen Verfahren vorgestellt. Das Finite-Element-Programmsystem DURST (DURchströmung und STofftransport) wurde in seinen Grundzügen bereits in den beiden ersten Förderungsphasen des Forschungsvorhabens zusammen mit dem Institut für Strömungsmechanik und Elektronisches Rechnen an der Universität Hannover entwickelt.

Die Arbeiten zur Geräteentwicklung konzentrierten sich auf die Praxiserprobung der neu entwickelten Multipacker-Kombisonden, die in den mehrere Monate dauernden Tracer-Versuchen mit Erfolg eingesetzt wurden. Das speziell für diesen Gerätetyp entwickelte EDV-Programm hat sich bewährt.

Die Rechengeschwindigkeit des Finite-Element-Programms DURST/ROCKFLOW wurde durch die Implementierung von schnelleren Gleichungslösern erhöht. Zur besseren Anpassung an komplexe Modellstrukturen trägt die neu eingeführte Möglichkeit einer freien Wahl der Anfangsrandbedingungen bei. Die Simulation von Mehrphasenströmungsvorgängen wurde theoretisch aufbereitet.

Die hydraulischen in-situ Versuche im BK-Bereich des Felslabors bildeten auch in der Phase III des Bohrlochkranzversuchs den Schwerpunkt der Arbeiten. Versuche zur spannungsabhängigen Permeabilität des geklüfteten Gebirges wurden im peripheren Bereich des Laborstollens durchgeführt, die Tracer-Versuche sowie die umfangreichen Vorversuche im zentralen Bereich des Laborstollens. Die Tracer-Versuche dienten der Ermittlung der Schadstofftransportgeschwindigkeit im geklüfteten Fels.

RESUME

L'analyse de la manière dont la roche d'accueil autour d'un dépôt final potentiel agit comme barrière sur les substances radioactives ou toxiques et la détermination du champ hydraulique potentiel sont des éléments de base importants dans l'évaluation des techniques de sécurité. Pour évaluer le mode de propagation des substances contaminées et toxiques dans la roche, il est nécessaire de procéder à des recherches sur l'hydraulisme de la roche où on détermine le mode d'écoulement des eaux et leur capacité à transporter des substances de traçage conservatives (sel) et non conservatives (température).

Dans le cadre de la collaboration germano-suisse dans le domaine du stockage final, l'Institut fédéral de géosciences et des ressources naturelles (section mécanique de la roche et géologie de la construction) a travaillé de 1991 à 1993 à la troisième phase de développement du projet de recherche "Test hydraulique dans un système de diaclases". Comme les précédentes phases de développement, la troisième a concentré principalement sur la mise au point des méthodes et de techniques. Le présent rapport décrit en détail le perfectionnement des installations de mesure utilisées et les procédés numériques employés. Il résume les informations obtenues par les essais in situ réalisés au laboratoire souterrain de la Cédra au Grimsel et présente les résultats de la simulation de processus d'écoulement et de transport selon une méthode numérique (DURST) et une méthode analytique. Dans les deux premières phases de la recherche, le système de programme des éléments finis DURST (DURchströmung und STofftransport) avait déjà été mis au point dans ses grandes lignes en collaboration avec "l'Institut für Strömungsmechanik und Elektronisches Rechnen" de l'Université d'Hanovre.

Les travaux de mise au point des appareils se concentrent sur des essais pratiques avec les nouvelles sondes combinées à packers multiples qui ont été développées. Ces sondes ont été utilisées avec succès dans les essais de traçage qui ont duré plusieurs mois. Le programme de traitement de l'information qui avait spécialement été mis au point pour ce type d'appareil a fait ses preuves.

La vitesse de calcul du programme des éléments finis DURST/Rockflow a été augmentée en recourant à des solveurs d'équations plus rapides. Cette nouvelle possibilité contribue à choisir librement des conditions secondaires initiales pour mieux s'adapter à des structures de modèles complexes. Des processus d'écoulement à plusieurs phases ont été simulés théoriquement.

Les essais hydrauliques in situ dans la zone BK du laboratoire souterrain ont aussi été au centre des travaux de la phase III du test hydraulique dans un système de diaclases. Des essais sur la perméabilité non-linéaire de la roche diaclasée ont été réalisés dans la zone périphérique de la galerie du laboratoire, les essais de traçage ainsi que les nombreux essais préliminaires dans la partie centrale de la galerie du laboratoire. Les essais de traçage ont servi à déterminer la vitesse de transport des matières nocives dans la roche diaclasée.

CONTENT

Summary	IX
Zusammenfassung	X
Résumé	XI
Content	XII
List of Figures	XVI
List of Tables	XXIV
1. Introduction and Objectives	1
1.1 Project Investigations at the BK Site	1
1.2 Further Investigations at the BK Site	4
2. Technical Development of Flow Test Equipment	7
2.1 Packer and Probe Systems	
2.1.1 Mechanical Extension Packers	8
2.1.2 Pluggable Hose Packers	8
2.1.3 Pluggable Hose Packers with Electronic Probes (Passive Multipackers)	8
2.1.4 Pluggable Multipacker Multifunctional Probe System (Active Multipackers)	9
2.2 Data Acquisition Systems	11
2.2.1 Process Control with HP process control computer and multiprogrammer	11
2.2.2 Data Recording with PC und Multifunctional Probe System	15
2.2.3 Data Recording with Dataloggers	18
2.3 Pump System	18
2.4 Long-term Perspectives and Future Developments	18
3. Theory of Multiphase Flow in Fractured Porous Media	21
3.1 Principles of Multiphase Flow Process	21
3.1.1 General	21

	<u>Page</u>	
3.1.2	Capillary Pressure Curve	23
3.1.3	Permeability Curve	23
3.2	Capillary Pressure / Saturation Relation	25
3.3	Relative Permeability / Saturation Relation	28
3.4	Multiphase Flow in Fractured Porous Media	30
4.	Software Development	33
4.1	Data Acquisition	33
4.1.1	Graphical User Interface PC_MULI	33
4.1.2	Functional Principle	37
4.1.3	Future Development	37
4.2	Program System DURST/ROCKFLOW	37
4.2.1	Flow Model SM2	38
4.2.2	Transport Model TM2	38
4.2.3	Gas Model GM2	38
4.2.3.1	General Field Equations	39
4.2.3.2	Ideal Gas Flow	41
4.2.3.3	Actual Gas Flow	42
4.2.3.4	Time-related Semi-Discretion	43
4.2.3.5	BUBNOW-GALERKIN Method	44
4.2.4	Network Generator	45
4.2.5	Graphics Processor	46
5.	Hydraulic Testing in the BK Area	47
5.1	Tests in Area BoUS 3 - BoBK 3	47
5.1.1	Flow Test VE 485 (BoBK 3)	47
5.1.2	Flow Test VE 487 (BoBK 3)	50
5.1.3	Constant Flow Test VE 491 (BoBK 3)	51
5.1.3.1	Test Procedure	51
5.1.3.2	THEIS Evaluation	52
5.1.4	Flow and Recovery Test VE 494 (BoBK 3)	56
5.1.5	Constant Flow and Recovery Test VE 511 (BoBK 2)	57
5.2	Tests in the Central BK Area	59
5.2.1	Pressure Buildup Tests VE 478 und VE 484	59
5.2.2	Interference Test VE 479	62
5.2.3	Fluid Logging Tests	62

	<u>Page</u>	
5.2.4	Multiple Source Crosshole Test (MSCT) VE 496 - VE 513	68
6.	Tracer Testing and Test Simulation	71
6.1	Tracer Test VE 483 (Salt): BoBK 14 ---> BoBK 8	71
6.1.1	Course and Documentation of Tracer Test VE 483	71
6.1.2	Numerical Simulation of Tracer Test VE 483	75
6.2	Tracer Test VE 493 (Salt): BoBK 14 ---> BoBK 10	80
6.2.1	Course and Documentation of Preliminary Tests	80
6.2.1.1	Test VE 488 and VE 489 (Pressure Buildup Tests)	81
6.2.1.2	Conductivity Measurement in Borehole BoBK 10	85
6.2.1.3	Flow (Outflow) Test VE 492, Borehole BoBK 14	86
6.2.2	Course and Documentation of Tracer Test VE 493	93
6.2.3	Numerical Simulation of Tracer Test VE 493	105
6.3	Salt/Heat Tracer Test VE 520: BoBK 5 ---> BoBK 15	108
6.3.1	Test Installation	108
6.3.2	Course of Test	108
6.3.3	Description of Results	109
6.3.4	Evaluation	114
6.3.4.1	Transmissivity and Fracture Aperture	114
6.3.4.2	Breakthrough Times	115
6.3.4.3	Mass Balance	117
6.3.4.4	Flow Velocity	118
6.3.4.5	Thermal Conductivity	119
6.3.5	Analytical Modelling	121
6.3.5.1	Fracture Model	121
6.3.5.2	Model Computations	124
6.3.5.3	Discussion of Results	130
6.3.6	Numerical Modelling	130
6.3.6.1	Model Description	131
6.3.6.2	Flow Conditions	134
6.3.6.3	Discussion of Results	148
7.	Desk Study	149
7.1	Objectives of the Desk Study	149
7.2	Various Projects at the Grimsel Test Site and their Objectives	149
7.3	In-situ Hydraulic Tests at the GTS	151
7.3.1	Testing Technology	152

	<u>Page</u>	
7.3.2	Measurement Technology	152
7.3.3	Methods of Hydraulic Test Interpretation	153
7.4	Numerical Models for Simulation of Hydraulic Tests	154
7.4.1	Fracture System Flow Test: DURST/ROCKFLOW	154
7.4.2	Ventilation	155
7.4.3	Migration	155
7.4.4	Other Numerical Models	157
7.4.4.1	Rock Hydraulics	157
7.4.4.2	Tension Propagation	158
7.4.4.3	Heat Propagation	158
7.5	Procedure for Development of a Repository in Granite	158
8.	Summary	160
8.1	Results of Phase III of the Fracture System Flow Test	160
8.2	Planned Future Investigations	162
9.	References	164

LIST OF FIGURES

Figure 1.1:	Grimsel Test Site - Generalised diagram of BK area	2
Figure 1.2:	Grimsel Test Site - Fan arrangement of boreholes in BK area	3
Figure 2.1:	Packer systems for flow tests	7
Figure 2.2:	Components of multipacker multifunctional probe system	10
Figure 2.3:	Data acquisition system	12
Figure 2.4:	Data transmission of passive probes: time division multiplex method	13
Figure 2.5:	Data transmission of passive probes: principle of signal modulation within the probes in time division multiplex method	14
Figure 2.6:	Data acquisition using PC for multifunctional probe system	15
Figure 2.7:	Multifunctional probe	16
Figure 2.8:	Principle of digital transmitting multifunctional probe	17
Figure 2.9:	Characteristic of excentric pump	19
Figure 2.10:	Design of excentric pump	20
Figure 3.1:	Porous medium model	22
Figure 3.2:	Mobile segment of a two-phase flow system (HELMIG 1993)	24
Figure 3.3:	Capillary pressure / saturation functions a) Linear, b) COREY curve, c) LEVERETT function	26
Figure 3.4:	Relative permeability / saturation functions	30
Figure 4.1:	Information flow diagram, PC_MULI	34
Figure 4.2:	Example of screen contents, PC_MULI	35
Figure 4.3:	Program functions, PC_MULI	36
Figure 4.4:	Grid geometry for imaging of a fracture surface between boreholes BoBK 9 and BoBK 5	45

	<u>Page</u>
Figure 4.5: Refined network area around the source (Enlargement of segment of Figure 4.4)	46
Figure 5.1: VE 485 - Pressure and flow rate in boreholes BoBK 3 and BoUS 3 as a function of time	48
Figure 5.2: VE 485 - Measured and calculated pressure in borehole BoUS 3 in first test phase (2 days)	49
Figure 5.3: VE 485 - Measured and calculated pressure in borehole BoUS 3 over entire test period (20 days)	49
Figure 5.4: VE 487 - Pressure in boreholes BoBK 3 and BoUS 3 and flow rates in borehole BoBK 3 as a function of time	50
Figure 5.5: VE 487 - Relation between pressure and flow rate in boreholes BoBK 3 and BoUS 3	51
Figure 5.6: VE 491 - Pressure in boreholes BoBK 3 and BoUS 3 and flow rates in borehole BoBK 3 as a function of time	52
Figure 5.7: VE 491 - Relation between pressure and flow rate in boreholes BoBK 3 and BoUS 3	53
Figure 5.8: VE 491 - Measured and calculated pressure in borehole BoUS 3 during first test phase	53
Figure 5.9: VE 491 - Transmissivity calculated after the THEIS solution as a function of test duration	54
Figure 5.10: VE 491 - Measured and calculated pressure in borehole BoUS 3 as well as flow rate in borehole BoBK 3 throughout the entire test phase	55
Figure 5.11: VE 494 - Measured pressure in boreholes BoBK 3 and BoUS 3 as well as flow rate in borehole BoBK 3 as a function of time	56
Figure 5.12: VE 494 - Pressure in borehole BoBK 3 as a function of normalised time	57
Figure 5.13: VE 511 - Pressure in borehole BoBK 2 as a function of time	58
Figure 5.14: VE 511 - Pressure in borehole BoBK 2 as a function of normalised time	58

	<u>Page</u>
Figure 5.15: VE 478 - Pressure measured in boreholes in the central BK area as a function of time	60
Figure 5.16: VE 484 - Pressure measured in boreholes in the central BK area as a function of time	61
Figure 5.17: VE 479 - Interference test: Pressure measured in boreholes in the central BK area as a function of time	63
Figure 5.18: Fluid logging in borehole BoBK 4 (GEOTEST measurement)	64
Figure 5.19: Fluid logging tests in the central BK area: spatial location of inflow sites	66
Figure 5.20: Conductivity log of borehole BoUS 3	67
Figure 5.21: Multiple source crosshole test: positions of packers and probes	68
Figure 5.22: VE 502 - Pressures in boreholes BoBK 5 and BoBK 15 and flow rate in borehole BoBK 5 as a function of time	69
Figure 5.23: VE 510 - Pressures in boreholes BoBK 4 and BoBK 10 and flow rate in borehole BoBK 10 as a function of time	70
Figure 6.1: VE 483 - Pressure and injection rate in borehole BoBK 14 as a function of time	73
Figure 6.2: VE 483 - Pressure and injection rate in the central BK area boreholes as a function of time	74
Figure 6.3: VE 483 - Measured parameters pressure, discharge and electrical conductivity in extraction borehole BoBK 8 as a function of time	75
Figure 6.4: VE 483 - Simulation of tube flow	76
Figure 6.5: VE 483 - Results of parameter variation (tube flow)	77
Figure 6.6: VE 483 - Simulation as a 2D model a) Conductivity as a function of time for source and sink b) Conductivity for various times above the source-sink axis	79
Figure 6.7: Laboratory tunnel, flow pathways of tracer tests (schematic)	80
Figure 6.8: VE 493 - Prognosis of tracer breakthrough time in the extraction borehole	81

	<u>Page</u>
Figure 6.9: VE 489 - Pressure in borehole BoBK 8 as a function of time (measurement with multifunctional probes)	83
Figure 6.10: VE 489 - Pressure in borehole BoBK 8 as a function of time (enlargement of section from Fig. 6.9)	83
Figure 6.11: VE 489 - Hydraulic head in borehole BoBK 8 as a function of time (measurement with multifunctional probes)	84
Figure 6.12: VE 489 - Temperature in borehole BoBK 8 as a function of time (measurement with multifunctional probes)	84
Figure 6.13: VE 489 - Temperature, pressure and packer pressure of multifunctional probe 5 in borehole BoBK 8 as a function of time	85
Figure 6.14: VE 489 - Conductivity measurement before and after flushing in borehole BoBK 10 and derived packer positions	86
Figure 6.15: Core view, borehole BoBK 10, depth 19.5-21.0 m	87
Figure 6.16: Core view, borehole BoBK 10, depth 21.0-22.5 m	88
Figure 6.17: VE 492 - Flow rate in borehole BoBK 14 as a function of time (3 h after beginning of test)	90
Figure 6.18: VE 492 - Pressure in boreholes BoBK 4, 9, 14 as a function of time (3 h after beginning of test)	90
Figure 6.19: VE 492 - Pressure in borehole BoBK 8 as a function of time (28 h after beginning of test, measurement with multifunctional probes)	91
Figure 6.20: VE 492 - Pressure in borehole BoBK 8 as a function of time (3 h after beginning of test, measurement with multifunctional probes)	91
Figure 6.21: VE 490 - Flow rate in borehole BoBK 14 (injection) and pressures in boreholes BoBK 4, 9, 14 as a function of time	92
Figure 6.22: VE 490 - Flow rate in borehole BoBK 14 (injection) and pressures in boreholes BoBK 4, 9, 14 as a function of time (enlargement of section from Fig. 6.21)	92
Figure 6.23: VE 493 - Possible tracer flow pathway	93
Figure 6.24: Location of leakages 1 and 3	94

	<u>Page</u>
Figure 6.25: VE 493a and b - Manually measured conductivities at leakages and in borehole BoBK 10 as a function of time	95
Figure 6.26: VE 493a and b - Manually measured discharges of leakages and in borehole BoBK 10 as a function of time	95
Figure 6.27: VE 493b - Conductivity in borehole BoBK 10 as a function of time (49 days from beginning of test)	96
Figure 6.28: VE 493 - Conductivity in borehole BoBK 10 as a function of time (12 days from beginning of test)	96
Figure 6.29: VE 493b - Flow rates in borehole BoBK 14 (injection) and BoBK 10 (extraction) as a function of time (49 days from beginning of test)	97
Figure 6.30: VE 493b - Pressures in boreholes BoBK 9, 13, 14 (Fan A) as a function of time (49 days from beginning of test)	97
Figure 6.31: VE 493b - Pressures in boreholes BoBK 5, 15, 16 (Fan B) as a function of time (49 days from beginning of test)	98
Figure 6.32: VE 493b - Pressures in boreholes BoBK 4, 7, 12 (Fan C) as a function of time (49 days from beginning of test)	98
Figure 6.33: VE 493b - Pressure in borehole BoBK 6 (Fan D) as a function of time (49 days from beginning of test)	99
Figure 6.34: VE 493b - Pressures in boreholes BoBK 17 and 18 (Fan D) as a function of time (49 days from beginning of test)	99
Figure 6.35: VE 493b - Pressure in borehole BoBK 8 (measurement with multifunctional probe) as a function of time (49 days from beginning of test with 8 events)	100
Figure 6.36: VE 493b - Pressure in borehole BoBK 8 (measurement with multifunctional probe) as a function of time (3 hours with event 4)	100
Figure 6.37: VE 493b - Temperature and conductivity in borehole BoBK 8 (measurement with multifunctional probe) as a function of time (3 hours with event 4)	101
Figure 6.38: VE 493b - Conductivity in borehole BoBK 8 (manually measured) and borehole BoBK 10 (electronic measurement) as a function of time (49 days from beginning of test)	102
Figure 6.39: VE 493 - Mass balance of tracer	102

	<u>Page</u>
Figure 6.40: Electrical conductivity 0-1 g/l NaCl	103
Figure 6.41: Electrical conductivity 0-10 g/l NaCl	104
Figure 6.42: Electrical conductivity 0-200 g/l NaCl	104
Figure 6.43: FE model for tracer tests (tube flow)	106
Figure 6.44: VE 493 - Transport computation, comparison of conductivities from measurement and model results	107
Figure 6.45: Hydraulic heads in the BK area at beginning of test a) overall view, b) enlargement of segment, c) in "fan" B	110
Figure 6.46: Breakthrough curves of salt tracer at outflow of borehole BoBK 15 and leakage near the location of BoBK 4	111
Figure 6.47: Flow rate at boreholes BoBK 5 and BoBK 15 and leakage as well as injection pressure as a function of time throughout the entire injection phase	112
Figure 6.48: Temperatures at both installed temperature sensors and at the multifunctional probes in borehole BoBK 16	113
Figure 6.49: Temperatures in intervals 2, 3 and 4 of borehole BoBK 9 as a function of time	113
Figure 6.50: Effective fracture aperture as a function of transmissivity acc. to equation 6.3 for various degrees of relative roughness	115
Figure 6.51: Beginning of breakthrough curve for salt tracer (scale on right) and its derivation (scale on left) for extraction borehole BoBK 15	116
Figure 6.52: Temperature curve within extraction borehole BoBK 15 after 225 h (scale on right) and its derivation (scale on left)	117
Figure 6.53: Mass balance - Amount introduced into borehole BoBK 5 and removed from extraction borehole and most important leakage as well as a cumulative curve of entire amount removed up to end of the experiment	118
Figure 6.54: Thermal conductivity of core samples from borehole BoBK 15 taken near the most important fracture at a depth of 25 m as a function of temperature	120

	<u>Page</u>
Figure 6.55: a) Thermal conductivity of core samples from borehole BoBK 15 as a function of distance from the fracture with air as pore filling (dry) and water as pore filling (wet) b) Effective porosity of the same core samples determined according to equation 6.5 as a function of distance from the fracture	120
Figure 6.56: Model geometry of source-sink stream in a fracture	122
Figure 6.57: Thermal breakthrough time as a function of thermal conductivity for various fracture apertures ($q = 1.5$ l/min)	126
Figure 6.58: Thermal breakthrough time as a function of flow rate for various thermal conductivities	127
Figure 6.59: Temperature distribution within (a1-a3) and orthogonal (b1-b3) to the fracture at three different times (1 = 10 h, 2 = 200 h, 3 = 600 h; $q = 0.9$ l/min, $\lambda = 2.9$ W/(m·K), $2w = 3.3$ mm)	129
Figure 6.60: Thermal breakthrough time as a function of distance between source and sink for three different flow rates ($q = q_{inj} = q_{extr}$) ($\lambda = 2.9$ W/(m·K), $tb_{\ominus} = 337$ Std)	131
Figure 6.61: Position and extent of the modelled single fracture in the BK area	132
Figure 6.62: Spatial discretisation, representation of the coupling of 1D matrix elements and 2D fracture elements	132
Figure 6.63: Spatial discretisation of hydraulic conductive elements a) overall, b) source-sink area	133
Figure 6.64: Hydraulic heads (a) and flow rates (b) as isosurfaces for a purely source-sink stream	136
Figure 6.65: Flow field for a purely source-sink stream	136
Figure 6.66: Comparison between modelled and measured breakthrough curve for salt tracer ($k_f = 2.5 \cdot 10^{-4}$ m/s, $2w = 50$ mm)	136
Figure 6.67: Comparison between modelled and measured breakthrough curve for temperature ($\lambda = 2.9$ W/(m·K))	137
Figure 6.68: Hydraulic heads (a) and flow velocities (b) as isosurfaces in the presence of an impermeable barrier ($k_f = 1.5 \cdot 10^{-4}$ m/s, $2w = 10$ mm)	138

	<u>Page</u>
Figure 6.69: Flow field with impermeable barrier between source and sink	139
Figure 6.70: Comparison between modelled and measured breakthrough curve for salt tracer ($D_L = 8\text{ m}$, $D_T = 1\text{ m}$) for borehole BoBK 15	140
Figure 6.71: Comparison between modelled and measured breakthrough curve for temperature ($\lambda = 2.9\text{ W/(m}\cdot\text{K)}$) for borehole BoBK 15	140
Figure 6.72: Comparison between modelled and measured temperature curve for borehole BoBK 16	141
Figure 6.73: Temperature distribution at three different times (a = 50 h, b = 150 h, c = 500 h)	142
Figure 6.74: Hydraulic heads (a) and flow velocities (b) in the presence of a countercurrent ($k_f = 0.9 \cdot 10^{-4}\text{ m/s}$, $2w = 10\text{ mm}$)	144
Figure 6.75: Flow field in the presence of a natural countercurrent	145
Figure 6.76: Comparison between modelled and measured breakthrough curve for salt tracer for borehole BoBK 15 in the presence of a countercurrent ($D_L = 8\text{ m}$, $D_T = 1\text{ m}$)	145
Figure 6.77: Comparison between modelled and measured thermal breakthrough curve ($\lambda = 2.9\text{ W/(m}\cdot\text{K)}$) for borehole BoBK 15 in the presence of a countercurrent	146
Figure 6.78: Comparison between modelled and measured thermal breakthrough curve ($\lambda = 2.9\text{ W/(m}\cdot\text{K)}$) for borehole BoBK 16 in the presence of a countercurrent	146
Figure 6.79: 2D, purely conductively modelled thermal breakthrough curve and measured temperatures in borehole BoBK 9 ($\lambda = 3.5\text{ W/(m}\cdot\text{K)}$) in the presence of a countercurrent	147
Figure 7.1: Repository evaluation procedure	159

LIST OF TABLES

Table 4.1:	File management, PC_MULI	35
Table 5.1:	Inflow sites detected by fluid logging and acc. to PAHL et al. (1992)	65
Table 6.1:	Installation protocol, tracer test VE 483	72
Table 6.2:	VE 483 - Parameter variation in transport computations	77
Table 6.3:	Comparison of parameters in simulation of tracer tests with the finite element (FE) model DURST	78
Table 6.4:	Installation protocol, tracer tests VE 488/489	82
Table 6.5:	Installation protocol, tracer tests VE 492/493	89
Table 6.6:	Hydraulic boundary conditions, tracer test VE 493	94
Table 6.7:	Model parameters for flow computation	105
Table 6.8:	Model parameters for transport computation	107
Table 6.9:	Range of transmissivities observed in boreholes BoBK 5 and 15 as well as mean values and standard deviations	114
Table 6.10:	Model parameters used for the test and sensitivity analysis for λ , $2w$ and q	125
Table 6.11:	Comparison of test and model parameters	128
Table 7.1:	Methods of hydraulic test evaluation	153

1. Introduction and Objectives

1.1 Project Investigations at the BK Site

Geohydraulic investigations are a prerequisite to assessing migration of contaminants and toxic substances in rock formations surrounding engineered repository systems assuming leakage from emplaced waste containers. Tracer tests are used to determine water flow patterns and migration rates of contaminants in fractured rock as dependent on hydraulic gradients, the presence of open fractures in the rock and air inclusions.

Investigation of geological host formations and determination of the hydraulic potential field are essential for defining repository concepts and for site safety analyses. Construction of a repository may induce local mechanical disturbance, resulting in new migration routes in the rock. Such phenomena must be taken into account when assessing site suitability and planning a repository.

Research by Nagra (National Cooperative for the Disposal of Radioactive Waste, Wetztingen), the GSF (Research Centre for Environmental Sciences, Dept. IFT, Braunschweig) and the BGR (Federal Institute for Geosciences and Natural Resources, Hannover) at the Grimsel Test Site in Switzerland aims, on the one hand, to test and develop suitable investigative methods and, on the other hand, to carry out model computations on the basis of measured data. Individual effects are analysed more closely and program codes are validated by means of specific experiments based on predictive calculations.

Following construction of the Grimsel Test Site in 1983, with the objective of collecting experimental data in-situ and evaluating and testing experimental techniques within the framework of site assessment programmes for radioactive waste repositories, the initial phase of the fracture system flow test was concluded in 1987. The second phase was completed at the end of 1990 and a report on the results submitted (PAHL et al. 1992).

Work in the third phase of the fracture system flow test, which was completed at the end of 1993, has essentially been based on the experience and knowledge gained in preceding phases. The work was guided by in-situ experiments at the Grimsel Test Site, as in previous years (Fig. 1.1: Generalised diagram of BK area; Fig. 1.2: Fan arrangement of boreholes in central BK area).

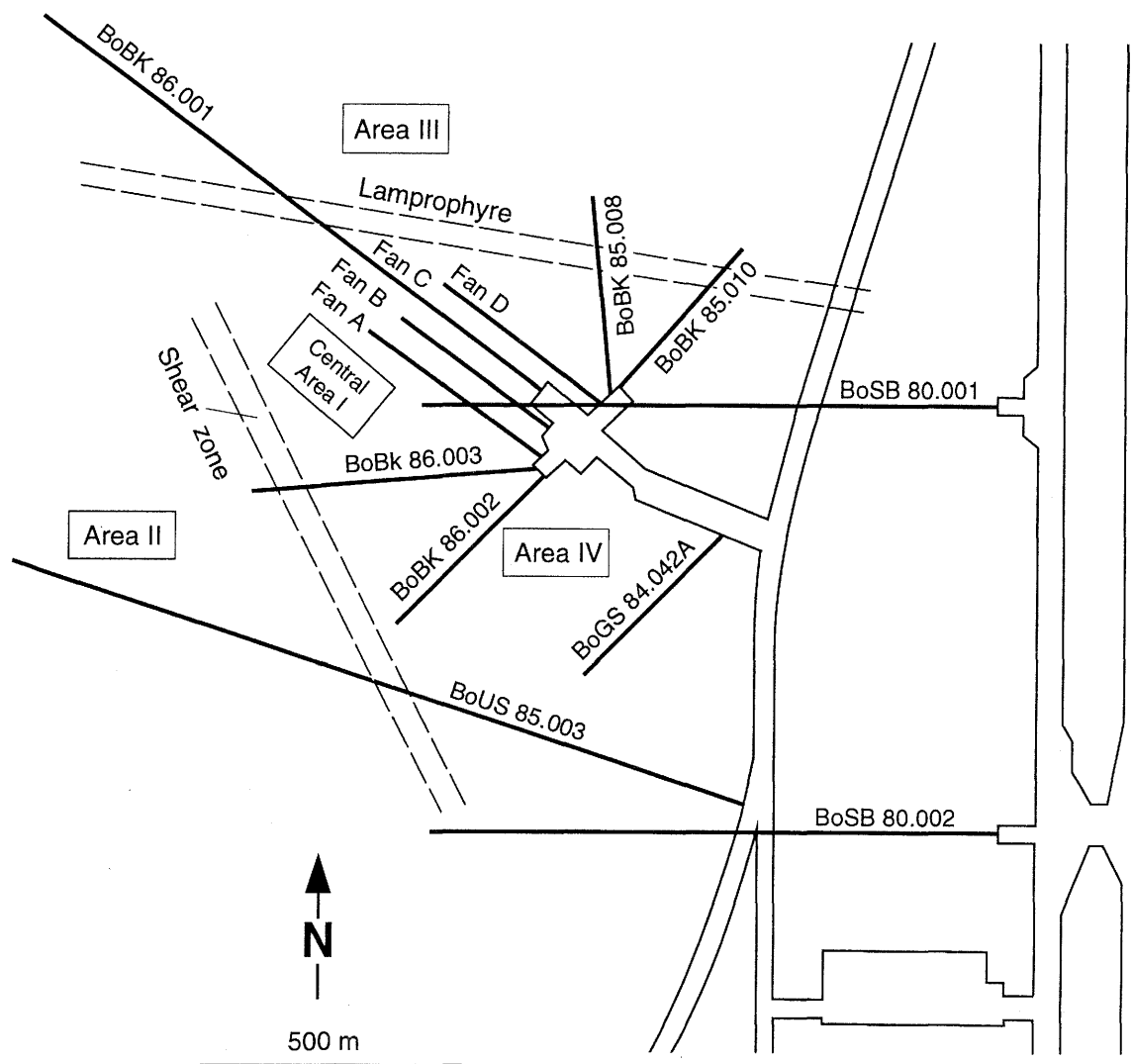


Figure 1.1: Grimsel Test Site - Generalised diagram of BK area

Tracer tests were used for longer flow distances (Section 6). Another area of emphasis was estimating the dependence of transmissivity on stress (Section 5). Aside from the testing itself, work on the mechanical and pneumatic packer systems and the new multifunctional probe systems contributed to automation of procedures (Section 2). Interpretation of the in-situ test data using the numerical FE program DURST/ROCKFLOW was continued. Building on program modules developed in the past years, work also began on models of multiphase flow processes (Section 3). The scope of the pre-processing and post-processing routines was also expanded (Section 4).

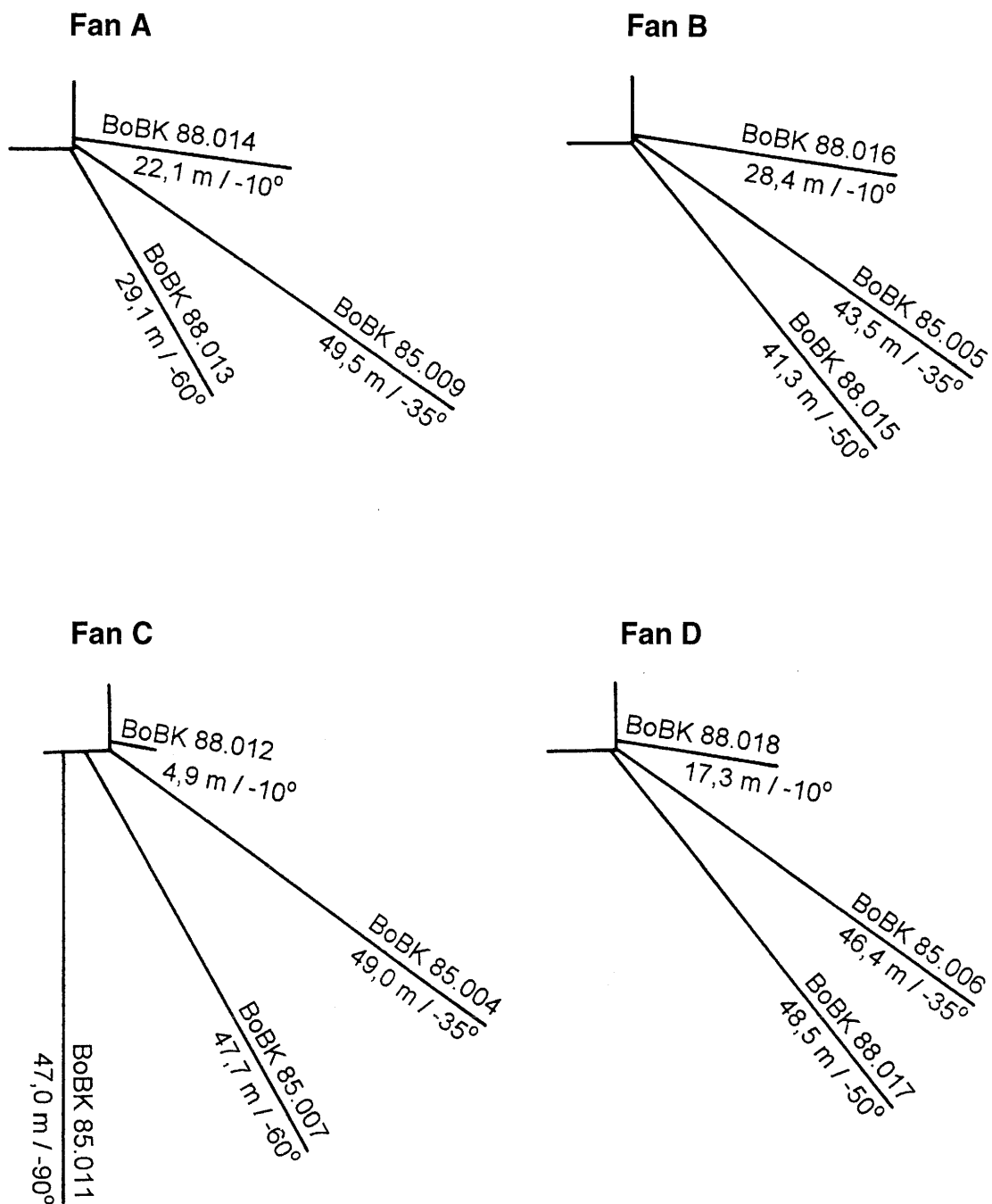


Figure 1.2: Grimsel Test Site - Fan arrangement of boreholes in BK area

Within the framework of this cooperative project, the BGR carried out its own test programme at the BK site in consultation with Nagra; in addition to the general objectives of the research work this programme also addressed specific methods and equipment used to analyse flow parameters, as well as simulation of material transport processes in fractured rock masses.

1.2 Further Investigations at the BK Site

Within the framework of the cooperative project, Nagra carried out its own test programme at the BK site, which, in addition to the general objectives of the research work, also addressed specific matters concerning methods and equipment relevant to developing exploration concepts for the HLW and L / ILW repository programmes.

Fluid Logging in Inclined Boreholes

In inclined boreholes, conventional fluid logging methods for localising water inflow sites and quantifying flow rates are only useful to a certain degree. In the contributory project "Fluid Logging with Fixed Probes", alternative test apparatus and evaluation methods were developed to determine inflow profiles for subhorizontal and high-drift-angle boreholes.

The logging equipment consists of a series of temperature sensors inserted into the borehole via injection tubes; the borehole is then shut in with a packer. In this way, fluid logging experiments can be carried out in the packered borehole interval under differing pressure regimes.

In the fracture system flow test, temperature-fluid logging experiments were carried out using two different probe systems: a sensor cable with PT-100 temperature sensors at 1-metre intervals and a fibre-optical temperature sensor with the same spatial resolution.

The test results show that temperature-fluid logging with a fixed sensor series is a suitable method for locating inflow sites. Analytical evaluation methods were also developed that facilitate quantification of water inflow.

Multiple Source Crosshole Test

In moderately fractured rock formations, performance and interpretation of hydraulic crosshole tests presents special difficulties since the spatial variability of such fracture networks cannot be described with simple deterministic or stochastic models.

Using the complex multipacker apparatus in the fracture system flow test, a test concept was developed that improved the spatial resolution of the hydraulically active fracture structures at the BK site. An essential element of this concept is the performance of short crosshole hydrotests in as many spatially separate boreholes as possible.

Since classical analytical rules prove unsuitable for evaluation of such tests and numerical methods are usually too complicated, a new spectral evaluation method was developed. This method was verified on the basis of synthetic data and, finally, applied successfully to the available field data. It was seen that in particular the "early-

time" period is significant for interpretation of crosshole data. Monitoring of hydrotests carried out in spatially separate boreholes proved to be a sensitive instrument for discriminating between model variations.

Salt/Heat Tracer Test

The two tracers salt and heat are suitable for describing complementary transport properties of fracture networks. The conservative tracer salt migrates along fractures in an advective-dispersive manner, whereas heat also propagates diffusively along the accessible rock surface into the rock matrix. Thus a description of heat transport can contribute to determining the diffusion characteristics of a fracture network.

The salt/heat tracer test at the BK site was realised in the form of a small-scale dipole tracer test (approx. 10 m injection-extraction distance). During the 4-week testing phase, salt concentration, temperature, pressure and flow rates were measured at the injection and extraction holes with a high time resolution; these measurements supplied excellent data sets for subsequent modelling work.

Following conclusion of the actual salt/heat tracer test, the same test apparatus was used in a second tracer experiment in which the injection and extraction boreholes were interchanged. Salt alone was used as the tracer in this reversed flow field tracer test.

The salt/heat tracer test was modelled using the numerical FRACTURE code developed at the ETH Zurich especially for coupled transport.

The modelling work showed that salt transport in the BK fracture network is extremely dispersive. The strong retardation of the thermal breakthrough curve makes it clear that, even over short distances, substance transport does not occur along extensive individual fractures, but rather through a system of subsidiary fracture structures.

Visualisation and Hydrogeological Modelling

An important step in characterising a complex fracture network is derivation of a conceptual model from the measured data obtained in a wide variety of different hydrogeological investigations.

For this purpose, the graphics software AVS was used to create a three-dimensional model of the BK site. This model includes geometric structures in the greater site area (tunnels, caverns, larger geological units) and local structural information gained from core analyses, etc. The model can also integrate the results of hydrogeological investigations (e.g. fluid logging, hydrotests, pressure level monitoring) and be subjected to consistency tests.

Further strategies involved development of complex fracture network models based on analyses which integrate geostructural information and the results of hydraulic crosshole tests.

2. Technical Development of Flow Test Equipment

2.1 Packer and Probe Systems

Figure 2.1 provides an overview of the packer systems used by the BGR at the BK site. Specific test objectives defined measuring equipment requirements and thus the most suitable packer systems in each case.

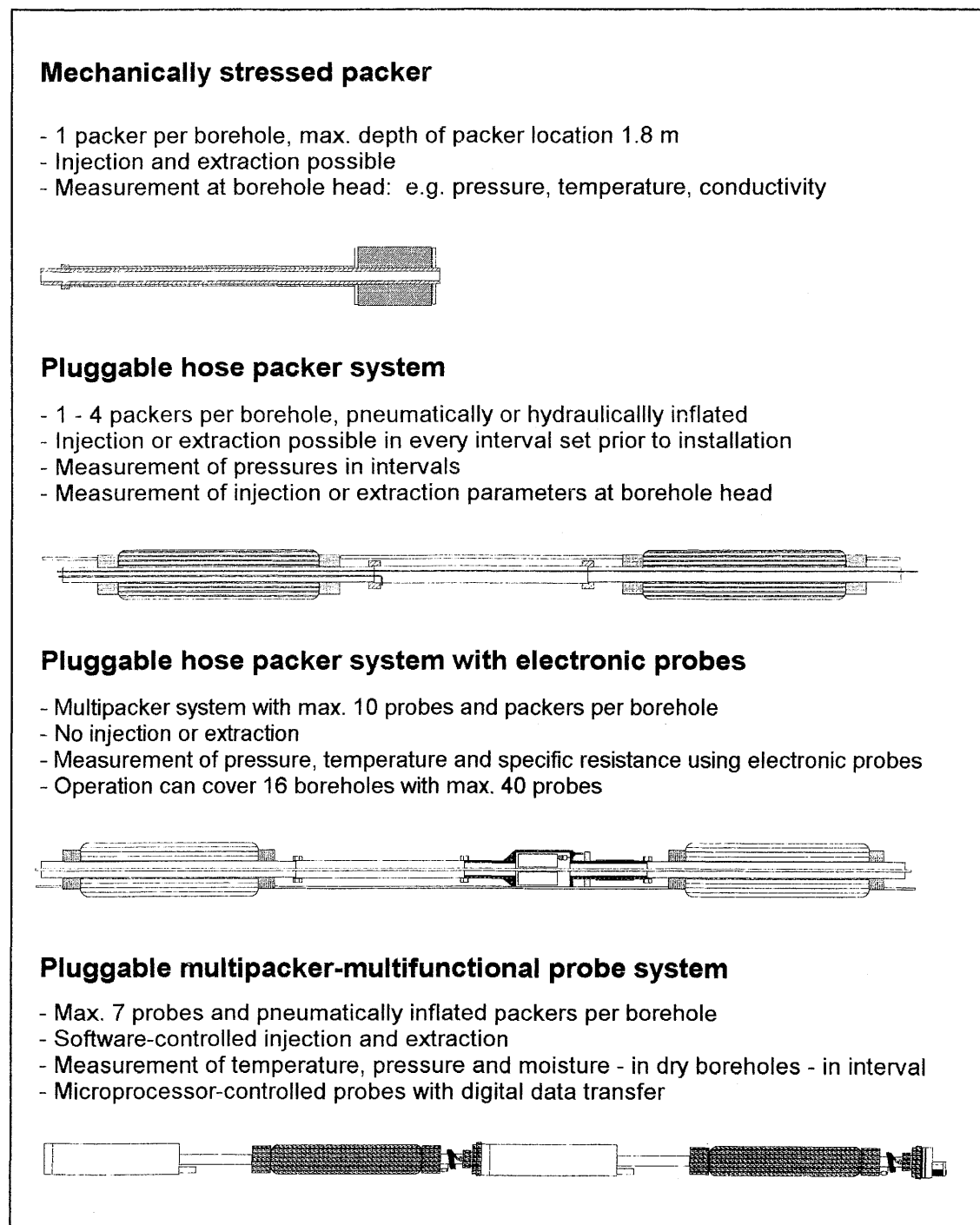


Figure 2.1: Packer systems for flow tests

2.1.1 Mechanical Packers

Mechanical packers are used to shut in boreholes not requiring interval packering for experimental purposes. Currently, sensors can only be installed externally to the boreholes. An alternative method is to carry out injection and extraction through tubes. Mechanical packers are available for borehole diameters of 86, 101 and 146 mm.

2.1.2 Pluggable Hose Packers

A pluggable hose packer system consists of 1 to 4 hydraulically or pneumatically inflated packers. Pressure measurements are carried out externally to the boreholes through capillaries extended into the intervals. Further pressure measurements can be carried out via tubes. Injection and extraction can be performed in an interval of any length as set prior to installation. Subsequent alteration of interval lengths or positions usually means that the entire system has to be dismantled and re-installed, requiring a detailed installation protocol. Interval temperatures are also measured using resistance thermometers in 4-wire versions with 2 triple packers of this type. The measuring cable in the injection tubes is decoupled at the borehole head by means of a pressure-proof sluice. The pressure actually present in the injection interval is not recorded with any degree of precision, since frictional losses within the tubes are very difficult to calculate, especially when higher injection rates are involved.

2.1.3 Pluggable Hose Packers with Electronic Probes (Passive Multipackers)

In pluggable hose packer systems with electronic probes, pressure, temperature and electrical resistance are measured directly by electronic probes installed in the measuring intervals. The individual system components - probes 1 m long, packers 1 to 2 m long and spacer tubes 2 m long - can be installed in any order desired. As many as 10 probes and packers can be used in a borehole. The system thus offers a high degree of flexibility regarding selection of the measuring intervals. Injection and extraction are not possible since the measuring cable is in the tubes. This system is thus only suitable for observation of separate borehole segments and is a passive element in hydraulic testing.

The system has now been shown to be reliable in tests lasting several months. Installation times have been reduced to three boreholes per day, assuming the equipment has been pre-tested. Although in-situ operational times of well over 1 year have been achieved, use in long-term testing is not recommended. Individual defects and subsequent damage could destroy large parts of the test apparatus due to direct electronics-borehole contact and the serial nature of the measuring segment.

2.1.4 Pluggable Multipacker-Multifunctional Probe System (Active Multipackers)

Digital transfer, addressable multifunctional probes are integrated into pluggable multipacker-multifunctional probe systems. The injection line, the compressed air line used to fill the packers and the signal cable all pass through the packer-probe system. Multipackers of this type comprise three different components (Fig. 2.2):

- End probe with plug (bottom probe);
- Probe-packer systems, termed injection probes in the following text;
- End packers with connection plug (top packer).

A complete multipacker requires several injection probes, a bottom probe to close off the testing tube and a top packer providing connections for the supply cables (plugs). The signal cable and the compressed air line are connected to the plug of the top packer external to the injection tube. This facilitates placement of the probe segment at greater depths through the existing, and much more economical, injection tubes. The probes are identical in design and readily interchangeable.

The measuring intervals are connected to the injection line running through the probe segment via computer-controlled cutoff valves. All intervals can be opened and closed at will, facilitating a large number of injection and extraction procedures. In addition, the injection pressures are measured directly at the injection point; this reduces the effects of injection line frictional losses to insignificance.

This system is particularly well-suited for use in rock with low to medium permeabilities and is intended for quick tests due to the short installation time.

In borehole BoBK 85.008, termed BoBK 8 in the following text (this applies to all borehole references), measurements were carried out resulting in uniform data quality using a testing tube of four injection probes over a period of 10 months. Once the packer was filled, an injection ball-valve jammed due to over-stressing of the ball. Removal of the system posed no problems. The electronic components were not damaged in the process. The parallel arrangement of the testing tubes is a major advantage of this system. Potential electronic defects would cut off the probe from the specific lead and thus not block the entire multipacker.

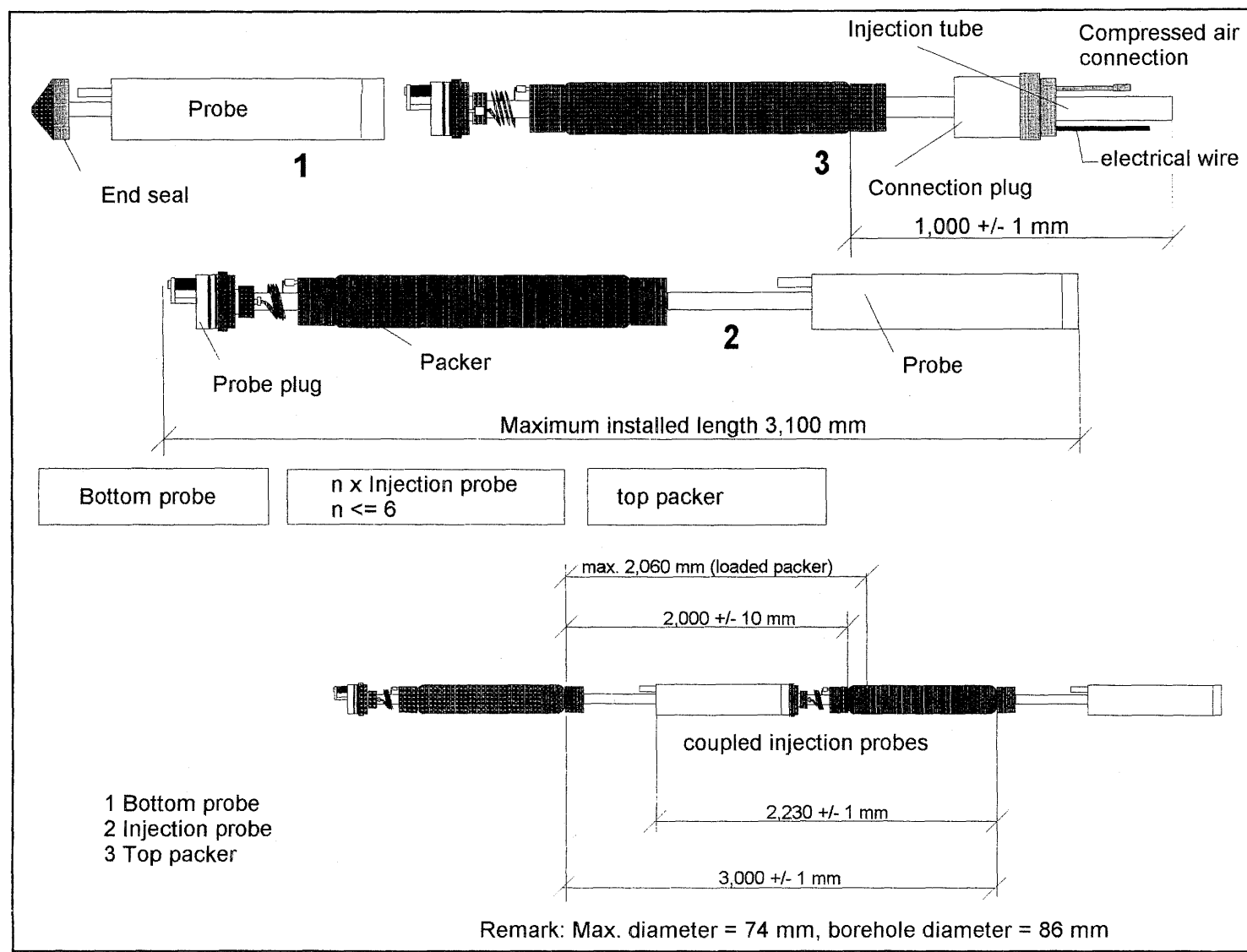


Figure 2.2: Components of multipacker-multifunctional probe system

2.2 Data Acquisition Systems

The data recording systems tested in the fracture system flow test are listed below:

- HP-9000-300 process control computer with Basic 4.0/5.0 and multiprogrammer
Resolution: - Voltage measurement: 0-1 V in 4,095 increments
- Probes: e.g. 0..50°C in 50,000 increments

- Multifunctional probe system with IBM-compatible computer and Geocom interface
Resolution: - Voltage measurement: 0-1.3 V in 65,535 increments
- Probes: e.g. 0..50°C in 16,383 increments (digitised in borehole)

- Datalogger "Hydra PM2526", Fluke
Resolution: - Voltage measurement: 0-300 V in 30,000 increments
- Probes: not possible

2.2.1 Process Control with HP Process Control Computer and Multiprogrammer

In Phase III, central data recording was done on the HP process control computer. The process control computer collates data on temperature, pressure and electrical resistance received from the electrical borehole probes as well as up to 32 additional sets of signals from the BK cavern. The computer-controlled flow tests were also performed with this system. Figure 2.3 shows the data acquisition system.

An HP process control computer controls the testing procedure, monitors the course of the test and logs the measurement data via the peripheral devices. The boreholes in which electronic probes are installed are queried by the HP multiprogrammer, whereby the level converters function as drivers. The time division multiplex probe system, termed pulse-pause modulation, is shown in Figure 2.4. Five leads carry the energy supply to the probes, as well as stimulation and signal transmission in the whole system. Figure 2.5 illustrates the functional principle of the modulator required in every probe. The data measured in the tunnel are standardised to a great extent by various amplifiers and then transferred to the A/D-converter in the multiprogrammer. The flow volume can be regulated in relation to a given value via a digital interface in the multiprogrammer.

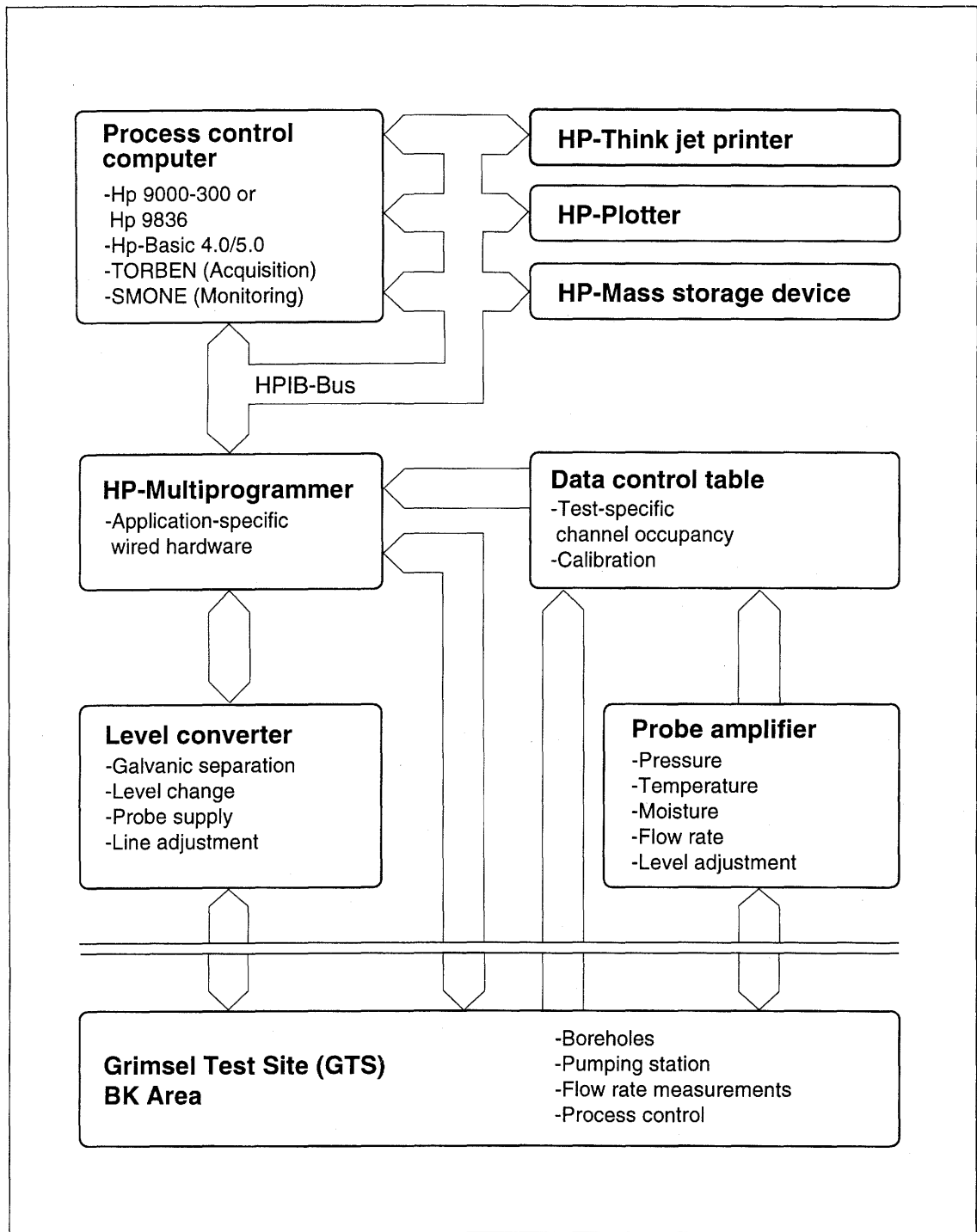


Figure 2.3: Data acquisition system

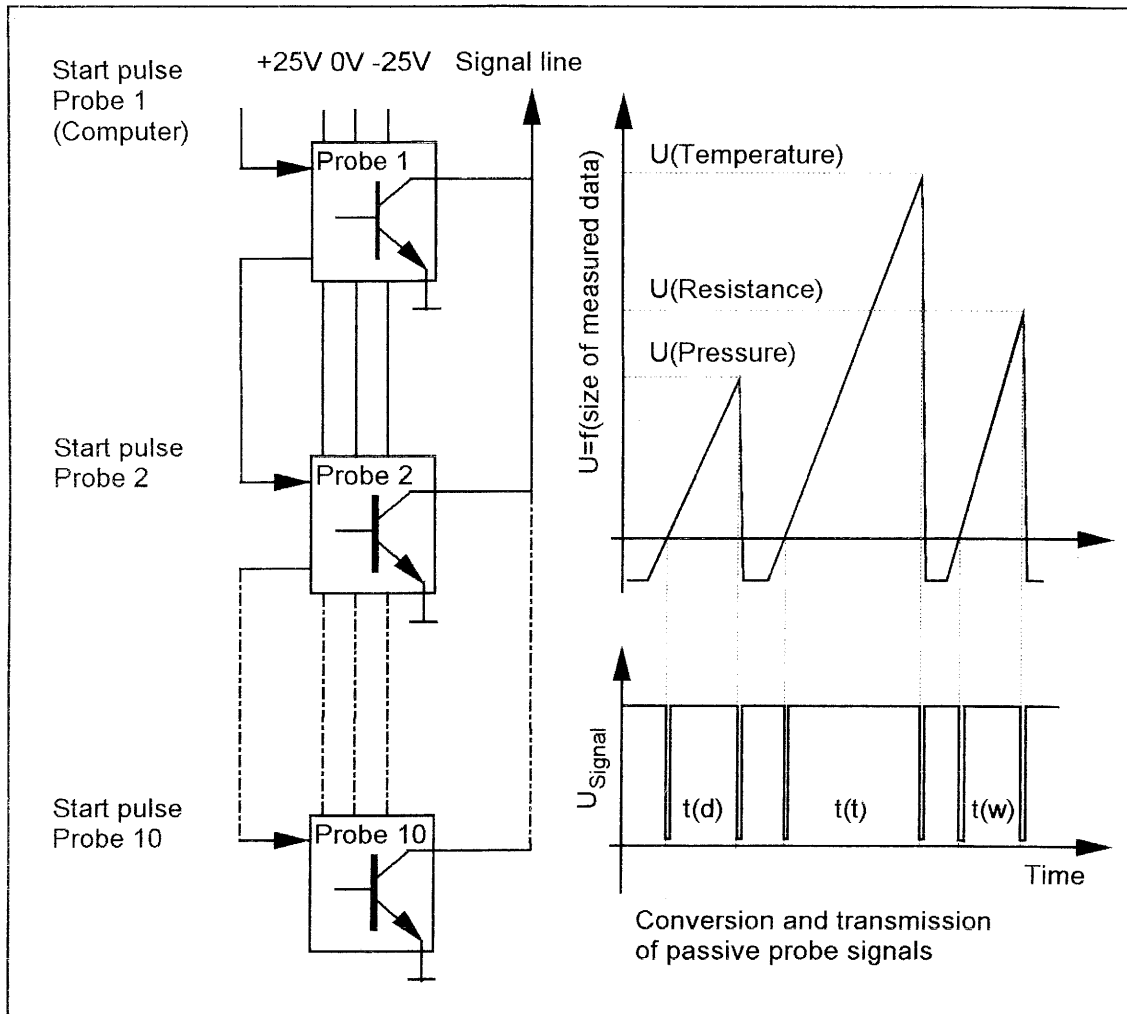


Figure 2.4: Data transmission of passive probes: time division multiplex method

The entire HP data acquisition system was damaged by a lightning strike in August of 1991. All of the stages connected with the boreholes were rendered defective, along with parts of the level converter. Damage to the probes is described in detail in the 1991 annual report (LIEDTKE et al. 1992). Improved lightning protection was thus an objective for the next experimental phase. To increase the operational redundancy of the system, the HP data acquisition equipment that had been used for data processing and testing in Hannover was also installed at the Grimsel Test Site. An additional level converter and two corresponding replacement modules were also installed. A newly developed measuring instrument is now used for probe testing and to support calibration of the electronic probes.

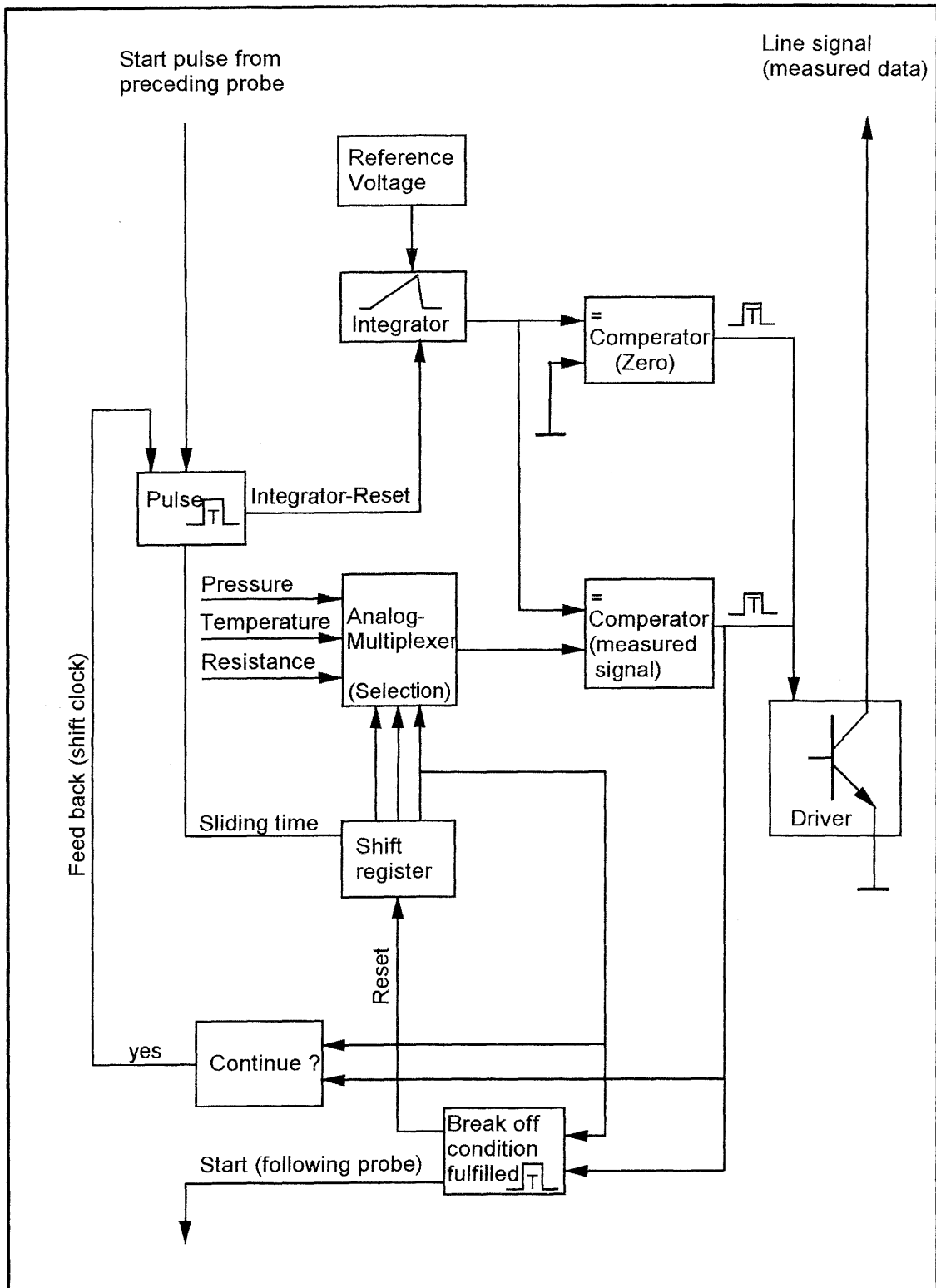


Figure 2.5: Data transmission of passive probes: principle of signal modulation within the probes in time division multiplex method

2.2.2 Data Recording with PC and Multifunctional Probe System

The multifunctional probe system has been subjected to testing and used as a supplementary system in the fracture system flow test since 1991. The compact system (Fig. 2.6) consists of a portable IBM-compatible PC with the MS-DOS measuring and control program PC_MULI, a Geocom interface, a power-pack and, currently, 8 multifunctional probes. Each probe (Fig. 2.7) measures the parameters temperature, pressure, moisture and packer pressure in the intervals, also called segments. In water-filled boreholes, the moisture sensor is replaced by a sealing plug. Probes can be commanded to carry out the functions "open interval", "shut in interval" and "close packer", the latter only prior to shutting in the borehole. Figure 2.8 illustrates the principle of a digital multifunctional probe.

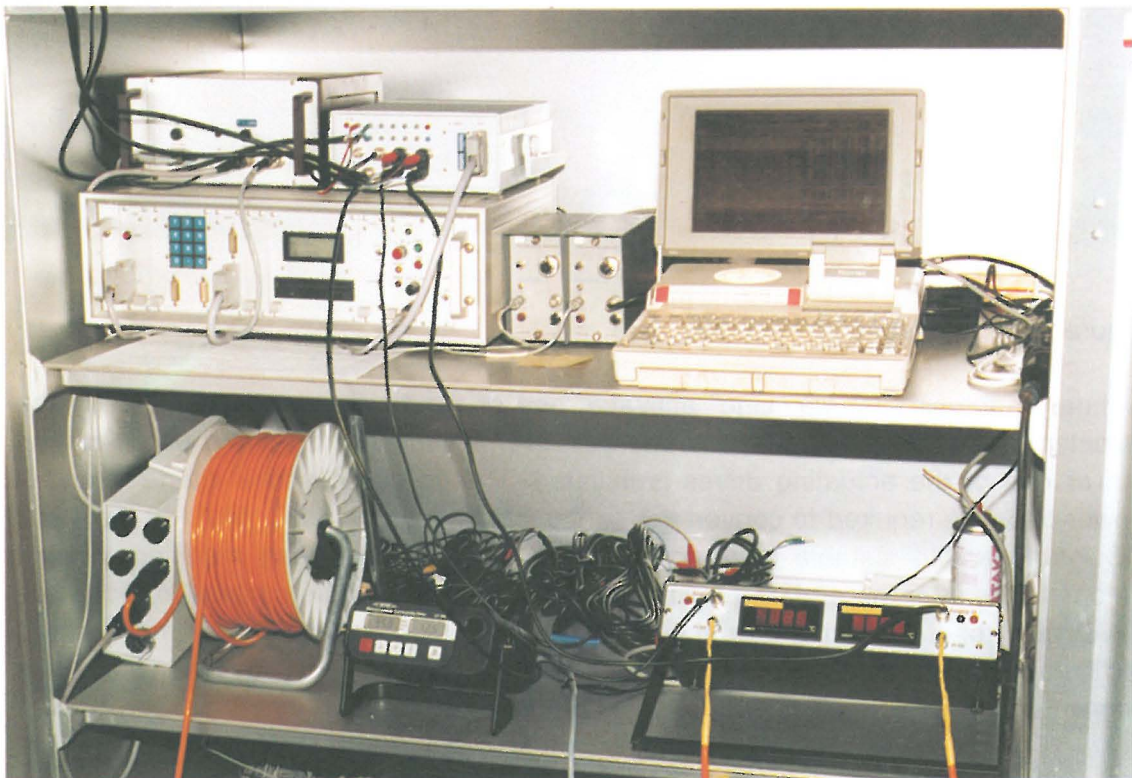


Figure 2.6: Data acquisition using PC for multifunctional probe system

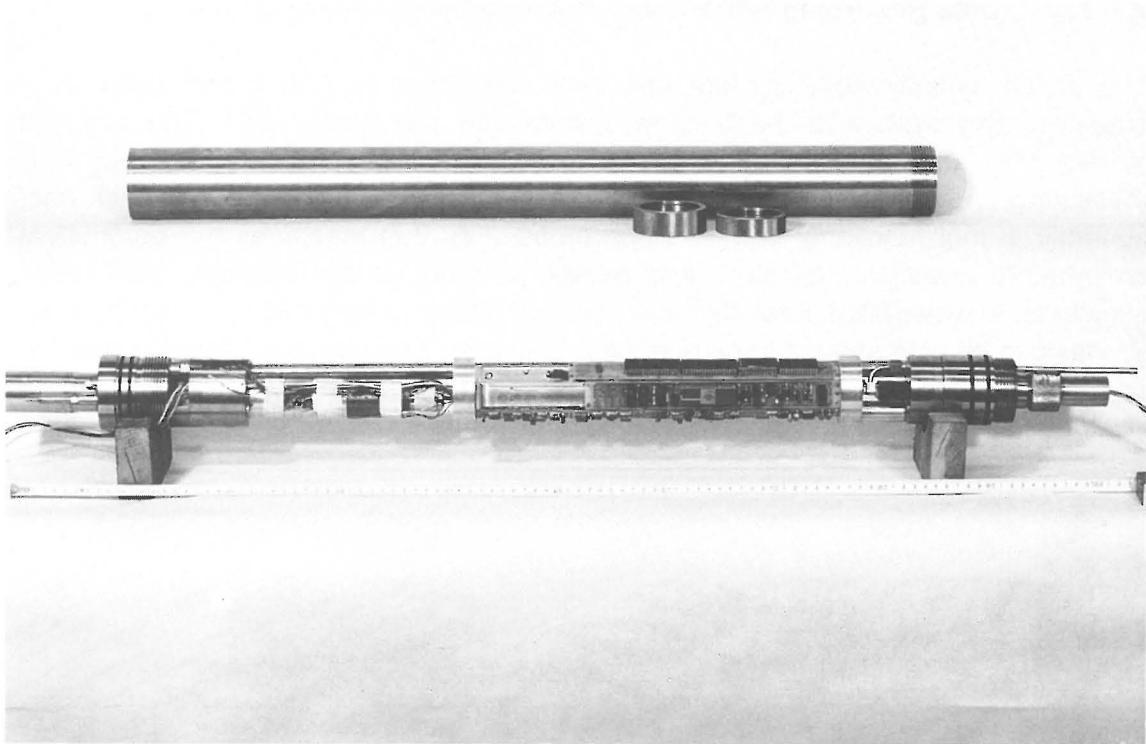


Figure 2.7: Multifunctional probe

A binary address sent via "Line" activates one of the four possible functions in the selected probe. Depending on the address, the measuring program is either carried out or one of the actuating drives is initiated. The so-called active interface and a power-pack are required to convert the control commands from PC_MULI at the serial PC interface into suitable lead signals. The interface has been modified to start automatically after the end of a mains voltage drop off. Suitable calibration aids were developed for the multifunctional probes. A distributor, called a "line multiplexer", facilitates connection of four measuring segments to each interface and also has a connector for additional distributors.

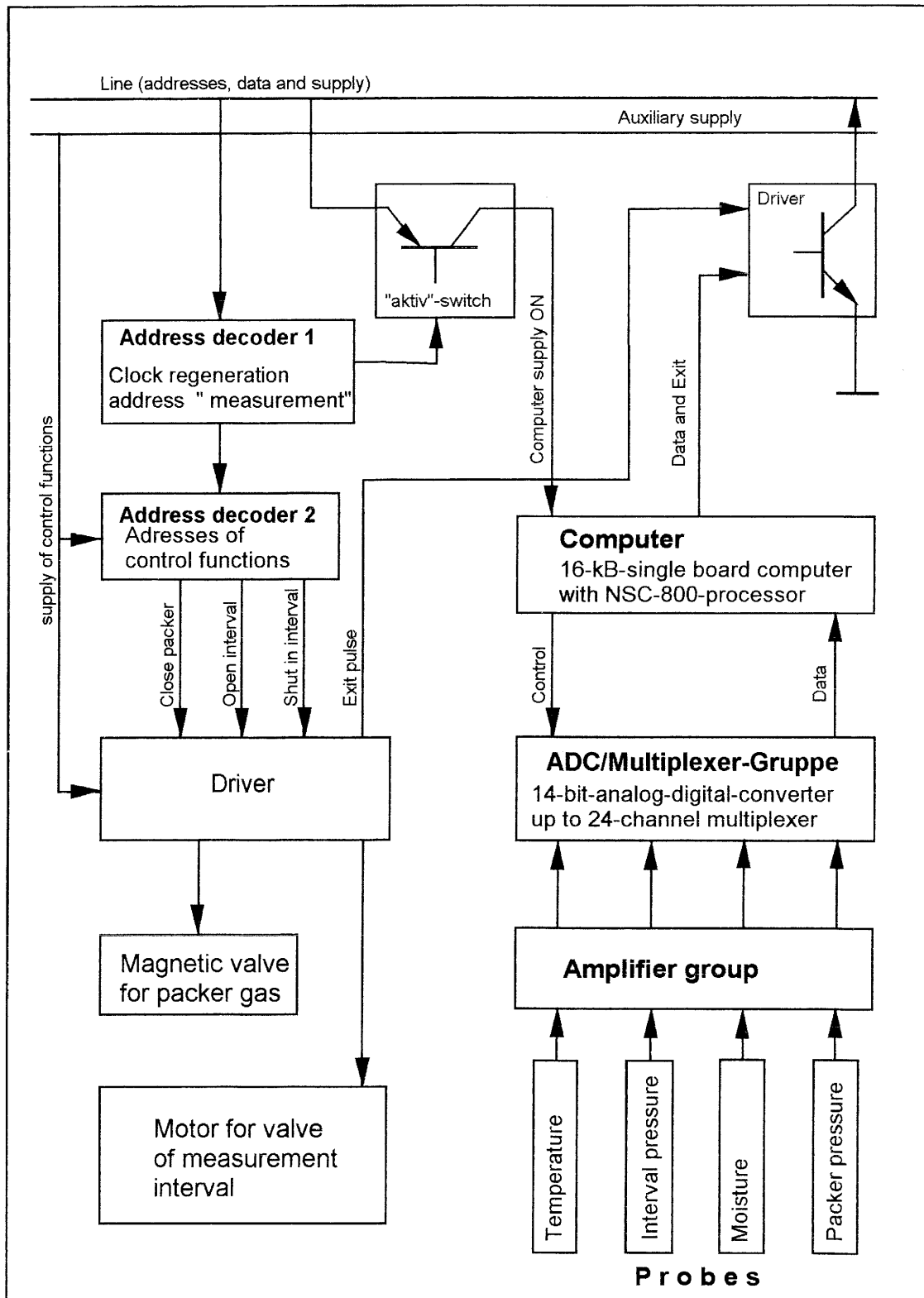


Figure 2.8: Principle of digital transmitting multifunctional probe

2.2.3 Data Recording with Dataloggers

In salt tracer test VE 493, a Fluke "Hydra PM2526" datalogger was used, which proved excellent for datalogging of such minor measuring tasks. The data were transferred using the software provided to the PC via a serial interface. The datalogger has preliminary memory capacity for 2,047 logging cycles with a maximum of 21 parameters expressed in 5 1/2-place form without the PC connection.

2.3 Pump System

During the reporting period, the Hammelmann pump system was replaced by a smaller aggregate installed on a laboratory wagon which was thus more mobile than the old system. The reciprocating pump injects at a maximum rate of 18 l/min, reaching pressures of up to 130 bar. An overcurrent cutoff protects motor and pump and ensures operational availability. A double filter system with 200 µm filters was installed upstream from the pump to prevent artificial obstruction of the fractured rock. The system is capable of injecting continuously for 21 days running without maintenance.

A self-lubricating forced eccentric pump was acquired for long-term testing. The pump characteristics plotted in Figure 2.9 were measured in the laboratory. The aggregate is also mounted on a mobile frame (Fig. 2.10). The manufacturer claims that a constant pumping rate of 20 l/min can be maintained against a pressure of 60 bar. The excess is returned through the pump intake muff via a manually adjusted bypass and not, as previously, returned to the tracer liquid reservoirs. This lightens the load on the filter system and increases in-use times. The actual pumped volume, 28 l/min, is 40% higher than the manufacturer's claim.

2.4 Long-term Perspectives and Future Developments

Optimum combination of the systems makes it possible to carry out even complex experiments extending over several months. When it comes to tests lasting a matter of years, only use of the promising electronic probes in combination with active multipackers would seem to be a realistic proposal on the basis of current technological potential.

Simultaneous recording of all parameters at a sampling rate of 1-10 seconds per measuring cycle as required for the Nagra MSCT experiment is only possible to a limited extent with the available equipment. To achieve a useful frequency analysis of the raw data, the parameters would have to be measured simultaneously or quasi-simultaneously, perhaps at a much higher sampling rate as well, whereby the bandwidth of the signals would have to be limited prior to digitalisation in order to fulfil the conditions for Shannon's sampling theorem. This would require essential changes in the measuring technique used. It must be doubted whether the use of passive multipackers makes sense with the current setup. Here as well, active multipackers

would be more likely to result in further progress. If the sensors were to be installed in the boreholes, instead of in the cavern, sampling rates of 10 measuring cycles per second with 64 channels and a resolution of 16 bits could realistically be expected on the basis of current technology.

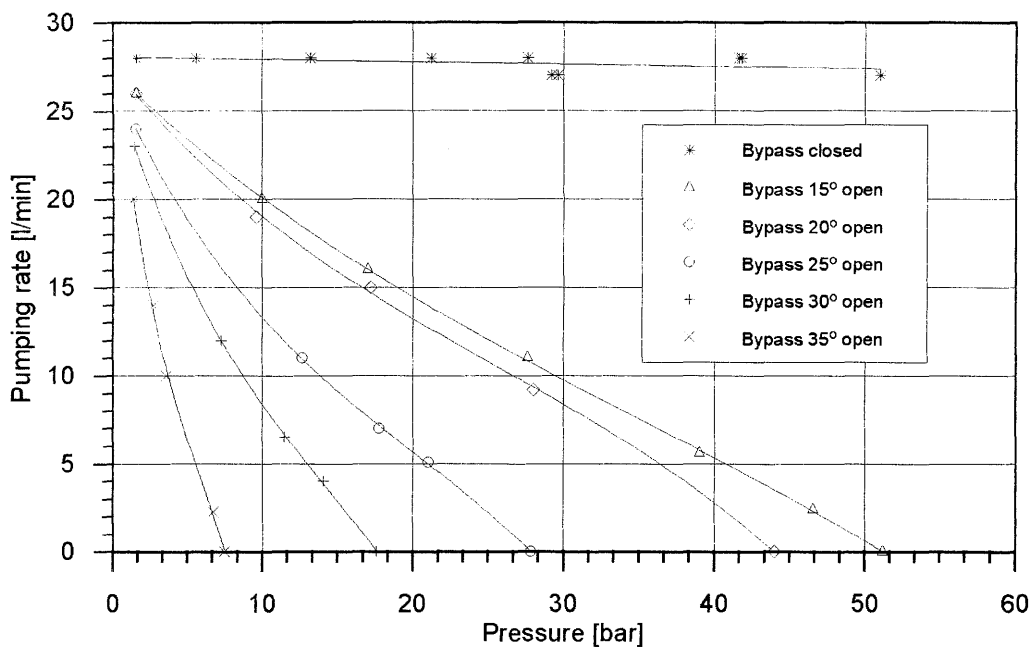


Figure 2.9: Characteristic of excentric pump

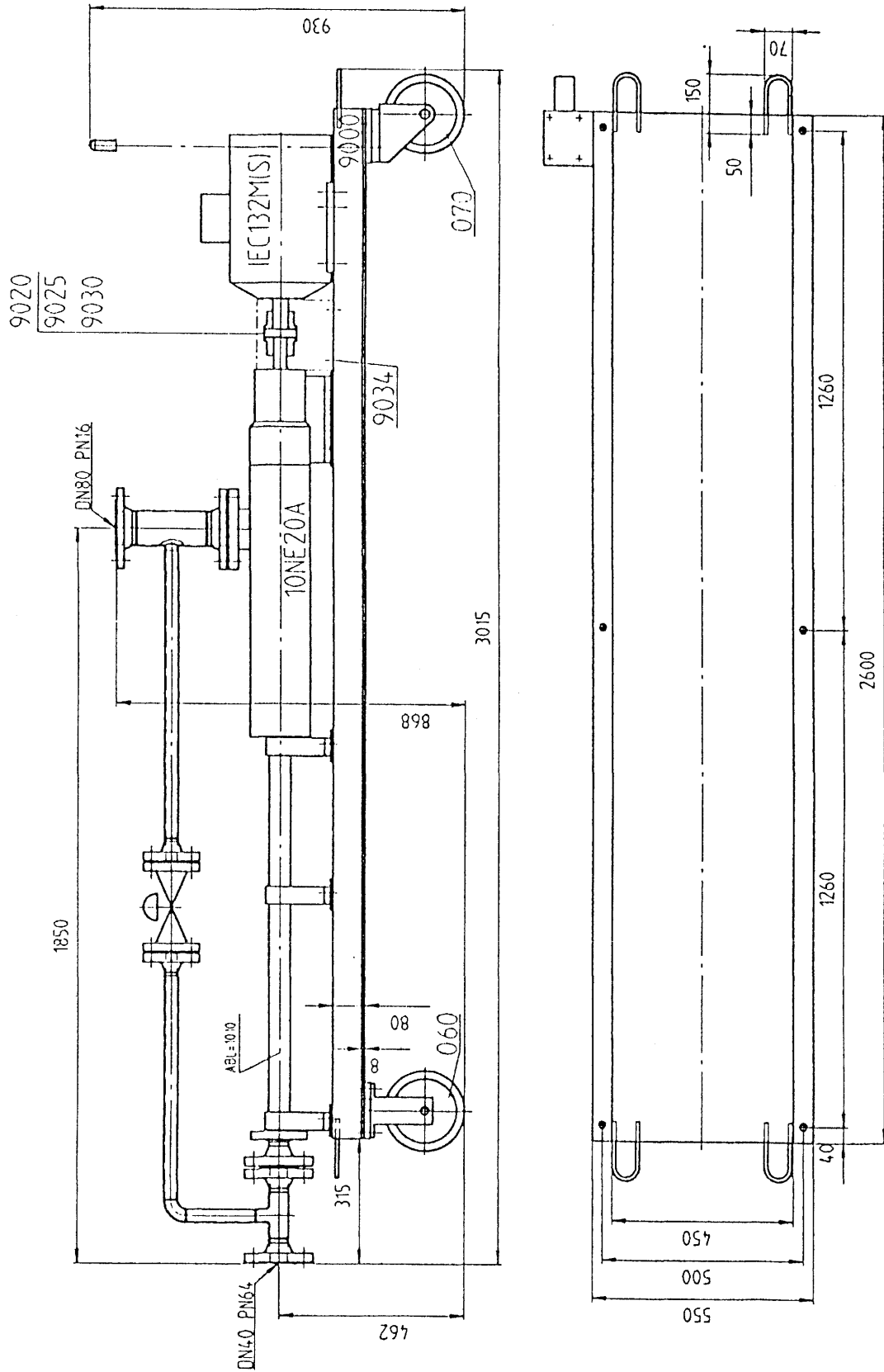


Figure 2.10: Design of excentric pump

3. Theory of Multiphase Flow in Fractured Porous Media

3.1 Principles of Multiphase Flow Processes

3.1.1 General

Multiphase flow is a process involving several mutually immiscible fluids, for example water and oil. Water and gas would be relevant fluids for the GTS rock laboratory. The results of investigations in the BK area suggest that such flow processes may be relevant here. Work therefore began in Phase III on developing the theoretical basis of multiphase flow processes, the objective being to implement the transport mechanisms of multiphase flow in the finite element (FE) program DURST, as well as to use it as an independent module (see also Section 4.2.3 below).

First a concept has to be worked out that covers the existing geological structures. A model approach describing the rock matrix as a porous medium with integral discrete fractures (shear zones) has proved suitable for describing the host rock in this case (HELMIG & ZIELKE 1991). An essential prerequisite for this model concept of fractured rock is the coupling of discrete model elements (fractures, shear zones) with continuous elements (rock matrix).

To obtain a realistic approximation of multiphase flow processes in fractured porous media, the fluid phases as such and their mutual interdependence must be described within the geological framework. Theoretical approaches were formulated and integrated in mathematical formulae reflecting, on the one hand, the relations between capillary pressures and degrees of saturation and, on the other hand, those between relative permeabilities and degrees of saturation for water in fractured systems (HELMIG & MORITZ 1993). The influences of fracture topography can be taken into account by employing a geostatistical (fractal) model (HELMIG 1993).

To integrate in a numerical model the influence of capillary pressure and specific degrees of saturation on multiphase flow behaviour, "capillary pressure / saturation" and "relative permeability / saturation" relations were analysed and processed numerically (HELMIG 1993).

The analytical and semi-empirical formulae used are dependent on a small number of parameters. Several key terms are presented in this Section.

In the free pore space (porosity volume), saturation S_α of phase α is defined as

$$S_\alpha = \frac{\text{Volume of fluid } \alpha}{\text{Total volume of pore space}} \quad (\text{Eq. 3.1})$$

The sum of the saturation levels for all phases present in the pore space is "one".
Residual saturation $S_{\alpha r}$ is the irreducible saturation level for a fluid in the pore space.

- $S_{\alpha} > S_{\alpha r}$ Phase is mobile and continuous, pressure is transmitted
 $S_{\alpha} < S_{\alpha r}$ Phase is discontinuous, pressure is not transmitted

The amount of residual saturation depends on the irregularity of the pore structure. Residual saturation can be explained as a network of capillary tubes as in Figure 3.1: when the two wider tubes are drained by capillary pressure, contact with the water in the contact tube is cut off. The water is then hydraulically isolated and can no longer be pressed out through the horizontal tube.

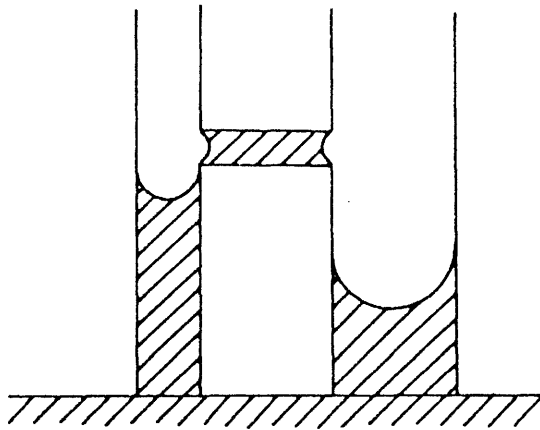


Figure 3.1: Porous medium model

Flow processes of a specific phase can only take place in pore space not occupied by residual saturation. Residual saturation is thus a "dead space volume" for other phases. Saturation of a phase in this area is termed effective saturation, S_e :

$$S_e = \frac{S_w - S_{wr}}{1 - S_{wr} - S_{nr}} \quad (\text{Eq. 3.2})$$

- whereby S_w [-] = Saturation of wetting phase
 S_{wr} [-] = Residual saturation of wetting phase
 S_{nr} [-] = Residual saturation of nonwetting phase

3.1.2 Capillary Pressure Curve

The phenomenon of capillary pressure is required to explain which is the wetting and which the nonwetting phase. Capillary pressure is exerted along the interface between two immiscible fluids. The fluid on the concave side of the membrane-like interface is the wetting phase, that on the convex side the nonwetting phase. In an oil/water system, water is the wetting, oil the non-wetting phase. The pressure curve is discontinuous at the junction between the two fluids for reasons having to do with balance. This difference between phase pressure of fluid 1 and fluid 2 is termed capillary pressure p_c .

$$p_c = p_n - p_w \quad (\text{Eq. 3.3})$$

whereby p_n = Phase pressure of nonwetting phase
 p_w = Phase pressure of wetting phase

The PLATEAU equation (also known as the LAPLACE equation for capillary pressure) describes the relation of surface curvature to capillary pressure:

$$p_c = \gamma \cdot \left(\frac{1}{R_1} + \frac{1}{R_2} \right) \quad (\text{Eq. 3.4})$$

whereby R_1, R_2 [m] = Curvature radii of the surface
 γ [N/m] = Interface tension (temperature-dependent)

Equation 3.4 shows that capillary pressure falls with increasing radii of curvature and is thus inversely proportional to pore width. The relation of saturation S_w and capillary pressure is termed the capillary pressure curve, the course of which depends on the properties of the porous medium as well as those of the phases.

3.1.3 Permeability Curve

The relation of saturation S_w and permeability is termed the permeability curve. The flow of a fluid α through a completely saturated porous medium is described one-dimensionally by Darcy's law:

$$q_\alpha = \frac{k_\alpha}{\mu_\alpha} \cdot \frac{\Delta P_\alpha}{L} \quad (\text{Eq. 3.5})$$

whereby k_α [m²] = Effective permeability
 $\Delta P_\alpha/L$ [-] = Pressure gradient in flow direction
 μ_α [Pa·s] = Dynamic viscosity

The effective permeability depends on the porosity of the conducting medium and the relative width of the pores. In anisotropic conducting media, permeability differs

according to flow direction. The effective permeability is independent of the fluid properties (in contrast to hydraulic conductivity k_f).

Analogous to the terminology of saturation in a two-phase system, relative permeabilities k_{rw} and k_{rn} are used to describe the permeabilities of the wetting (k_{rw}) and nonwetting (k_{rn}) phases. The relation between relative and effective permeability is expressed as permeability under saturated flow conditions k_{sat} :

$$k_{\alpha} = k_{r\alpha} \cdot k_{sat} \tag{Eq. 3.6}$$

whereby $0 \leq k_{r\alpha} \leq 1$

Thus relative permeability depends on the saturation of the phase under observation, since flow of one phase is hindered to the extent the amount of the other phase increases. Figure 3.2 shows the normal course of the permeability curve in a two-phase system. HELMIG (1993):

"The sharp increase in k_{rw} shows that the larger pores are first filled by the nonwetting phase. When S_w drops, the average pore size which is filled by the wetting fluid decreases. This is shown by the rapid drop in k_{rn} . This means that the nonwetting fluid occupies larger pores than the wetting fluid at levels above S_{nr} ."

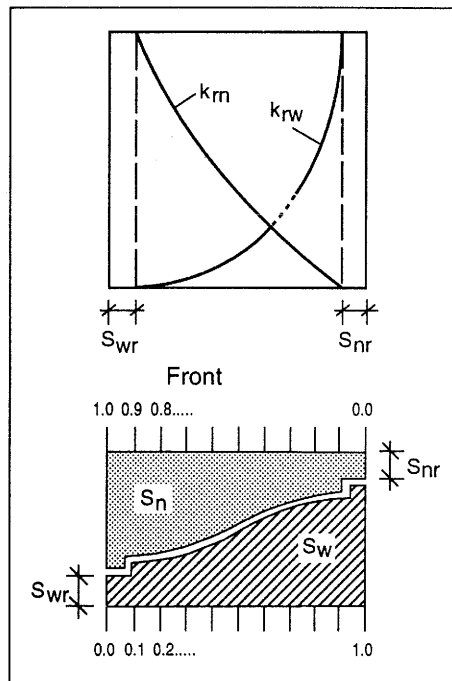


Figure 3.2: Mobile segment of a two-phase flow system (HELMIG 1993)

In the past, work in the field of permeability / saturation relations was dominated by research on two-phase flow of oil and water. Under certain conditions (adsorbed water surrounds the rock completely, lowering the friction coefficient in the flow channels) the relative permeability of the oil is greater than one and thus greater than that seen in saturated fluid. The example demonstrates that the relative permeability / saturation curve must first be determined experimentally for a specified area, then the resulting parameters used to adapt the analytical or semi-empirical formulae.

We will not include derivation of the formulae for a three-phase system here (e.g. oil - water - gas), since this constellation is clearly of minor importance in the GTS area. The equations listed above would be complemented by a component representing the third phase. The equation for saturation would then be:

$$S_w + S_G + S_O = 1 \quad (\text{Eq. 3.7})$$

Capillary pressure curves must be plotted for the three possible interactions of the three phases present. See, for example, the papers by SNELL (1962) and STONE (1970) on experimental derivation of these relations.

3.2 Capillary Pressure / Saturation Relation

On the basis of equation 3.3, capillary pressure is expressed as a function of saturation of the wetting phase in each case:

$$p_c = p_c(S_w) \quad (\text{Eq. 3.8})$$

This function depends on specific soil and phase parameters, which are incorporated in the formula as surface tension and angle between surface of wetting phase and fracture wall. The geometry of the pore space, and thus saturation, is taken into account in the radius r . It is thus impossible to determine the relation between capillary pressure and saturation analytically. Extensive scientific experiments, particularly in the fields of soil physics and deposit exploration, aim at simple empirical formulae with as few parameters as possible. Figure 3.3 shows various approaches after BROOKS & COREY (1964) and LEVERETT (1941), as well as the linear dependence for comparative purposes.

The linear function is described by equation 3.9:

$$p_c = \begin{cases} -p_{cmax} & \text{for } S_w \leq S_{wr} \\ -p_{cmax} \cdot \frac{S_{wmax} - S_w}{S_{wmax} - S_{wr}} & \text{for } S_{wr} \leq S_w \leq S_{wmax} \\ 0 & \text{for } S_w \geq S_{wmax} \end{cases} \quad (\text{Eq. 3.9})$$

whereby p_c [Pa] = Capillary pressure
 p_{cmax} [Pa] = Capillary pressure at saturation S_{wr}
 S_{wr} [-] = Residual saturation
 S_{wmax} [-] = Maximum saturation ($S_{wmax} > S_{wr}$)
 = $1 - S_{nr}$

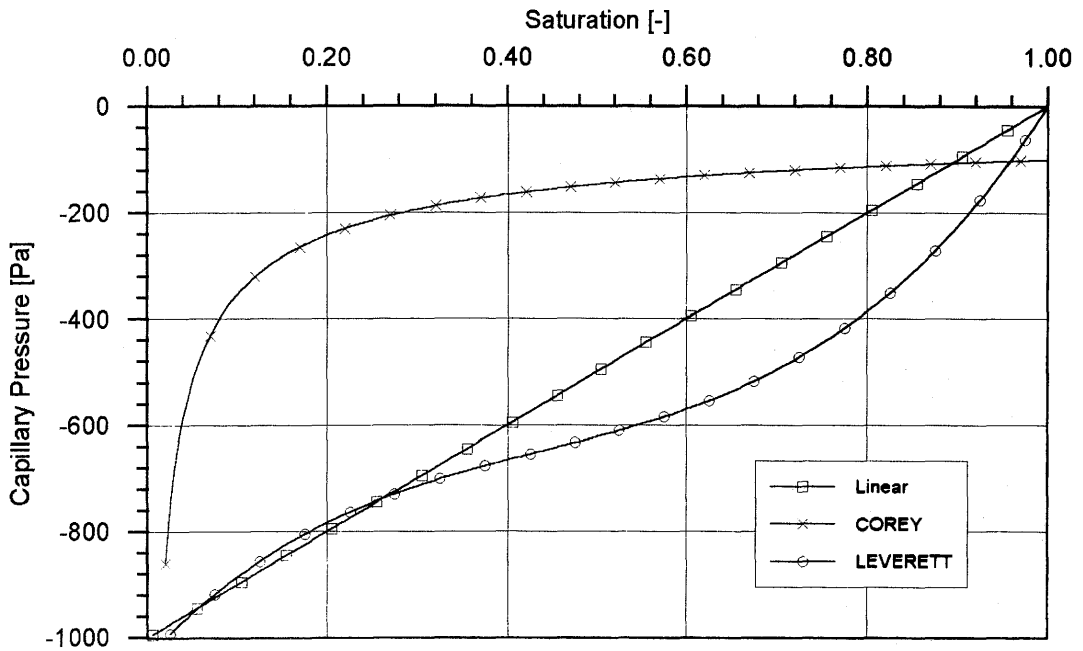


Figure 3.3: Capillary pressure / saturation functions
 a) Linear, b) COREY curve, c) LEVERETT function

The capillary pressure / saturation relations integrated in ROCKFLOW stem from the work of BROOKS & COREY (1964) on movement of water in non-saturated soil zones:

$$p_c = -p_b \cdot \left(\frac{1}{S^*} \right)^{\frac{1}{\lambda}} \tag{Eq. 3.10}$$

whereby $S^* = \frac{S_w - S_{wr}}{1 - S_{wr}}$ (Eq. 3.11)

p_b [Pa] = Bubbling pressure, lowest gas phase pressure
 (p_b is assumed as lowest capillary pressure)
 λ [-] = Pore size distribution index

LEVERETT (1941) describes a dependence between capillary pressure and saturation similar to the COREY formula, which, however, leads to a different curve shape (see Fig. 3.3). The LEVERETT function is:

$$p_c = -p_b \cdot \sigma(T) \cdot f \quad (\text{Eq. 3.12})$$

$$\text{whereby } f = 1.417(1 - S^*) - 2.120(1 - S^*)^2 + 1.263(1 - S^*)^3 \quad (\text{Eq. 3.13})$$

after PRUESS (1987)

and $\sigma(T)$ [N/m]= Surface tension

In the paper by VAN GENUCHTEN (1980), capillary pressure / saturation relations as well as relative permeability / saturation relations are presented as analytical solutions for non-saturated soils (see Section 3.3). Saturation S_e' is related to the matrix potential by the following equation:

$$S_e' = \frac{S_w - S_{wr}}{1 - S_{nr} - S_{wr}} \cdot \left[\frac{1}{1 + (A|p_c|)^B} \right]^\lambda \quad (\text{Eq. 3.14})$$

whereby S_{nr} [-] = Residual gas saturation
 S_{wr} [-] = Residual water saturation
 A, B [-] = Curve adapting parameters
 λ [-] = $1 - 1/B$

Parameters A and B were determined by VAN GENUCHTEN for different porous media. PRUESS (1987) used equation 3.14 in the TOUGH code so that only the forming parameter λ is required to calculate the capillary pressure.

$$p_c = \begin{cases} 0 & \text{for } S_w \geq S_{wmax} \\ -p_o \cdot \left\{ [S_e']^{-1/\lambda} - 1 \right\}^{1-\lambda} & \\ -p_{max} & \text{for } p_o \cdot \left\{ [S_e']^{-1/\lambda} - 1 \right\}^{1-\lambda} \geq p_{max} \end{cases} \quad (\text{Eq. 3.15})$$

$$\text{whereby } S_e \text{ [Pa]} = \frac{S_w - S_{wr}}{S_{wmax} - S_{wr}} \quad (\text{Eq. 3.16})$$

p_{max} [Pa] = Maximum capillary pressure
 p_o [Pa] = Initial pressure
 S_{wmax} [-] = $1 - S_{nr}$

Equation 3.16 in VAN GENUCHTEN's theoretical approach resembles the formula for S^* in the approach of BROOKS & COREY, but uses the expression for maximum saturation instead of the value "one" in equation 3.11.

3.3 Relative Permeability / Saturation Relation

The literature contains several concepts for describing the connection between relative permeability and saturation. Most of these approaches are derived from in-situ experiments involving two-phase flow in porous media. In some cases, curve adaptation parameters are used which, strictly understood, apply only to the area under investigation and therefore require verification by field data for other areas. Examples of the various approaches include:

- The linear function (eq. 3.17, 3.18)
- Method acc. to HUYAKORN & PINDER (1978) (eq. 3.19, 3.20)
- Method acc. to GRANT (1977)
- Method acc. to FATT & KLIKOFF (1959) (eq. 3.21, 3.22)
- Method acc. to BROOKS & COREY (1964) (eq. 3.23, 3.24)
- Method acc. to BURDINE (1953),
- Method acc. to VAN GENUCHTEN (1980) (eq. 3.25, 3.26).

The simplest approach to describing the dependence between relative permeability and saturation is the linear relation, for wetting ($k_{rw} = f(S_w)$) between S_{wr} and S_{wmax} as well as for the nonwetting phase:

$$k_{rw} = \begin{cases} 0 & \text{for } S_w < S_{wr} \\ \frac{1}{S_{wmax} - S_{wr}} \cdot S_w - \frac{S_{wr}}{S_{wmax} - S_{wr}} & \text{for } S_{wr} < S_w < S_{wmax} \\ 1 & \text{for } S_w > S_{wmax} \end{cases} \quad (\text{Eq.3.17})$$

$$k_{rn} = 1 - k_{rw} \quad (\text{Eq.3.18})$$

HUYAKORN & PINDER (1978, cited in HELMIG 1993) selected a slightly less linear relation. The saturation limits S_{wr} and S_{nr} are both set at 0.2, resulting in the following relations:

$$k_{rw} = \begin{cases} 0 & \text{for } S_w < 0.2 \\ \frac{(S_w - 0.2)^2}{0.36} & \text{for } 0.2 < S_w < 0.8 \\ 1 & \text{for } S_w > 0.8 \end{cases} \quad (\text{Eq. 3.19})$$

$$k_{rn} = \begin{cases} 1 & \text{for } S_w < 0.2 \\ \frac{(0.8 - S_w)^2}{0.36} & \text{for } 0.2 < S_w < 0.8 \\ 0 & \text{for } S_w > 0.8 \end{cases} \quad (\text{Eq. 3.20})$$

FATT & KLIKOFF (1959) carried out extensive experiments to determine the influence of partial soil saturation on multiphase flow. This work was occasioned by observation of flow processes in oil reservoirs and benefited from experience with simulation of such processes. PRUESS (1987) summarised the results obtained by FATT & KLIKOFF and arrived at the relation:

$$k_{rw} = (S^*)^3 \quad (\text{Eq. 3.21})$$

$$k_{rn} = (1 - S^*)^3 \quad (\text{Eq. 3.22})$$

whereby S^* as in equation 3.11

Reference was made in section 3.2 to the work of BROOKS & COREY (1964) on investigations of two-phase gas - water flow. The authors define relative permeability of a wetting fluid as follows using equation 3.16 and the definition of S_e therein:

$$k_{rw} = \left[\frac{S_w - S_{wr}}{1 - S_{wr} - S_{nr}} \right]^4 = [S_e]^4 \quad (\text{Eq. 3.23})$$

The following equation applies to relative permeability of the nonwetting fluid:

$$k_{rn} = [1 - S_e^2] \cdot [1 - S_e]^2 \quad (\text{Eq. 3.24})$$

GRANT (1977) arrives at a 4th-order potentiation for the wetting phase, as proposed by BROOKS & COREY, in his investigations of flow behaviour in a geothermal system dominated by fracture flow.

BURDINE (1953) derived a relation between relative permeability and saturation by introducing a curve factor based on grain size distribution. This relation is only useful if the curve factor and the pore radius are known for the wetting and the nonwetting phase. The orders of magnitude for these parameters can be determined in the laboratory. HARRINGTON (1949) and GATES & TEMPELAAR-LIETZ (1972) have documented close correlation of BURDINE approaches by means of measurements. It hardly seems possible to use the BURDINE formulae for two-phase flow in fractured rock, in particular for design computations, due to the many different influencing factors that also occur in varying constellations; we mention it here for the sake of completeness.

Reference was made to the work of VAN GENUCHTEN (1980) in section 3.2. The equation for relative permeability, similarly to the capillary pressure function, depends on saturation S_e (eq. 3.16) and a parameter λ that must be determined on the basis of in-situ measurements.

$$k_{rw} = \begin{cases} 0 & \text{for } S_w < S_{wr} \\ \sqrt{S_e} \cdot \left\{ 1 - (1 - [S_e]^{1/\lambda})^\lambda \right\}^2 & \text{for } S_{wr} < S_w < S_{wmax} \\ 1 & \text{for } S_w > S_{wmax} \end{cases} \quad (\text{Eq. 3.25})$$

First approximation, nonwetting phase:

$$k_{rn} = 1 - k_{rw} \quad (\text{Eq. 3.26})$$

Figure 3.4 compares two approaches to a solution for the relative permeability / saturation relation.

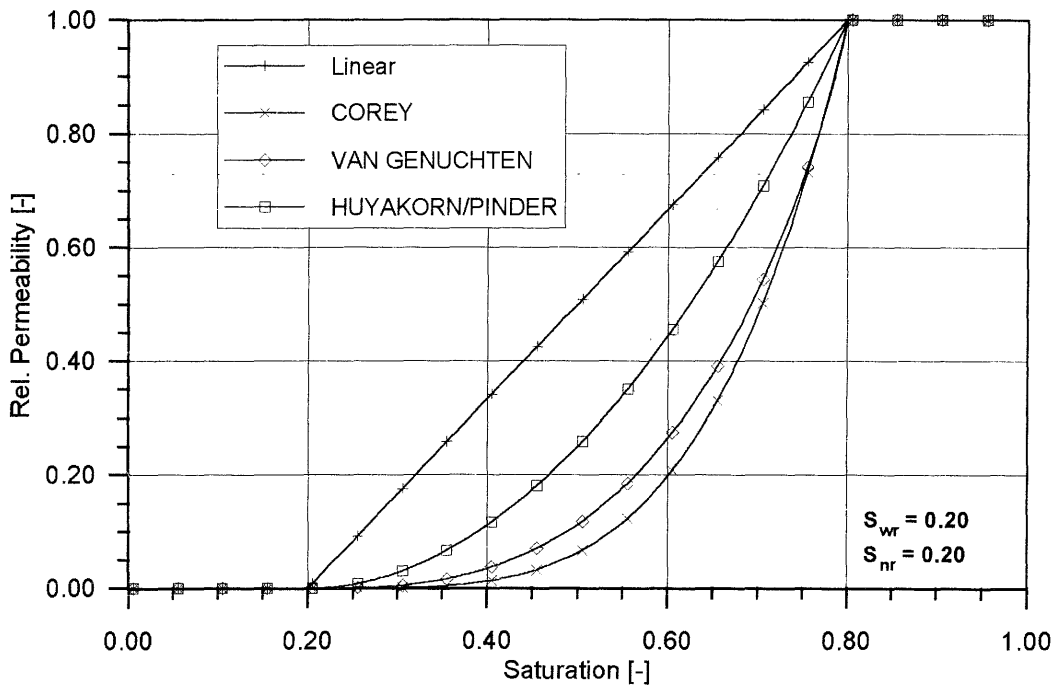


Figure 3.4: Relative permeability / saturation functions

3.4 Multiphase Flow in Fractured Porous Media

The approaches described in the previous Sections to determining the relative permeability / saturation relation and the capillary pressure / saturation relation that generally apply to porous media require revision when the multiphase flow process takes place mainly in single fractures. In general, properties of fractures such as dimensions or aperture are very difficult to determine. Since it is known that the geometry of the fractures is decisive for flow behaviour, it is appropriate to use statistical methods to describe them.

geometry of the fractures is decisive for flow behaviour, it is appropriate to use statistical methods to describe them.

A modelling approach based on "finite plane-parallel plates" makes it possible to describe the fracture pore space in terms of fracture aperture distribution. This means the fracture pore space is understood as a discrete series of small plane-parallel plates with variable apertures.

With the help of such a geostatistical model, PRUESS & TSANG (1990), among others, investigated two-phase flow in a fracture. They formulated the capillary pressure as follows

$$p_c = \frac{\sigma \cdot 2 \cdot \cos \alpha}{b_c} \quad (\text{Eq. 3.27})$$

whereby σ [-] = Standard deviation
 b_c [m] = Fracture aperture
 α [rad] = Angle between surface of wetting phase and fracture wall

WANG & NARASIMHAN (1985) designate the fracture aperture as "cut-off aperture" (b_c), meaning the fracture aperture that must not be exceeded if the fracture is to be filled with water.

$b \leq b_c$: wetting phase

$b \geq b_c$: nonwetting phase

PRUESS et al. (1990) formulate as follows for the degree of saturation:

$$S_w = \frac{1}{2} \operatorname{erfc} \left[\frac{\log \bar{b}/b_c + \sigma^2 \cdot \ln 10}{\sqrt{2} \sigma^2} \right] \quad (\text{Eq. 3.28})$$

The saturation of the wetting phase depends here only on the relation between the mean fracture aperture (\bar{b}), cut-off aperture (b_c) and standard deviation σ . Equation 3.28 thus formulates the functional relation between capillary pressure (via b_c from eq. 3.27) and the degree of saturation as dependent on the pore geometry of the fracture.

The decisive influence of fracture topography on permeability and thus on multiphase flow behaviour was not recognised until recent years.

ROMM (1966) was the first to publish results of two-phase flow tests (water - kerosene) in artificial fractures between plane-parallel plates. These investigations presuppose that the permeability of the rock matrix is negligible and that the flow process is propagated along fracture systems only. The result is a linear dependence

between relative permeability and saturation ($k_{rw} = S_w$ and $k_{rn} = S_n$ for $0 < k_{ra} < 1$) and thus

$$k_{rw} + k_{rn} = 1 \quad (\text{Eq. 3.29})$$

More recent studies (PERSOFF et al. 1991 and PRUESS et al. 1990) demonstrate that fracture wall roughness and fracture aperture cannot necessarily be neglected when describing relative permeability. PRUESS & TSANG (1990) demonstrate that the sum of relative permeabilities for the wetting and nonwetting phases may be considerably below "one".

A comparison of the results derived from such theoretical models with those obtained in experimental investigations is one of the objectives of a GTS research project for which approval is pending.

4. Software Development

Efforts in the field of software development concentrated mainly on datalogging with the program PC_MULI and further development of the numerical model DURST/ROCKFLOW.

4.1 Data Acquisition

4.1.1 Graphical User Interface PC_MULI

Concurrently with development of the multifunctional probe system (active multipackers), system control was realised using the graphical user interface PC_MULI installed on an external computer. The software is written in Turbo-Pascal 5.0 and runs on IBM-compatible PCs under MS-DOS.

Figure 4.1 shows the information flow pathways. PC_MULI allows the operator to monitor and influence the process via the interactive graphical user interface. Prior to an experimental run, the computer requires information on the injection probes in use and other on-site sensors. The required data (configuration of experiment, calibration data and channel occupancy) are entered by the operator in dialogue masks, then stored in packed form together with the measured data on the hard disk or diskette in ASCII format (Table 4.1). Copies of all default data are stored in the file group "DEFAU.*".

Process status and measured data are shown on the monitor in rationally organised screen pages (Fig. 4.2). Figure 4.3 shows a compendium of possible program functions. It is not necessary to access the program source text either to configure the experiment or during the experiment. All probe functions can be actuated via menu control during measurement. The graphics can be scaled individually at any time. The program automatically carries out extensive documentation of the experimental work. Most operator errors are detected and corrected.

When the program is run up, all of the initialising information is loaded from the default files and measurement is switched on automatically. Some of the functions are password-protected (i.e. only authorised persons have access), for instance alteration of probe addressing or access to specific probe parameters.

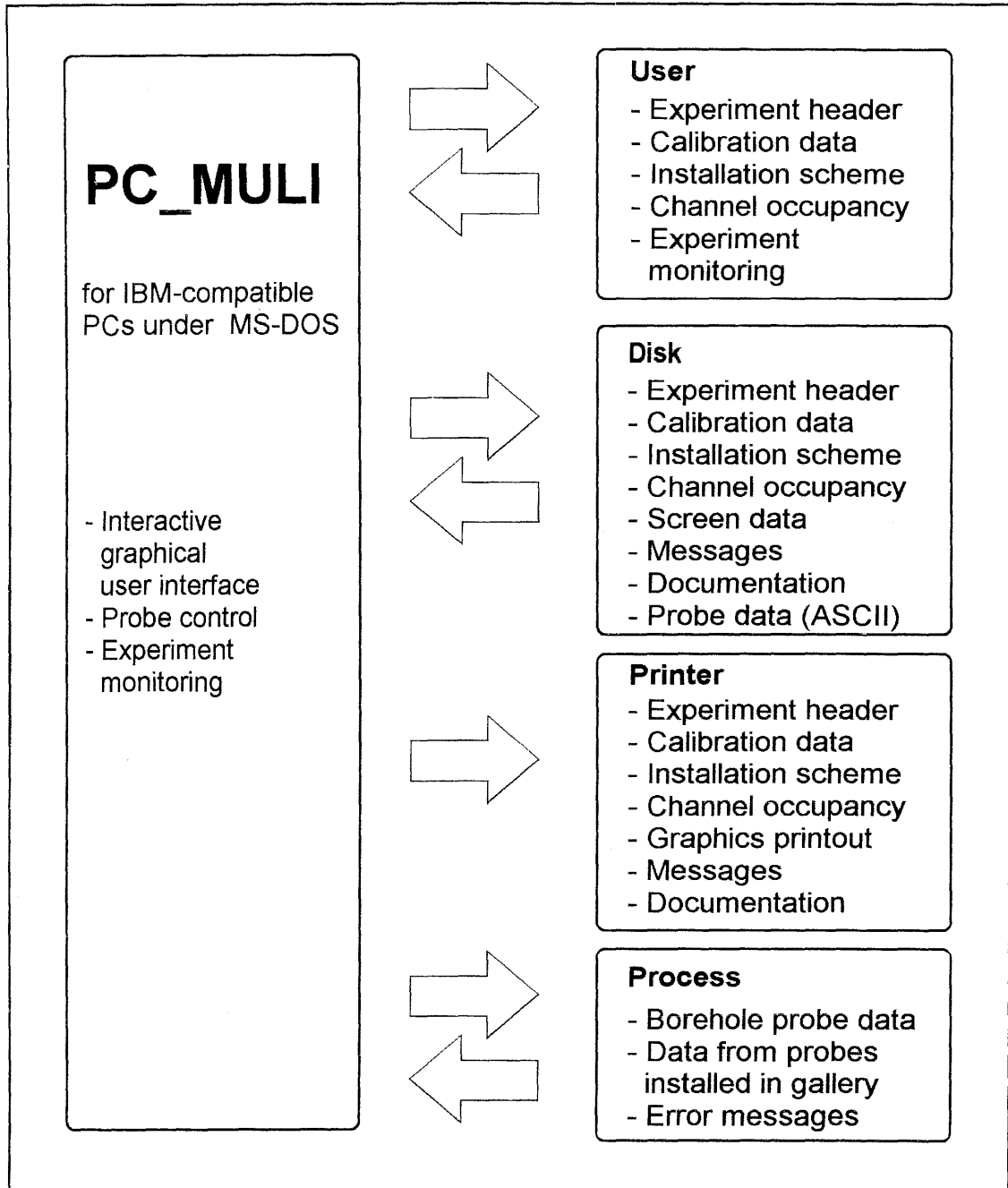


Figure 4.1: Information flow diagram, PC_MULI

Table 4.1: File management, PC_MULI

File group VExx... (xxx = {0,1,999})		
File name = File group + appendix		used appendices
Type of data	Binary (packed)	ASCII (Text)
Header	.HDR	.HDP
Initialisation (calibration, channel occupancy)	.INI	.INP
Experiment configuration (installation scheme)	.KON	.KOP
Data for screen reset	.OUT	
Data from probes installed in the gallery		ANA.DAT
Data of probes installed in boreholes, xx = {1,1,8}		Sxx.DAT
Documentation created by PC_MULI (messages)		.PRO
Documentaion created by user (notices)		.NOT

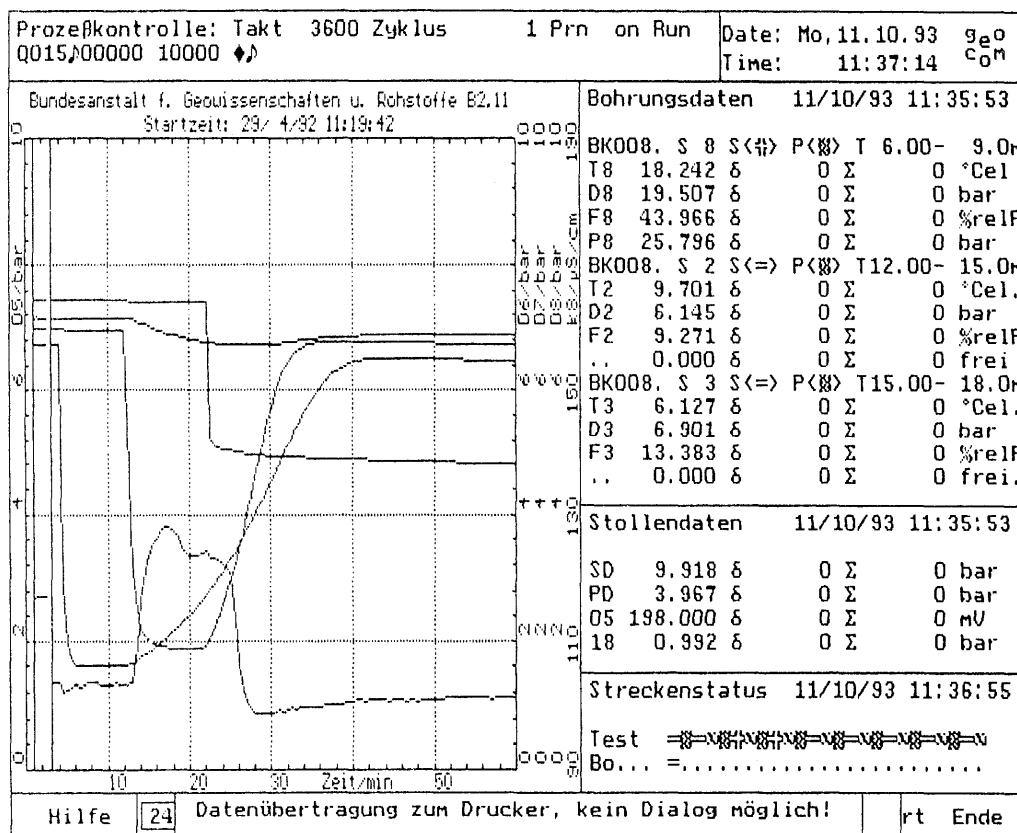


Figure 4.2: Example of screen contents, PC_MULI

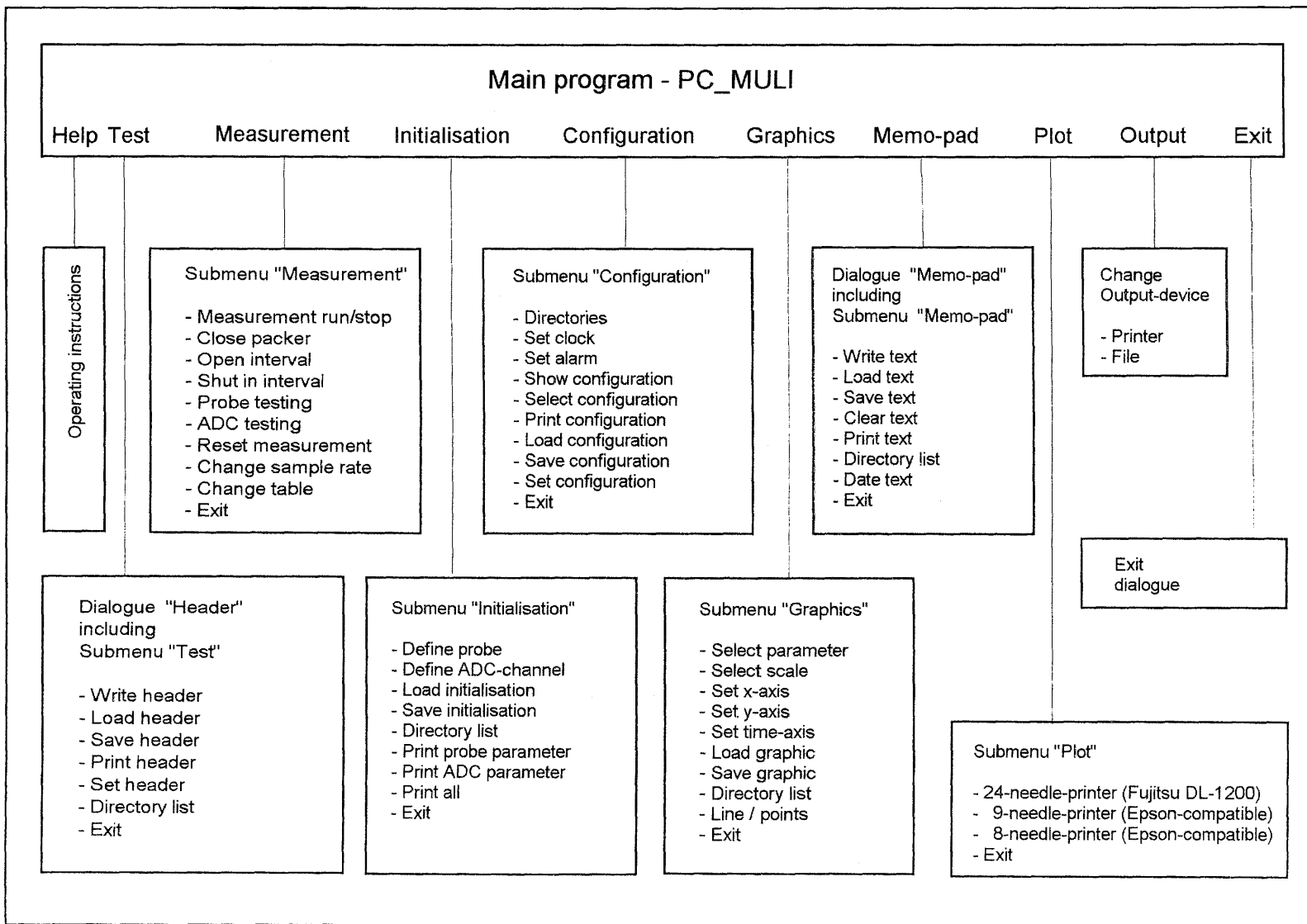


Figure 4.3: Program functions, PC_MULI

4.1.2 Functional Principle

PC_MULI is written 100% in high-level programming language and does not use any direct BIOS calls. This practically eliminates the risk of conflicts with any background programs.

The user interface is controlled via event flags that are continuously sampled in an endless loop. A brief procedure queries the keyboard buffer for keyboard inputs. If a key has been actuated, a procedure is initiated that fulfils the actual measuring procedure, i.e. checks a flag array for incoming events. If a flag has been raised, the function allocated to it is started. Otherwise, the endless loop is processed further. The maximum sampling rate depends essentially on the processing speed of the computer. On the Toshiba T1600 used in-situ, the sampling interval can be shortened to 10 seconds per measuring cycle via the menu. 48 parameters are queried, processed and stored in less than 4 seconds. Thus other functions can be carried out if the computer is not occupied with a priority measuring cycle.

4.1.3 Future Development

Future experiments can be remote-controlled using PC_MULI. The process functions could be controlled by interactive set parameters following a further software expansion. The modular program structure and Turbo-Pascal 5.0 development environment allow for numerous expansion alternatives without exceeding the available RAM capacity.

4.2 Program System DURST/ROCKFLOW

The work on this topic within the framework of the fracture system flow test was carried out in cooperation with the Institute for Flow Mechanics and Electronic Computation of the University of Hannover (Prof. Zielke). The objective was adaptation of the existing DURST programs (e.g. PAHL et al. 1992) to the specific requirements of fracture network modelling and development of a program code for simulation of multiphase flow processes.

All programs in the DURST/ROCKFLOW family run on the VAX computers at the BGR as well as on high-powered IBM-compatible PCs. The use of PCs is particularly advantageous when design computations are to be carried out in-situ at the test site.

4.2.1 Flow Model SM2

No essential improvements were made in the flow model during the report period (LEGE & ZIELKE 1993). The flow model was adapted to the transport model, integrating possible computation of non-steady flow fields.

4.2.2 Transport Model TM2

The description of further developments in the TM2 transport model is taken mainly from the work of LEGE & ZIELKE (1993). The developments concern mainly improvement of user-friendliness and increasing computing speed.

Establishment of an in-core memory plan made it possible to retain much more computation data in the computer's main memory than previously. In numerous simulation runs for program verification, computer performance was seen to have increased by a factor of "2". Conversion of the program to double-precision arithmetic was completed; internal error management was improved. Program code organisation was improved and the user handbook revised to replace the remaining vagaries with precise information. An interface for the DALI graphics system was installed.

4.2.3 Gas Model GM2

The GM2 gas model, the module for gas flow computation in the DURST/ROCKFLOW program, is a further development of the existing gas model GM (ROCKFLOW manual, module GM2, 1993). A CG (conjugated gradient) equation-solver was implemented, the memory techniques converted to complete in-core processing of the problem and the interface format adapted to be compatible with the GSS graphics interface. The gas module is the result of work on multiphase processes in fractured porous media.

The gas model can be used to calculate steady and non-steady gas flow. Pressures and flow volumes that change over time can be entered at any model nodes as boundary conditions. The computation results provided by the GM2 program include nodal pressures, densities and discharge volumes. Darcy velocities per element can also be calculated for set points.

The element types and their spatial arrangement are analogous to the flow model for fluid media (SM2). For use in graphic evaluation, XDALI is a version of the post-processor DALI adapted to gas flow parameters (see Section 4.2.5).

4.2.3.1 General Field Equations

In addition to Darcy's linear law of filtration

$$\begin{bmatrix} v_x \\ v_y \\ v_z \end{bmatrix} = -\frac{1}{\mu} \begin{bmatrix} k_{xx} & k_{xy} & k_{xz} \\ k_{yx} & k_{yy} & k_{yz} \\ k_{zx} & k_{zy} & k_{zz} \end{bmatrix} \cdot \begin{bmatrix} \frac{\delta(p + \rho g z)}{\delta x} \\ \frac{\delta(p + \rho g z)}{\delta y} \\ \frac{\delta(p + \rho g z)}{\delta z} \end{bmatrix} \quad (\text{Eq. 4.1})$$

in vectored form

$$\underline{v} = -\underline{k} \cdot \frac{1}{\mu} \cdot \text{grad} (p + \rho g z) \quad (\text{Eq. 4.2})$$

the continuity equation

$$\phi \frac{\delta \rho}{\delta t} + \rho \left(\frac{\delta v_x}{\delta x} + \frac{\delta v_y}{\delta y} + \frac{\delta v_z}{\delta z} \right) = \rho q \quad (\text{Eq. 4.3})$$

in vectored form

$$\phi \dot{\rho} + \text{div}(\rho \underline{v}) = \rho \cdot q \quad (\text{Eq. 4.4})$$

is used as a basis for calculation of pressures involved in spatial gas flow analysis. The following parameters are defined in the Cartesian coordinate system (x, y, z):

h [m]	= Hydraulic head
	= Pressure head (p/ρg) + geodetic head z [m]
ρ [kg/m ³]	= Gas density as a function of pressure
ρ̇ [kg/(m ³ ·s)]	= Derivation of gas density in time
μ [kg/(m·s)]	= Dynamic viscosity
v _x [m/s]	= Darcy velocity in direction of x axis
v _y [m/s]	= Darcy velocity in direction of y axis
v _z [m/s]	= Darcy velocity in direction of z axis
<u>k</u> [m ²]	= Symmetrical permeability tensor
φ [%]	= Porosity
q [m ³ /s]	= Gas added per unit of volume

Instead of the continuity equation, the equivalent integral equation

$$\int_V \phi \phi \dot{\rho} dV + \int_V \phi \text{div}(\rho \underline{v}) dV = \int_V \phi \rho q dV ; \forall \phi \in T \quad (\text{Eq. 4.5})$$

is used, whereby T represents a certain number of test functions φ that can be explained in the sense of the fundamental lemma of the variational computation. Partial integration results in a weak form of the continuity equation

$$\int_V \varphi \phi \dot{\rho} \, dV - \int_V (\text{grad } \varphi)^T \underline{\rho} \, \underline{v} \, dV = - \int_S \varphi \rho \, v_n \, dS + \int_V \varphi \rho q \, dV; \quad \forall \varphi \in T \quad (\text{Eq. 4.6})$$

whereby V [m³] = Gas carrier volume
 S [m²] = Gas carrier surface volume,
 sum of partial surface areas S_1 and S_2
 v_n [m/s] = Darcy velocity in direction of the external perpendiculars n
 (perpendicular on S , pointing outwards)

In combination with Darcy's laws acc. to equations 4.1 and 4.2, equation 4.6, finally, provides the functional equation

$$\langle \varphi \phi, \dot{\rho} \rangle + b(\varphi, h) = l(\varphi) \quad \forall \varphi \in T \text{ mit } \varphi = 0 \text{ auf } S_1 \quad (\text{Eq. 4.7})$$

$$\text{whereby } \langle \varphi \phi, \dot{\rho} \rangle := \int_V \varphi \phi \dot{\rho} \, dV \quad (\text{Eq. 4.8})$$

$$b(\varphi, h) := \int_V (\text{grad } \varphi)^T \underline{k} \frac{1}{\mu} \rho \text{ grad } (p + \rho g z) \, dV \quad (\text{Eq. 4.9})$$

$$l(\varphi) := - \int_{S_2} \varphi \rho \, v_n \, dS + \int_V \varphi \rho q \, dV \quad (\text{Eq. 4.10})$$

Assuming that

$$b(\varphi, h) = b(h, \varphi)$$

the differential expression

$$\text{div} \left(-\underline{k} \frac{1}{\mu} \rho \text{ grad } (p + \rho g z) \right)$$

is symmetrical. In this case, a semi-discrete functional equation can be generated with the aid of the time integration method, which can be treated as a boundary value problem using the BUBNOW-GALERKIN method (see Section 4.2.3.4).

To formulate the boundary conditions, surface S must be divided into two partial areas S_1 and S_2 . DIRICHLET's boundary condition is to apply to S_1 :

$$h = h_0 \quad (\text{Eq. 4.11})$$

NEUMANN's boundary condition is to apply to S_2 :

$$v_n = - \underline{n} \underline{k} \frac{1}{\mu} \text{grad} (p + \rho g z) = v_{n0} \quad (\text{Eq. 4.12})$$

To obtain a numerical solution of equation 4.7, a semi-discrete functional equation is generated using a time integration method (4.2.3.4), this equation can be treated as a boundary value problem acc. to the BUBNOW-GALERKIN method (4.2.3.5).

4.2.3.2 Ideal Gas Flow

The density ρ of ideal gas can be described by

$$\rho = \frac{M \cdot p}{R_m \cdot T} = \frac{p}{R \cdot T} \quad (\text{Eq. 4.13})$$

whereby M [kg/kmol] = Molecular density
 R_m [J/(kg·J)] = Universal gas constant
 R [J/(kmol·K)] = Special gas constant ($R = R_m/M$)
 T [K] = Absolute temperature

Under isothermic conditions, equation 4.13 can be converted as follows:

$$\frac{\delta \rho}{\delta t} = \frac{1}{R \cdot T} \cdot \frac{\delta p}{\delta t} \quad \text{oder} \quad \dot{\rho} = \frac{1}{R \cdot T} \cdot \dot{p} \quad (\text{Eq. 4.14})$$

Darcy's law is derived, leaving gravity out of account, as follows:

$$\underline{v} = - \underline{k} \frac{1}{\mu} \text{grad} (p) \quad (\text{Eq. 4.15})$$

Substituted in equation 4.6, equations 4.14 and 4.15 result in the **integral equation for solution of ideal gas flow without considering gravity and rock compressibility**:

$$\int_V \phi \phi \dot{\rho} dV - \int_V (\text{grad} \phi)^T \left[\rho \underline{k} \frac{1}{\mu} \text{grad} p \right] dV =$$

$$- \int_S \phi \left[\rho \underline{k} \frac{1}{\mu} \text{grad} p \right] \underline{n} dS + \int_V \phi p q dV; \quad \forall \phi \in T \quad (\text{Eq. 4.16})$$

4.2.3.3 Actual Gas Flow

In the case of actual gas flow, the formula for gas density (eq. 4.13) is extended by the gas deviation factor:

$$\rho = \frac{M \cdot p}{\sigma(p) \cdot R_m \cdot T} = \frac{\rho}{\sigma(p) \cdot R \cdot T} \quad (\text{Eq. 4.17})$$

whereby M [kg/kmol] = Molecular density
 R_m [J/(kg·K)] = Universal gas constant
 R [J/(kmol·K)] = Special gas constant ($R = R_m/M$)
 T [K] = Absolute temperature
 $\sigma(p)$ [-] = Gas deviation factor

Under isothermic conditions, equation 4.17 results in

$$\frac{\delta \rho}{\delta t} = \frac{1}{R \cdot T} \cdot \left[\frac{1}{\sigma} \frac{\delta p}{\delta t} - \frac{p}{\sigma^2} \frac{d\sigma}{dp} \frac{\delta p}{\delta t} \right] \quad \text{or}$$

$$\frac{\delta \rho}{\delta t} = \frac{1}{\sigma \cdot R \cdot T} \cdot \left[1 - \frac{p}{\sigma} \frac{d\sigma}{dp} \right] \cdot \frac{\delta p}{\delta t} \quad (\text{Eq. 4.18})$$

Using the expression for ρ (eq. 4.17), equation 4.18 results in:

$$\frac{\delta \rho}{\delta t} = \rho \cdot \left[\frac{1}{p} - \frac{1}{\sigma} \frac{d\sigma}{dp} \right] \cdot \frac{\delta p}{\delta t} \quad \text{or} \quad \frac{\delta \rho}{\delta t} = \rho \cdot \beta \cdot \frac{\delta p}{\delta t} \quad (\text{Eq. 4.19})$$

β is thereby termed the gas compressibility factor:

$$\beta = \frac{1}{\rho} \frac{d\rho}{dp} = \left[\frac{1}{p} - \frac{1}{\sigma} \frac{d\sigma}{dp} \right] \quad (\text{Eq. 4.20})$$

The continuity equation (eq. 4.5) is as follows using Darcy's law acc. to equation 4.15, leaving gravity and rock compressibility out of consideration:

$$\int_V \varphi \phi \beta \rho^2 g h \, dV + \int_V (\text{grad } \varphi)^T \left[\rho \frac{k}{\mu} \text{grad } p \right] dV =$$

$$\int_S \varphi \left[\rho \frac{k}{\mu} \text{grad } p \right] \underline{n} \, dS + \int_V \varphi \rho q \, dV; \quad \forall \varphi \in T \quad (\text{Eq. 4.21})$$

The influence of gravity can be introduced into the equation in the form of piezometric pressure head.

$$h = \frac{1}{g} \int_p \frac{dp}{\rho(p)} + z \quad (\text{Eq. 4.22})$$

The expression "grad p" is thus expressed as "grad(ρ g h)". Continuing differentiation acc. to x_j and t, the result is the **integral equation for solution of actual gas flow with gravity influence**:

$$\begin{aligned} \int_V \varphi \phi \beta \rho^2 g \dot{h} dV + \int_V (\text{grad } \varphi)^T \rho^2 g \underline{k} \frac{1}{\mu} \text{grad } h dV = \\ \int_S \varphi \rho^2 g \underline{k} \frac{1}{\mu} \text{grad } h \underline{n} dS + \int_V \varphi \rho q dV; \quad \forall \varphi \in T \end{aligned} \quad (\text{Eq. 4.23})$$

4.2.3.4 Time-Related Semi-Discretion

To approximate the local derivation difference

$$\dot{h} = \frac{\delta h}{\delta t} \quad (\text{Eq. 4.24})$$

the hydraulic head $h = h(x, y, z, t)$ is observed at two times, t_n and $t_{n+1} = t_n + \Delta t$. $h_n(x, y, z)$ designates the hydraulic head h at points (x, y, z) at the time t_n . Linear interpolation between t_n and t_{n+1} results in:

$$h(x, y, z, t) \approx (1 - \Theta) h_n + \Theta h_{n+1} \quad (\text{Eq. 4.25})$$

and
$$\dot{h} = \frac{h_{n+1} - h_n}{\Delta t} \quad (\text{Eq. 4.26})$$

with
$$t = t_0 + \Theta \Delta t$$

Using this approximation, the functional equation (eq. 4.7) is converted into the following semi-discrete functional equation:

$$\begin{aligned} \frac{1}{\Delta t} \langle \varphi \phi, h_{n+1} - h_n \rangle + (1 - \Theta) b(\varphi, h_n) + \Theta b(\varphi, h_{n+1}) = l(\varphi) \\ \forall \varphi \in T \text{ mit } \varphi = 0 \text{ auf } S_1 \end{aligned}$$

or

$$\frac{1}{\Delta t} \langle \varphi \phi, h \rangle + \Theta b(\varphi, h) = r(\varphi) \quad \forall \varphi \in T \text{ mit } \varphi = 0 \text{ auf } S_1 \quad (\text{Eq. 4.27})$$

whereby

$$\langle \varphi \phi, h \rangle := \int_V \varphi \phi \beta \rho^2 g h_{n+1} dV \quad (\text{Eq. 4.28})$$

$$b(\varphi, h) := \int_V (\text{grad } \varphi)^T \rho \underline{K} \text{grad } h_{n+1} dV \quad (\text{Eq. 4.29})$$

$$\begin{aligned} r(\varphi) &:= \frac{1}{\Delta t} \int_V \varphi \phi \beta \rho^2 g h_n dV \\ &\quad - (1 - \Theta) \int_V (\text{grad } \varphi)^T \rho \underline{K} \text{grad } h_n dV \\ &\quad - \int_{S_2} \varphi \rho v_{n0} dS + \int_V \varphi \rho q dV \end{aligned} \quad (\text{Eq. 4.30})$$

$$\underline{K} = \rho g \underline{k} \frac{1}{\mu} \quad (\text{Eq. 4.31})$$

The method gives an oscillating solution for $\theta = 0.5$, which is attenuated by $\theta > 0.5$ (ROCKFLOW manual, module GM2, 1993). Computations should therefore be carried out with $\theta = 1.0$. The time integration method described here leads to an equation with spatial derivations only. Thus the present problem can be treated as a stationary problem, e.g. employing the BUBNOW-GALERKIN procedure.

4.2.3.5 BUBNOW-GALERKIN Method

The exact solution $h = h(x, y, z)$ is defined by an approximate solution $\bar{h} = \bar{h}(x, y, z)$. Using RITZ's approach

$$\bar{h}(x, y, z) = \bar{h}_0(x, y, z) + \sum_{k=1}^n c_k \omega_k(x, y, z) \quad \bar{h}_0 = h_0, \omega_k = 0 \text{ on } S_1 \quad (\text{Eq. 4.32})$$

this solution leads to calculation of the coefficients c_1, c_2, \dots, c_n via the semi-discrete functional equation (eq. 4.27), in which h is replaced by \bar{h} . The functional equation can also be written out as an algebraic system

$$\begin{aligned} \sum_{k=1}^n \left[\frac{1}{\Delta t} \langle \varphi_i \phi, \omega_k \rangle + \Theta b(\varphi_i, \omega_k) \right] c_k = \\ r(\varphi_i) - \frac{1}{\Delta t} \langle \varphi \phi, \bar{h}_0 \rangle - \Theta b(\varphi, \bar{h}_0) \quad i = 1(1)n \end{aligned} \quad (\text{Eq. 4.33})$$

The test function system $\varphi_1, \varphi_2, \dots, \varphi_n$ must be selected using a suitable method. With $\varphi_i = \omega_i$, the equation 4.33 results in the special form

$$\frac{1}{\Delta t} \langle \omega_i \phi, \bar{h} \rangle + \Theta b(\omega_i, \bar{h}) = r(\omega_i) \quad i = 1(1)n \quad (\text{Eq. 4.34})$$

4.2.4 Network Generator

The NG2-D network generator was further developed to accommodate two-dimensional areas with any form and fracture zones (TANIGUCHI 1992). This module is now part of the model family DURST, so that the generated networks can be imported directly. This meant a considerable reduction of the time required to make and vary map grids. It is possible to define areas within the boundaries to be modelled that are divided into approximately equal elements. A suitable choice of element size facilitates successive size reduction of the elements from the boundary of the model to the middle (Figs. 4.4, 4.5). In this way, the number of elements required for numerical simulation can be reduced by a considerable amount as compared to imaging of the same area with elements of equal size. This reduces the computing time and memory requirement of DURST/ROCKFLOW (LEGE & ZIELKE 1993).

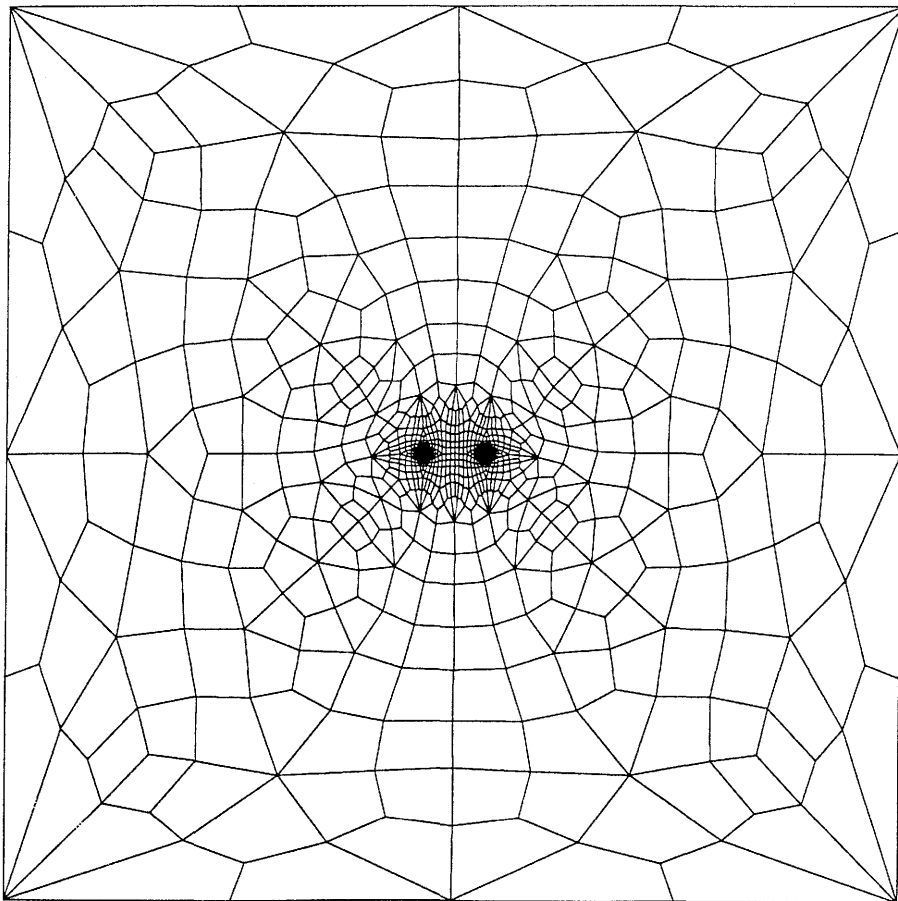


Figure 4.4: Grid geometry for imaging of a fracture surface between boreholes BoBK 9 and BoBK 5

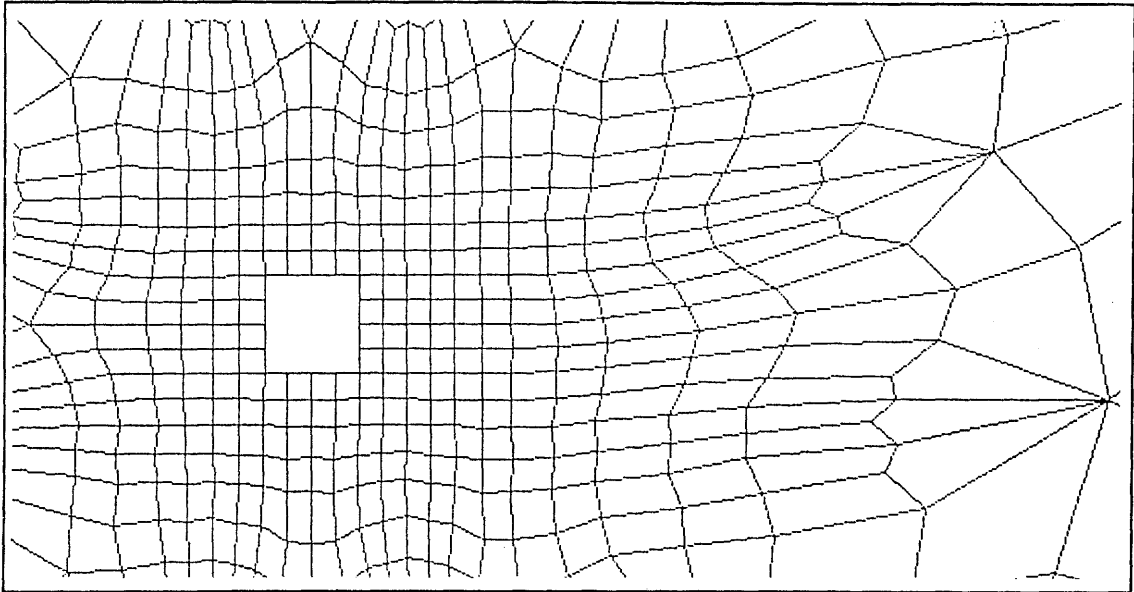


Figure 4.5: Refined network area around the source
(Enlargement of segment of Figure 4.4)

4.2.5 Graphics Processor

Work was continued on the graphics processor DALI and has been brought to a preliminary conclusion with implementation of the GSS-format graphical interface in all program modules of the DURST/ROCKFLOW program system. Research projects are on the drawing board in which further developments will aim at more rapid conversion of the relatively large amounts of data from modules of the transport model. Coupling with database systems and the AVS graphics system is also planned.

5. Hydraulic Testing in the BK Area

5.1 Tests in Area BoUS 3 - BoBK 3

5.1.1 Flow Test VE 485 (BoBK 3)

A 3-week flow test with **constant flow rate** was carried out in borehole BoBK 3 (June/July 1991) to investigate flow geometry and the dependence, if any, of hydraulic conductivity on pressure. The borehole penetrates the foliation zone shown in Figure 1.1 and is connected to borehole BoUS 3. The fractured area in borehole BoBK 3 is at a depth of about 63-66 m; above the foliation zone, the rock around the borehole is, for the most part, free of fractures. Tracer tests and fluid logging in borehole BoUS 3 (see section 5.2.3) revealed two fractures at depths of 109 m and 119 m. Assuming a straight-line connection of the fracture systems of the two boreholes, the spatial distance between them is approximately 25 m.

The objective of test VE 485 was to measure the outflow in BoBK 3 at different heads using volume-controlled measuring procedures, thereby monitoring pressure data in both boreholes. Prior to commencement of the test, boreholes BoBK 3 and BoUS 3 were shut in on a long-term basis with packers at the borehole heads, such that pressure in the two boreholes had reached near-maximum at 39 bar. The initial hydraulic conditions were thus defined to a great extent. On the basis of previous design computations, five test segments were analysed at the following stages:

1.	0.8 l/min	26.6. - 28.6.	2 days
2.	2.0 l/min	28.6. - 01.7.	3 days
3.	4.0 l/min	01.7. - 04.7.	3 days
4.	6.0 l/min	04.7. - 05.7.	1 day
5.	4.0 l/min	05.7. - 08.7.	3 days
6.	2.0 l/min	08.7. - 11.7.	3 days
7.	0.8 l/min	11.7. - 15.7.	4 days

Figure 5.1 shows the results for this 19-day period. A salient feature of the data is that pressure in the two boreholes is rather parallel, whereby in flow borehole BoBK 3 the jump occurs in conjunction with each flow rate change. Borehole BoUS 3, at least 25 m away, reacts without much delay to changes in borehole BoBK 3.

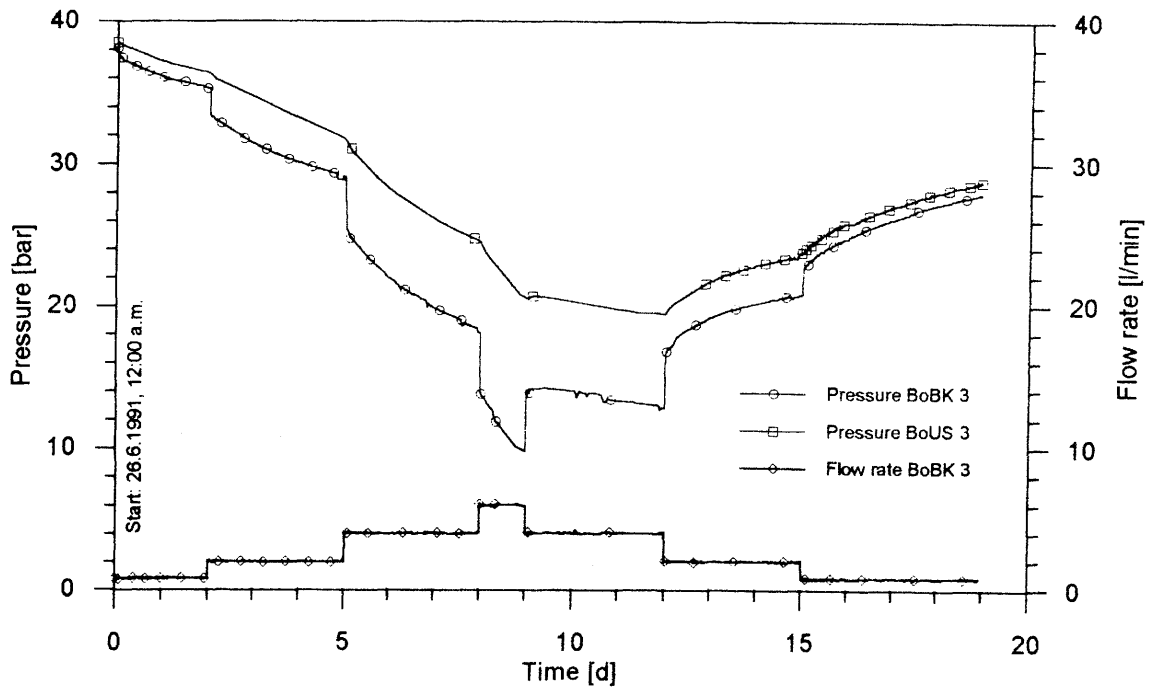


Figure 5.1: VE 485 - Pressure and flow rate in boreholes BoBK 3 and BoUS 3 as a function of time

Approximate evaluation of the first test phase is possible using the method of THEIS assuming symmetric radial flow in the BoBK 3 area on the basis of the differential pressure in relation to the initial value. Strictly speaking, the pre-conditions for the THEIS method are not fulfilled due to the line source approach; however, in this way, the initial values obtained are favourable for numerical simulation. The transmissivity resulting for borehole BoBK 3 as well as for borehole BoUS is $T = 9.0 \cdot 10^{-8} \text{ [m}^2/\text{s]}$ (see Fig. 5.2). On the other hand, the storage coefficients for the two boreholes differ widely, assuming a radius of 0.043 m for the outflow borehole and 25 m as the distance to the observation borehole. A value with a realistic order of magnitude results only from the more distant observation borehole, namely $S = 9.0 \cdot 10^{-6} \text{ [-]}$.

On the basis of the values determined after THEIS solution, numerical model computations were carried out with a finite difference program for various parametric combinations. For $T = 8.0 \cdot 10^{-8} \text{ [m}^2/\text{s]}$ and $S = 1.5 \cdot 10^{-5} \text{ [-]}$, borehole BoUS 3 agrees closely with computation and logging results over the entire test period and for the pressure range investigated, 20-40 bar (see Fig. 5.3). Thus no particular dependence of rock hydraulic conductivity on interval pressure is recognisable.

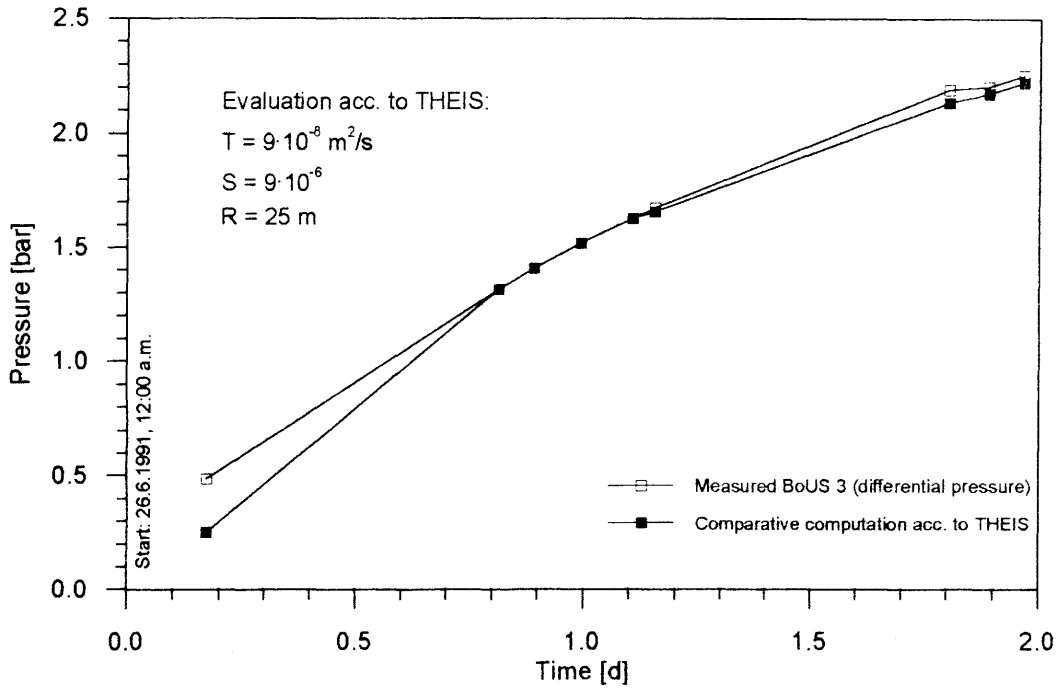


Figure 5.2: VE 485 - Measured and calculated pressure in borehole BoUS 3 in first test phase (2 days)

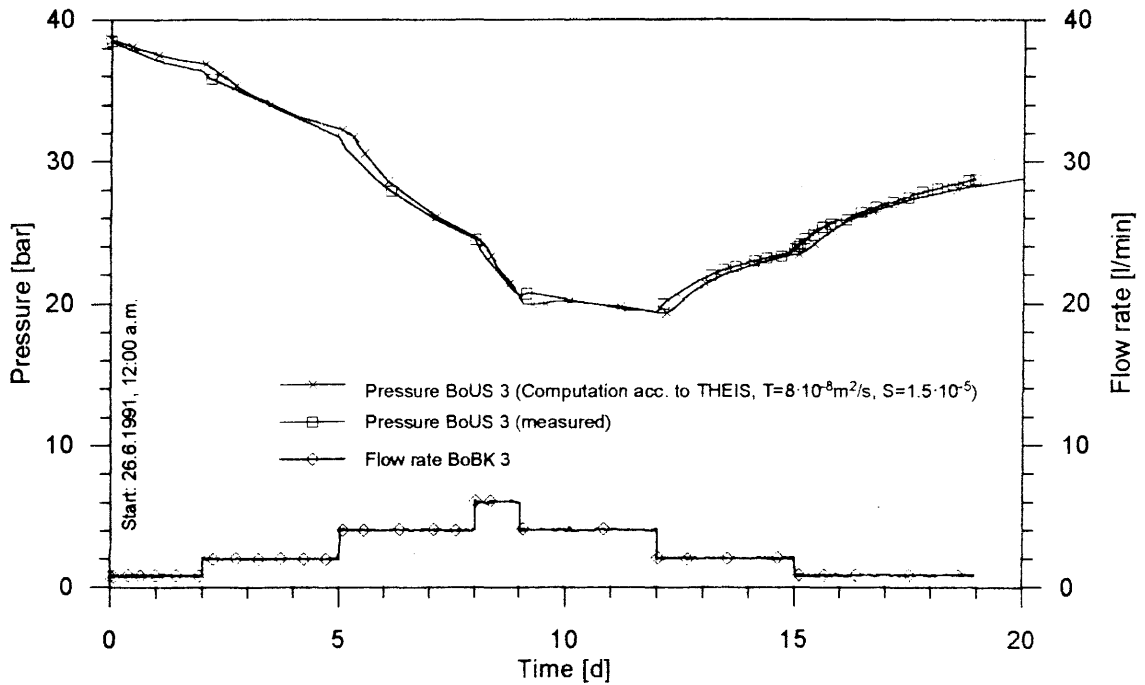


Figure 5.3: VE 485 - Measured and calculated pressure in borehole BoUS 3 over entire test period (20 days)

5.1.2 Flow Test VE 487 (BoBK 3)

A further multilevel flow test with three constant pressure stages in borehole BoBK 3 was carried out from August to mid-October 1991. On the basis of the results of test VE 485 (see section 5.1.1), the duration of the individual phases was increased by a considerable margin to 14 days, ensuring that the flow rate reached steady final values. The curves in Figure 5.4 show that this was the case after 5-7 days. The pressure in borehole BoUS 3 also reached a constant final value from an initial maximum during this period.

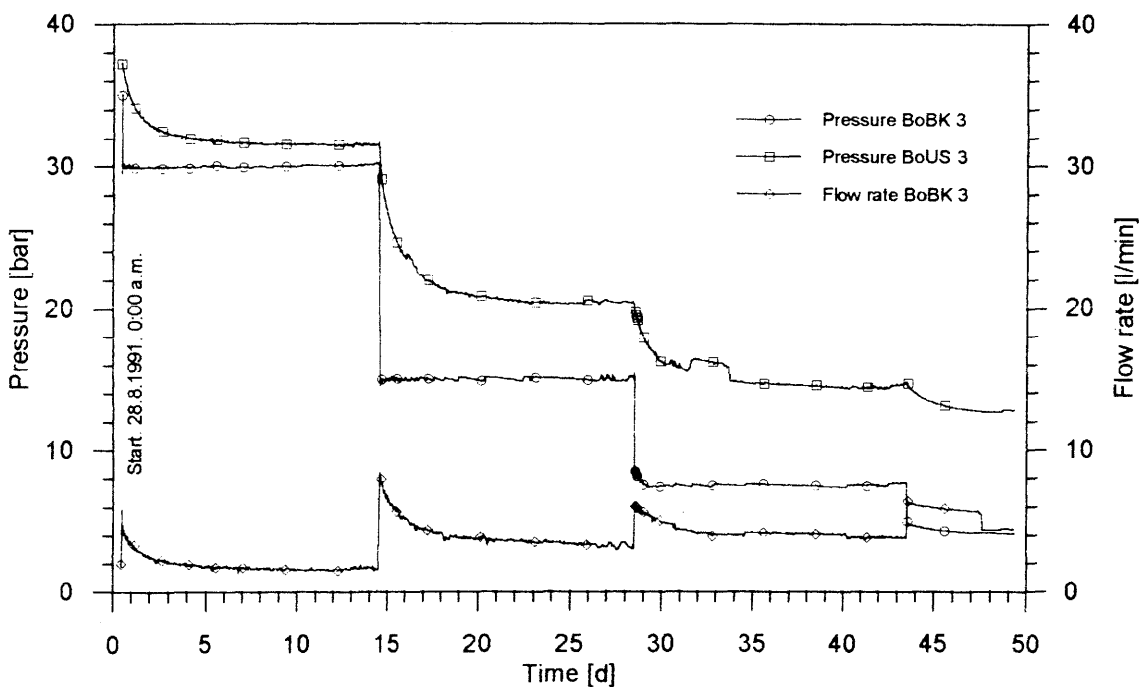


Figure 5.4 VE 487 - Pressure in boreholes BoBK 3 and BoUS 3 and flow rates in borehole BoBK 3 as a function of time

A pressure difference remains between boreholes BoBK 3 and BoUS 3 at the end of each test phase; the larger this difference is the lower the level of pressures or the greater the flow rate. Figure 5.5 illustrates the linear relation between the final flow rates and pressures (steady hydraulic conditions).

This linear relation results in a pressure level of 25.5 bar in borehole BoBK 3 and 28.2 bar in borehole BoUS 3, assuming a flow rate of 2 l/min, and thus in a pressure difference of 2.7 bar. These values correlate well with the results of test VE 485 (see Fig. 5.1). This also applies if the assumed flow rate is 4.0 l/min, in which case the calculated pressure in borehole BoBK 3 is 5.5 bar and in borehole BoUS 3 12.8 bar. The 4.0 l/min level is the maximum discharge level obtainable on a long-term basis when borehole BoBK 3 is opened. The pressure in borehole BoUS 3 then reaches a final low value of approximately 12 bar.

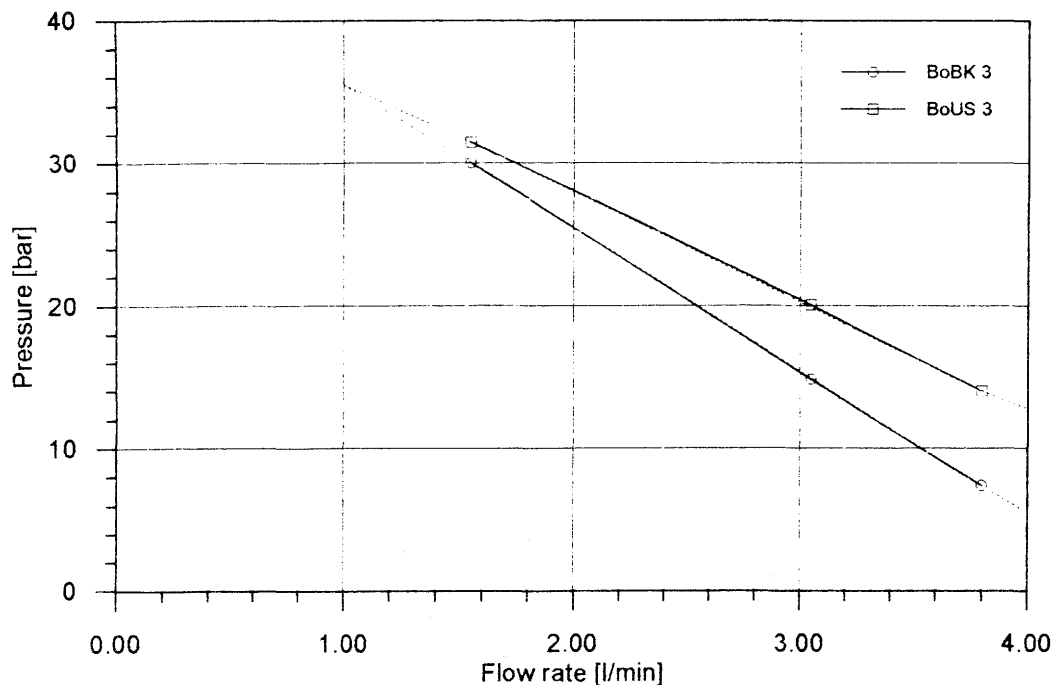


Figure 5.5: VE 487 - Relation between pressure and flow rate in boreholes BoBK 3 and BoUS 3

5.1.3 Constant Flow Test VE 491 (BoBK 3)

5.1.3.1 Test Procedure

A flow test in borehole BoBK 3 with a constant flow rate in 5 stages of 14 days each was carried out in early 1992. The flow rates $q = 0.75 / 1.50 / 3.00 / 0.75$ [l/min] were controlled by the process control system and the pressures in borehole BoBK 3 and borehole BoUS 3 were recorded. The objective of this test was to build on and add to knowledge gained in the previous tests VE 485 and VE 487 on flow processes in this rock area.

The test was begun on 10.01.92 after both observation boreholes had previously been shut in on a long-term basis and the pressure had reached a final value in each case of 40 bar. Following conclusion of the test on 19.03.92, borehole BoBK 3 was shut in again. Figure 5.6 shows the pressures in both boreholes and the flow rate in borehole BoBK 3.

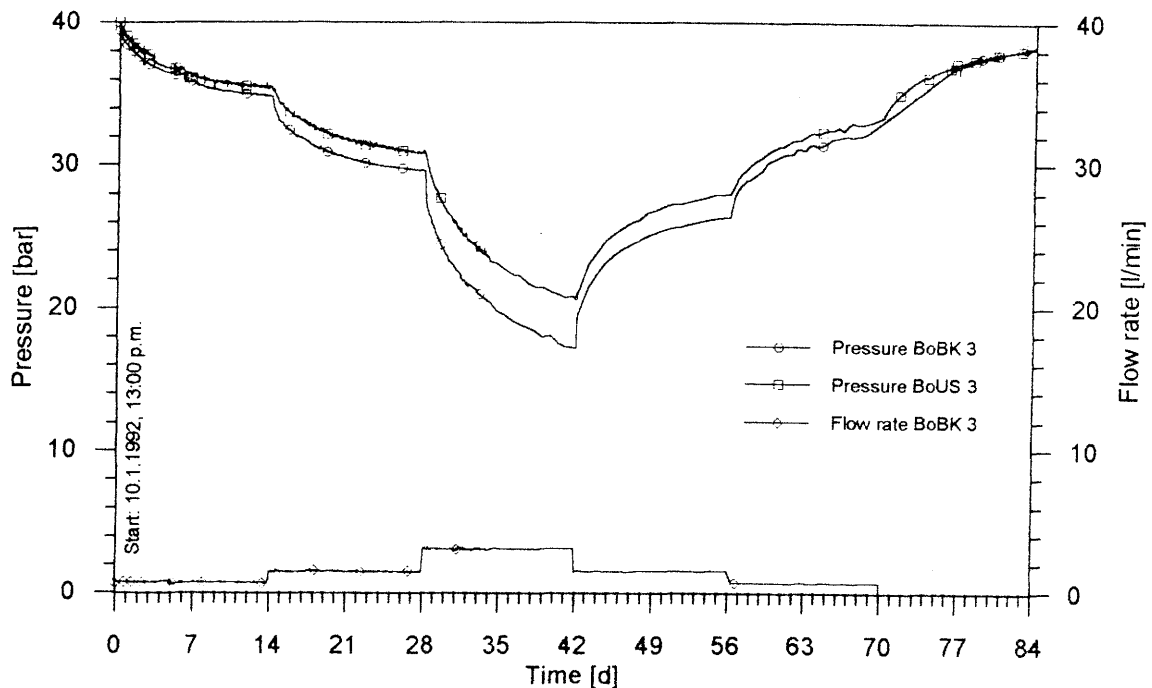


Figure 5.6: VE 491 - Pressure in boreholes BoBK 3 and BoUS 3 and flow rates in borehole BoBK 3 as a function of time

The results confirm the experience gained in comparable test configurations that a parallel pressure curve results with every change in flow rate following a sudden pressure change in borehole BoBK 3 and a subsequent transition phase lasting only a few minutes in both boreholes. The final pressure value approximates steadiness in the first test phase only. The following final values for individual flow rates in borehole BoUS 3 are obtained by extrapolation :

$q = 0.75$ [l/min] :	$p = 34.5$ [bar]
$q = 1.55$ [l/min] :	$p = 29.0$ [bar]
$q = 3.00$ [l/min] :	$p = 18.0$ [bar]

Figure 5.7 shows the resulting linear relation.

5.1.3.2 THEIS Evaluation

Due to the steady flow field upon commencement of the test, the first test phase can be evaluated using the simple solution of THEIS. Figure 5.8 shows the measured values for observation borehole BoUS 3, about 25 m away, in the form of differential pressure and the curve calculated after the THEIS solution. The corresponding parameters are thus:

$$T = 8.0 \cdot 10^{-8} \text{ [m}^2\text{/s]} \quad \text{and} \quad S = 8.0 \cdot 10^{-6} \text{ [-]}$$

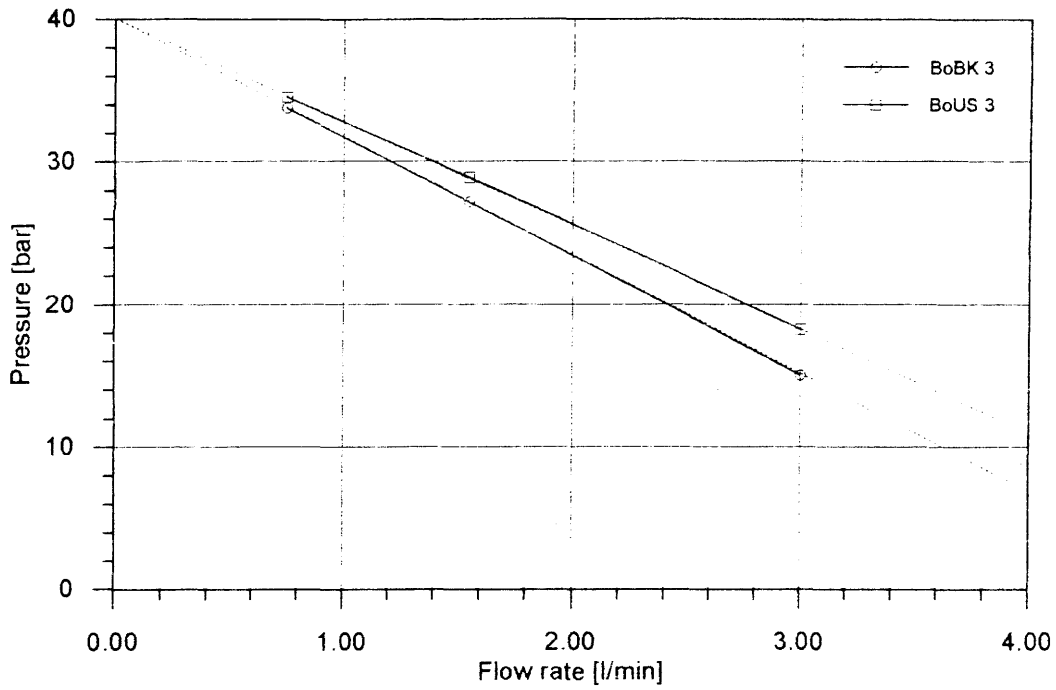


Figure 5.7: VE 491 - Relation between pressure and flow rate in boreholes BoBK 3 and BoUS 3

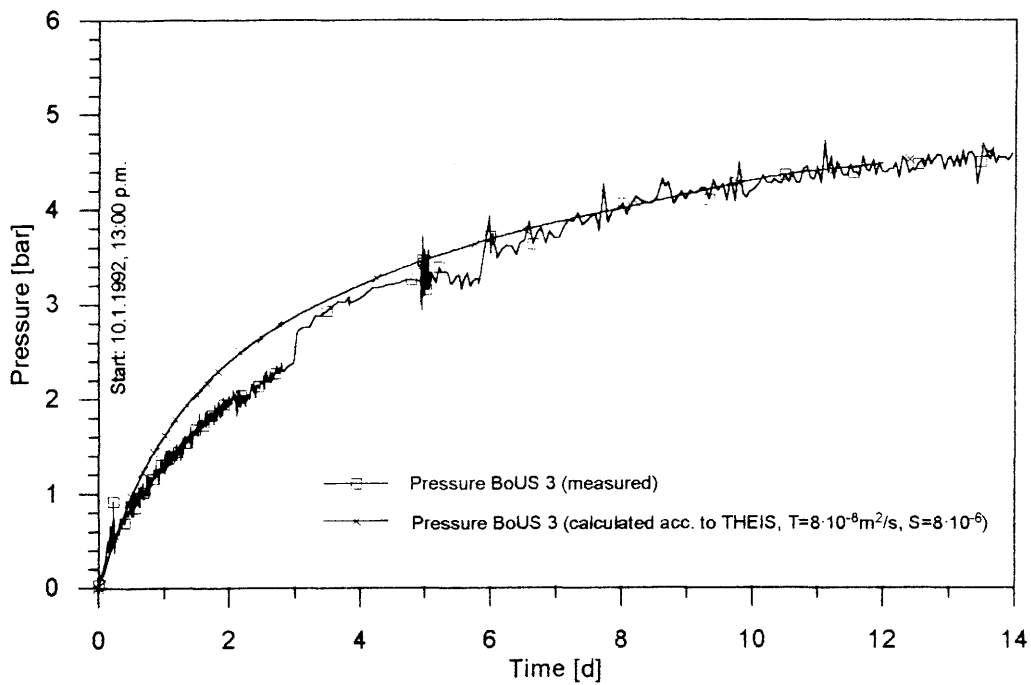


Figure 5.8: VE 491 - Measured and calculated pressure in borehole BoUS 3 during first test phase

In order to record the influence of test duration on transmissivity, various periods were evaluated after the THEIS solution in the first test phase. Figure 5.9 shows that a reproducible long-term transmissivity of $T = 8.25 \cdot 10^{-8} \text{ m}^2/\text{s}$ was first determined for a test duration of more than two days.

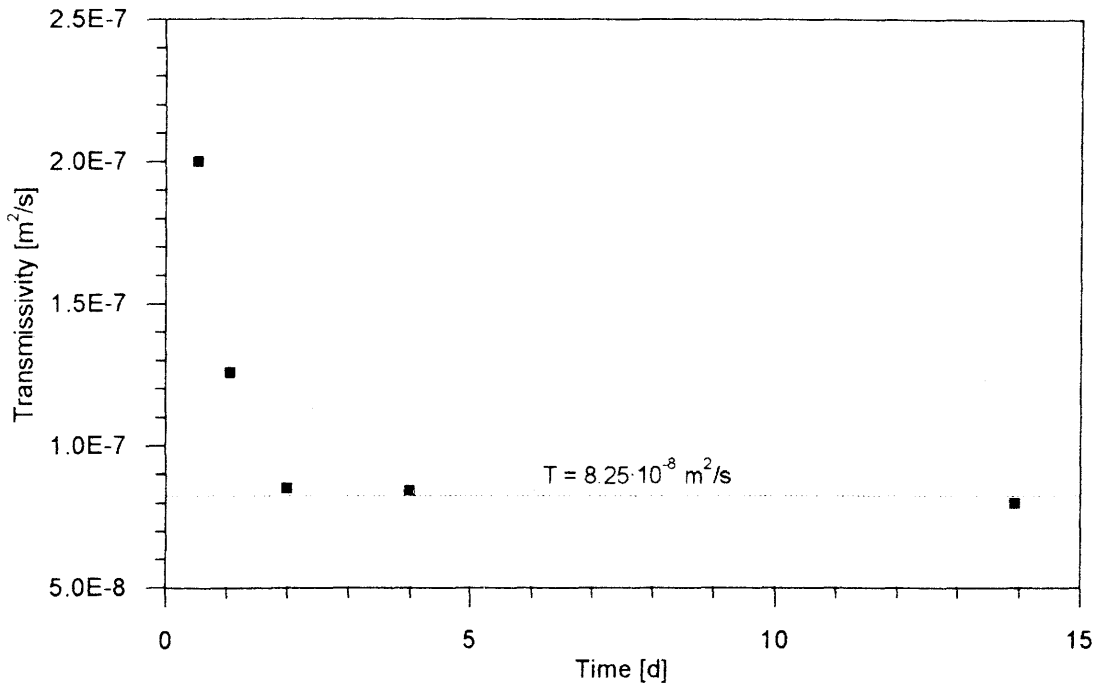


Figure 5.9: VE 491 - Transmissivity calculated after the THEIS solution as a function of test duration

Computations based on a homogeneous two-dimensional model, taking into account the pressure in borehole BoUS 3 in test VE 485, also resulted in a transmissivity of $T = 8.0 \cdot 10^{-8} \text{ m}^2/\text{s}$ and a storage coefficient of $S = 1.5 \cdot 10^{-5}$ [-]. Test VE 491 was recalculated on the basis of these values. Figure 5.10 shows the results for a point 25 m away from the line sink.

Very close agreement with the measured values is seen in the first three test phases. In the model computations for the final three test phases, on the other hand, the resulting final value is too low and nearly constant, which generally does not correspond to test results. Besides slight deviations in flow rate and, possibly, overly coarse discretisation, the explanation is mainly to be sought in the model of an infinitely extensive aquifer. This is clearly indicated above all by the growing difference between calculated and measured pressures at changed flow rates. A laterally bounded aquifer in the model would show greater pressure rises. This means that this test clearly reflects the influence of a hydraulic boundary in the form of, at least, a no-flow boundary, due to the delay of both drawdown and recovery. Such a barrier might be the lamprophyre zone about 10 m from the fracture system connecting boreholes BoBK 3 and BoUS 3.

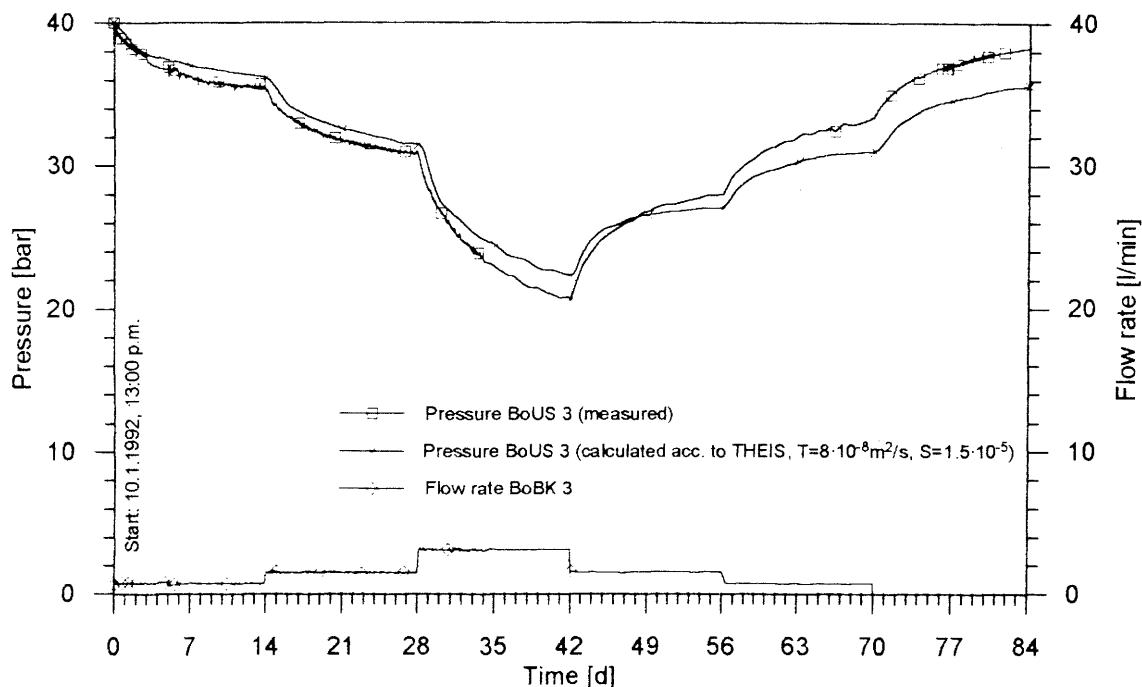


Figure 5.10: VE 491 - Measured and calculated pressure in borehole BoUS 3 as well as flow rate in borehole BoBK 3 throughout the entire test phase

The pressures in borehole BoBK 3 cannot be derived on the basis of these parameters (as in test VE 485). Even taking hydraulic "disturbance factors" into account (e.g. skin effects, wellbore storage), the practically parallel pressure curve in the two tested boreholes remains inexplicable. It must therefore be assumed that the rock, hydrothermally decomposed in this area, contains flow paths with raised hydraulic conductivity and that a linear flow field is predominant in the initial phase of a hydraulic test. Since the propagation rate of the radius of influence and thus establishment of a steady flow field depend almost solely on hydraulic diffusivity (T / S = transmissivity / storage coefficient), the rapid pressure reaction in borehole BoUS 3 shows that steady conditions are established fairly instantaneously. This means that, considering solely the pressures in the extraction borehole, the transmissivity of the rock can be determined, but not its storage coefficient.

In principle, test VE 491 thus confirms that the results at various pressure levels and uniform hydraulic parameters can be correlated with sufficient accuracy.

5.1.4 Flow and Recovery Test VE 494 (BoBK 3)

Test VE 494 comprises two phases (see Fig. 5.11):

- Uncontrolled outflow from borehole BoBK 3 (10 days);
- Recovery until initial hydraulic head - 40 bar - is reached (> 70 days).

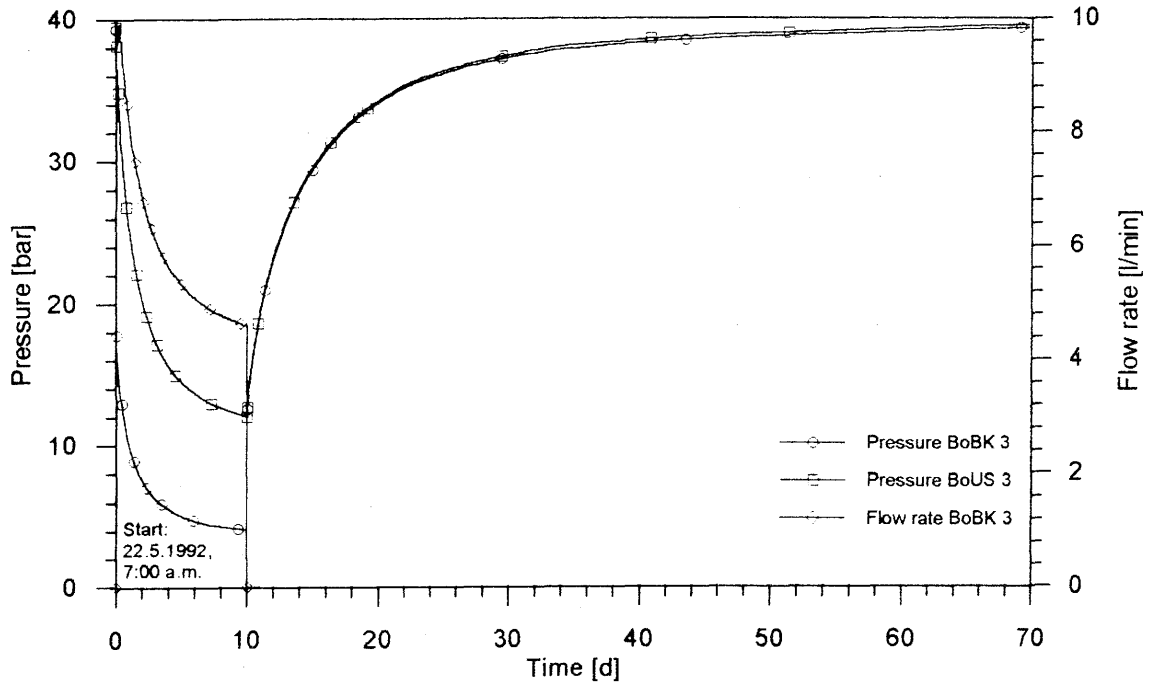


Figure 5.11: VE 494 - Measured pressure in boreholes BoBK 3 and BoUS 3 as well as flow rate in borehole BoBK 3 as a function of time

The objective of the test was a comparison of transmissivity, which is derived from the pressure buildup curve calculated after the THEIS recovery method, with transmissivity as determined in the earlier constant flow tests (tests VE 485 and VE 491).

Figure 5.11 shows the pressures measured in boreholes BoBK 3 and BoUS 3 as well as the flow rate in borehole BoBK 3. No steady state had been established at the end of the flow phase (flow rate 4.6 l/min.). The total volume of water extracted was 85 m³ at a mean flow rate of 5.9 l/min. Following shutting-in of the system, the pressure difference between boreholes BoBK 3 and BoUS 3 is compensated within a few minutes and pressure increases synchronously in the two boreholes, an indication of an unsaturated state (leaky aquifer). Figure 5.12 shows the pressure increase in borehole BoBK 3 for the normalised time.

Transmissivity is determined with the help of a tangent at the inflection point on the curve. The pressure change is thus 25 bar within one decade. Transmissivity calculated after the THEIS solution is therefore:

$$T = \frac{2.3 \cdot Q}{4 \cdot \pi \cdot \Delta h} = \frac{2.3 \cdot 5.9 / 60000}{4 \cdot \pi \cdot 250} = 7 \cdot 10^{-8} \left[\frac{\text{m}^2}{\text{s}} \right]$$

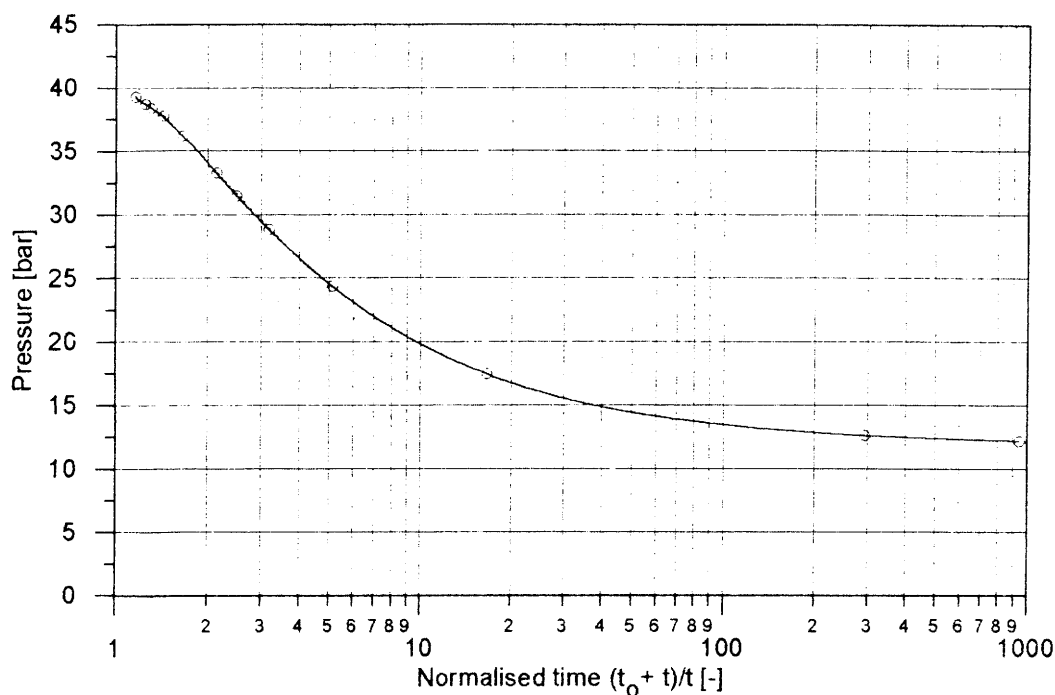


Figure 5.12 VE 494 - Pressure in borehole BoBK 3 as a function of normalised time

As a rule, the transmissivities determined on the basis of various test and evaluation types show only slight deviations ($7 \cdot 10^{-8}$ to $9 \cdot 10^{-8}$ [m^2/s]). A prerequisite is that test periods of sufficient length be considered. Transmissivity values from short-term tests are always greater, up to $T = 10^{-6}$ [m^2/s]. On the other hand, we can also confirm the results of an earlier pressure buildup test carried out in 1985/86 (borehole BoBK 3 did not exist at the time) showing a transmissivity of $T = 10^{-7}$ [m^2/s] for borehole BoUS 3 (cf. PAHL et al. 1992).

5.1.5 Constant Flow and Recovery Test VE 511 (BoBK 2)

Borehole BoBK 2 was tested for the first time in November 1992 within the framework of the multiple source crosshole tests (MSCT, see Section 5.2.4) carried out in a cooperative effort by Nagra and BGR. This borehole has a direct connection to the fracture system in the central BK area, but reacts only minimally to pronounced changes in borehole BoBK 3. The initial test pressure was 21.4 bar. A very low flow rate was measured following opening of the borehole. After a brief transition phase, the rate was somewhat more than 0.2 l/min. The total discharge volume of 5.0 l means an average discharge of 0.33 l/min for the 15-minute flow phase. The initial pressure was approximated about 24 h after shutting in the borehole (Fig. 5.13).

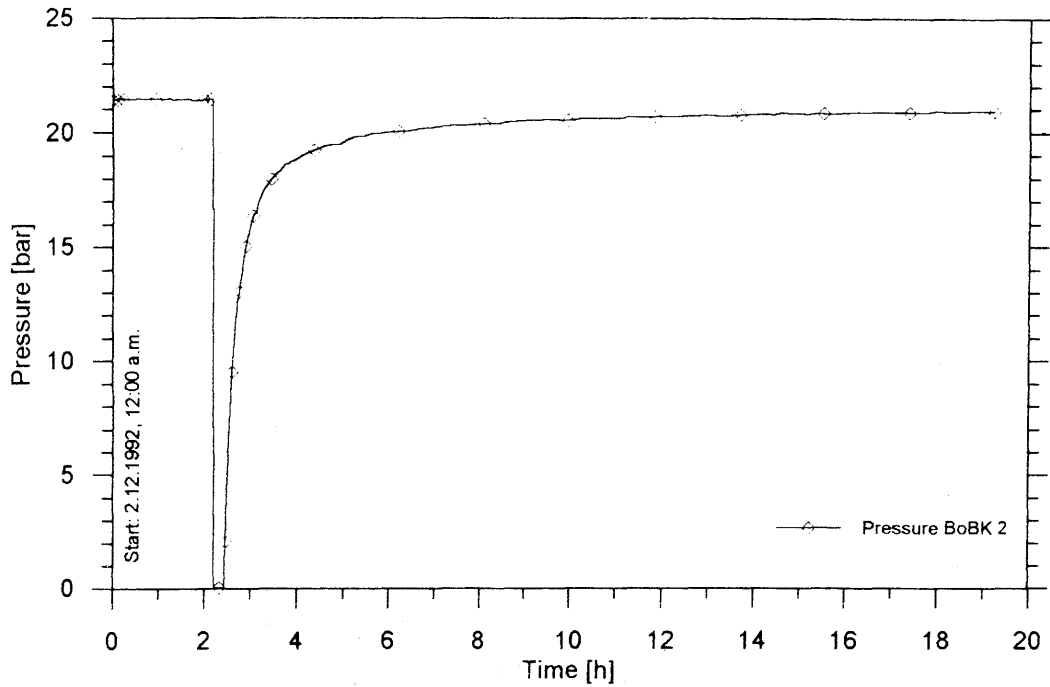


Figure 5.13: VE 511 - Pressure in borehole BoBK 2 as a function of time

Evaluation after the recovery method of THEIS (see Fig. 5.14) results in transmissivity as follows:

$$T = \frac{2.3 \cdot Q}{4 \cdot \pi \cdot \Delta h} = \frac{2.3 \cdot 0.33 / 60000}{4 \cdot \pi \cdot 133} = 7.6 \cdot 10^{-9} \left[\frac{\text{m}^2}{\text{s}} \right]$$

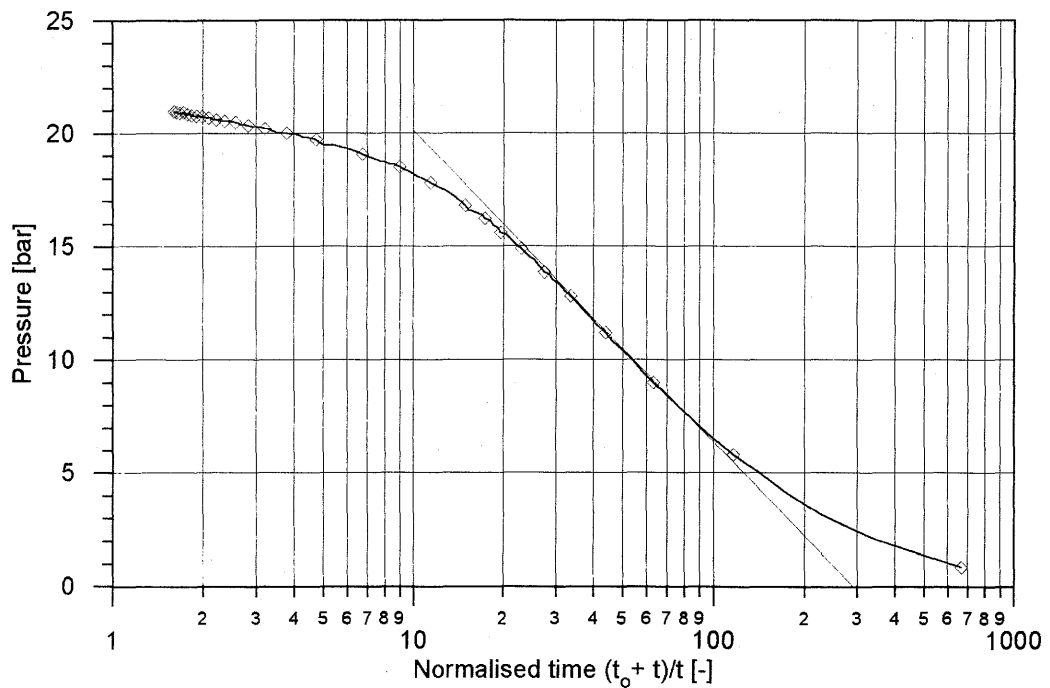


Figure 5.14: VE 511 - Pressure in borehole BoBK 2 as a function of normalised time

5.2 Tests in the Central BK Area

5.2.1 Pressure Buildup Tests VE 478 and VE 484

Pressure buildup in the central BK area was investigated in two long-term tests lasting several weeks each. Twenty boreholes (including the peripheral boreholes BoSB 1, BoUS 3 and BoGS 41A) with approx. 30 observation points were involved in each test. The installed packers were controlled at regular intervals by on-site personnel at the GTS. The datalogging proved dependable so that long-term measurements in the rock laboratory did not require the presence of BGR personnel.

A selection of measured data is shown in Figures 5.15 (test VE 478) and 5.16 (test VE 484) for Fan A (boreholes BoBK 9/13/14), Fan B (boreholes BoBK 5/15/16), Fan D (boreholes BoBK 6/17/18) and borehole BoBK 10.

Test VE 478 covered a period of three weeks (Fig. 5.15). Long-term pressure increase was nearly parallel in all boreholes. The absolute values differ due to varying probe installation depths. A level of 6 bar was reached in relation to tunnel level, but this value is not final. The pressure buildup rate was approx. 0.2 bar/d after fading of the transient initial phase. This course was also typical of the central area measurement segments not shown. Borehole BoBK 10, at right angles to the borehole fans, had a pressure buildup rate of 0.17 bar/d.

A further pressure buildup test (VE 484) was carried out subsequent to tracer test VE 483 in 1991. The initial pressure level was approx. 5 bar, i.e. approx. 2 bar greater than in test VE 478 in relation to tunnel level. However, much higher pressure buildup rates were recorded in the parallel fans - approx. 0.30 bar/d (Fig. 5.16) following a transient phase. Pressure increase slowed one week after the beginning of the test until a final level of approx. 9 bar in relation to tunnel level was reached. The somewhat lower final value in the upper interval of borehole BoBK 5 is due to a lower level of water outflow into the tunnel. The pressure buildup in borehole BoBK 10 was also somewhat slower in this test; the final value reached was, however, comparable.

In earlier tests (VE 450, VE 474), much lower pressure buildup rates of max. 0.1 bar/d were measured. Long-term opening of boreholes BoBK 3 and BoUS 3 lowered pressure levels in the neighbouring rock considerably at the time. Since, however, the opening of these two boreholes did not produce noticeable changes in pressure heads in the central area, the various pressure increases could not be attributed to influences from this rock area. A plausible explanation for the varying behaviour recorded would be variable recovery rates, due possibly to changes in dammed lake levels or weather conditions.

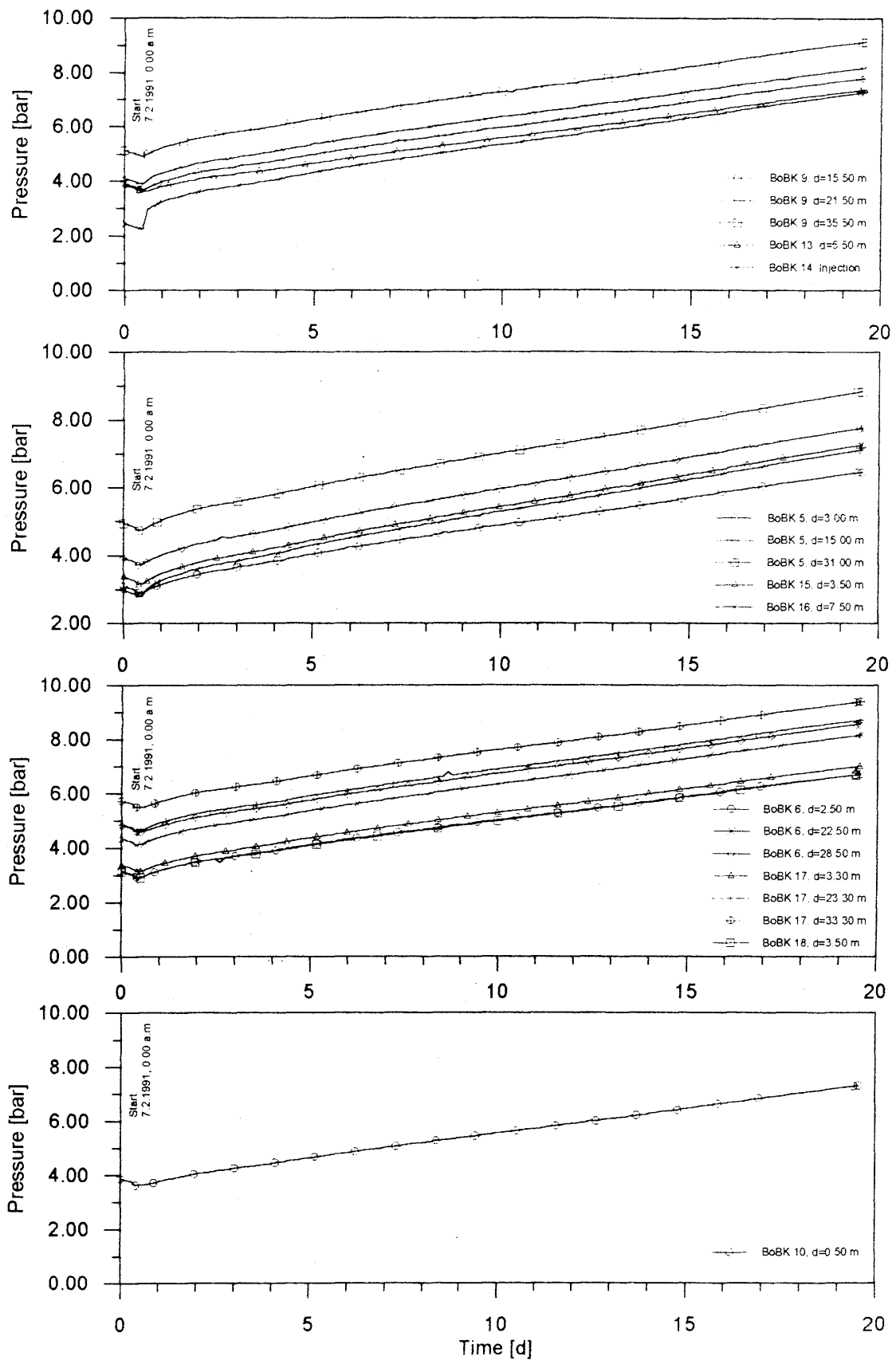


Figure 5.15: VE 478 - Pressure measured in boreholes in the central BK area as a function of time

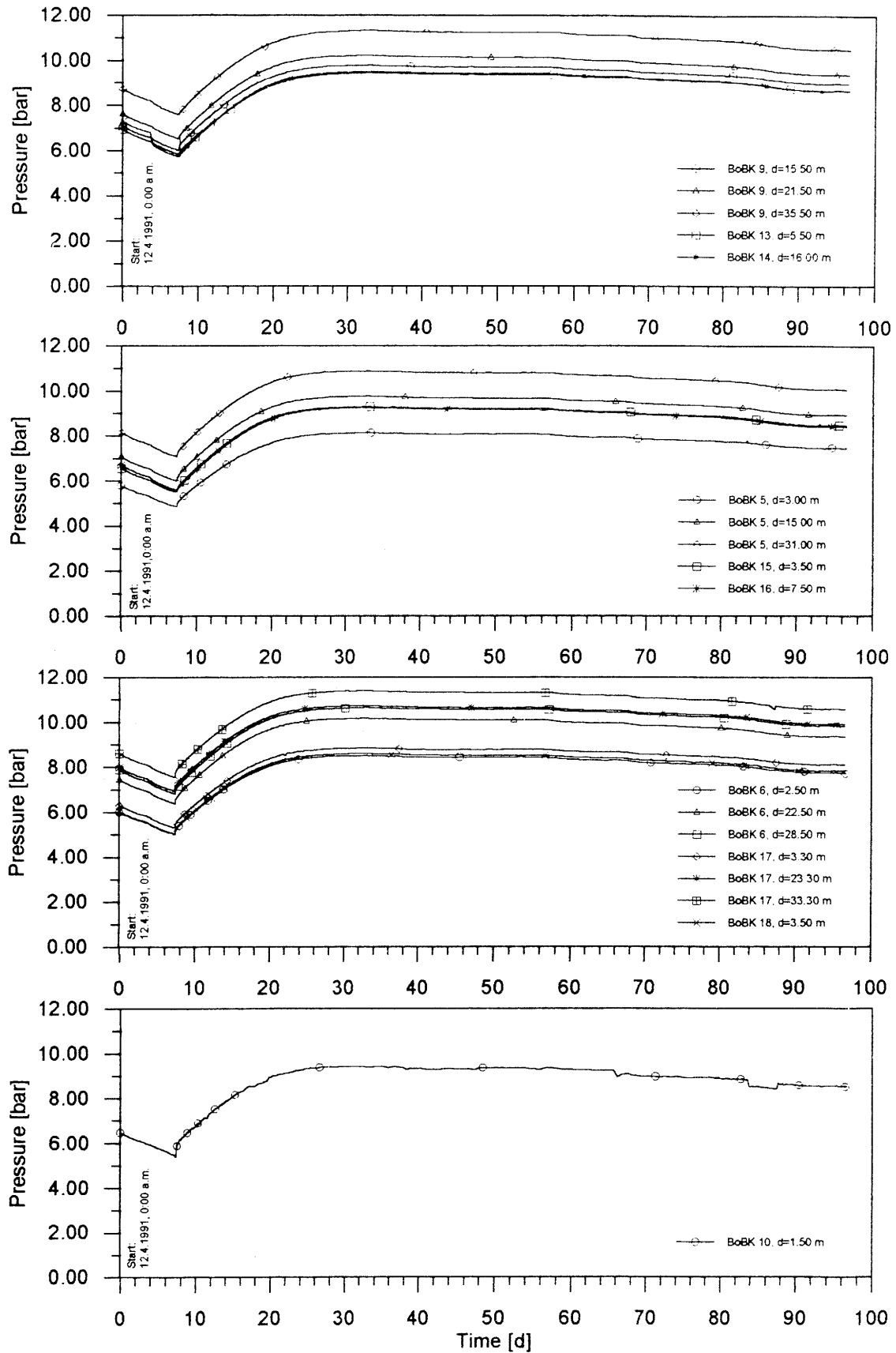


Figure 5.16: VE 484 - Pressure measured in boreholes in the central BK area as a function of time

When the US borehole was open in 1988/89, pressure in borehole BoBK 2 was always lower than 11 bar.

Pressure in borehole BoBK 2 climbs only when boreholes BoBK 3 and BoUS 3 are shut in over a longer time and borehole BoBK 3 is packed off before the lamprophyre zone (max. 20.1 bar in August of 1991). It can be stated that the hydraulic boundary conditions are changed if, as performed in the tests of 1991, a high head level is reached in area II (see Fig. 1.1) because of packering borehole BoBK 3 and simultaneously a link is created to the central area via the lamprophyre zone. Due to numerous leakages, however, the pressure in the central area before the lamprophyre zone remained below 10 bar on a long-term basis (see Fig. 5.16), with the exception of borehole BoBK 2 at the edge. The decrease of pressure after reaching the maximum values is, therefore, to be explained by a temporary opening of the boreholes BoBK 3 and BoUS 3.

5.2.2 Interference Test VE 479

A special injection element was installed in borehole BoBK 14 in preparation for subsequent tracer test VE 483 (see section 6.1). The resulting pressure drop in the entire BK area was recorded as test VE 479 (Fig. 5.17). Immediately after opening of the borehole, discharge was > 50 l/min. Pressure drop-off varied from 1.5 to 2.5 bar in the observation boreholes during the test period. The clearest reaction was recorded in the middle interval at 15 m - 20 m in neighbouring borehole BoBK 9. In borehole BoBK 13 in the same fan, pressure drop-off was much slower, with a course nearly identical to that in the borehole farthest away, BoBK 10. The recovery phase following shut-in of borehole BoBK 14 led, however, to nearly parallel pressure increases in all boreholes in as little as 4-6 h.

5.2.3 Fluid Logging Tests

Nagra carried out various fluid logging tests in a total of 11 boreholes in the BK area during the reporting period. The objective of these tests was to detect hydraulically active fractures from which fluid entered the borehole and to determine mass flow in each case.

For this purpose, the fluid in the boreholes was replaced by highly saline brine 10 to 100 times more electrically conductive than the groundwater. If fluid enters the borehole from fractures, in this case at a rate of 2 l/min, the electrical conductivity of the borehole fluid is reduced at the inflow sites along with, perhaps, the temperature.

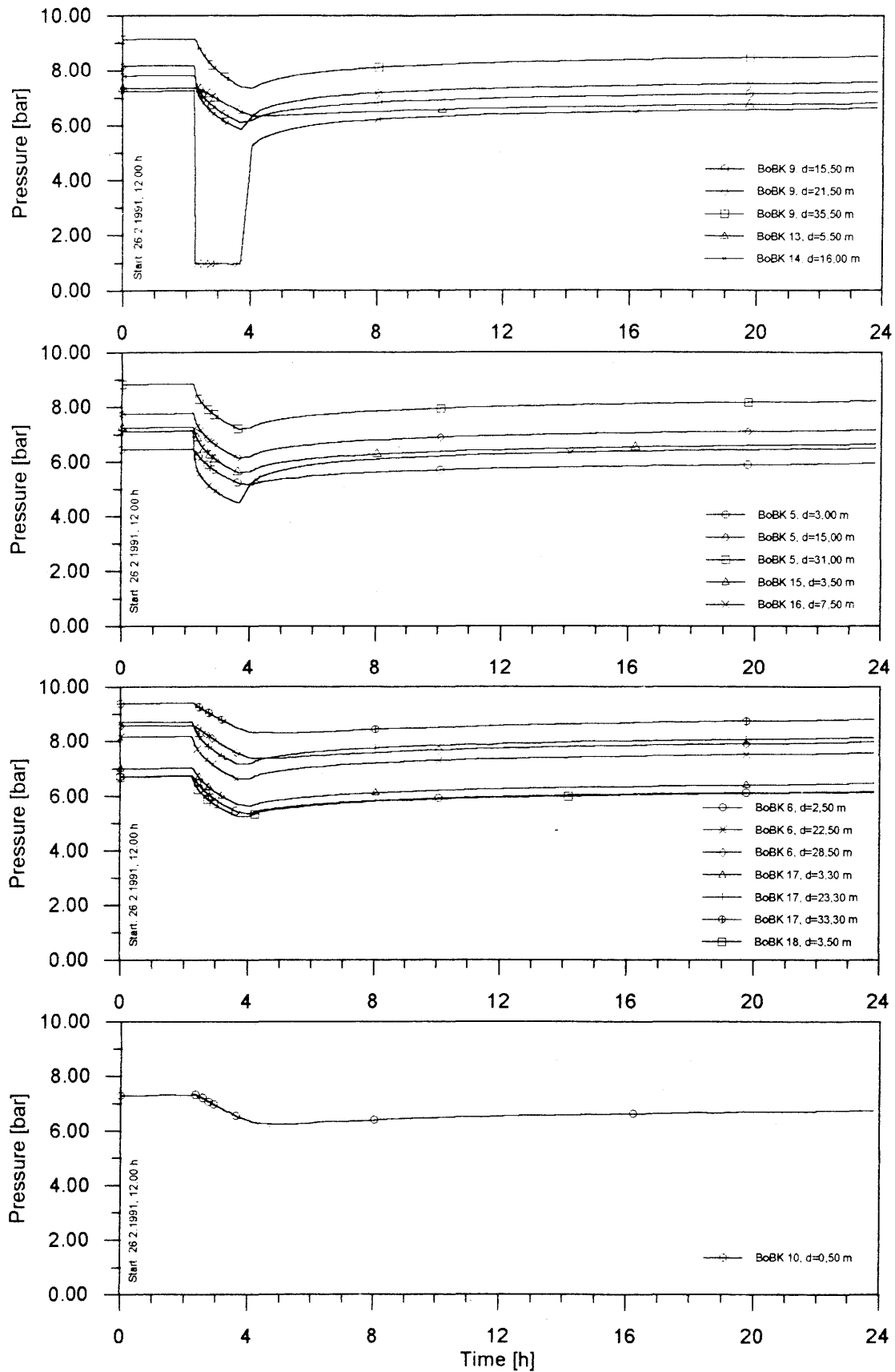


Figure 5.17: VE 479 - Interference test: Pressure measured in boreholes in the central BK area as a function of time

Using combined electrical conductivity and temperature probes, several successive logging runs were carried out in each borehole at intervals of a few minutes to determine the depth of the inflow sites and observe changes over time of temperature and electrical conductivity. The latter factor is important in drawing conclusions concerning mass flow and thus the decisive transport pathways in the rock. Figure 5.18 shows the example of the fluid logging results in borehole BoBK 4. A strong inflow is seen at a depth of 8 m and two further inflows, less strong, at 34 and 38 m.

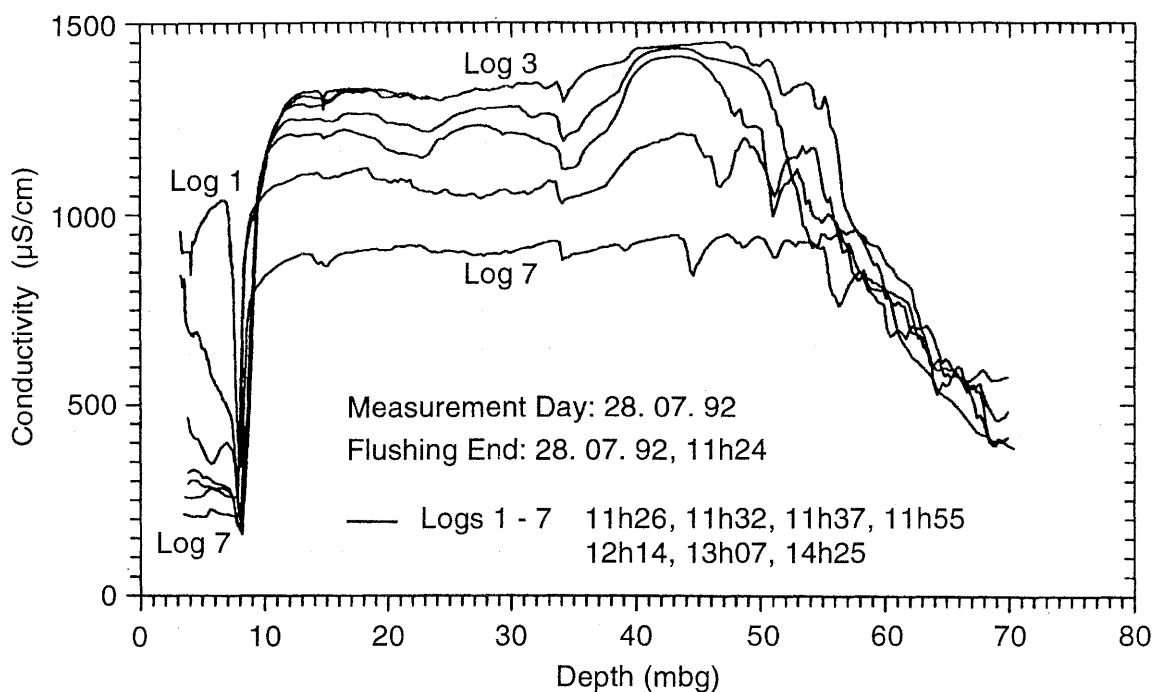


Figure 5.18: Fluid logging in borehole BoBK 4 (GEOTEST measurement)

Table 5.1 lists the inflow sites detected in this way in the 11 boreholes. Figure 5.19 shows the spatial location of the inflow sites or corresponding fractures. To facilitate presentation, neighbouring fractures were considered as single fractures. The fractures in red are those indicating the highest mass flow levels per borehole in fluid logging tests. Both top and perspective views show a clearly delimited band of networked fractures. This band is within a shear zone and characterises the essential flow pathways in the BK area.

Table 5.1: Inflow sites detected by fluid logging and acc. to PAHL et al. (1992)

Borehole	Depth [m]	Azimuth [°]	Dip Angle [°]	Water-bearing fractures acc. to PAHL et al. 1992	Rem.
BK 4	8.0	340	85	2.6 - 4.4	red
	34.0	135	80	6.8 - 7.4	
	38.0	145	80	7.8 - 8.2 8.7 - 9.3	
BK 5	5.5	215	80	14.1 - 17.0	red
	8.5	110	85	17.2 - 18.7	
	16.0	290	80	18.8 - 21.0	
	18.8	315	80		
	23.4	275	85		
	31.6	135	75		
	33.2	210	80		
	35.2	160	75		
40.0	190	70			
BK 6	6.5	135	85	21.4 - 24.0	red red
	16.3	330	75	25.4 - 26.4	
	20.2	310	80		
	23.3	300	80		
	26.7	300	80		
	40.5	140	80		
BK 7	4.5	170	85	24.6 - 27.0	red
	25.8	290	80	27.2 - 27.6	
	30.4	130	75	30.0 - 30.5	
	37.6	155	80		
BK 8	14.7	310	75	12.4 - 14.4	red
	21.8	210	80	15.8 - 17.1	red
	24.9	110	80	21.6 - 21.8	
	40.0	195	80	25.5 - 25.7 27.1 - 27.8	
BK 9	18.6	320	90	14.2 - 15.2	red
	28.3	310	75	18.3 - 19.3	red
	32.8	120	80	27.5	
	43.5	165	85	27.8 - 28.5	
	46.9	205	80	32.8 - 33.3	
BK 14	18.4	115	85	17.3 - 18.6	red
	20.3	125	90		
BK 15	25.3	135	85	25.0 - 25.1	red
	36.7	135	90	35.4 - 36.7	
BK 16	19.3	130	85	19.3 - 21.8	red
	22.1	135	90		red
BK 17	5.0	045	80	4.5 - 5.0	red
	27.0	030	85	24.0 - 24.5	
	34.6	150	80	26.0 - 26.5	
	43.0	335	80	28.5 - 28.8 33.9 - 34.6	
BK 18	15.0	135	80	8.0 - 9.3	
				14.0 - 16.5	

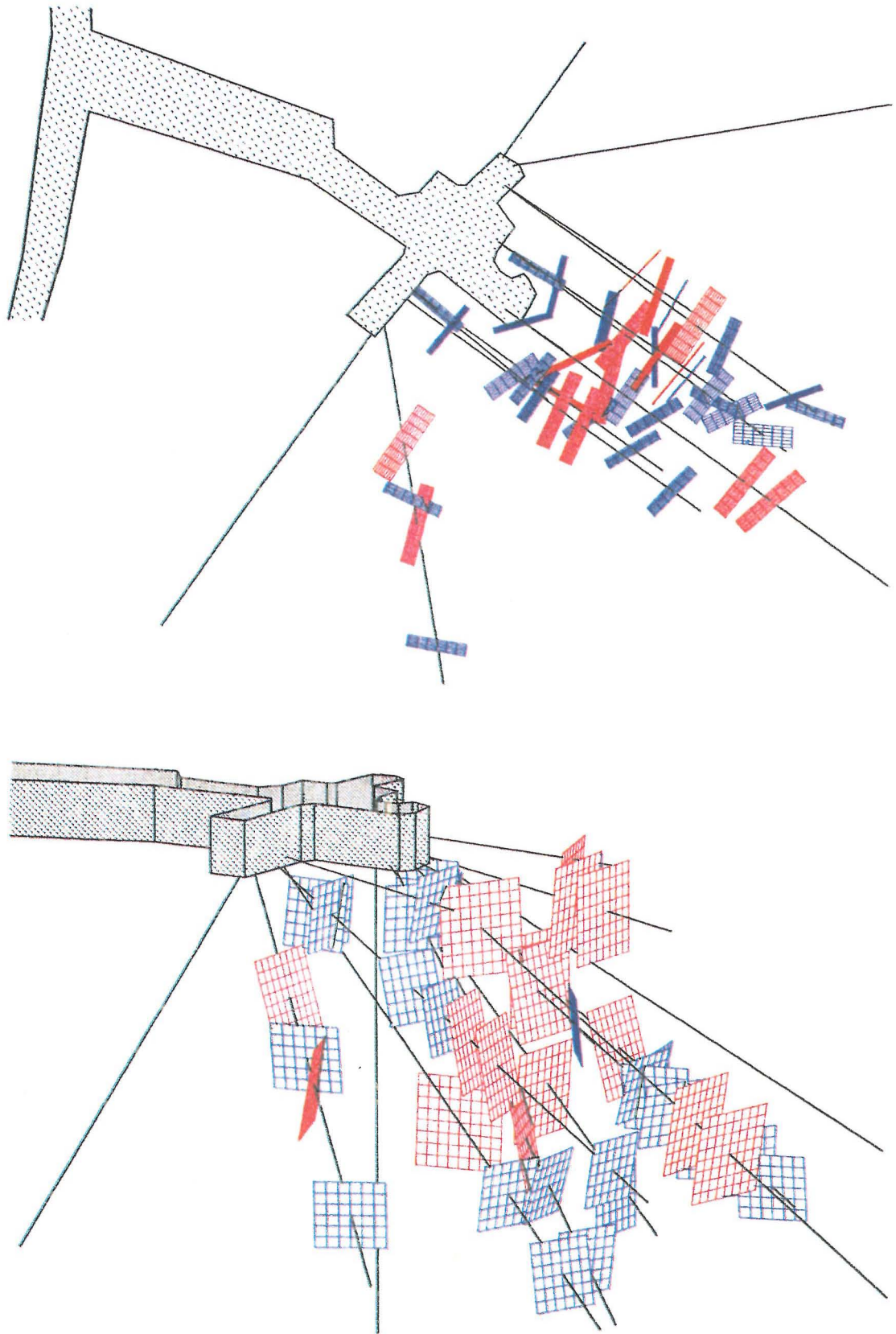


Figure 5.19: Fluid logging tests in the central BK area: spatial location of inflow sites

As a complement to these tests, the BGR ran a conductivity log in borehole BoUS 3 on 18.10.91 to determine the position of the water-bearing fractures there. First, the borehole head packer was removed and a tube with a WTW conductometer was introduced into the borehole using a glass fibre rod and flushed to a depth of 130 m with tapwater. The lower conductivity level of the tapwater (16 $\mu\text{S}/\text{cm}$) then made it possible for the conductometer to detect areas of outflow of more conductive fracture water (Fig. 5.20). Since the overall discharge in this borehole is rather low (long-term discharge approx. 2 l/min when borehole BoBK 3 is opened), a relatively weak mixture of tapwater and groundwater was detected right after flushing, so that inflow sites were clearly indicated by max. values of approx. 40 $\mu\text{S}/\text{cm}$. The fracture zones bearing the most water are thus at 109 m and 119 m.

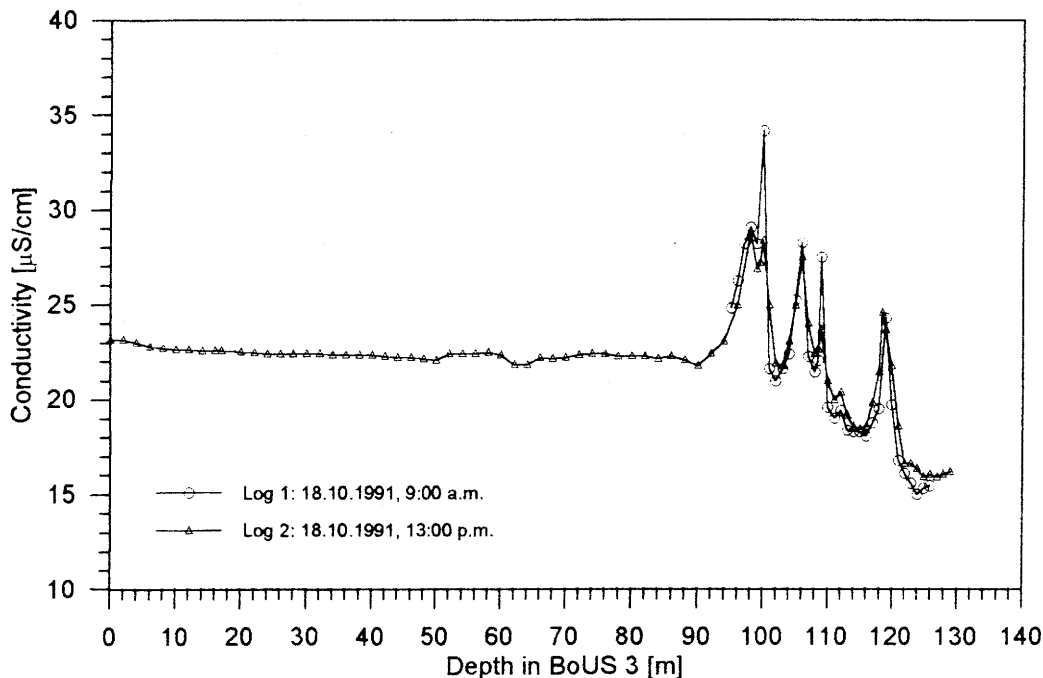


Figure 5.20: Conductivity log of borehole BoUS 3

This simple form of conductivity measurement has turned out to be practical and useful in qualitative determination of fracture zone locations. The entire test VE 487a, from removal to replacement of the packer with two logging runs (upwards and downwards), took about half a day.

5.2.4 Multiple Source Crosshole Test (MSCT) VE 496 - VE 513

The MSCT was conceived by Nagra and realised by BGR personnel and equipment. The positions of the packers and probes in the boreholes during the test is seen in Figure 5.21. The objective of the test was to develop a high-resolution hydraulic detection method to help determine diffusivity $D = T/S$ [m^2/s], i.e. the relation of transmissivity to storage coefficient in the central fracture system flow test area.

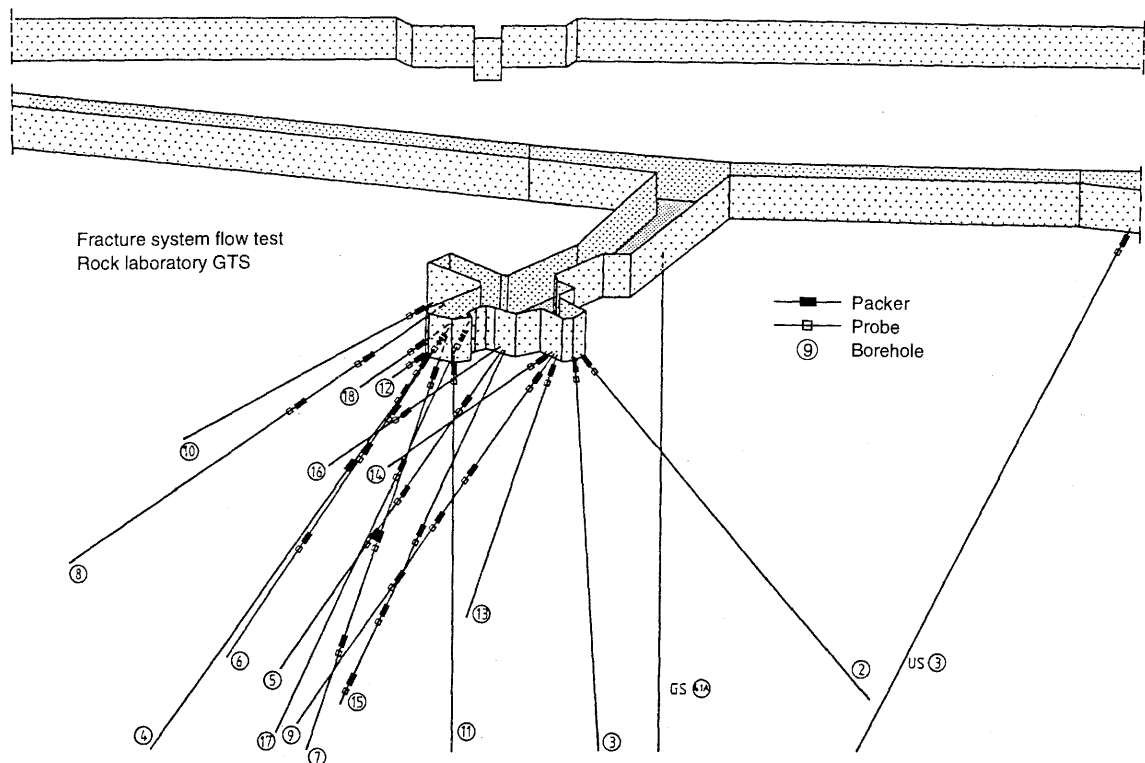


Figure 5.21: Multiple source crosshole test: positions of packers and probes

The MSCT comprised three preliminary tests (VE 496-498) and 15 individual tests (VE 499-513). Alternating hydraulic disturbances in the form of injection (constant flow) and extraction were generated at selected stimulation intervals for the specific boreholes. Observations covered pressure and temperature in the stimulation interval as well as pressure in all nearby boreholes. The changeover from injection to extraction was carried out when the pressure in the injection interval had reached a quasi-steady state. Subsequent extraction was continued until the amount of water injected had flowed out again.

Nagra requested the highest possible sampling rate since the data were to be subjected to spectral analysis, the potential and quality of which increases with higher sampling rates. A rate of one measuring cycle/10 s was realised for the digital channels; for the analog channels the rate was one cycle/30 s.

As illustrative examples, the results of tests VE 502 and VE 510 are shown in Figures 5.22 and 5.23. Pressure and flow rate in the test interval, as well as pressure behaviour, were plotted for an observation borehole in which a reaction was expected in spite of the brief test duration.

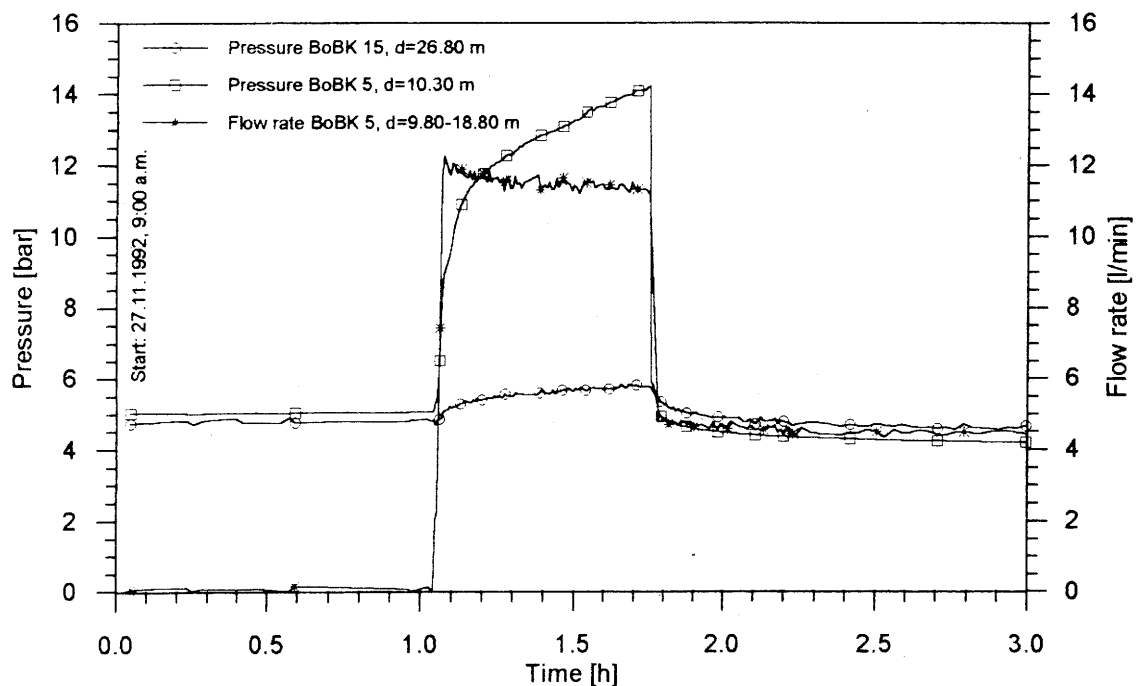


Figure 5.22: VE 502 - Pressures in boreholes BoBK 5 and BoBK 15 and flow rate in borehole BoBK 5 as a function of time

In test VE 510, borehole BoBK 10 was the injection/extraction borehole; borehole BoBK 4 was the observation borehole. Figure 5.23 shows that a pressure increase in BoBK 10 of approx. 11 bar does not induce a significant reaction in these boreholes. MARSCHALL and JOHNS (1993) published the initial results of the spectral analysis.

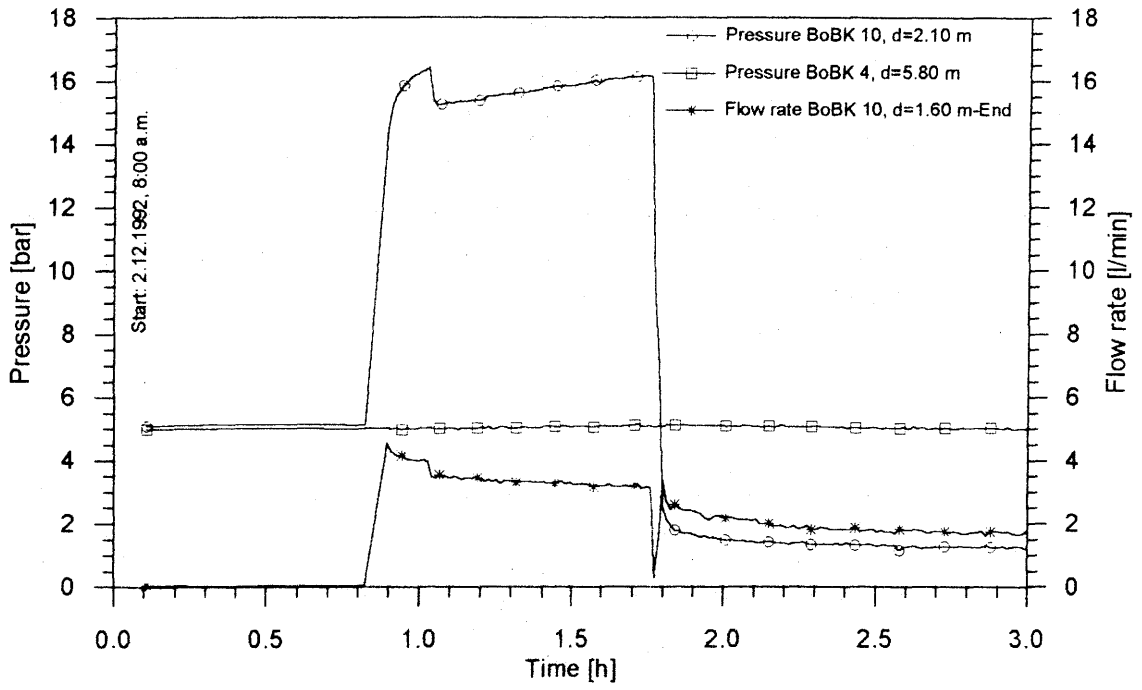


Figure 5.23: VE 510 - Pressures in boreholes BoBK 4 and BoBK 10 and flow rate in borehole BoBK 10 as a function of time

6. Tracer Testing and Test Simulation

6.1 Tracer Test VE 483 (Salt): BoBK 14 --> BoBK 8

6.1.1 Course and Documentation of Tracer Test VE 483

The objective of the test was to determine the flow velocity of a tracer over long distances. All boreholes with the exception of the injection borehole BoBK 14 (fan A) and the extraction borehole BoBK 8 were shut in, forcing the tracer to flow by the shortest route and through the fracture system with the greatest hydraulic conductivity from borehole BoBK 14 to BoBK 8. The distance tested, 25 m, was the greatest investigated in the BK area to date. Earlier testing had covered distances under 20 m (PAHL et al. 1992):

- from BoBK 4 to BoBK 5 (approx. 5 m)
- from BoBK 4 to BoBK 9 (approx. 10 m)
- from BoBK 9 to BoBK 6 (approx. 20 m)

The equipment configuration is seen in the schematic installation protocol (Table 6.1).

The test scheduling was as follows:

5.3.1991	10:00 a.m.	Beginning of injection in BoBK 14: 2.0 l/min at 20 μ S/cm Injection interval in BoBK 14: 16.00 m - final depth Extraction interval 1 in BoBK 8: 9.35 m - 18.65 m Extraction interval 2 in BoBK 8: 19.65 m - 29.00 m Flow rate extraction interval 1 and 2: 2 - 3 l/min
6.3.1991	10:00 a.m.	Change of conductivity of injection water to 1,000 μ S/cm
19.3.1991	10:00 a.m.	Change of conductivity of injection water to 20 μ S/cm
7.4.1991	10:00 a.m.	Change of injection rate to 0.2 l/min
15.4.1991		Injection stopped
19.4.1991		Extraction borehole BoBK 8 shut in

The most important results (flow rates, pressure buildup, electr. conductivity) are shown in Figures 6.1-6.3. The figures are all in relation to 1.3.91, 0:00 hours. Thus part of the previous history up to commencement of injections on 5.3.91 is covered. The injection rate was controlled by a process control system until 8.3.91, thereafter manually.

Table 6.1: Installation protocol, tracer test VE 483

Borehole	Packer position (m borehole depth)	Observation interval (m borehole depth)	Probe position (m borehole depth)	Remark
BoSB 80.001	0.00 - 0.50	0.50 - End	Tunnel	
BoBK 86.002	0.00 - 0.50	0.50 - End	Tunnel	
BoBK 86.003	0.00 - 0.50	0.50 - End	Tunnel	
BoBK 85.004	1.00 - 2.00	2.00 - 15.70	Tunnel	
	15.70 - 16.70	16.70 - 43.70	Tunnel	
BoBK 85.005	1.50 - 2.50	2.50 - 13.50	2.50 - 3.50	
	13.50 - 14.50	14.50 - 29.50	14.50 - 15.50	
	29.50 - 30.50	30.50 - End	30.50 - 31.50	
BoBK 85.006	1.00 - 2.00	2.00 - 21.00	2.00 - 3.00	
	21.00 - 22.00	22.00 - 27.00	22.00 - 23.00	
	27.00 - 28.00	28.00 - End	28.00 - 29.00	
BoBK 85.007	2.00 - 3.00	3.00 - 7.00	3.00 - 4.00	
	8.00 - 9.00	9.00 - End	9.00 - 10.00	
BoBK 85.008	8.35 - 9.35	9.35 - 18.65	Tunnel	Extraction Extraction
	18.65 - 19.65	19.65 - 29.00	Tunnel	
	29.00 - 30.00	30.00 - End	Tunnel	
BoBK 85.009	14.00 - 15.00	15.00 - 20.00	15.00 - 16.00	
	20.00 - 21.00	21.00 - 34.00	21.00 - 22.00	
	34.00 - 35.00	35.00 - End	35.00 - 36.00	
BoBK 85.010	0.00 - 0.50	0.50 - End	Tunnel	
BoBK 85.011	2.00 - 3.00	3.00 - End	3.00 - 4.00	
BoBK 88.012	1.80 - 2.80	2.80 - End	-	
BoBK 88.013	4.00 - 5.00	5.00 - End	5.00 - 6.00	
BoBK 88.014	1.00 - 2.00	2.00 - 14.90	Tunnel	Injection
	14.90 - 15.90	15.90 - End	Tunnel	
BoBK 88.015	2.00 - 3.00	3.00 - End	3.00 - 4.00	
BoBK 88.016	6.00 - 7.00	7.00 - End	7.00 - 8.00	
BoBK 88.017	1.80 - 2.80	2.80 - 21.80	2.80 - 3.80	
	21.80 - 22.80	22.80 - 31.80	22.80 - 23.80	
	31.80 - 32.80	32.80 - End	32.80 - 33.80	
BoBK 88.018	2.00 - 3.00	3.00 - End	3.00 - 4.00	
BoUS 85.003	0.00 - 0.50	0.50 - End	Tunnel	

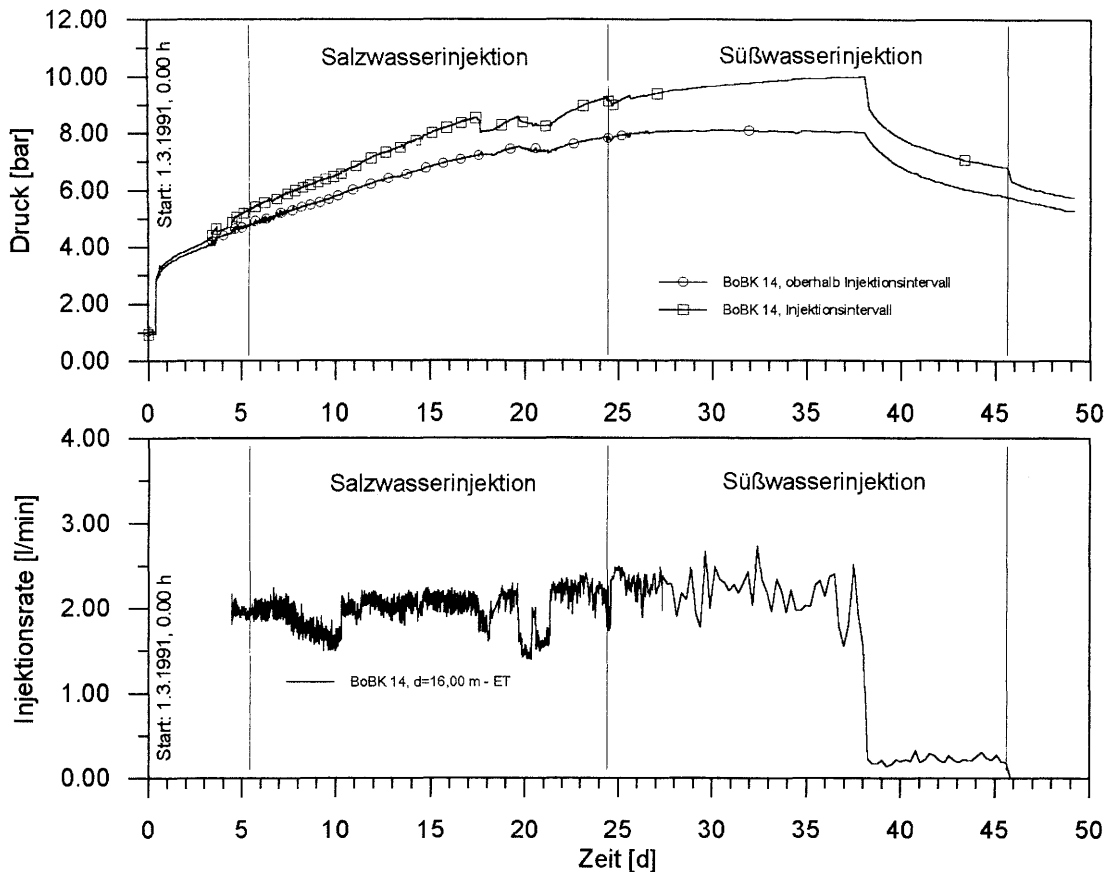


Figure 6.1: VE 483 - Pressure and injection rate in borehole BoBK 14 as a function of time

The injection pressure in borehole BoBK 14 and the pressure under the injection element are shown in Figure 6.1. In spite of the opened extraction borehole, the pressures climbed over a longer period in all other boreholes in a nearly parallel manner (approx. 5 bar throughout the test phase, see Fig. 6.2). The pressure increase in the opened observation borehole, BoBK 8, is approx. 1 bar lower than in the other boreholes throughout the test phase; this pressure increase is attributed to the small tube diameters in the conductometer. The discharge climbs in the course of the test from 2 l/min to 3 l/min.

Figure 6.3 shows the electrical conductivity in extraction borehole BoBK 8 in sum and separately for both observation intervals. The tracer breakthrough time from the injection interval in borehole BoBK 14 to the head of the borehole in BoBK 8 was approximately 24 h. This results in a mean flow velocity of approximately 1 m/h. The later reaction in the interval from 19.65 to 29.00 m is, strangely enough, blurred in the cumulative curve.

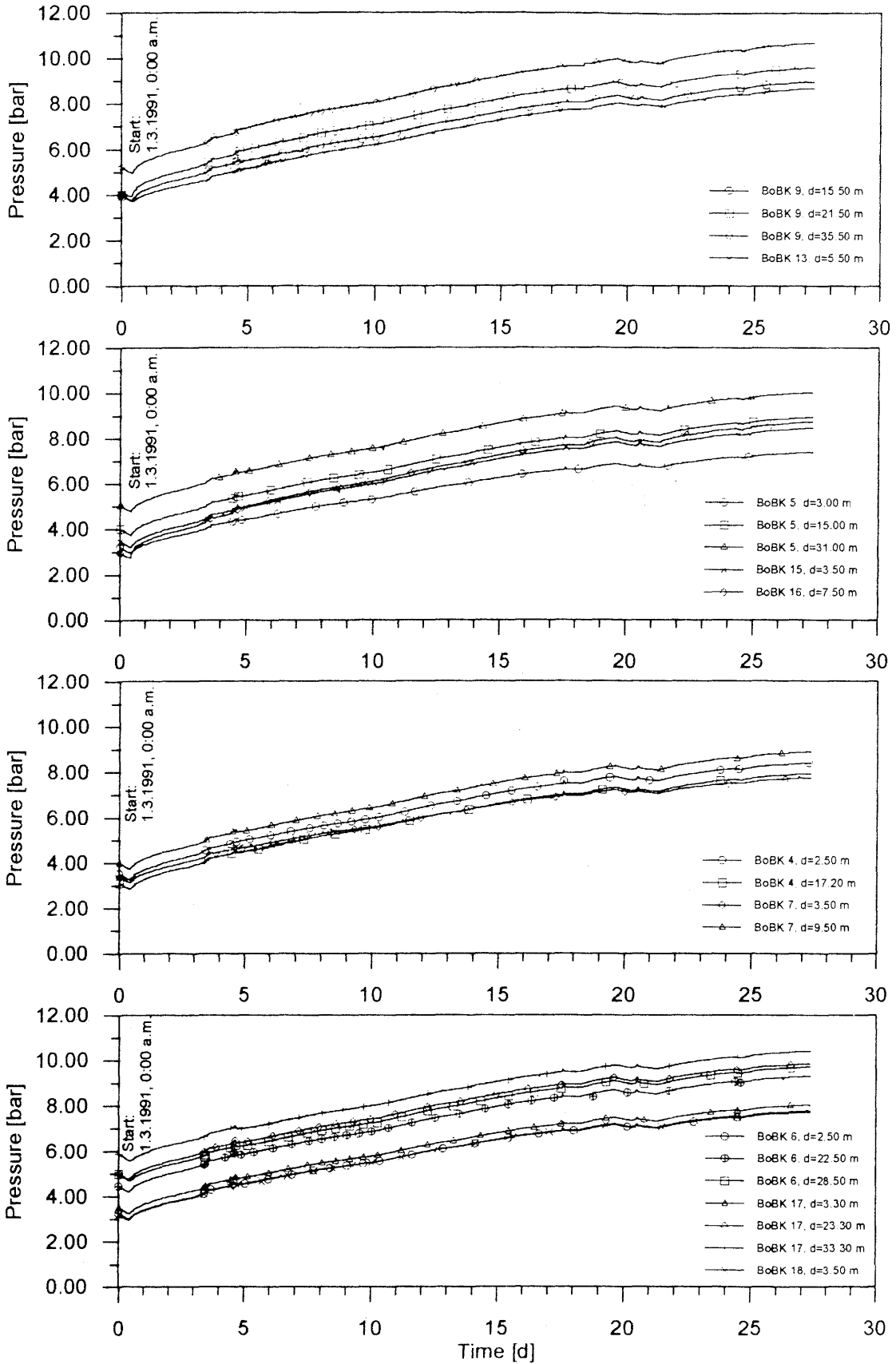


Figure 6.2: VE 483 - Pressure and injection rate in the central BK area boreholes as a function of time

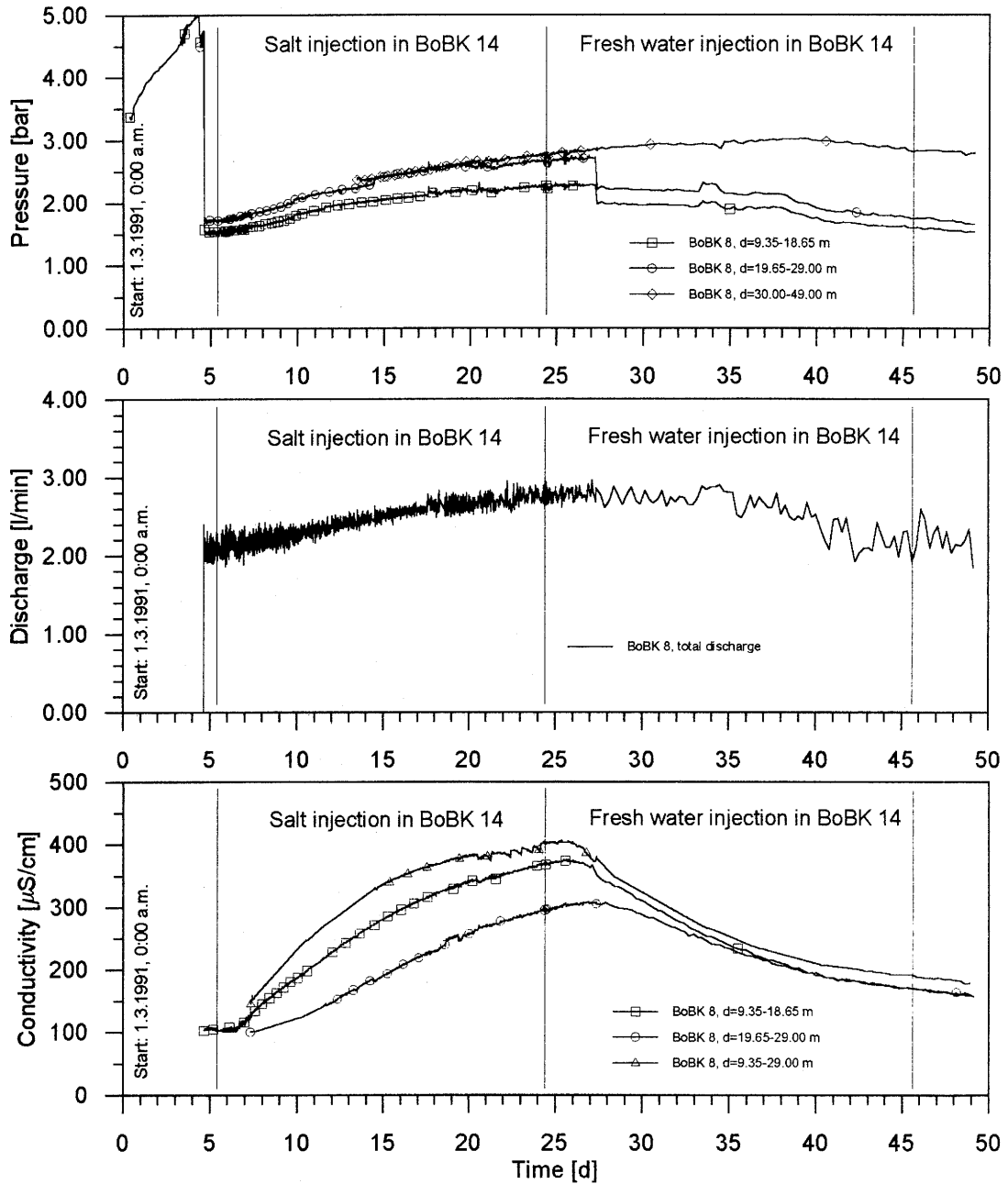


Figure 6.3: VE 483 - Measured parameters pressure, discharge and electrical conductivity in extraction borehole BoBK 8 as a function of time

6.1.2. Numerical Simulation of Tracer Test VE 483

Parallel to testing, a trend exploration of tracer concentrations was carried out for borehole BoBK 8 using the finite element (FE) program DURST. One- and two-dimensional models were employed. In both cases, flow and transport computations were done in accordance with the modular structure of DURST.

a) Flow computations with DURST SM-1D under the following boundary conditions (see Fig. 6.4)

Injection rate	q_i	=	2 l/min
Extraction rate	q_o	=	2 l/min
Hydraulic head at injection site	H_o	=	80 m
Hydraulic head at extraction site	H_u	=	0 m
30 1D-elements:	Length	l	= 1 m
	Cross-section	F	= 0.100 m ²
25 elements with hydr. conductivity	k_{f1}	=	10 ⁻³ m/s
5 elements with hydr. conductivity	k_{f2}	=	10 ⁻⁴ m/s at outflow
Steady flow field	S	=	0

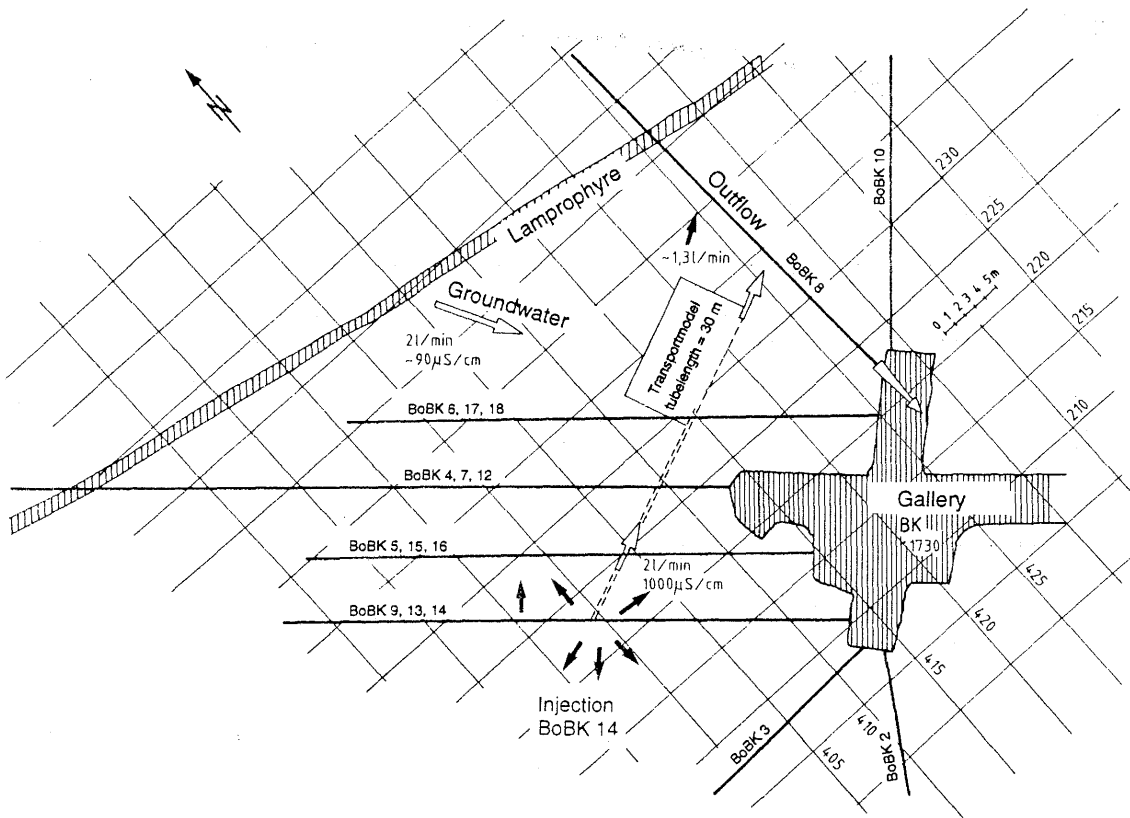


Figure 6.4: VE 483 - Simulation of tube flow

b) Transport computation with input values from the 1D flow model (Fig. 6.5):
 Four main variants with different time increments from 60 to 3,600 s and differing parametric settings were calculated (see Table 6.2). Results for the first variant without diffusion were unrealistic. The second variant showed a concentration rise in discharge borehole BoBK 8 that was too steep at $C_o = 1,000 \mu\text{S}/\text{cm}$. After reducing the velocity and increasing diffusion in the third variant, the characteristic of the test curve was not reflected. In the 4th variant, the concentration of the injection water was reduced to $C_o = 450 \mu\text{S}/\text{cm}$ to simulate mixture of the injected water with the inflowing groundwater.

Table 6.2: VE 483 - Parameter variation in transport computations

Variant	2 (1D)	3 (1D)	4 (1D)	5 (2D)
v [m/d]	28.8	14.4	14.4	7.2
D [m ² /s]	$1 \cdot 10^{-4}$	$3 \cdot 10^{-4}$	$3 \cdot 10^{-4}$	$5 \cdot 10^{-4}$
α_L [m]	-	-	-	0.1
α_T [m]	-	- <td -	0.01	
C_0 [μ S/cm]	1000	1000	450	450

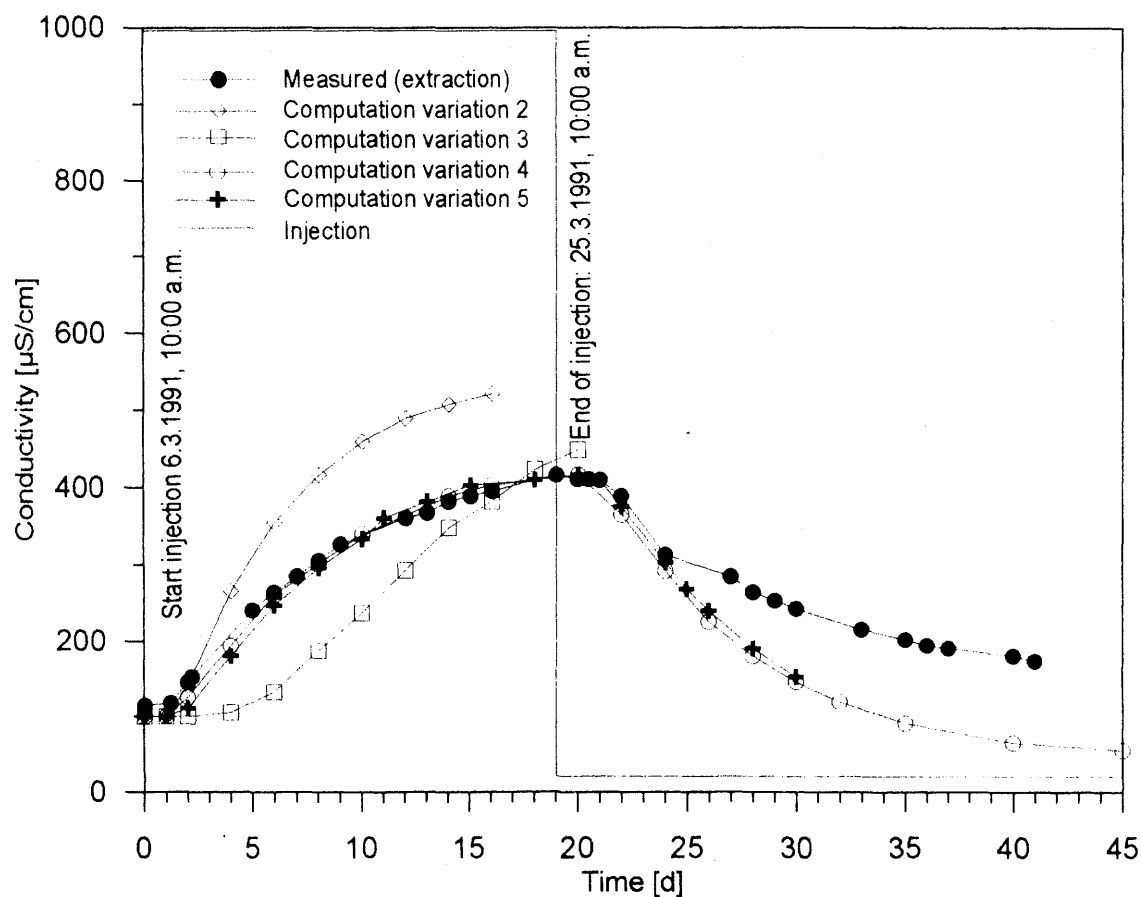


Figure 6.5: VE 483 - Results of parameter variation (tube flow)

c) Flow computation (2D) with a disc:

Taking advantage of the symmetry, only half the fracture was modelled. The boundary conditions under a) were applied for the most part.

d) Transport computation (2D) with a time increment of 3,600 s:

Scheidegger's dispersion principle was applied. Figure 6.6 shows a possible result. The disc consisted of 30 elements along the x axis (source-sink axis) and 13 elements along the y axis. On the x axis ($y=0$), the nodes are designated as 1-31. The source (injection) is at node 13, the sink (extraction) at node 29. Figure 6.6a shows electrical conductivity as a function of time for source and sink; Figure 6.6b shows the distribution of conductivity on the source-sink axis between nodes 1 and 31 for 8 selected times.

e) Comparison of computer results from various tracer tests at the same location:

Tracer test 298 (see also PAHL et al. 1992) was carried out at the same location in the BK area. Table 6.3 lists several parameters of the simulation of tracer test VE 483 in a comparison with those of LEGE & ZIELKE (1993), who processed test VE 298 in a 2D model with DURST.

Table 6.3: Comparison of parameters in simulation of tracer tests with the finite element (FE) model DURST

Parameter	1D-simulation (tube)	2D-simulation (disc)	2D-simulation (disc) LEGE & ZIELKE (1993)
Hydraulic conductivity k_{f1} [m/s]	10^{-3}	10^{-3}	$7 \cdot 10^{-5}$
Hydraulic conductivity k_{f2} [m/s]	10^{-4}	10^{-4}	-
Dispersion length a_L [m]	-	0.1	5.0
Dispersion length a_T [m]	-	0.01	1.0
Coefficient of diffusion D [m ² /s]	-	$5 \cdot 10^{-4}$	-

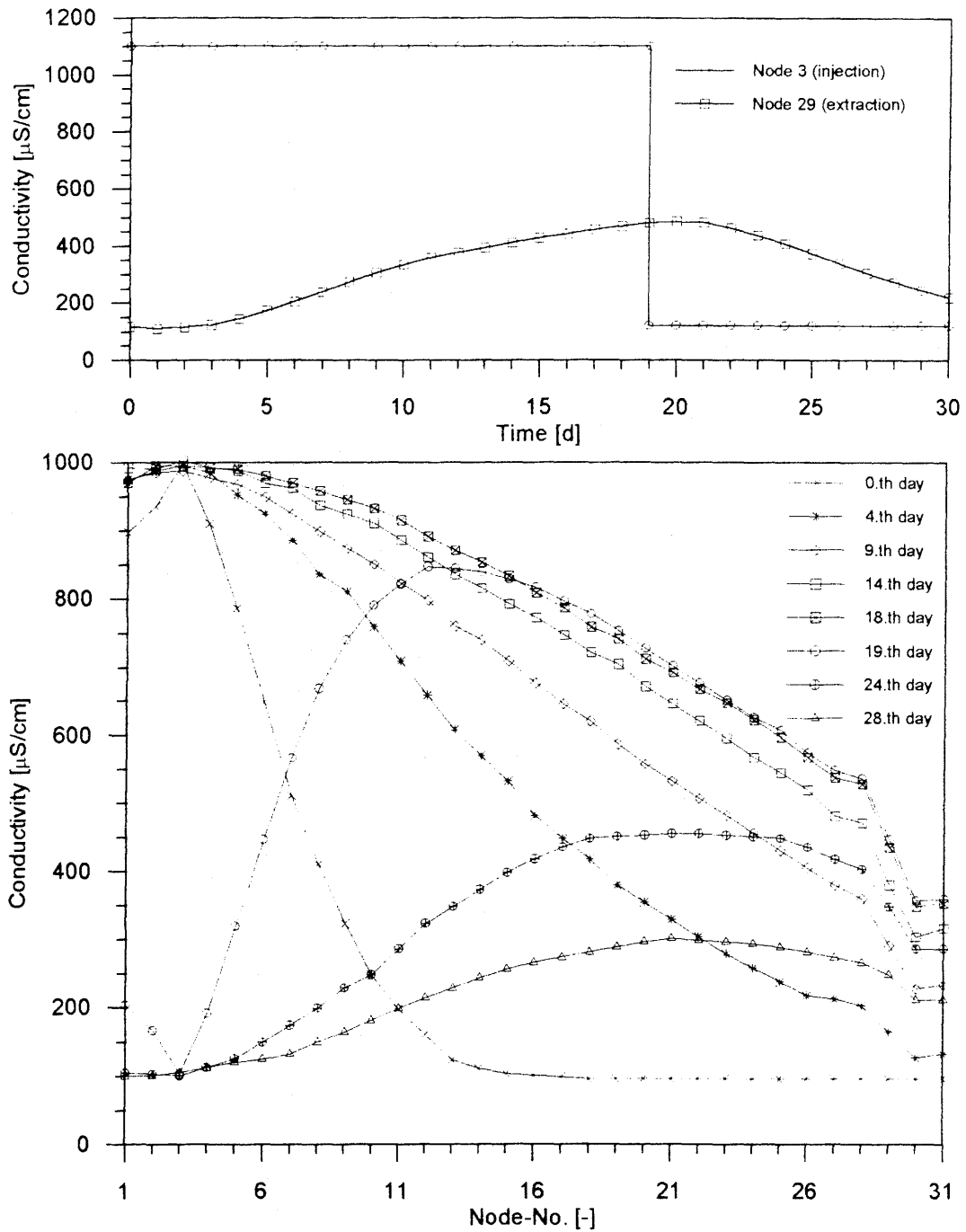


Figure 6.6: VE 483 - Simulation as a 2D model
 a) Conductivity as a function of time for source and sink
 b) Conductivity for various times above the source-sink axis

6.2 Tracer Test VE 493 (Salt): BoBK 14 --> BoBK 10

6.2.1 Course and Documentation of Preliminary Tests

The tracer tests VE 493a and 493b were carried out in 1992 and were based mainly on tracer test VE 483 from 1991 (see 6.1). Whereas the water in VE 483 had to overcome a distance of about 30 m through the rock (direct connection between BoBK 14 and BoBK 8), the flow pathway in 1992 was over 60 m long. In accordance with earlier data on the fractures, the water had to take a detour via borehole BoBK 8 to the lamprophyre to the north of the central test location (Fig. 6.7) to get to borehole BoBK 10.

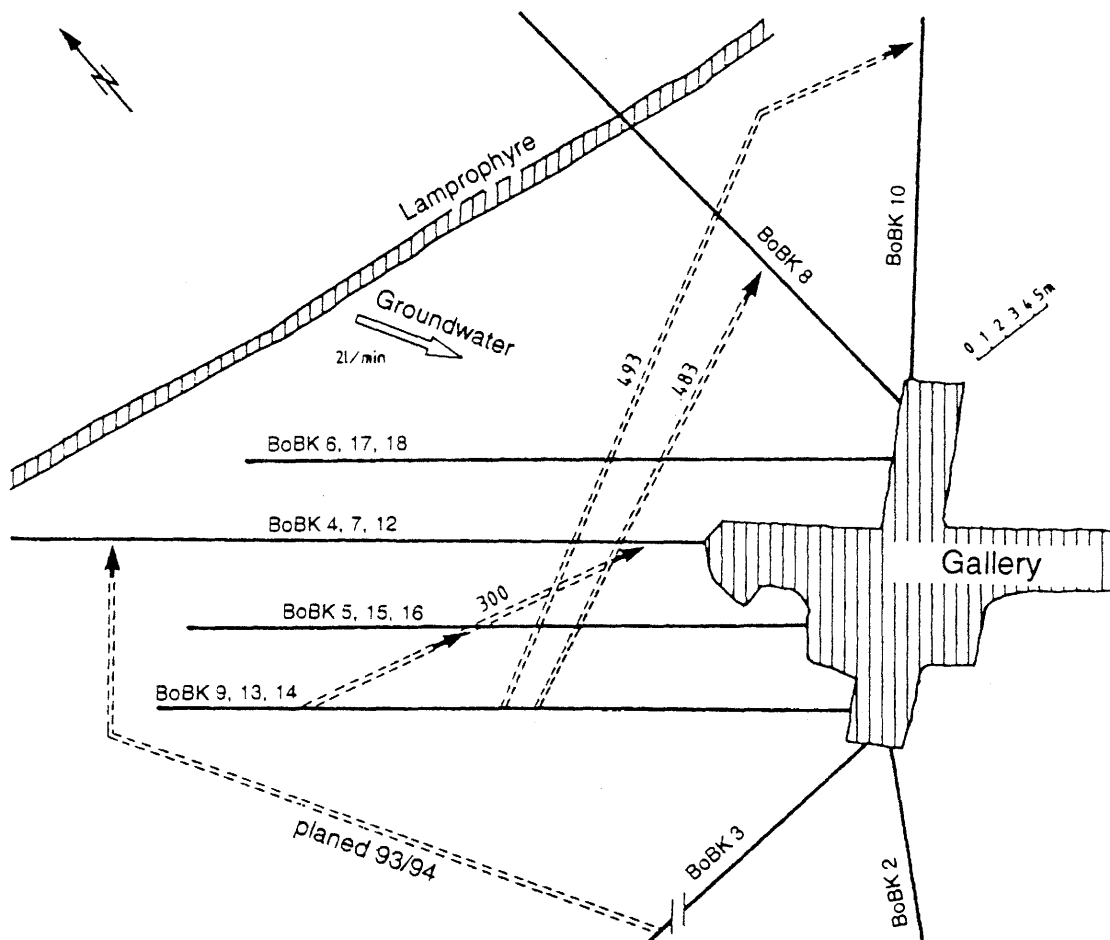


Figure 6.7: Laboratory tunnel, flow pathways of tracer tests (schematic)

The hydraulic conductivity of the rock in the vicinity of borehole BoBK 8 and the possible disturbed zone before the lamprophyre is two orders of magnitude lower than the conductivity of the most influential fracture zone at the central test location into which the brine was to be injected.

Computations with a tube flow model in the program DURST were carried out to estimate the breakthrough times and expected electrical conductivities. Figure 6.8 shows different conductivity curves from various model variations (with and without groundwater inflow, two parallel tubes, taking leakages into account). As it later turned out, these trend analyses corresponded only approximately to those measured in situ as to breakthrough time.

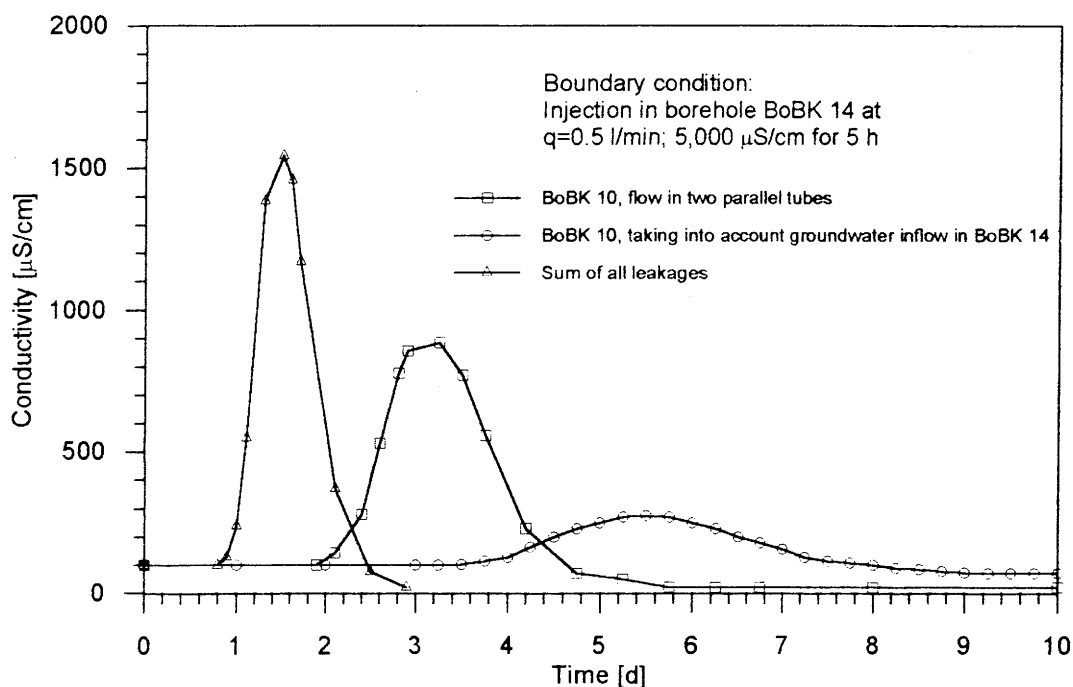


Figure 6.8: VE 493 - Prognosis of tracer breakthrough time in the extraction borehole

6.2.1.1 Tests VE 488 and VE 489 (Pressure Buildup Tests)

These tests were carried out as preliminary steps to tracer test VE 493. Table 6.4 shows the packer and probe protocol. All boreholes were shut in by means of mechanical and pneumatic packers. 4 combination probes were installed in borehole BoBK 8 for testing over this long period (> 2 months).

Figure 6.9 shows the interval pressures at 12, 15, 18 and 21 m in the borehole. Figure 6.10 shows an enlarged section of Figure 6.9 with the pressure recordings beginning on day 43 of the test. Figure 6.11 shows the corresponding hydraulic heads. Figure 6.12 can be used to demonstrate the measuring accuracy for temperature. Pressure, temperature and packer pressure for the deepest probe at a borehole depth of approx. 21 m are found in Figure 6.13.

Table 6.4: Installation protocol, tracer tests VE 488/489

Borehole	Packer position (m borehole depth)	Observation interval (m borehole depth)	Probe position (m borehole depth)	Remark
BoSB 80.001	0.00 - 0.50	0.50 - End	Tunnel	
BoBK 86.002	0.00 - 0.50	0.50 - End	Tunnel	
BoBK 86.003	0.00 - 0.50	0.50 - End	Tunnel	
BoBK 85.004	1.00 - 2.00	2.00 - 15.70	Tunnel	
	15.70 - 16.70	16.70 - 43.70	Tunnel	
BoBK 85.005	1.50 - 2.50	2.50 - 13.50	2.50 - 3.50	
	13.50 - 14.50	14.50 - 29.50	14.50 - 15.50	
	29.50 - 30.50	30.50 - End	30.50 - 31.50	
BoBK 85.006	1.00 - 2.00	2.00 - 21.00	2.00 - 3.00	
	21.00 - 22.00	22.00 - 27.00	22.00 - 23.00	
	27.00 - 28.00	28.00 - End	28.00 - 29.00	
BoBK 85.007	2.00 - 3.00	3.00 - 7.00	3.00 - 4.00	
	7.00 - 8.00	8.00 - End	8.00 - 9.00	
BoBK 85.008	10.00 - 11.00	11.00 - 13.00	11.00 - 12.00	Multi- functional probes
	13.00 - 14.00	14.00 - 16.00	14.00 - 15.00	
	16.00 - 17.00	17.00 - 19.00	17.00 - 18.00	
	19.00 - 20.00	20.00 - End	20.00 - 21.00	
BoBK 85.009	14.00 - 15.00	15.00 - 20.00	15.00 - 16.00	
	20.00 - 21.00	21.00 - 34.00	21.00 - 22.00	
	34.00 - 35.00	35.00 - End	35.00 - 36.00	
BoBK 85.010	1.50 - 2.50	2.50 - End	2.50 - 3.50	Extraction
BoBK 85.011	2.00 - 3.00	3.00 - End	3.00 - 4.00	
BoBK 88.012	1.80 - 2.80	2.80 - End	2.80 - 3.80	
BoBK 88.013	4.00 - 5.00	5.00 - End	5.00 - 6.00	
BoBK 88.014	1.00 - 2.00	2.00 - 14.90	Tunnel	
	14.90 - 15.90	15.90 - End	Tunnel	
BoBK 88.015	2.00 - 3.00	3.00 - End	3.00 - 4.00	
BoBK 88.016	6.00 - 7.00	7.00 - End	7.00 - 8.00	
BoBK 88.017	1.80 - 2.80	2.80 - 21.80	2.80 - 3.80	
	21.80 - 22.80	22.80 - 31.80	22.80 - 23.80	
	31.80 - 32.80	32.80 - End	32.80 - 33.80	
BoBK 88.018	2.00 - 3.00	3.00 - End	3.00 - 4.00	
BoUS 85.003	0.00 - 0.50	0.50 - End	Tunnel	

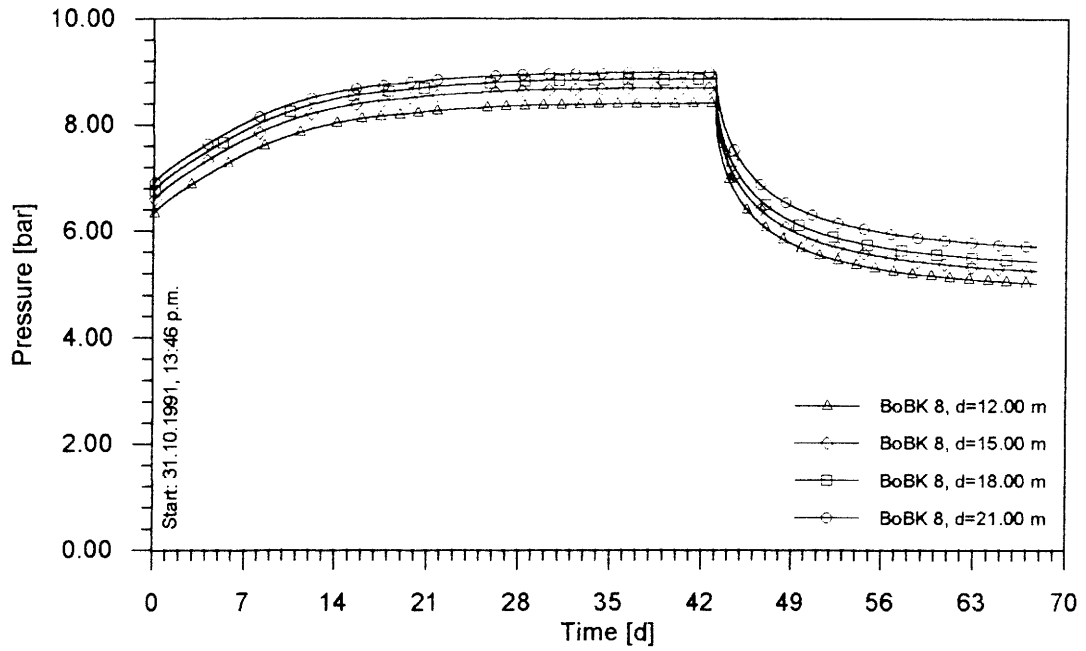


Figure 6.9: VE 489 - Pressure in borehole BoBK 8 as a function of time (measurement with multifunctional probes)

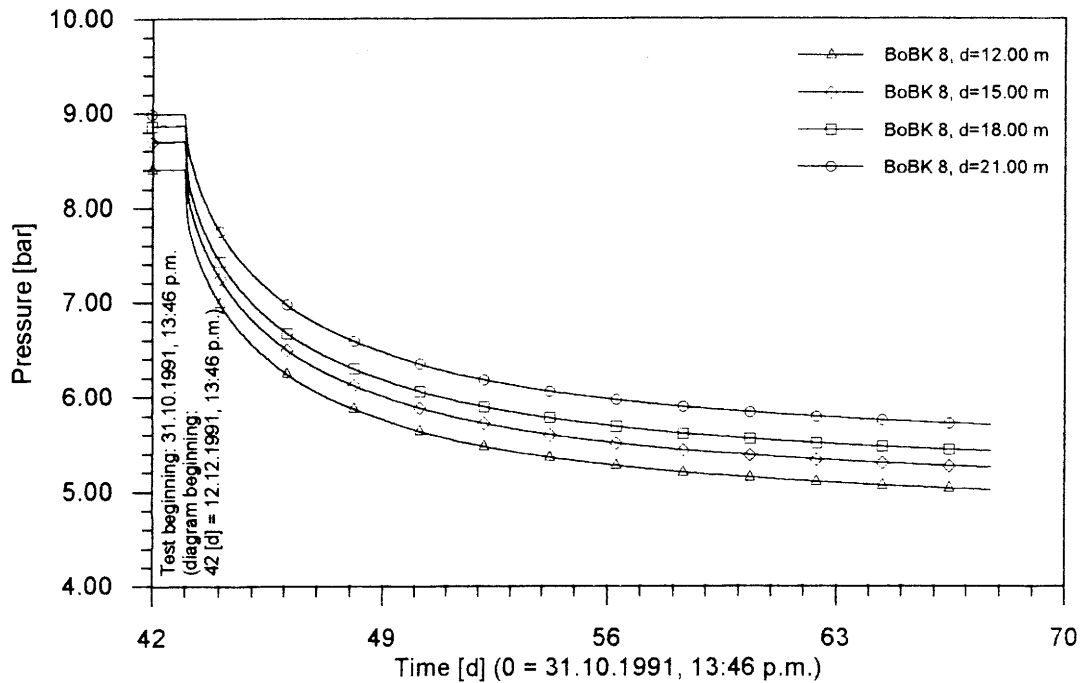


Figure 6.10: VE 489 - Pressure in borehole BoBK 8 as a function of time (enlargement of section from Fig. 6.9)

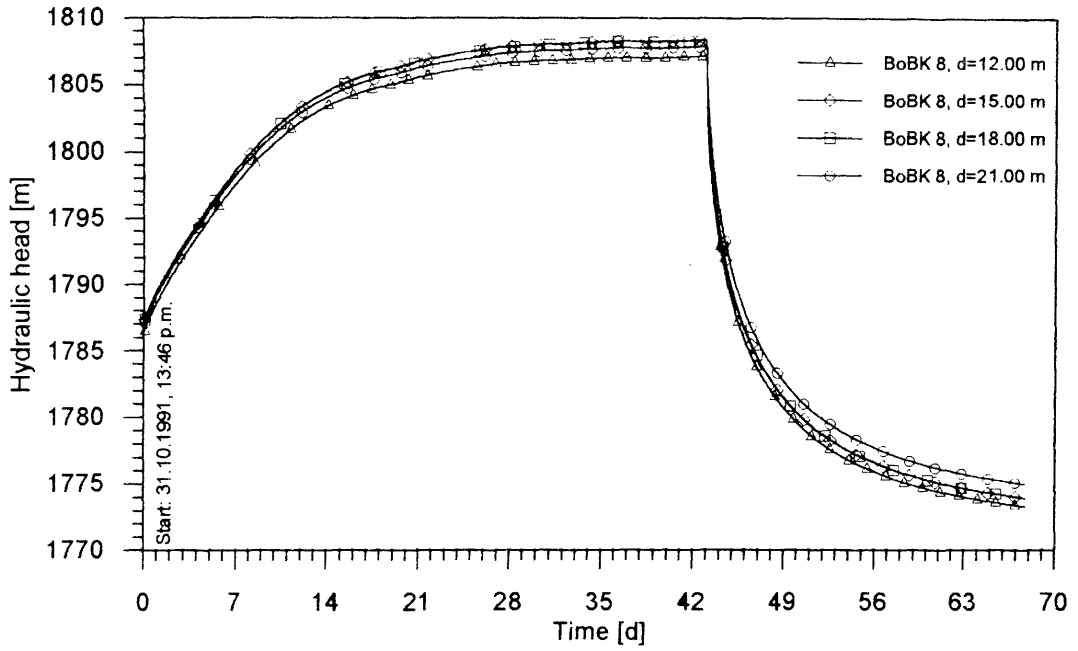


Figure 6.11: VE 489 - Hydraulic head in borehole BoBK 8 as a function of time (measurement with multifunctional probes)

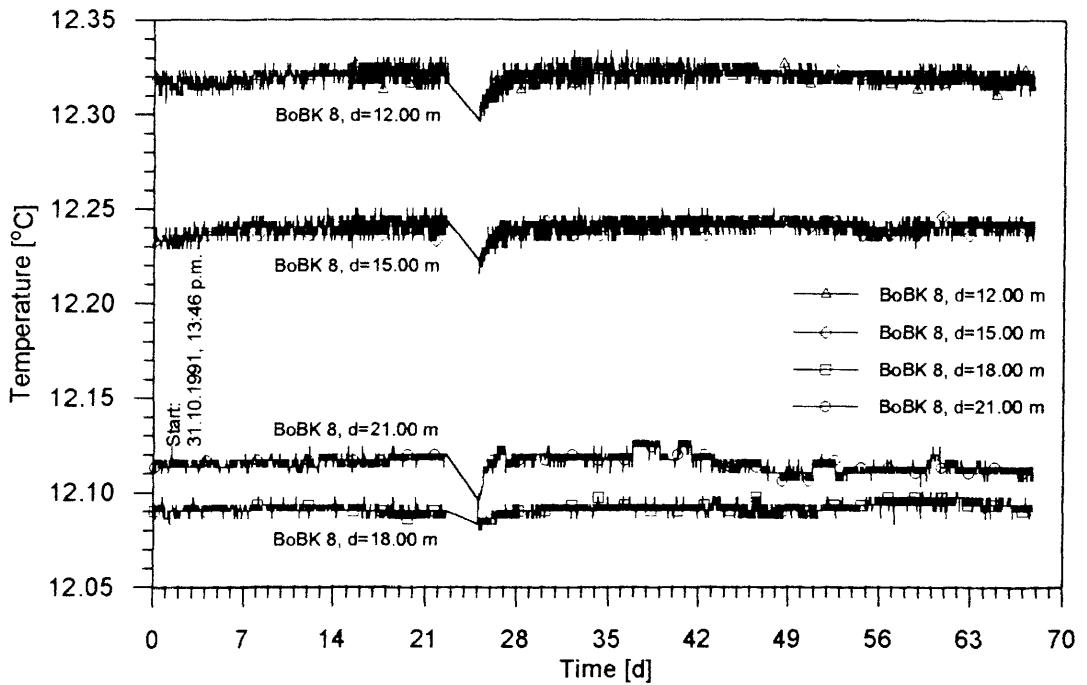


Figure 6.12: VE 489 - Temperature in borehole BoBK 8 as a function of time (measurement with multifunctional probes)

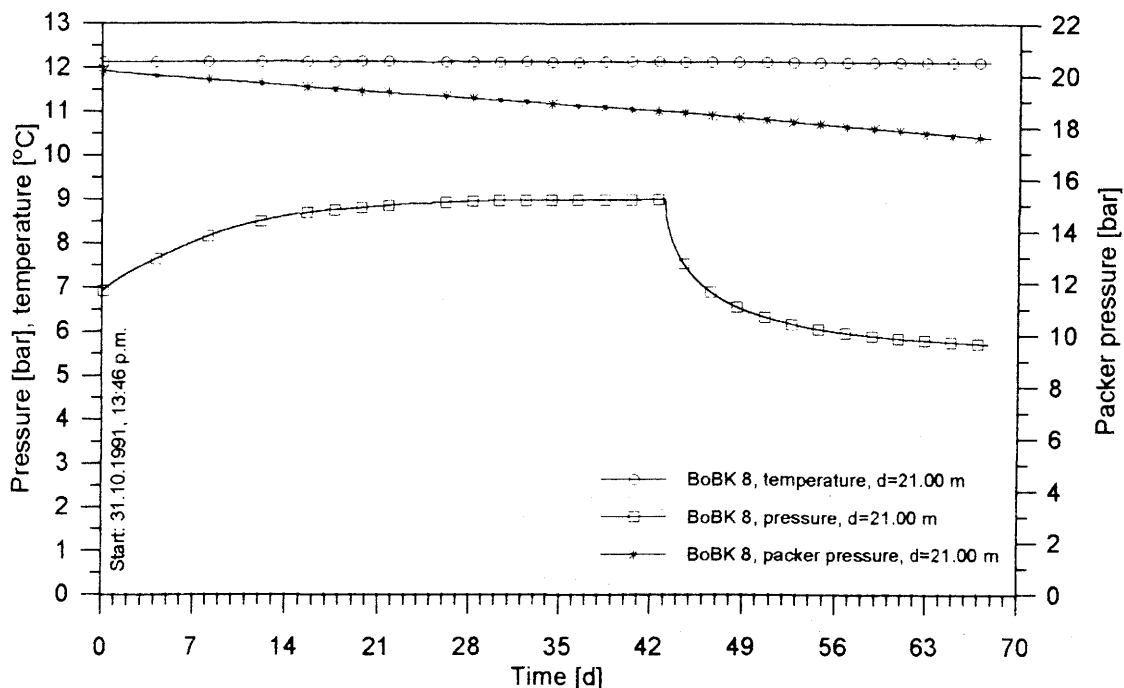


Figure 6.13: VE 489 - Temperature, pressure and packer pressure of multifunctional probe 5 in borehole BoBK 8 as a function of time

6.2.1.2 Conductivity Measurement in Borehole BoBK 10

In order to position the threefold packer element in borehole BoBK 10 with a degree of precision, it was necessary to know about the active water-bearing layer. Electrical conductivity was measured at intervals of about 1 h following flushing with fresh water. The next measuring location was not changed until the transient effect process of the probes was over. The results are seen in Figure 6.14. In addition to the most important water inflow site, the packer system installed later is also shown. For the following tests, the groundwater inflow site was established at a depth of 18.28 - 27.66 m. The fracture with the greatest discharge is found in this borehole segment, at about 20 m. Packer 3 (see Fig. 6.14) delimits the inflow from the lamprophyre and the rock behind it. Figures 6.15 and 6.16 show examples of core views from drill cores taken from borehole BoBK 10. Figure 6.15 clearly shows the hydraulically most important fracture system at between 19.80 and 20.80 m.

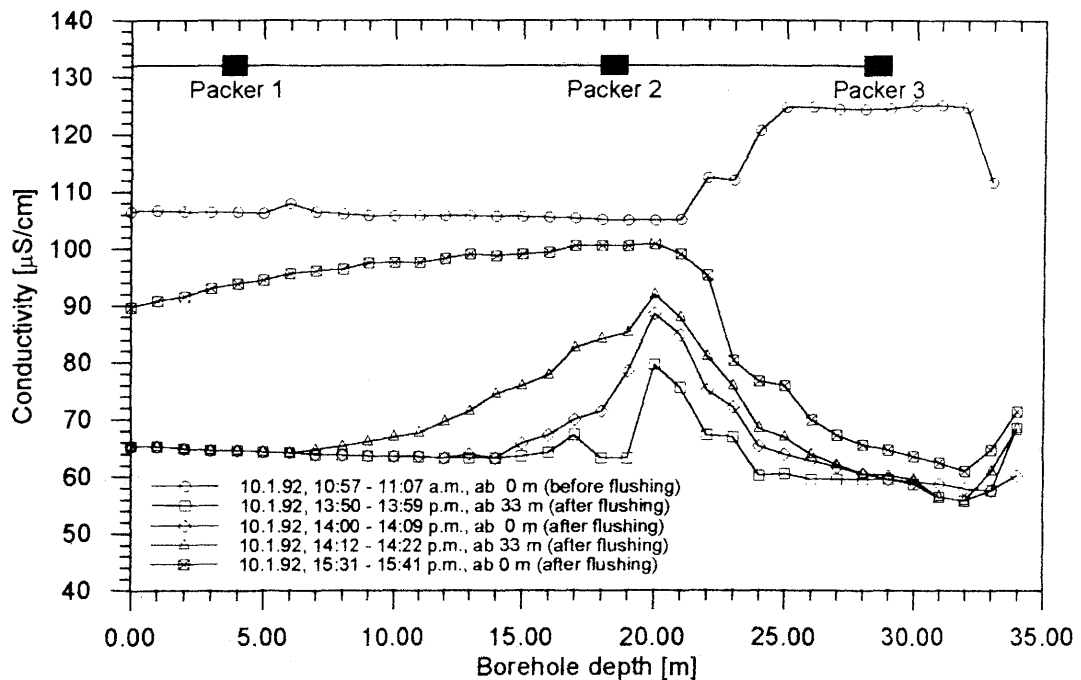


Figure 6.14: VE 489 - Conductivity measurement before and after flushing in borehole BoBK 10 and derived packer positions

6.2.1.3 Flow (Outflow) Test VE 492, Borehole BoBK 14

This test demonstrates the short-term behaviour of the hydraulic regime at max. discharge of approx. 30 l/min (Fig. 6.17). Figure 6.18 shows pressure in borehole BoBK 14; Figures 6.19 and 6.20 show pressures in borehole BoBK 8 at various depths (11-13 m, 14-16 m, 17-19 m, 21 m - end). Varying degrees of clear pressure reaction are evident in all areas.

A corresponding injection test, VE 490 (Fig. 6.21), shows little pressure reaction in the neighbouring borehole BoBK 9, and that on the basis of a value spread (Fig. 6.22) due to the relatively high levels of hydraulic conductivity and low water volumes. Table 6.5 shows the probe and packer positions.

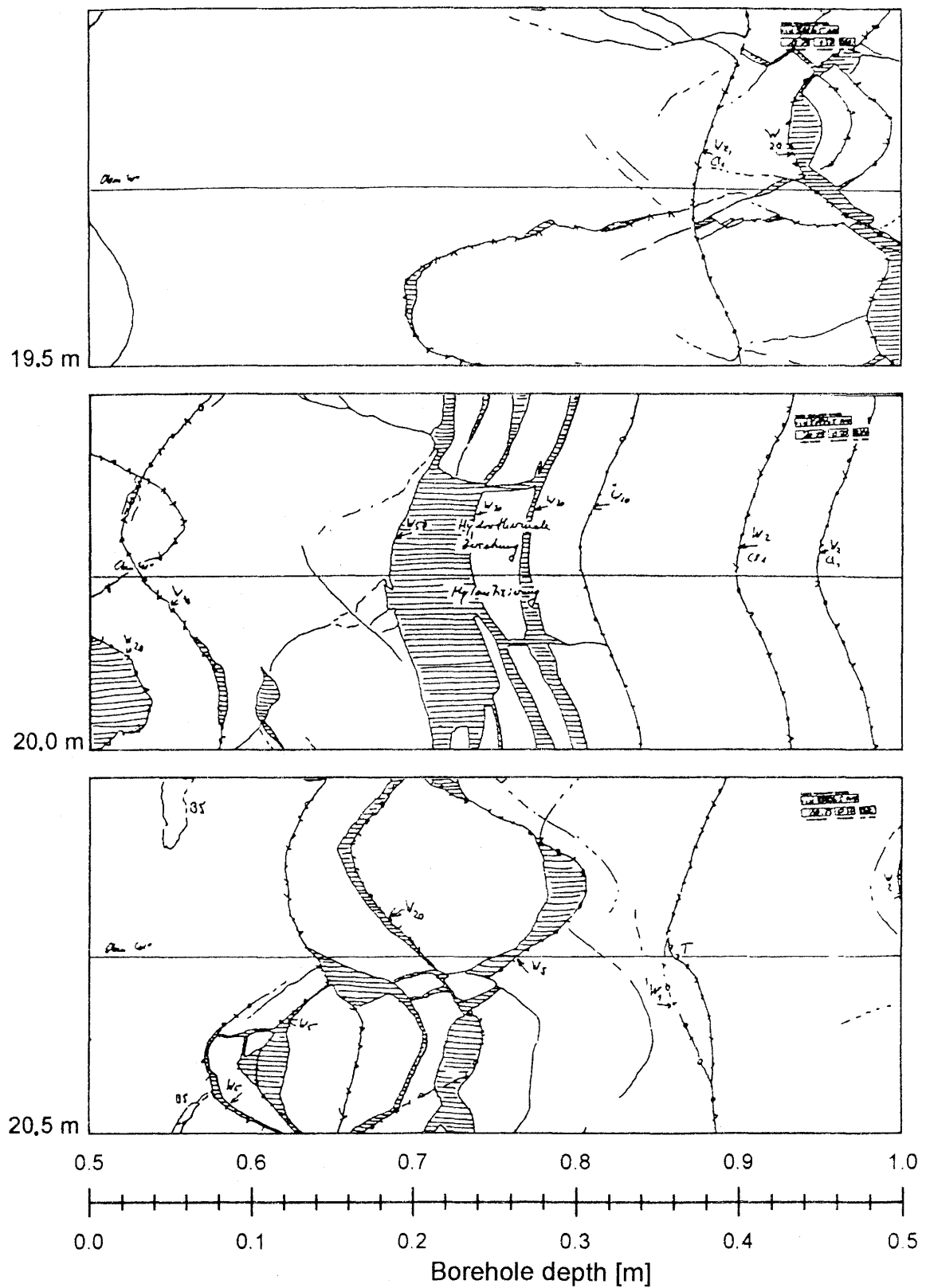


Figure 6.15: Core view, borehole BoBK 10, depth 19.5-21.0 m

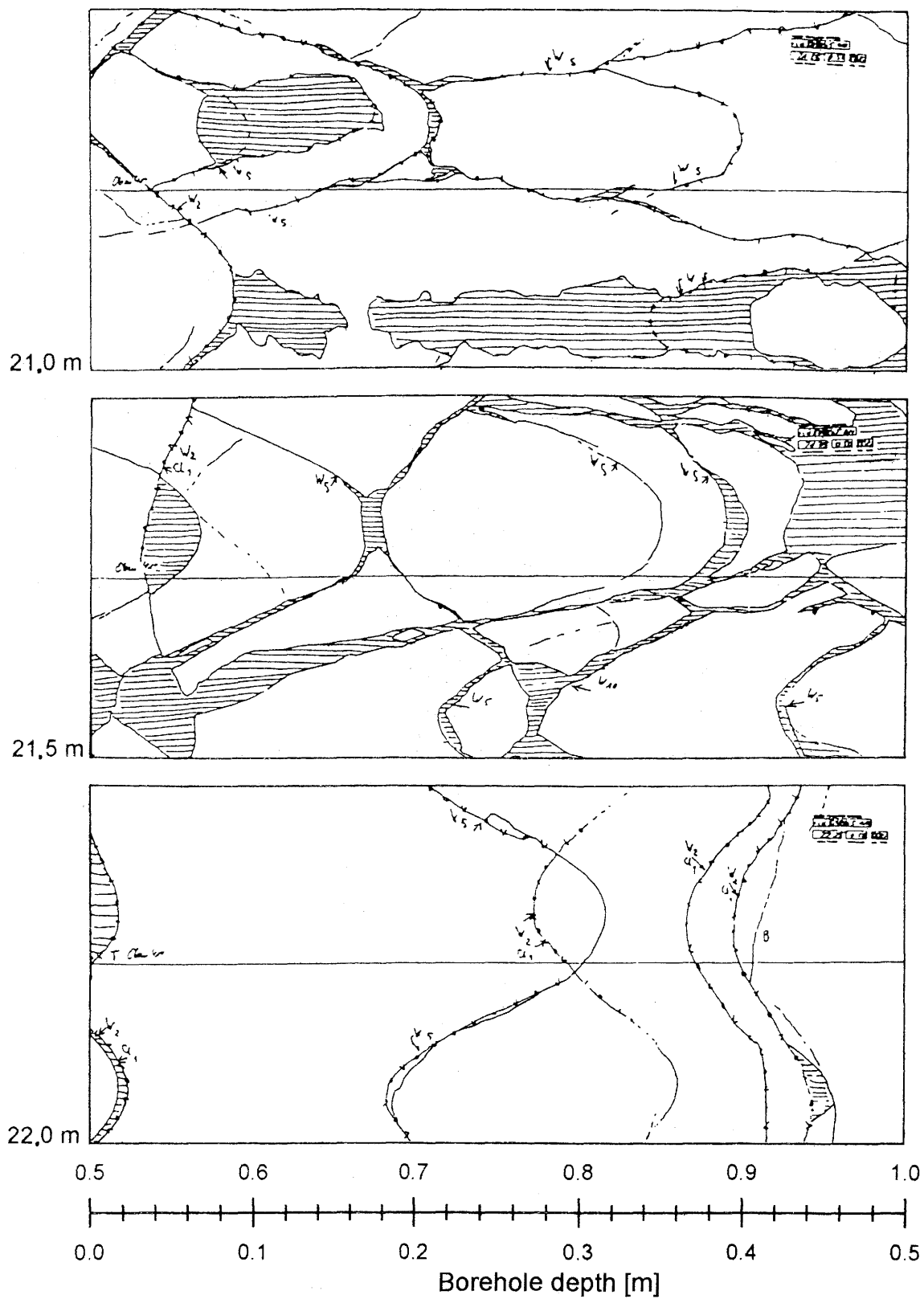


Figure 6.16: Core view, borehole BoBK 10, depth 21.0-22.5 m

Table 6.5: Installation protocol, tracer tests VE 492/493

Borehole	Packer position (m borehole depth)	Observation interval (m borehole depth)	Probe position (m borehole depth)	Remark
BoSB 80.001	0.00 - 0.50	0.50 - End	Tunnel	
BoBK 86.002	0.00 - 0.50	0.50 - End	Tunnel	
BoBK 86.003	0.00 - 0.50	0.50 - End	Tunnel	
BoBK 85.004	1.00 - 2.00	2.00 - 15.70	Tunnel	
	15.70 - 16.70	16.70 - 43.70	Tunnel	
BoBK 85.005	1.50 - 2.50	2.50 - 13.50	2.50 - 3.50	
	13.50 - 14.50	14.50 - 29.50	14.50 - 15.50	
	29.50 - 30.50	30.50 - End	30.50 - 31.50	
BoBK 85.006	1.00 - 2.00	2.00 - 21.00	2.00 - 3.00	
	21.00 - 22.00	22.00 - 27.00	22.00 - 23.00	
	27.00 - 28.00	28.00 - End	28.00 - 29.00	
BoBK 85.007	2.00 - 3.00	3.00 - 7.00	3.00 - 4.00	
	7.00 - 8.00	8.00 - End	8.00 - 9.00	
BoBK 85.008	10.00 - 11.00	11.00 - 13.00	11.00 - 12.00	Multi- functional probes
	13.00 - 14.00	14.00 - 16.00	14.00 - 15.00	
	16.00 - 17.00	17.00 - 19.00	17.00 - 18.00	
	19.00 - 20.00	20.00 - End	20.00 - 21.00	
BoBK 85.009	14.00 - 15.00	15.00 - 20.00	15.00 - 16.00	
	20.00 - 21.00	21.00 - 34.00	21.00 - 22.00	
	34.00 - 35.00	35.00 - End	35.00 - 36.00	
BoBK 85.010	2.00 - 3.00	3.00 - 17.25	3.00 - 4.00	Extraction
	17.25 - 18.25	18.25 - 27.66	18.25 - 19.25	
	27.66 - 28.66	28.66 - END	28.66 - 29.66	
BoBK 85.011	2.00 - 3.00	3.00 - End	3.00 - 4.00	
BoBK 88.012	1.80 - 2.80	2.80 - End	2.80 - 3.80	
BoBK 88.013	4.00 - 5.00	5.00 - End	5.00 - 6.00	
BoBK 88.014	1.00 - 2.00	2.00 - 14.90	Tunnel	Injection
	14.90 - 15.90	15.90 - End	Tunnel	
BoBK 88.015	2.00 - 3.00	3.00 - End	3.00 - 4.00	
BoBK 88.016	6.00 - 7.00	7.00 - End	7.00 - 8.00	
BoBK 88.017	1.80 - 2.80	2.80 - 21.80	2.80 - 3.80	
	21.80 - 22.80	22.80 - 31.80	22.80 - 23.80	
	31.80 - 32.80	32.80 - End	32.80 - 33.80	
BoBK 88.018	2.00 - 3.00	3.00 - End	3.00 - 4.00	
BoUS 85.003	0.00 - 0.50	0.50 - End	Tunnel	

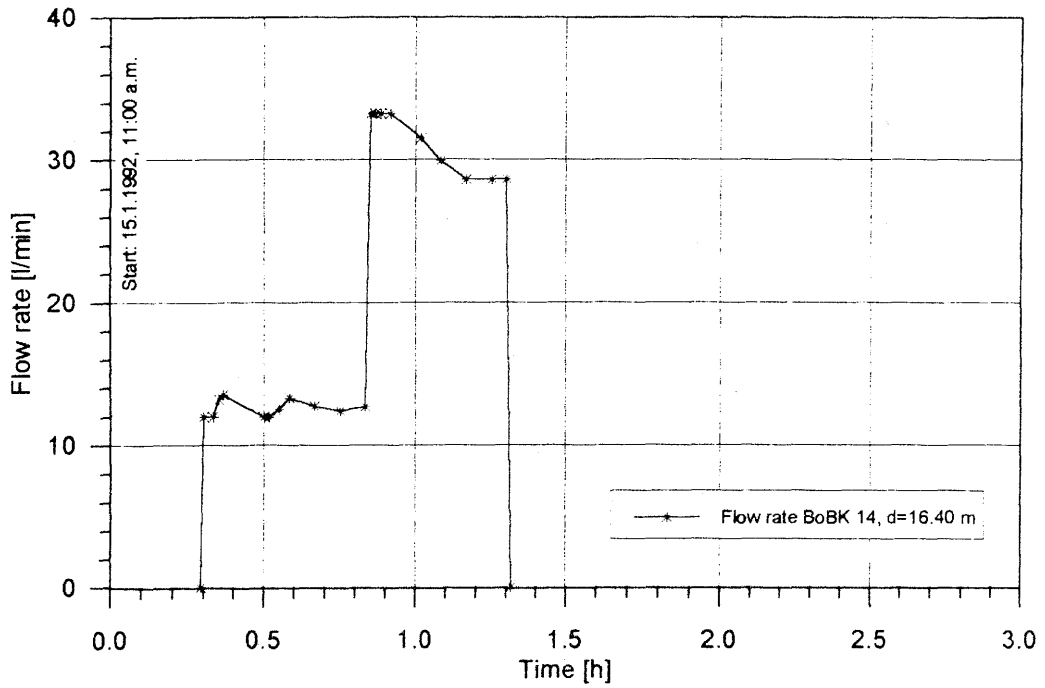


Figure 6.17: VE 492 - Flow rate in borehole BoBK 14 as a function of time (3 h after beginning of test)

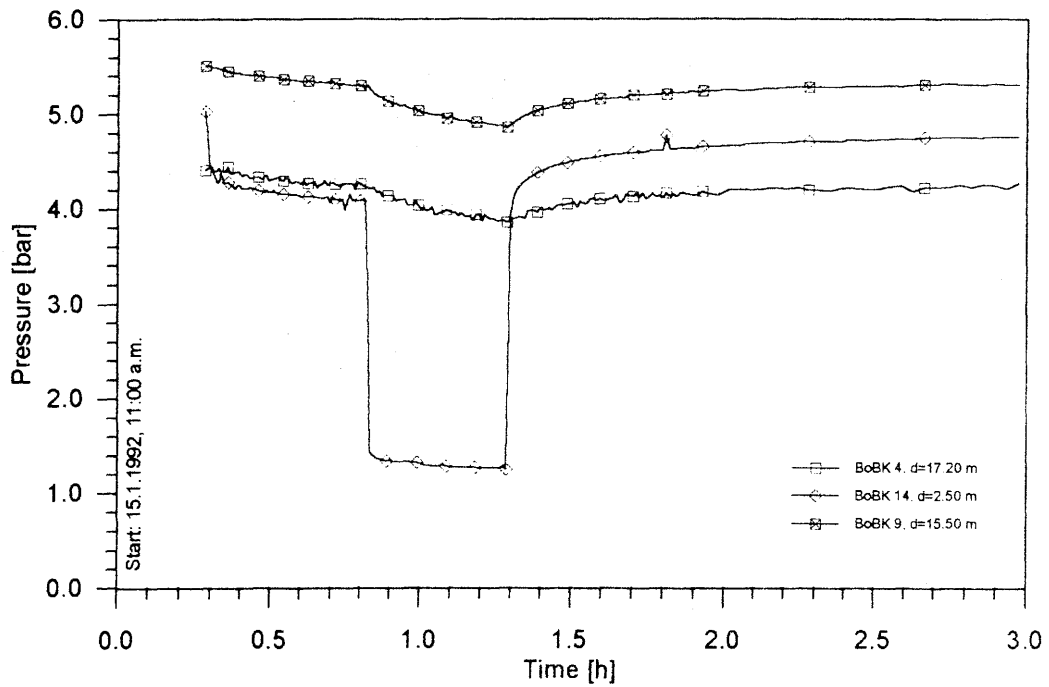


Figure 6.18: VE 492 - Pressure in boreholes BoBK 4, 9, 14 as a function of time (3 h after beginning of test)

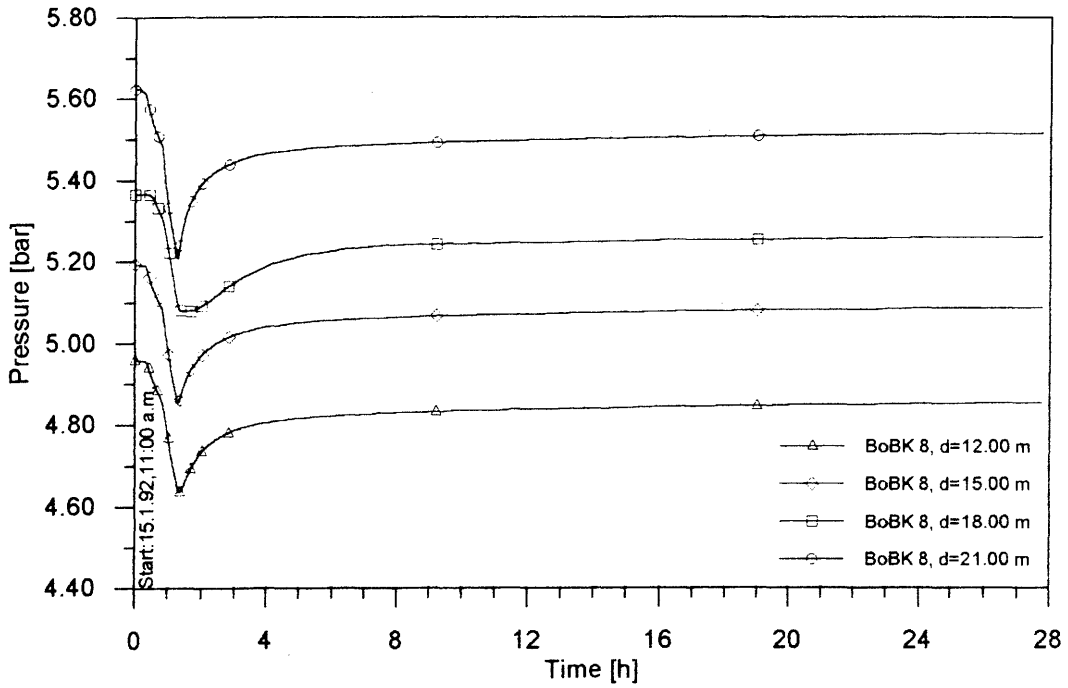


Figure 6.19: VE 492 - Pressure in borehole BoBK 8 as a function of time (28 h after beginning of test, measurement with multifunctional probes)

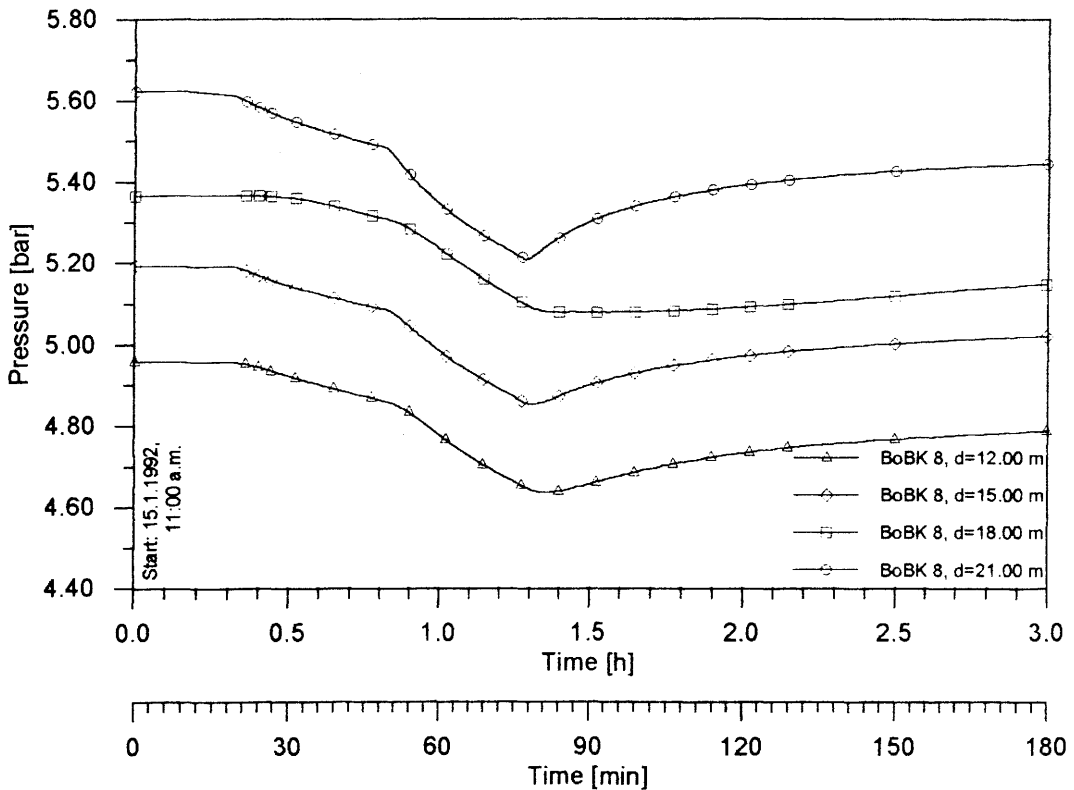


Figure 6.20: VE 492 - Pressure in borehole BoBK 8 as a function of time (3 h after beginning of test, measurement with multifunctional probes)

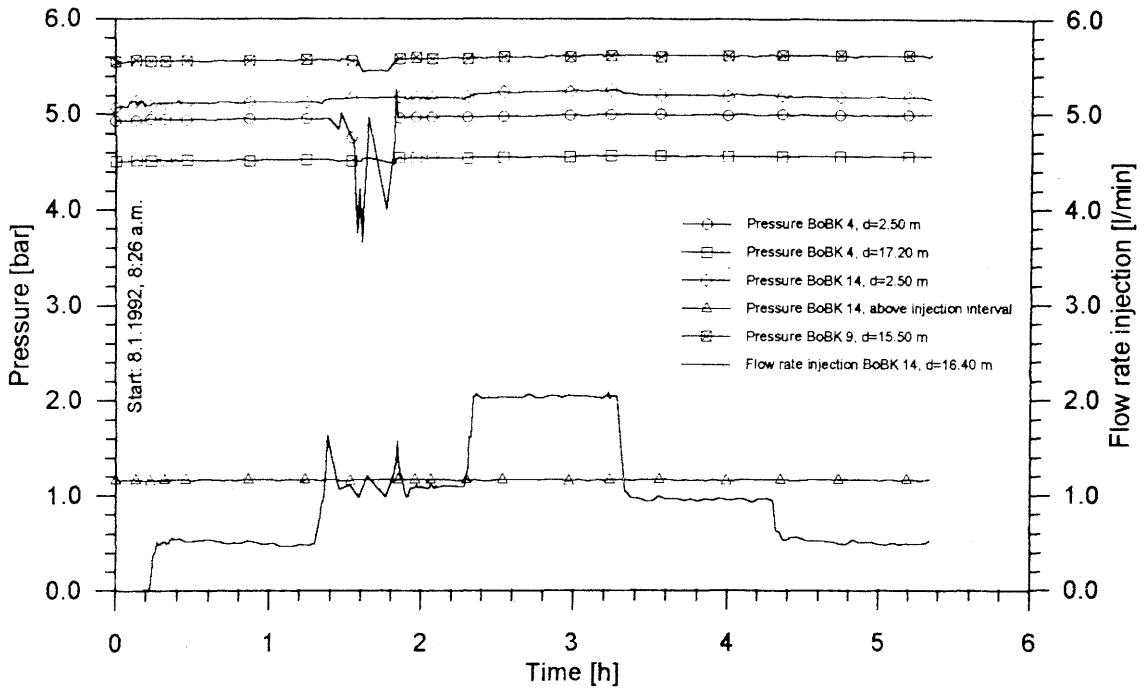


Figure 6.21: VE 490 - Flow rate in borehole BoBK 14 (injection) and pressures in boreholes BoBK 4, 9, 14 as a function of time

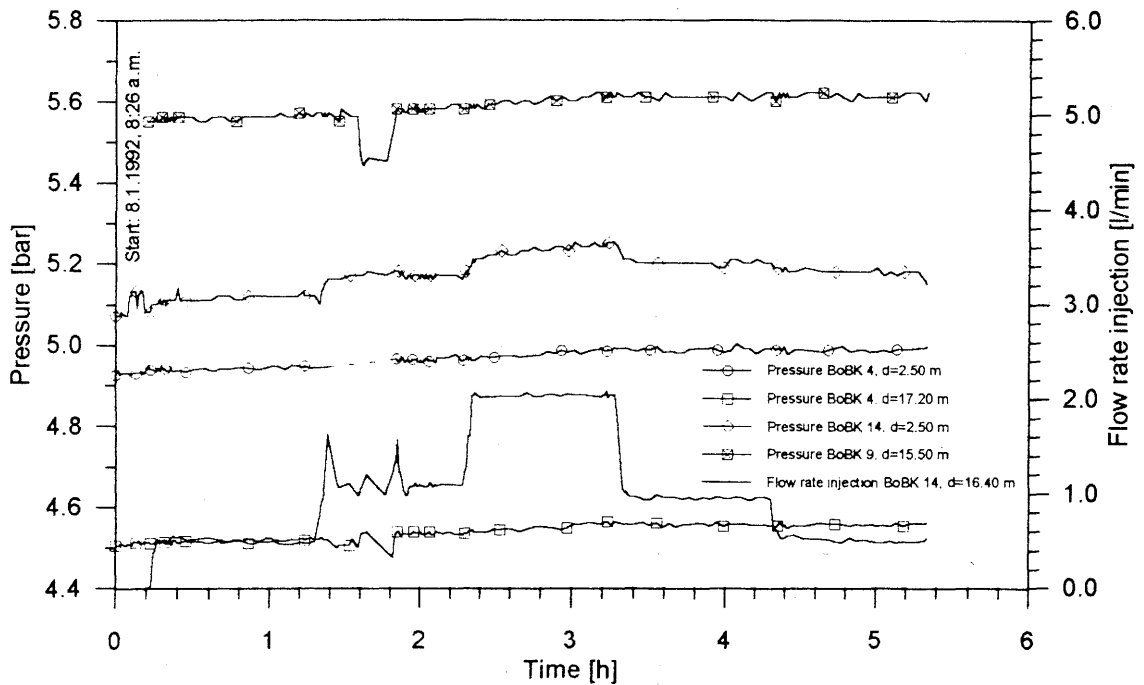


Figure 6.22: VE 490 - Flow rate in borehole BoBK 14 (injection) and pressures in boreholes BoBK 4, 9, 14 as a function of time (enlargement of section from Fig. 6.21)

6.2.2 Course and Documentation of Tracer Test VE 493

In this dipole tracer test, the brine flows from borehole BoBK 14 to BoBK 10. Figure 6.23 shows a possible pathway along the shortest connection via the fractures. The packer and probe positions were not changed in relation to earlier tests (e.g. tracer test VE 483) for reasons of reproducibility in all boreholes, with the exception of boreholes BoBK 8, 10 and 14. Borehole BoBK 8 was fitted with a 4-fold probe-packer system (multifunctional probes) (Table 6.5) and a 3-fold packer system for outflow was installed in borehole BoBK 10.

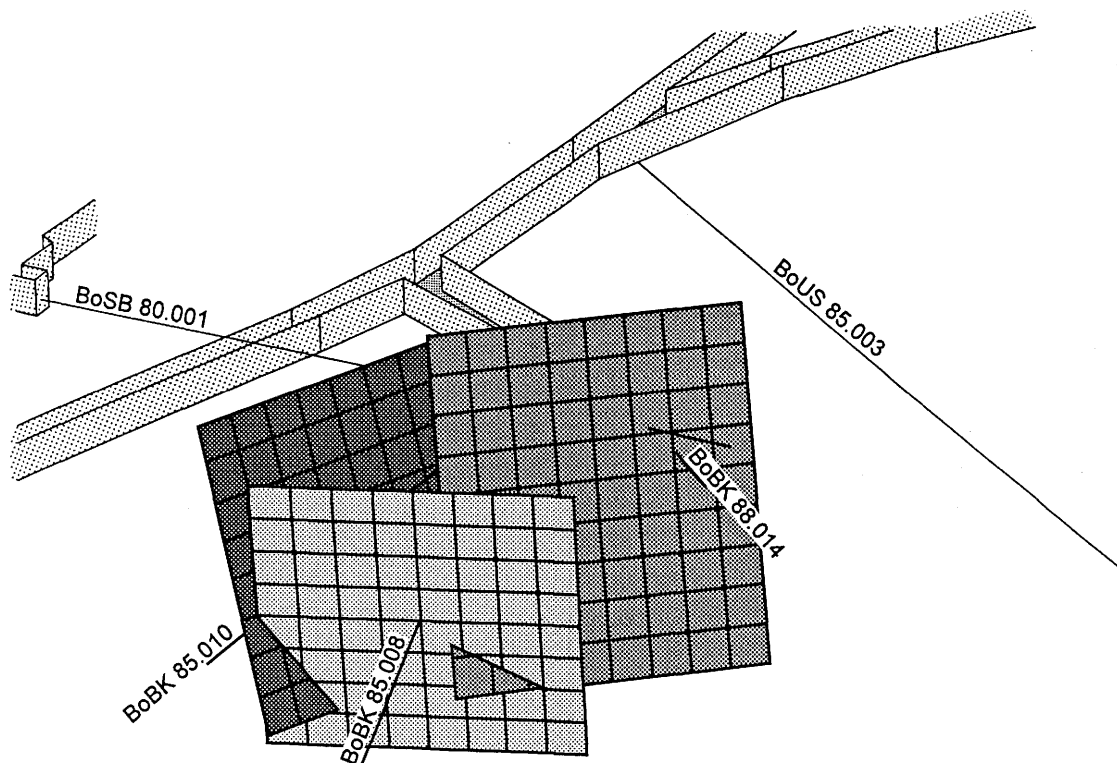


Figure 6.23: VE 493 - Possible tracer flow pathway

Boundary conditions:

- All boreholes with the exception of the injection and outflow boreholes are shut in
- An objective is a steady flow field
- Leakages around the tunnel roofs cannot be excluded as a possibility on the basis of the relatively impermeable rock around BoBK 8 and 10
- The groundwater is to flow out of the otherwise shut-in system in borehole BoBK 10 (depth 18.25-27.66 m) with as little friction as possible
- See Table 6.6 on the hydraulic boundary conditions for partial tests VE 493a and VE 493b

Table 6.6: Hydraulic boundary conditions, tracer test VE 493

Test	Start time	Rate of injection [l/min]	Conductivity [$\mu\text{S/cm}$]
VE 493a	19.03.1992, 10:00 a.m.	0.5	20
	20.03.1992, 10:00 a.m.	0.5	5,000
	20.03.1992, 15:00 a.m.	0.5	20
VE 493b	26.03.1992, 10:00 a.m.	1.0	10,000
	27.03.1992, 10:00 a.m.	1.0	20
	11.05.1992 (End of trial)	0.0	-

Data acquisition:

- Pressures, temperatures: in all boreholes
- Flow rates: boreholes BoBK 14, 10, all leakages
- Electrical conductivity: injection borehole, extraction borehole, leakages and borehole BoBK 8 (sporadically with brief openings of borehole).

Results:

In the observation period of one week (VE 493a) no clear changes in concentration were measured in the target borehole BoBK 10. The change in boundary conditions thereafter (VE 493b) produced significant results. The position of the leakages is seen in Figure 6.24. Figure 6.25 shows concentration measurements for leakages 1, 3 and borehole BoBK 10 at the outflow behind the conductometer, measured to check the electronic datalogging system. Discharge recordings at several leakages are seen in Figure 6.26. Figures 6.27-6.38 showt the electronically measured data.

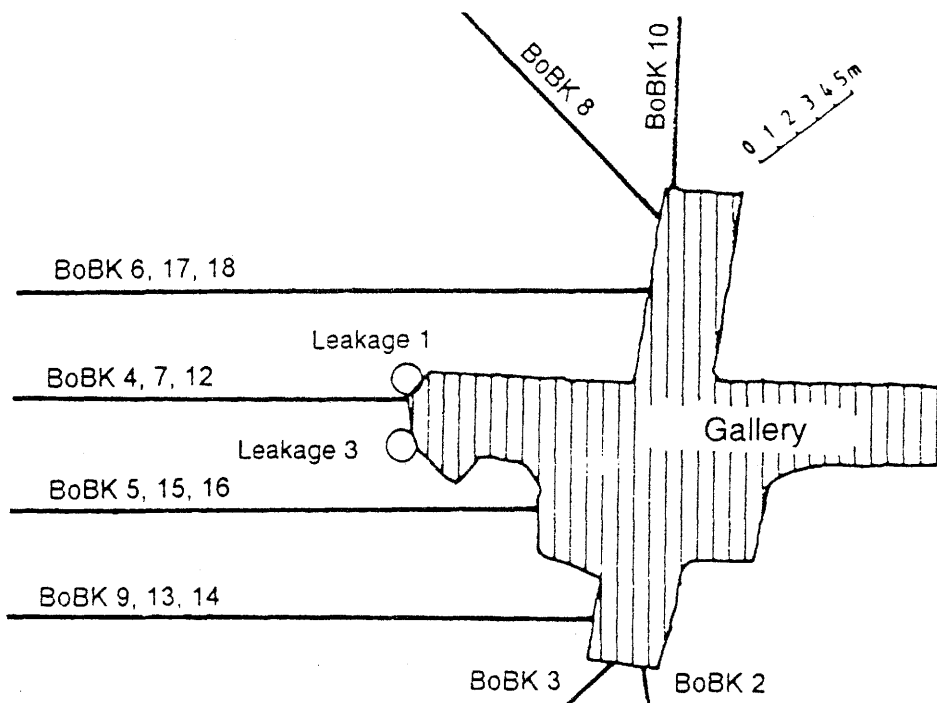


Figure 6.24: Location of leakages 1 and 3

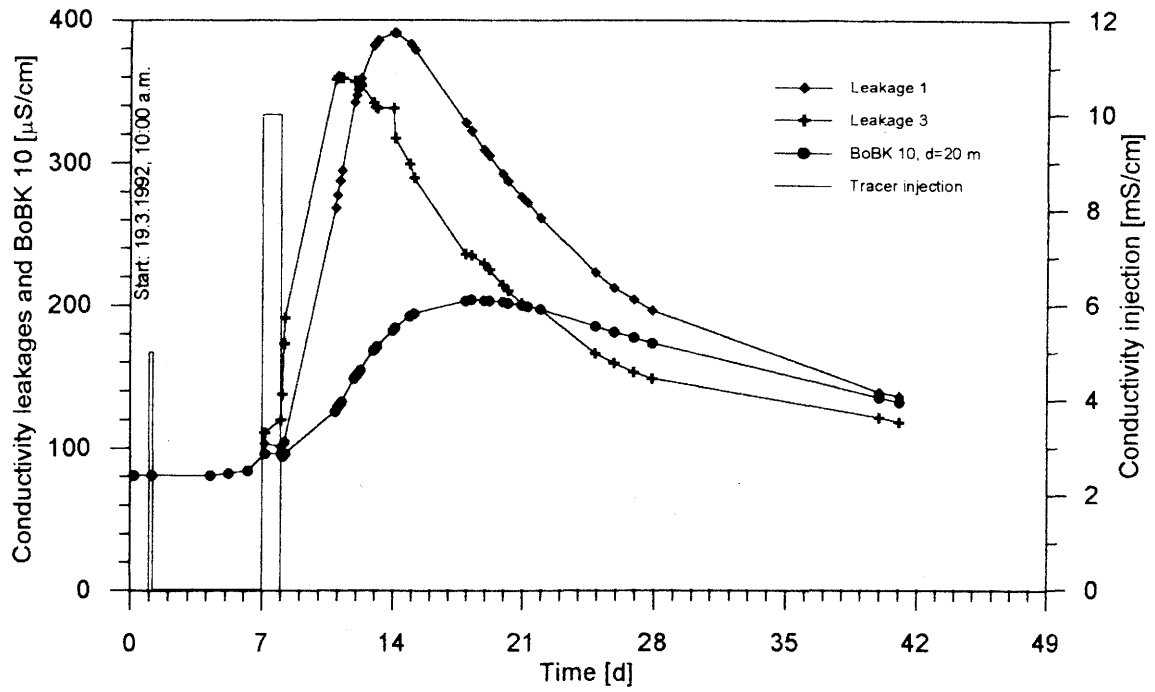


Figure 6.25: VE 493a and b - Manually measured conductivities at leakages and in borehole BoBK 10 as a function of time

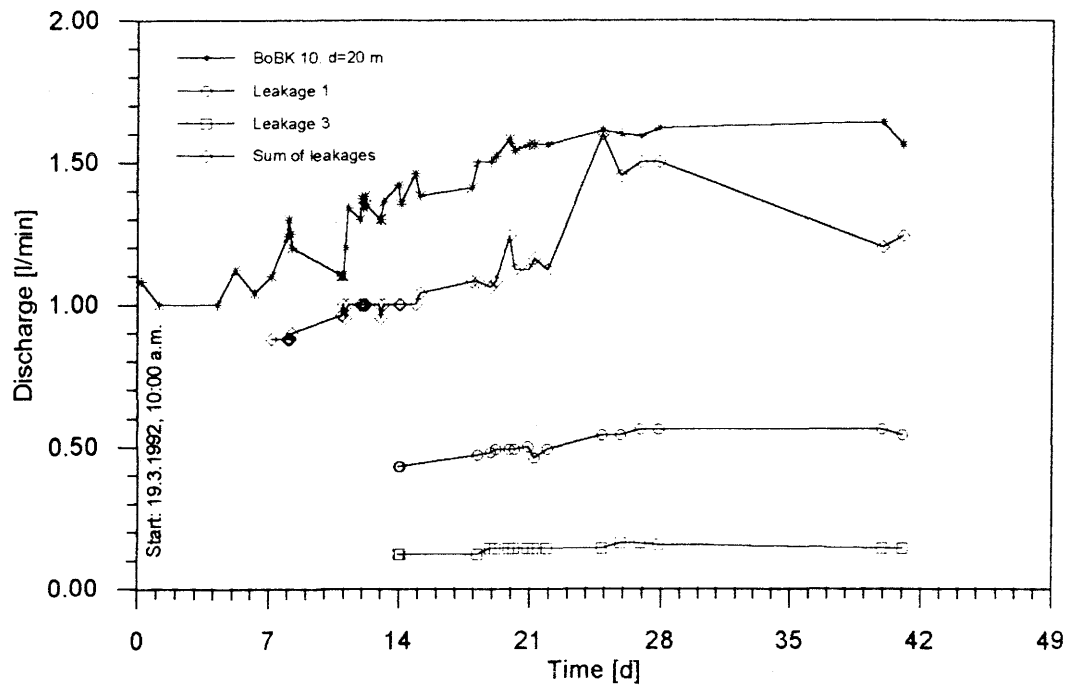


Figure 6.26: VE 493a and b - Manually measured discharges of leakages and in borehole BoBK 10 as a function of time

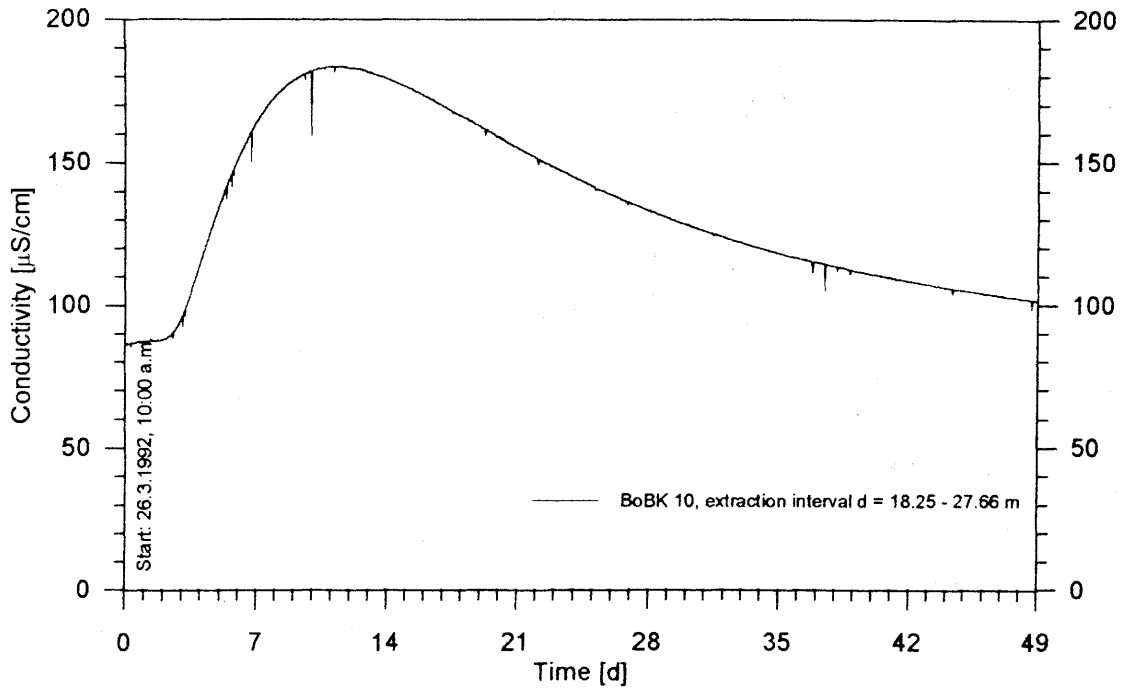


Figure 6.27: VE 493b - Conductivity in borehole BoBK 10 as a function of time (49 days from beginning of test)

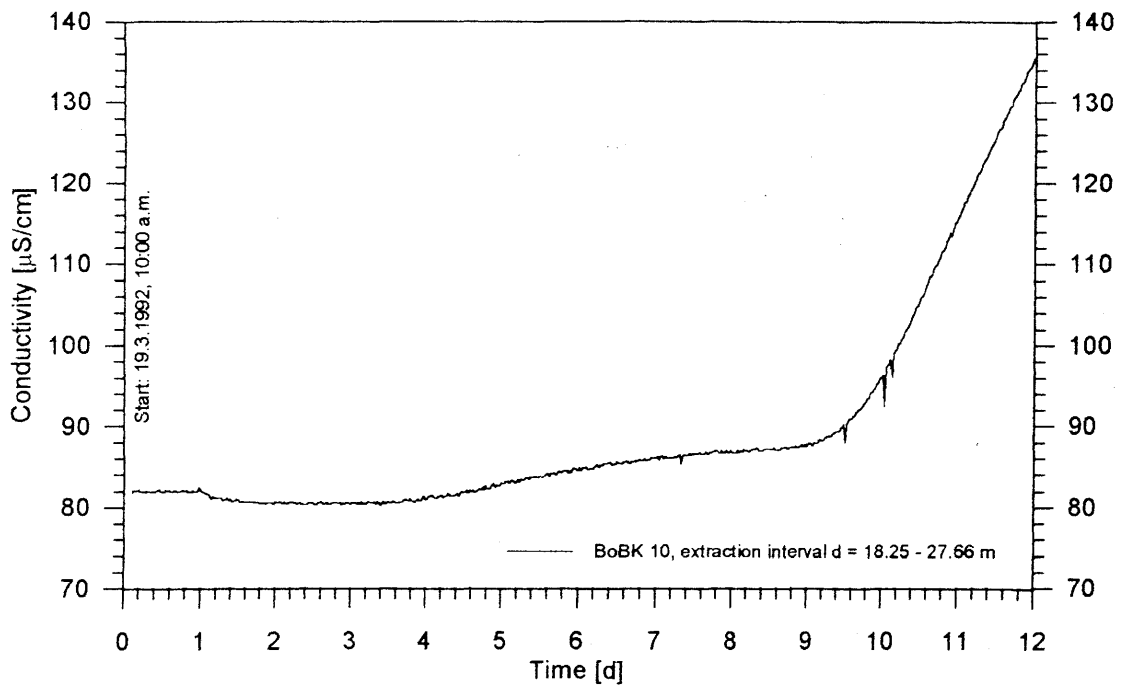


Figure 6.28: VE 493 - Conductivity in borehole BoBK 10 as a function of time (12 days from beginning of test)

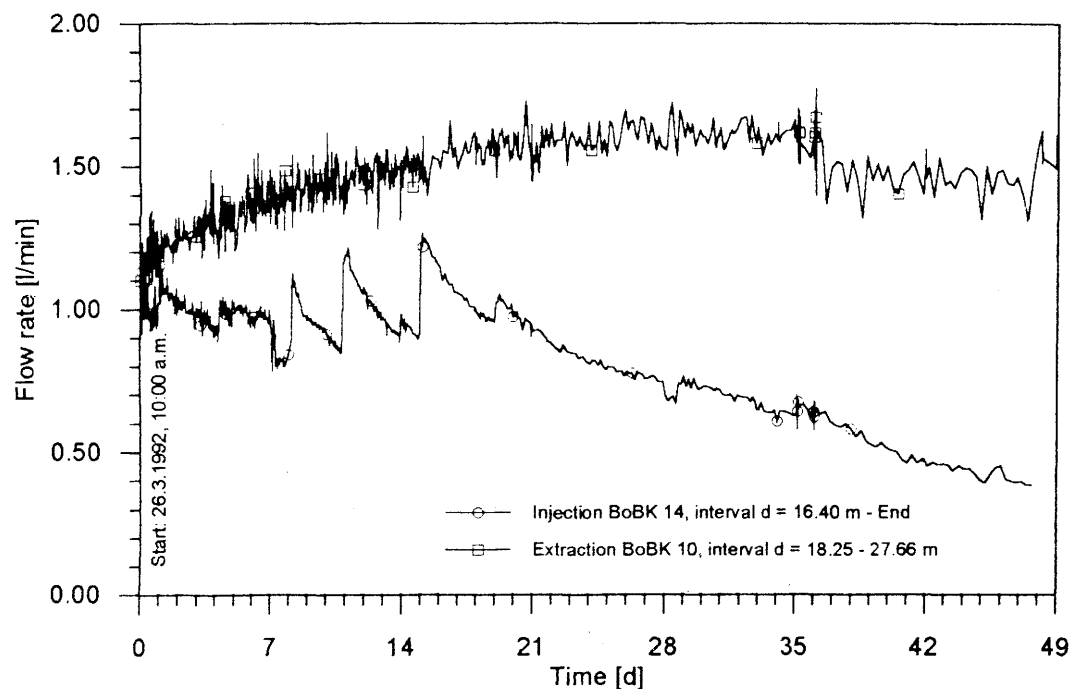


Figure 6.29: VE 493b - Flow rates in borehole BoBK 14 (injection) and BoBK 10 (extraction) as a function of time (49 days from beginning of test)

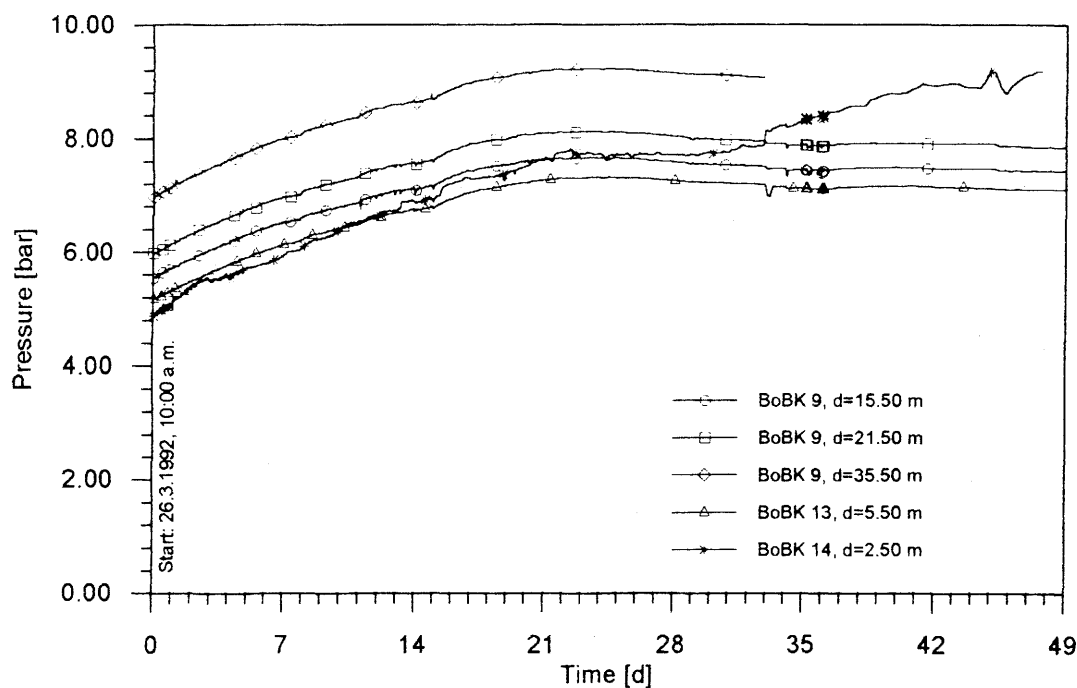


Figure 6.30: VE 493b - Pressures in boreholes BoBK 9, 13, 14 (Fan A) as a function of time (49 days from beginning of test)

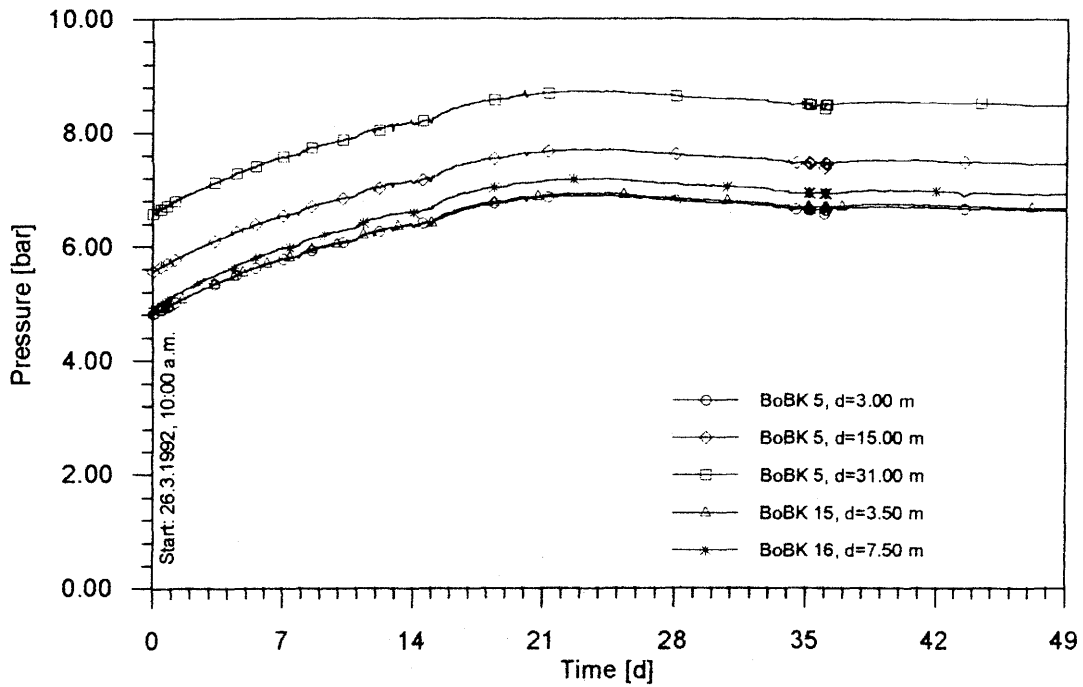


Figure 6.31: VE 493b - Pressures in boreholes BoBK 5, 15, 16 (Fan B) as a function of time (49 days from beginning of test)

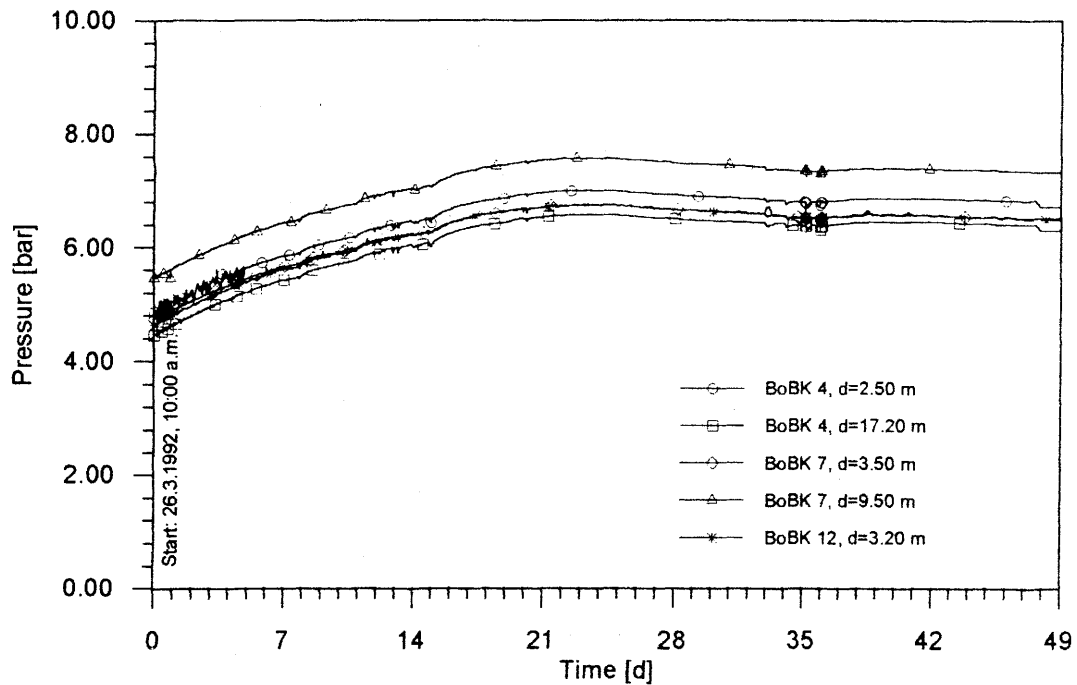


Figure 6.32: VE 493b - Pressures in boreholes BoBK 4, 7, 12 (Fan C) as a function of time (49 days from beginning of test)

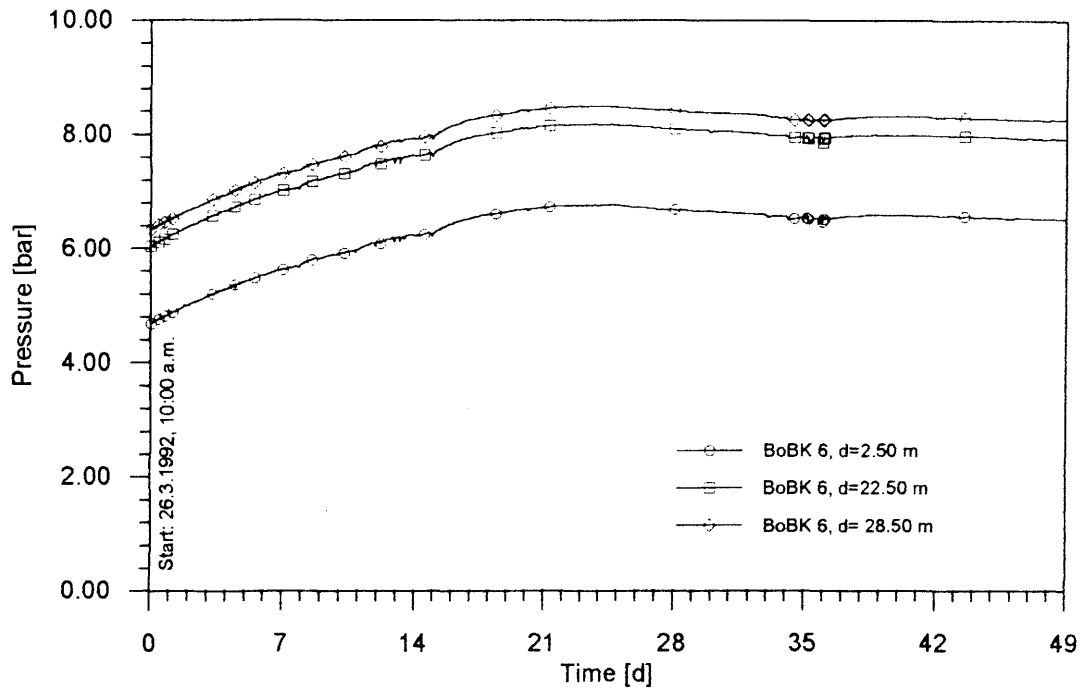


Figure 6.33: VE 493b - Pressure in borehole BoBK 6 (Fan D) as a function of time (49 days from beginning of test)

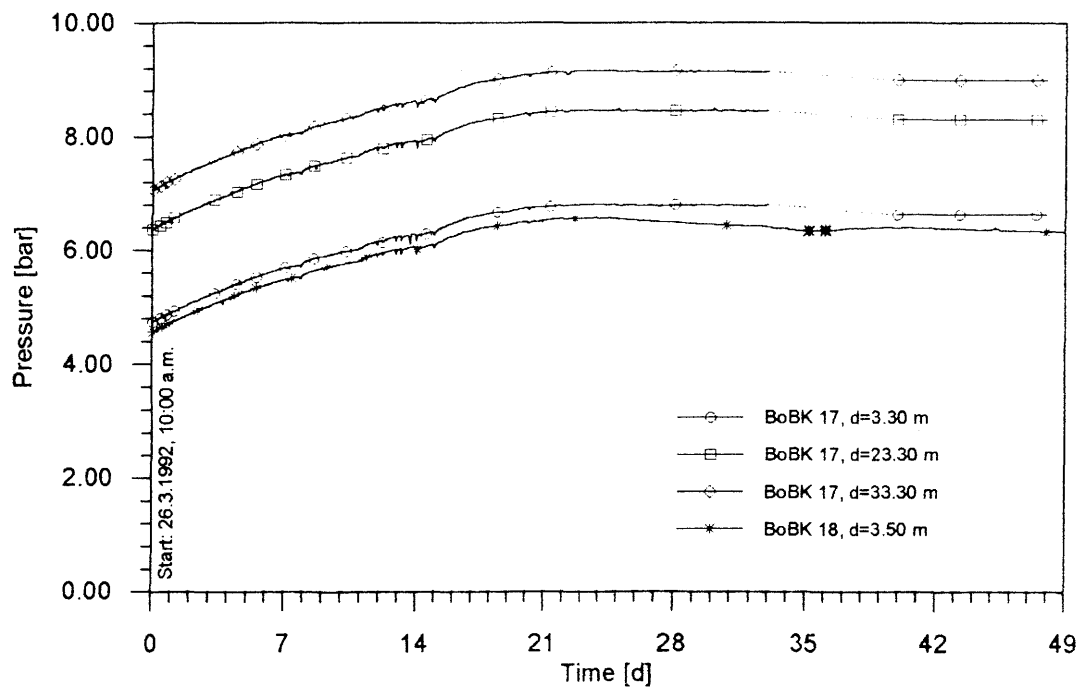


Figure 6.34: VE 493b - Pressures in boreholes BoBK 17 and 18 (Fan D) as a function of time (49 days from beginning of test)

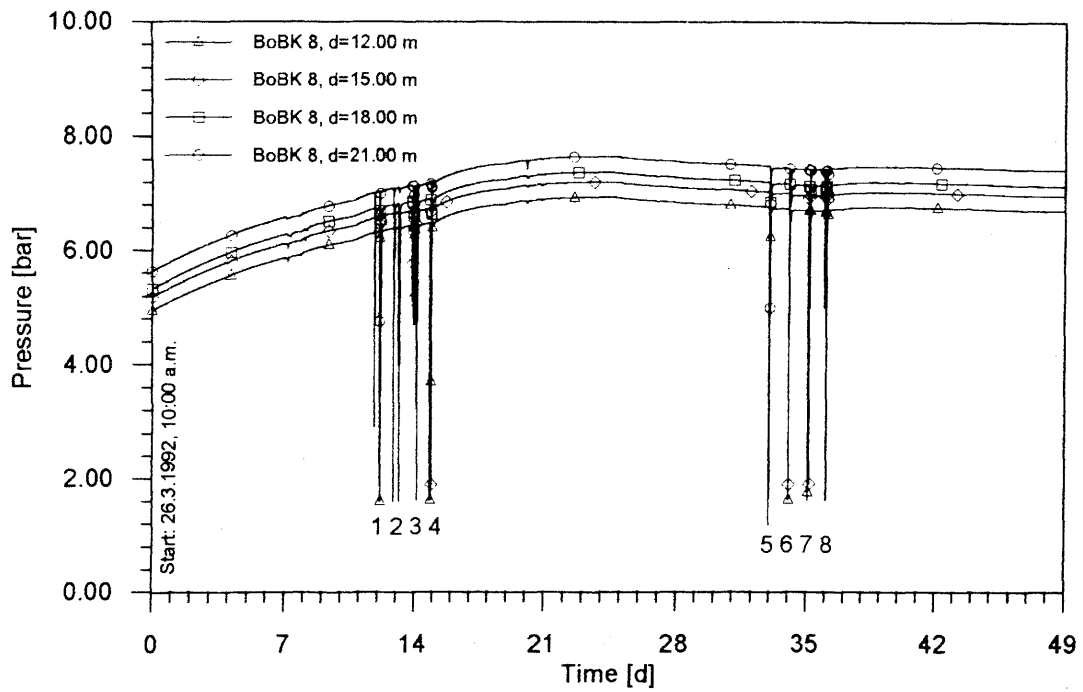


Figure 6.35: VE 493b - Pressure in borehole BoBK 8 (measurement with multifunctional probe) as a function of time (49 days from beginning of test with 8 events)

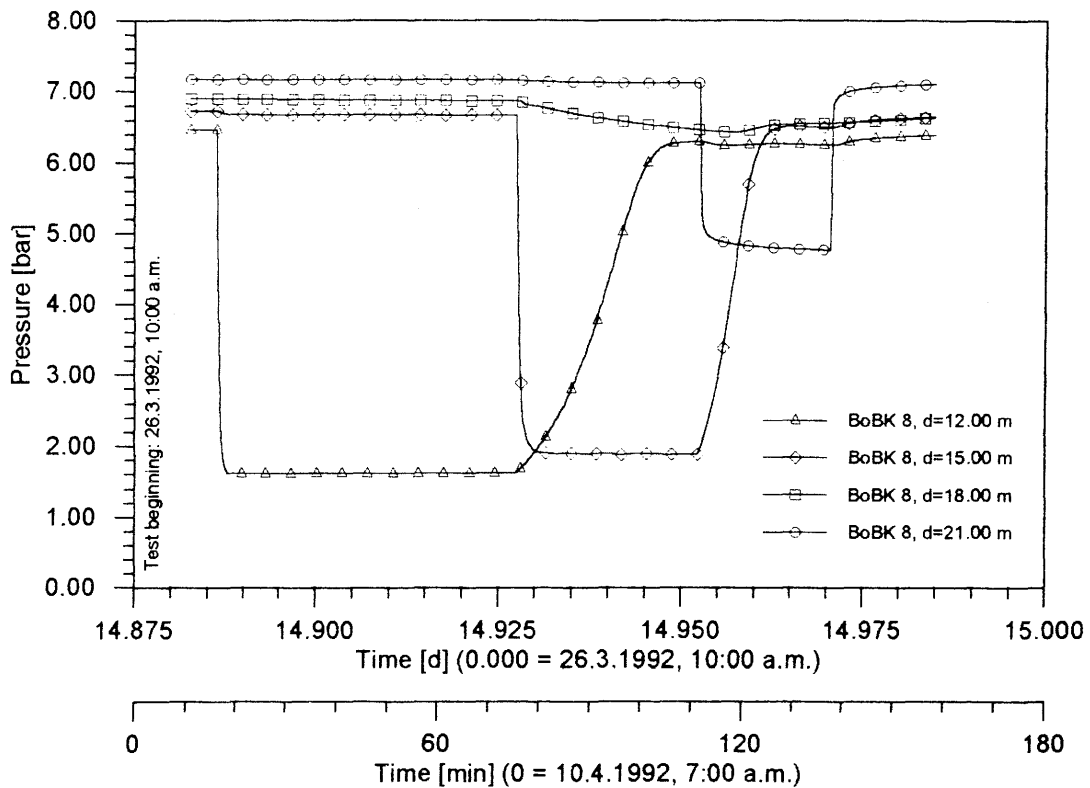


Figure 6.36: VE 493b - Pressure in borehole BoBK 8 (measurement with multifunctional probe) as a function of time (3 hours with event 4)

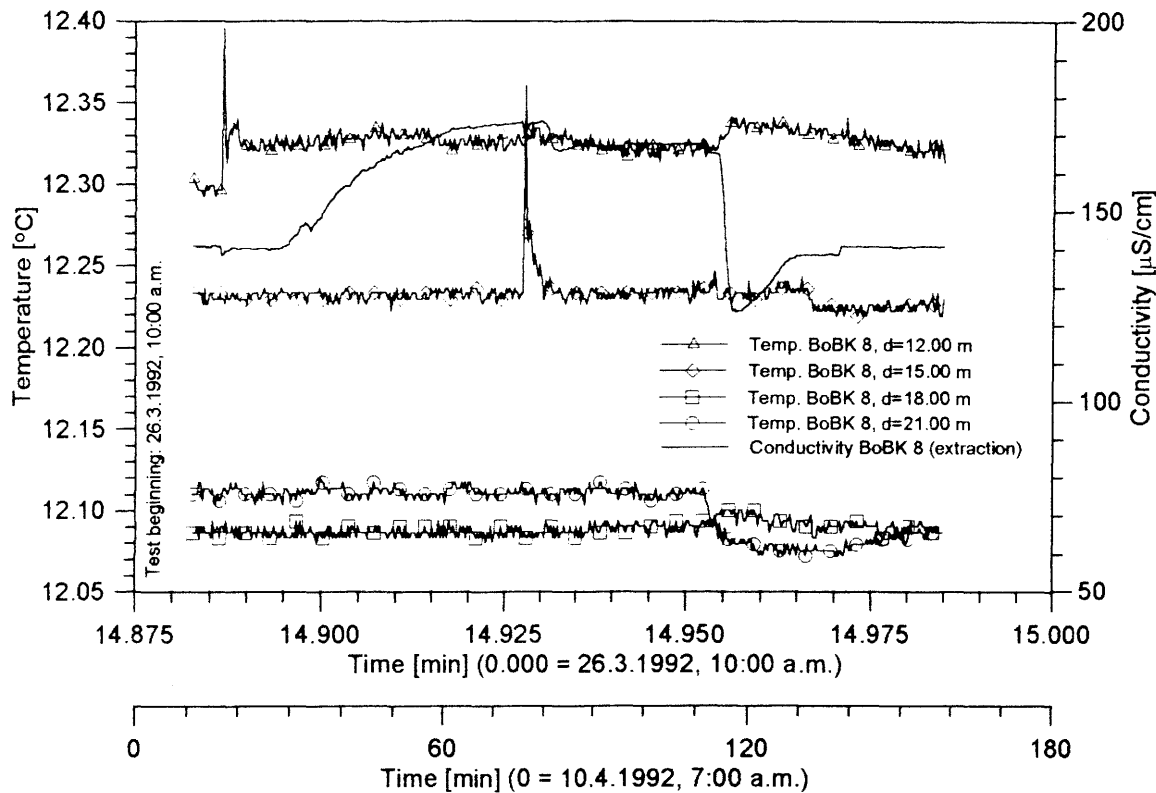


Figure 6.37: VE 493b - Temperature and conductivity in borehole BoBK 8 (measurement with multifunctional probe) as a function of time (3 hours with event 4)

During the test, several packered borehole segments in borehole BoBK 8 were opened briefly to measure electrical conductivity, then shut in again. These events, recognisable only as outliers in Figure 6.35, are shown at higher resolution in Figures 6.36 and 6.37 for marked event 4. Conductivity and temperature were also logged and are included. Figure 6.38 shows the conductivity data obtained by these intermittent measurements for 3 points in borehole BoBK 8 (11-13 m, 14-18 m, 20 m - final depth), together with conductivity in extraction borehole BoBK 10.

Figure 6.39 shows the mass balance, also taking into account the leakages. Following one day of injection of 1.0 l/min with 10,000 µS/cm, approx. 7,800 g of salt had been introduced into the rock. The tapwater injected subsequently had a conductivity of approx. 20 µS/cm. Using as a base value the conductivity of the groundwater at approx. 90 µS/cm, the result is a negative introduced volume of approx. 42 g of salt per day. This explains the decreasing injection volume in borehole BoBK 14. Thus a balancing of the masses had been reached before the test was concluded.

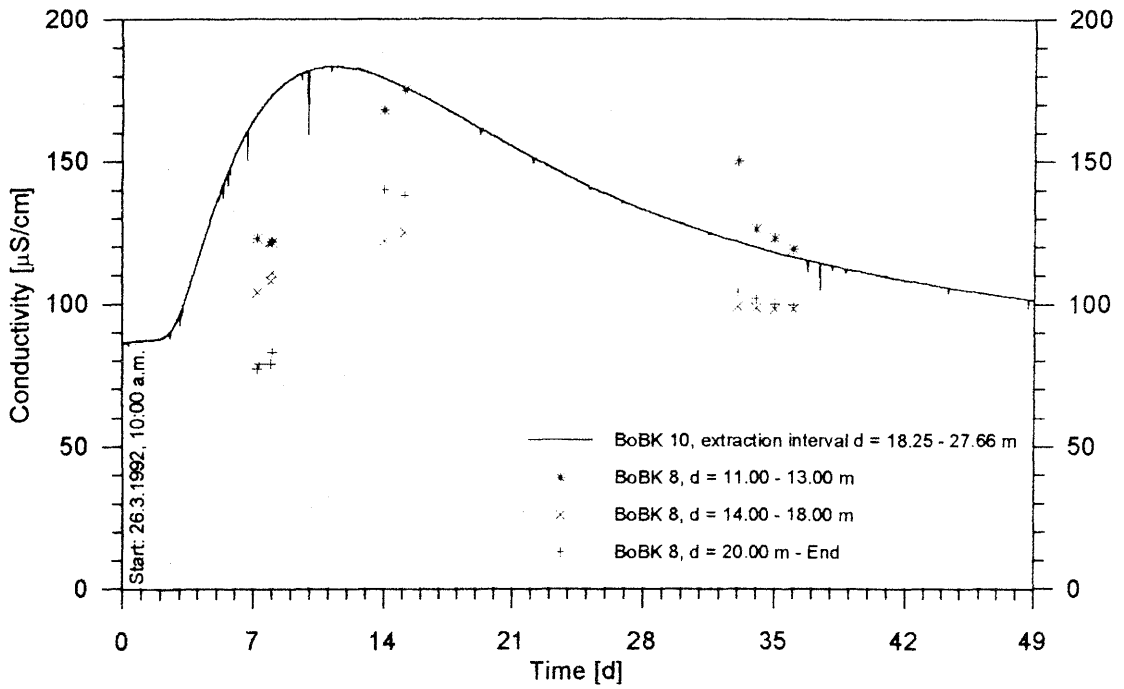


Figure 6.38: VE 493b - Conductivity in borehole BoBK 8 (manually measured) and borehole BoBK 10 (electronic measurement) as a function of time (49 days from beginning of test)

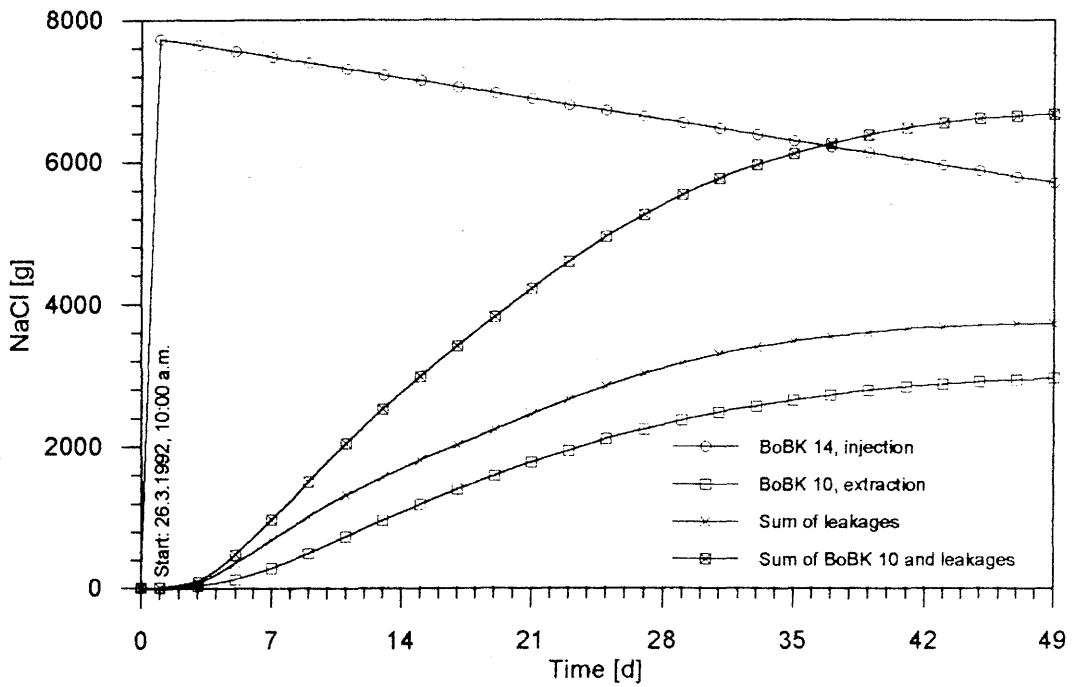


Figure 6.39: VE 493 - Mass balance of tracer

The electrical conductivity as a function of salt content is plotted in Figures 6.40-6.42 for various ranges up to 200 g/l NaCl. The measurements were carried out at the GTS with tapwater at a water temperature of 12°C. Linear dependence is indicated within some ranges:

$$L = 15.20 + 2266 \cdot \text{NaCl (g/l)} \text{ } [\mu\text{S/cm}] \quad \text{for } 0 - 2,000 \mu\text{S/cm} \quad (\text{Eq. 6.1})$$

$$L = 87.53 + 1656 \cdot \text{NaCl (g/l)} \text{ } [\mu\text{S/cm}] \quad \text{for } 2,000 - 15,000 \mu\text{S/cm} \quad (\text{Eq. 6.2})$$

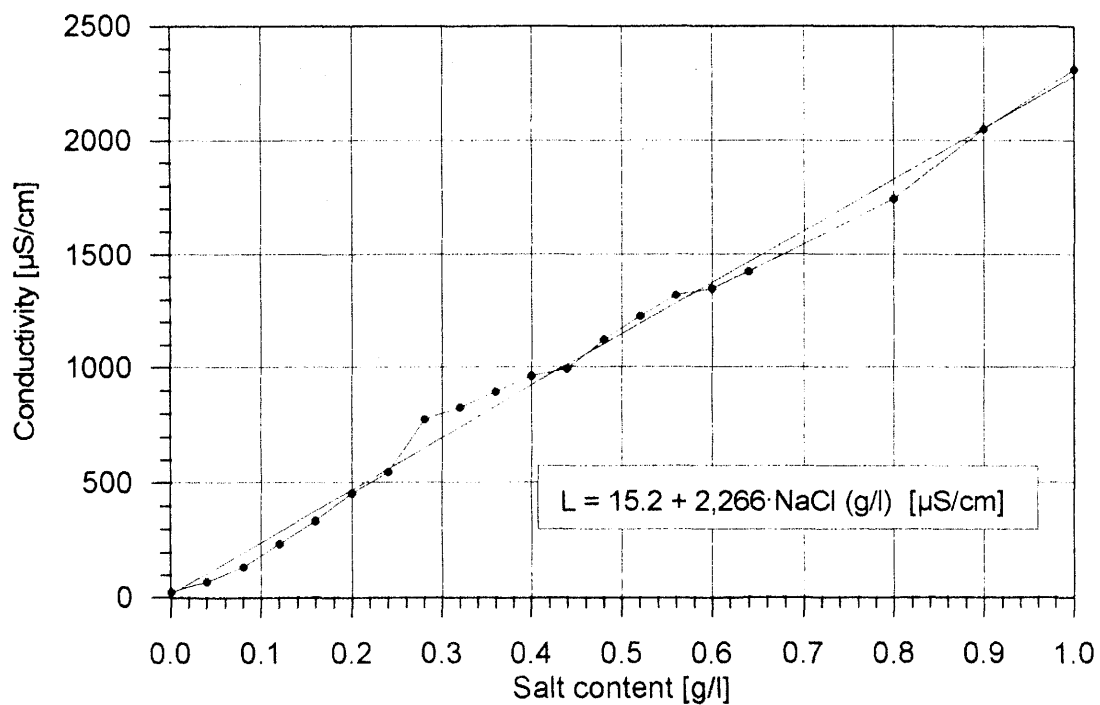


Figure 6.40: Electrical conductivity 0 - 1 g/l NaCl

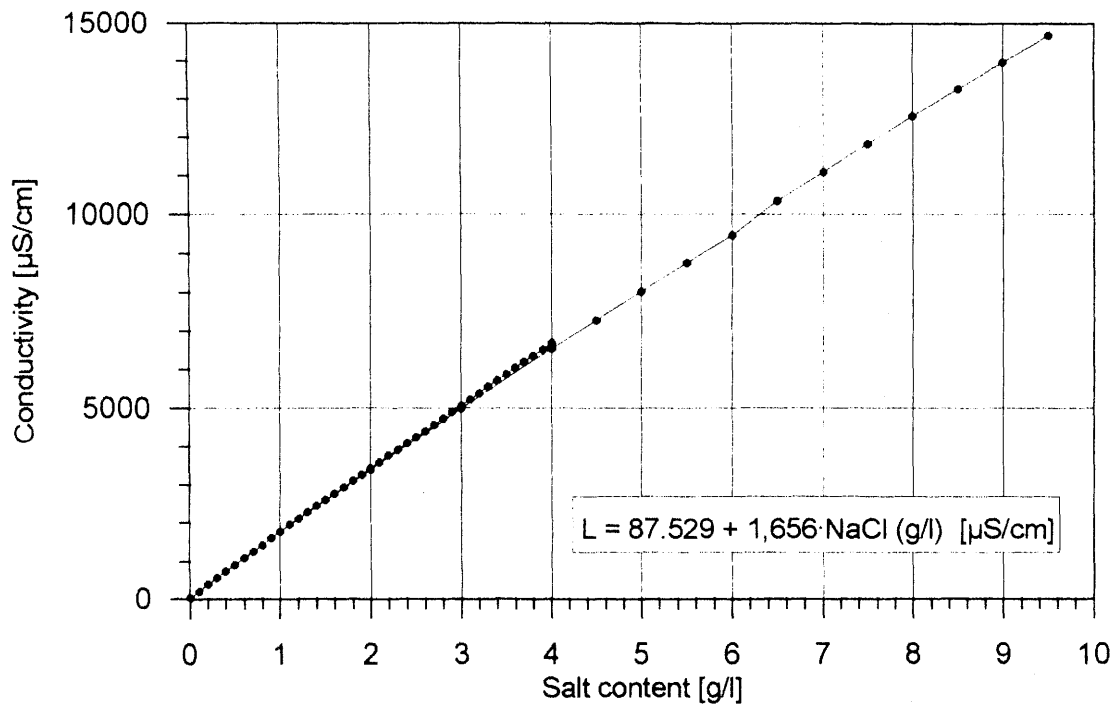


Figure 6.41: Electrical conductivity 0 - 10 g/l NaCl

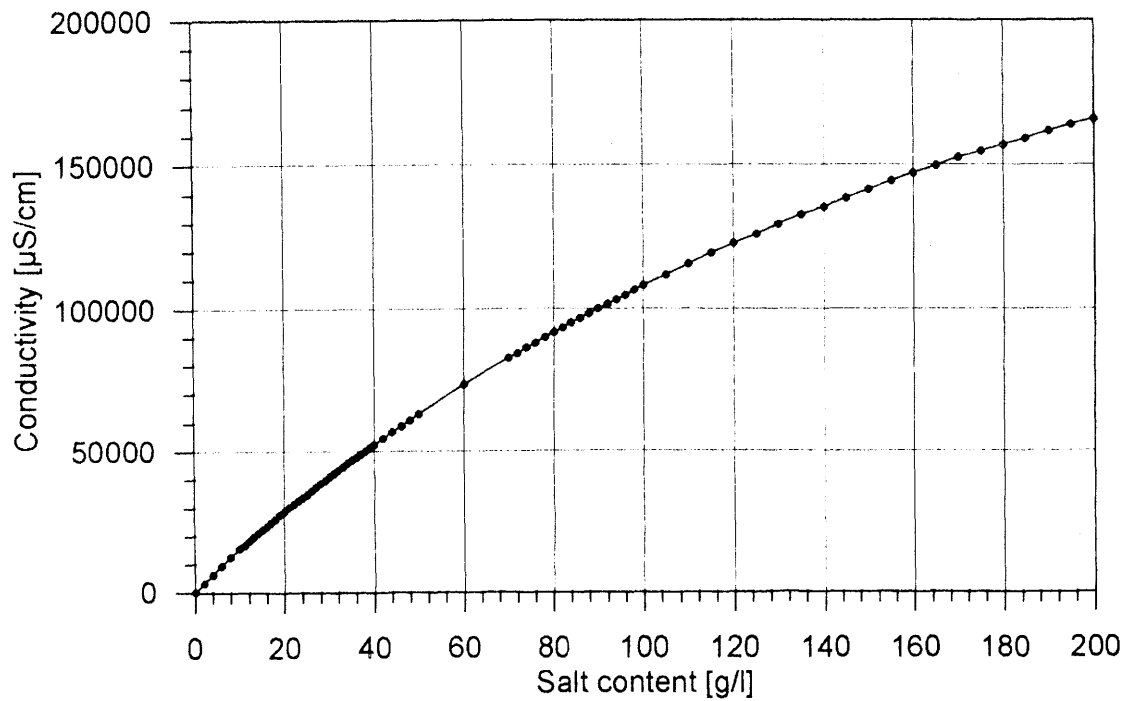


Figure 6.42: Electrical conductivity 0 - 200 g/l NaCl

6.2.3 Numerical Simulation of Tracer Test VE 493

A tube network was used for initial estimates. Figure 6.43 shows the direct flow pathway from borehole BoBK 14 via borehole BoBK 8 past the lamprophyre to BoBK 10. Taking into account the groundwater inflow and the leakages in the laboratory tunnel an initial, satisfactory comparison between the results of the computations and the in-situ measurements is possible (see Fig. 6.44). The results for leakages 1 and 3 are summarised for the computation.

The transport model was based on 1D tube elements in the FE program system DURST/ROCKFLOW. The boundary conditions of the flow network were the measured hydraulic heads and the discharge. The following parameters were used for flow computations (Table 6.7):

Element group	I:	Rock borehole BoBK 14 - BoBK 8
	II:	Rock borehole BoBK 8 - BoBK 10
	III:	Leakages
	IV:	Groundwater inflow
	V:	Storage elements (for substance transport)

Table 6.7: Model parameters for flow computation

Element group [-]	Cross-section [m ²]	k_f [m/s]	Total length [m]	No. of elements [-]
I	0.50	$8.0 \cdot 10^{-3}$	28.04	22
II	0.60	$2.5 \cdot 10^{-5}$	11.22	11
	0.10	$7.5 \cdot 10^{-5}$	12.50	11
	0.10	$7.5 \cdot 10^{-5}$	10.46	11
III	1.00	$2.0 \cdot 10^{-4}$	16.33	11
	0.30	$1.5 \cdot 10^{-5}$	7.83	11
IV	0.10	$4.0 \cdot 10^{-4}$	397.92	51
V	10.00	$4.0 \cdot 10^{-4}$	92.78	21

Pre-set hydraulic heads:

- Outflow borehole BoBK 10: 30 m
 - Leakages: 34 m
 - Groundwater inflow point: 500 m
- Flow rate, borehole BoBK 14: $q = 0.000017 \text{ m}^3/\text{s}$
 Storage coefficient: $S = 0$ (steady flow field)

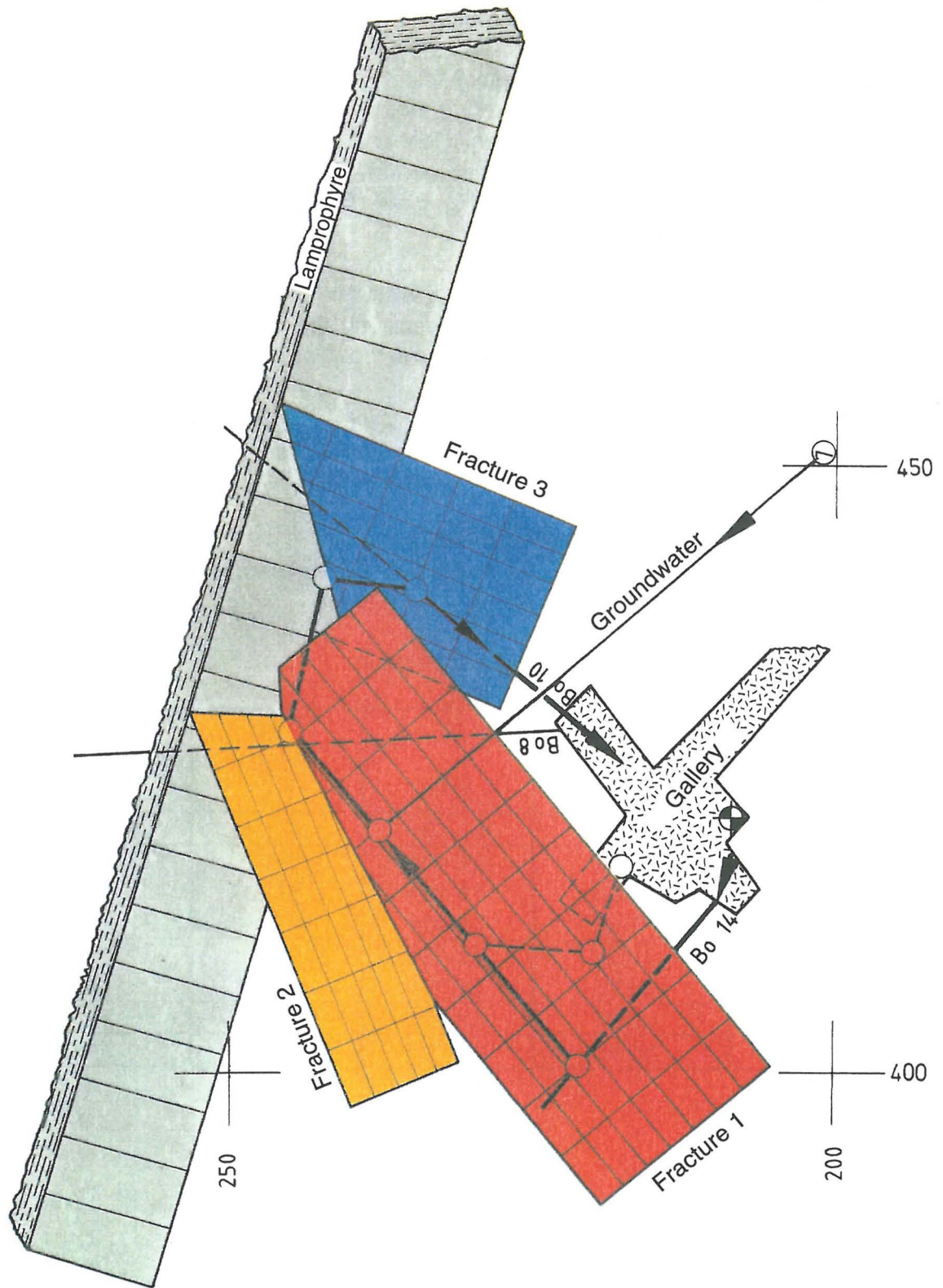


Figure 6.43: FE model for tracer tests (tube flow)

The following parameters are used for transport computation (Table 6.8):

Table 6.8: Model parameters for transport computation

Element group [-]	Porosity [-]	Diffusion coefficient [m ² /s]
I	1	30
II	1	1
	1	1
	1	25
III	1	10
	1	25
IV	1	30
V	1	1

The time increment was $\Delta t = 900s$. It was not possible to simulate the salt tracer delays measured in-situ until the storage elements (volume $10m^2 \cdot 92.78 m = 927.8 m^3$) were selected. They were not used during the observed time period due to their length. The diffusion coefficient used did not allow for transport of the salt to the end of the 92.78 m tube.

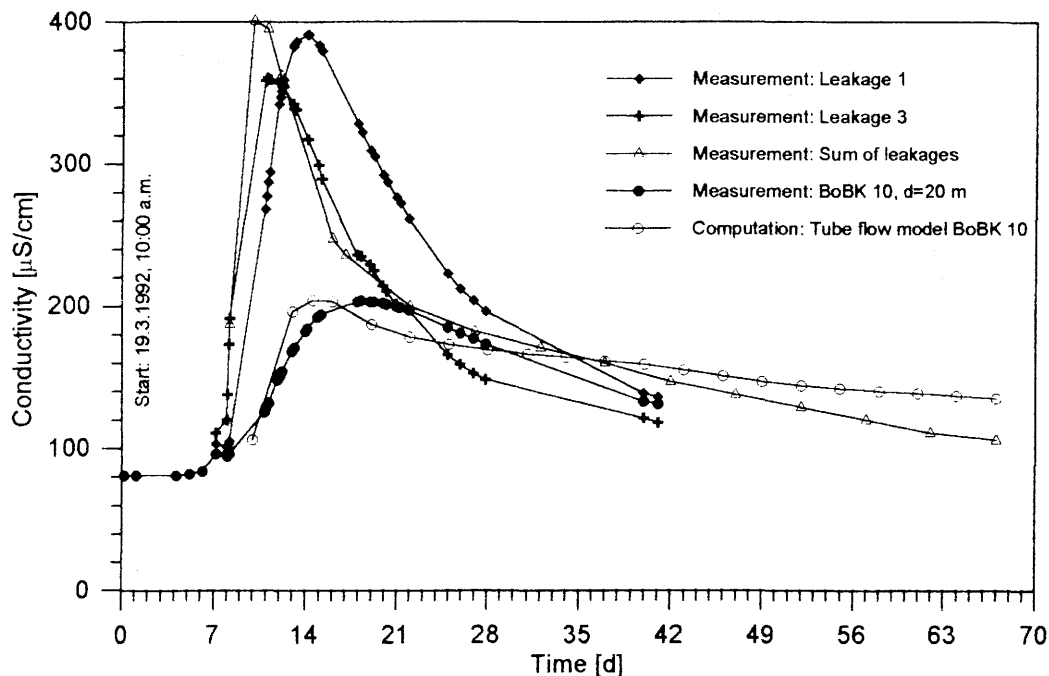


Figure 6.44: VE 493 - Transport computation, comparison of conductivities from measurement and model results

6.3 Salt/Heat Tracer Test VE 520: BoBK 5 --> BoBK 15

This test was conceived by Nagra and realised by BGR personnel using their own equipment. Boreholes BoBK 5 and 15 from fan B in the central BK area (see Figs. 1.1 and 1.2) were selected for the test, following a review of the MSCT results (see Section 5.2.4).

6.3.1 Test Installation

Fluid logging tests (see Section 5.2.3) indicated the greatest mass flow in borehole BoBK 5 at 20 m and in BoBK 15 at 25 m, so that these zones were selected for injection or extraction. Three packers were installed in both boreholes together with the tubes. This provided the best possible isolation of the fracture areas for a tracer test and made a further nearby interval available for observation of pressure changes. The intervals were thus:

BoBK 5: 9.80-18.80 m and 19.80-24.80 m
BoBK 15: 19.40-22.70 m and 23.70-26.70 m

Injection and extraction were performed in the deeper interval in each case. A temperature sensor was positioned in the tubing about 20 cm above the filter segment or fracture. Inlet and outlet temperatures were also measured at the head of the borehole to determine heat loss within the borehole. The heating device used was an 18 kW flow heater with its water cycle connected to the injection line via a heat exchanger. To measure the electrical conductivity of the water, a conductometer was installed at the outlet of the extraction borehole. Another conductometer was kept on hand for measurement at the leakages. The flow rates in the injection and extraction line were determined using two flowmeters, which were re-calibrated especially for this test.

Datalogging was by HP process control computer and PC, whereby important parameters such as temperature, electrical conductivity and pressure were recorded by both computers at the same time so that measuring would be ensured by the backup unit if one should fail. Flow rates and far-field pressures were recorded only by the HP system.

6.3.2 Course of Test

Prior to commencement of the actual test, the flow field was adjusted over a period of 2 days using injection/extraction of tapwater (same conductivity as groundwater), so that nearly steady flow conditions could be assumed. Salt/heat injection was begun on 1.3.1993 at 8:00 a.m. The heater was set at 60°C. Injection conductivity was 1,800 $\mu\text{S}/\text{cm}$ as tested randomly in the injection basin. The maximum rate with completely open intervals after the 2-day adjustment period was selected as the

extraction rate, in this case 3.4 l/min. Since Nagra desired an extraction/injection rate ratio of 2:1, the injection rate was adjusted accordingly (1.7 l/min).

After 3 days, a switchover to fresh water was made (80 $\mu\text{S}/\text{cm}$) at the same temperature in order to lengthen the tracer curve fade phase as much as possible with a planned test length of 4 weeks. The heater, on the other hand, was in use for 16 days, since no temperature reaction was seen in the target borehole after 2 weeks. The entire injection phase was ended after 22 days. In addition to continuous recording of electrical conductivity at the outflow of borehole BoBK 15, the separate conductometer was also used occasionally at the leakages to check on how far the tracer penetrated into other rock areas. The most interesting time intervals were recorded at the highest possible sampling rates (PC: 10 s, HP: 45 s).

6.3.3 Description of Results

Figure 6.45a shows the surface generated by the hydraulic heads measured in the BK area. The potential peak, determined by boreholes BoBK 2 and 3, is clearly visible. Earlier pressure buildup tests showed that this rock segment is weakly connected to the central BK area only via the lamprophyre zone (PAHL et al. 1992). The potential funnel created by opening the extraction borehole, BoBK 15, is comparatively small. A further minimum is clearly visible in the segment blowup (Fig. 6.45b), which is caused by the leakage above borehole BoBK 4. This leakage was considered as the pressure of an opened borehole (air pressure). The direction of view in both cases is out of the tunnel in the direction of the BK boreholes.

The third figure (Fig. 6.45c) shows a vertical section through the potential funnel within fan B of boreholes BoBK 5, 15 and 16. This presentation resulted from coordinate transformation. The forced gradient from injection point (5b = 2nd interval, BoBK 5) to the extraction point (15b) is obvious. There is, however, also a gradient to borehole BoBK 16 (16a), although it is not as pronounced. This means a flow to borehole BoBK 16 is also to be assumed, i.e. in the direction opposite to the actual target point. This assumption is confirmed by the temperature reaction during the course of the test in borehole BoBK 16.

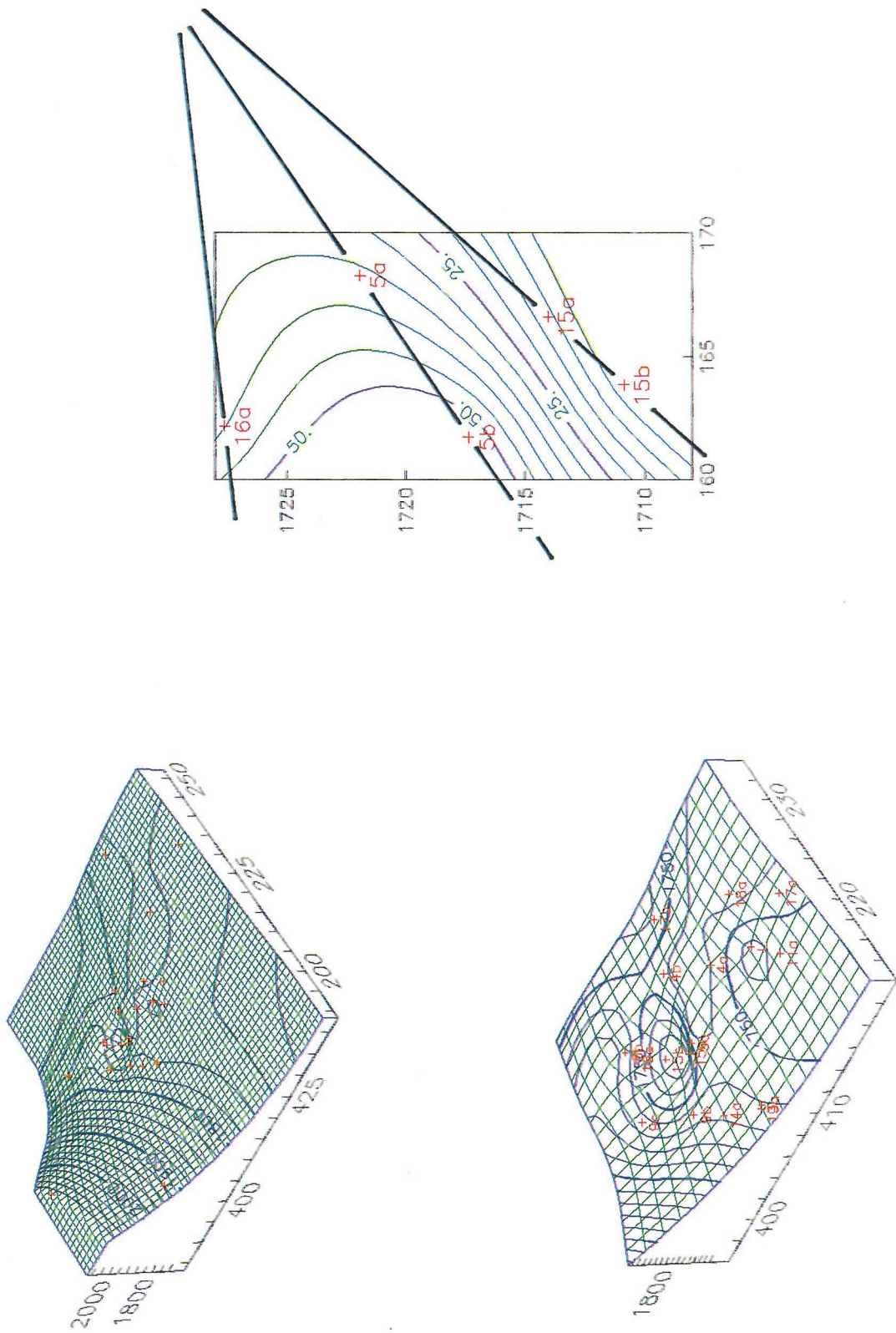


Figure 6.45: Hydraulic heads in the BK area at beginning of test
 a) overall view, b) enlargement of segment, c) in "fan" B

Figure 6.46 shows the breakthrough curve for the salt tracer throughout the entire injection phase (22 days). The curve maximum is reached after a little over 3 days, in accordance with the breakthrough time (Section 6.3.4), just after changing over to 80 $\mu\text{S}/\text{cm}$. The increased random noise near curve maximum was notable. This can be explained by assuming that the fresh water has arrived via the shortest flow pathways, while saltwater travelling by longer pathways is still flowing in evenly. Another elegant explanation would be mixing effects in the extraction interval. Such effects would have to cause similar noise at the beginning of the breakthrough curve, which makes this explanation less likely. The mixture is complete enough after 1-2 days to return to a smooth curve. Also plotted is measurement at a leakage near the location of borehole BoBK 4. Connecting the individual measurement points reveals a similar curve shape. The maximum height does not quite reach that of the extraction and has shifted slightly at later times. The fade is more rapid once the maximum has been reached and passed. Measurements recorded at other leakages were not plotted, since either no conductivity increases at all, or minimum increases only, were recorded there.

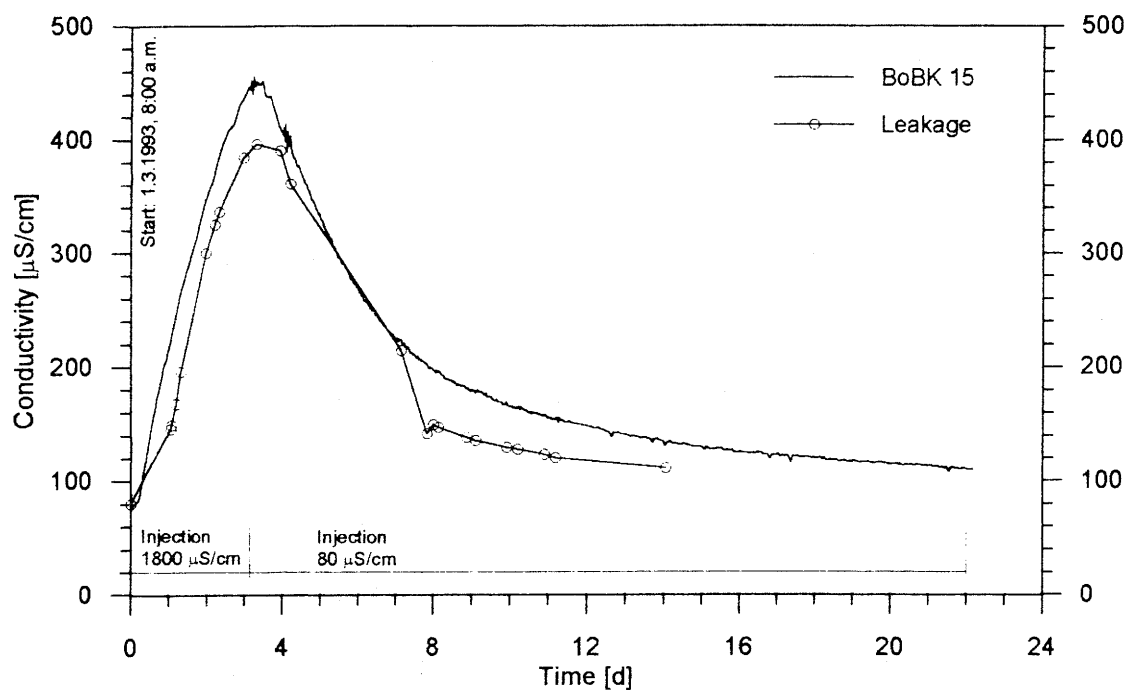


Figure 6.46: Breakthrough curves of salt tracer at outflow of borehole BoBK 15 and leakage near the location of BoBK 4

With regard to the corresponding extraction rate (Fig. 6.47), this dropped continuously from 3.4 to 2.4 l/min after initially being constant. In order to maintain the desired flow rate ratio of 2:1 as closely as possible, the injection rate was repeatedly readjusted to drop continuously as well. The leakage rate was nearly constant at 0.16 l/min.

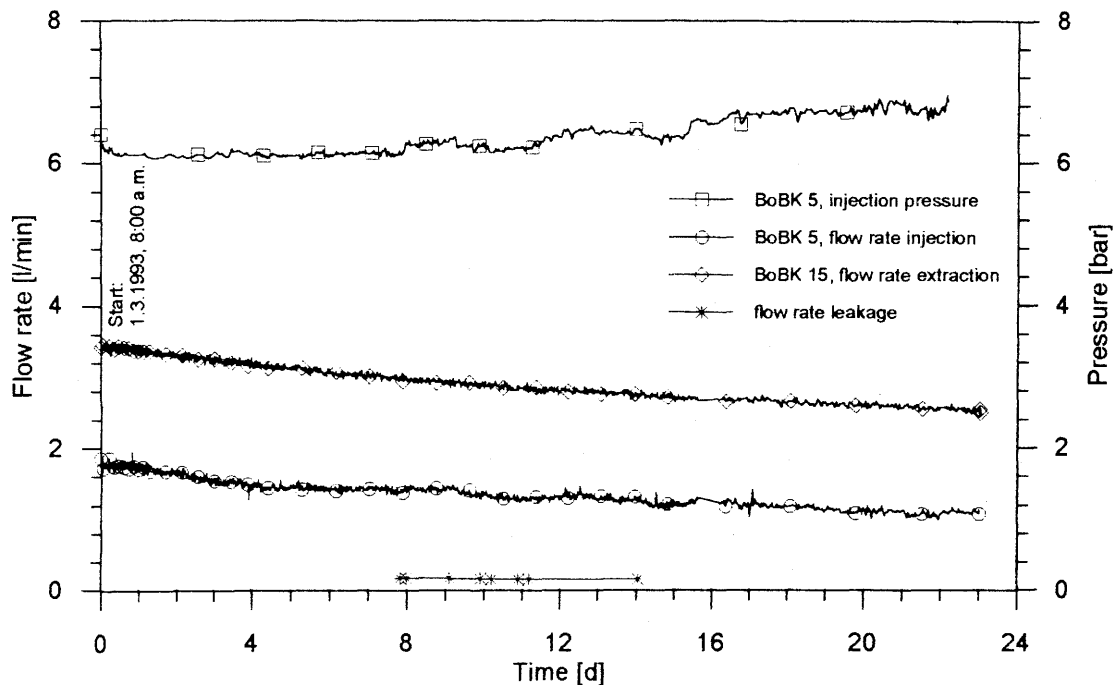


Figure 6.47: Flow rate at boreholes BoBK 5 and BoBK 15 and leakage as well as injection pressure as a function of time throughout the entire injection phase

The injection pressure was constant over a period of 8 days, then rose slowly from 6.2 bar to 6.8 bar. This rise was probably due to skin effects, e.g. clogging.

Figure 6.48 shows the temperatures measured by the two installed temperature sensors as function of time. It takes two days for the injection temperature to reach a constant value of approx. 30°C. This means that, at a set temperature of 60°C, 50% of the heat produced by the heater is lost on the way to the fracture, i.e. within the injection borehole. The temperature in the target borehole (lower curve) does not show a measurable rise until towards the end of the heating phase and rises up to the end of the injection phase by only about 0.02 K. Also plotted is the temperature of the multifunctional probe in borehole BoBK 16. Surprisingly enough, a temperature breakthrough was recorded there at about the same time as in borehole BoBK 15, although the pathway to there is longer. Besides this, the temperature rise, about 0.1 K, was much greater than in the actual target borehole. This phenomenon is considered in detail in the next chapter.

Borehole BoBK 9, in a parallel borehole fan, also showed temperature reactions in two of four packed intervals that are considerably greater than in the extraction borehole (Fig. 6.49). The probe in interval 1 was clearly defective due to water penetration so that the corresponding recorded data are of no significance. The two probes in the middle intervals indicated temperature rises of 0.2/0.25 K, beginning at just before 200 h and lasting until the end of the test.

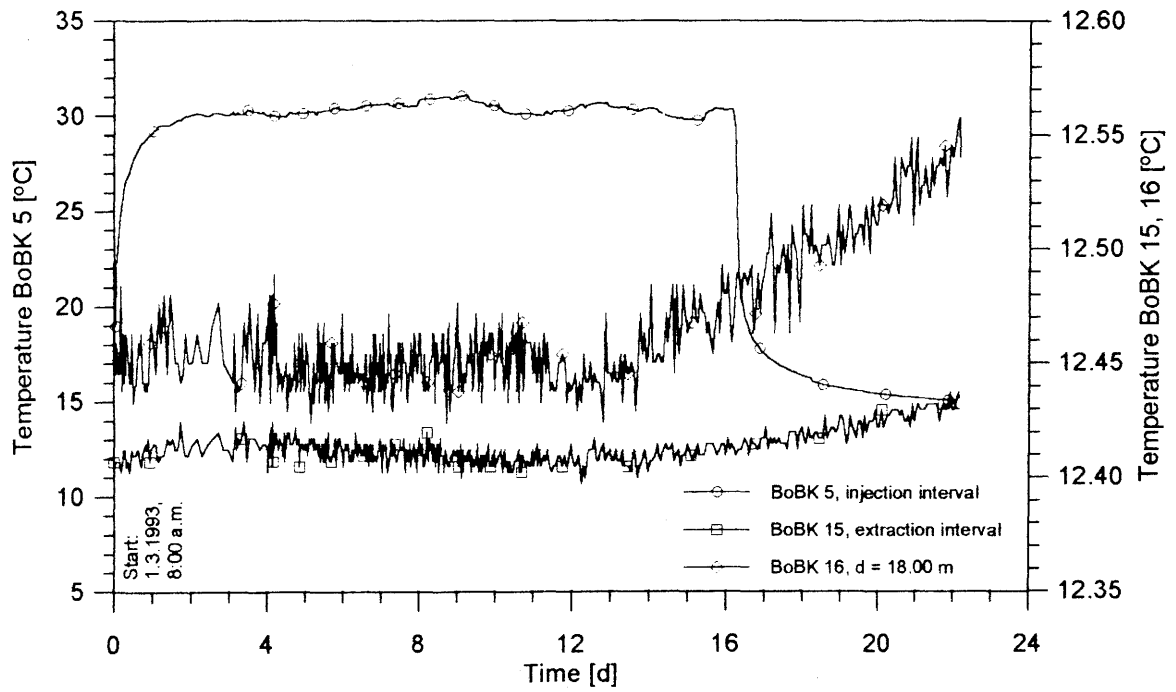


Figure 6.48: Temperatures at both installed temperature sensors and at the multifunctional probes in borehole BoBK 16

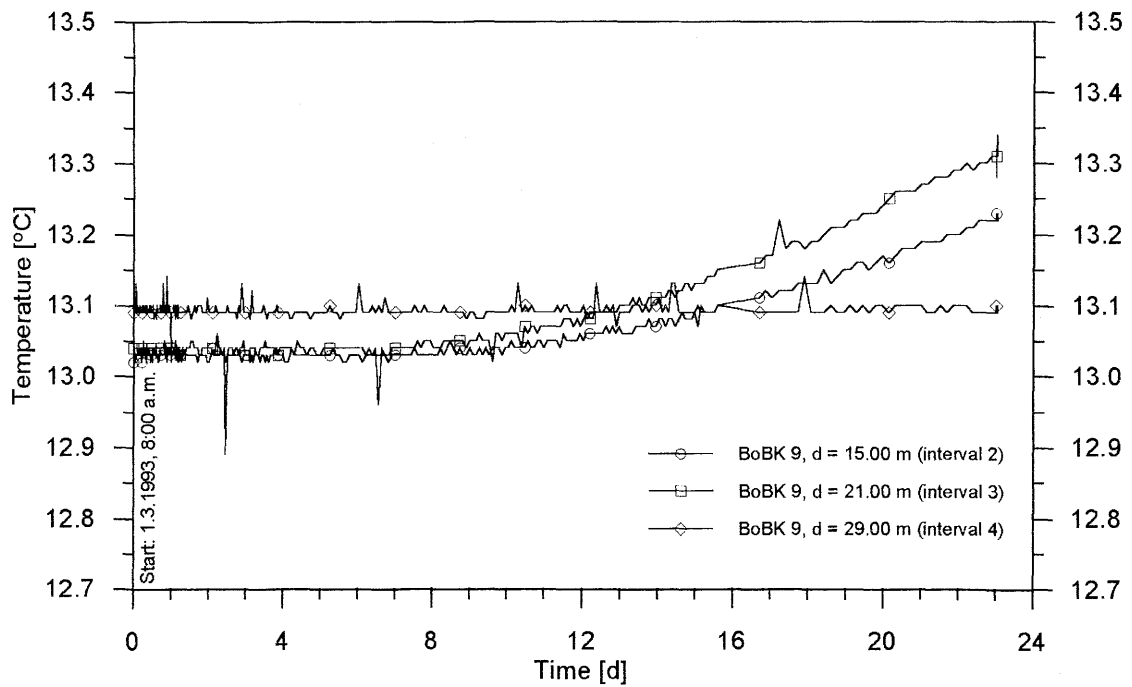


Figure 6.49: Temperatures in intervals 2, 3 and 4 of borehole BoBK 9 as a function of time

Interestingly enough, the conductivity sensors in all the probes did not react, not even in the middle intervals, so that the temperature rises there may not have been induced by advectively transported heat and may require a different explanation.

6.3.4 Evaluation

The following parameters were determined within the framework of this test:

- Transmissivity
- Mean effective fracture aperture
- Breakthrough time of salt tracer
- Breakthrough time of temperature
- Mass balance for salt tracer
- Flow velocity
- Thermal conductivity of surrounding rock matrix

In Section 6.3.5, with the help of analytical modelling, basic effects are modelled and an initial verification of the test results is attempted. The results are then used for a subsequent detailed numerical model (see Section 6.3.6).

6.3.4.1 Transmissivity and Fracture Aperture

Earlier tests provided the spectrum of transmissivities for boreholes BoBK 5 and 15 listed in Table 6.9, together with the corresponding mean values (GUYONNET & LAVANCHY 1992).

Table 6.9: Range of transmissivities observed in boreholes BoBK 5 and 15 as well as mean values and standard deviations

Borehole	Transmissivities (m ² /s)	Mean values ± std dev.
BoBK 5	1.3·10 ⁻⁵ - 8.4·10 ⁻⁷	5.1 ± 3.8·10 ⁻⁶
BoBK 15	1.0·10 ⁻⁵ - 8.4·10 ⁻⁷	4.7 ± 2.8·10 ⁻⁶
		4.9 ± 3.2·10⁻⁶

Using transmissivity T, the effective fracture aperture 2w can be determined according to the equation (JUNG 1986)

$$2w = \sqrt{\frac{C \cdot T}{8}} \quad (\text{Eq. 6.3})$$

employing an estimate of fracture roughness, with C as a function of relative roughness. Figure 6.50 shows the dependence of effective fracture aperture on transmissivity calculated from equation 6.3 for various roughnesses and conditions $h/2w$.

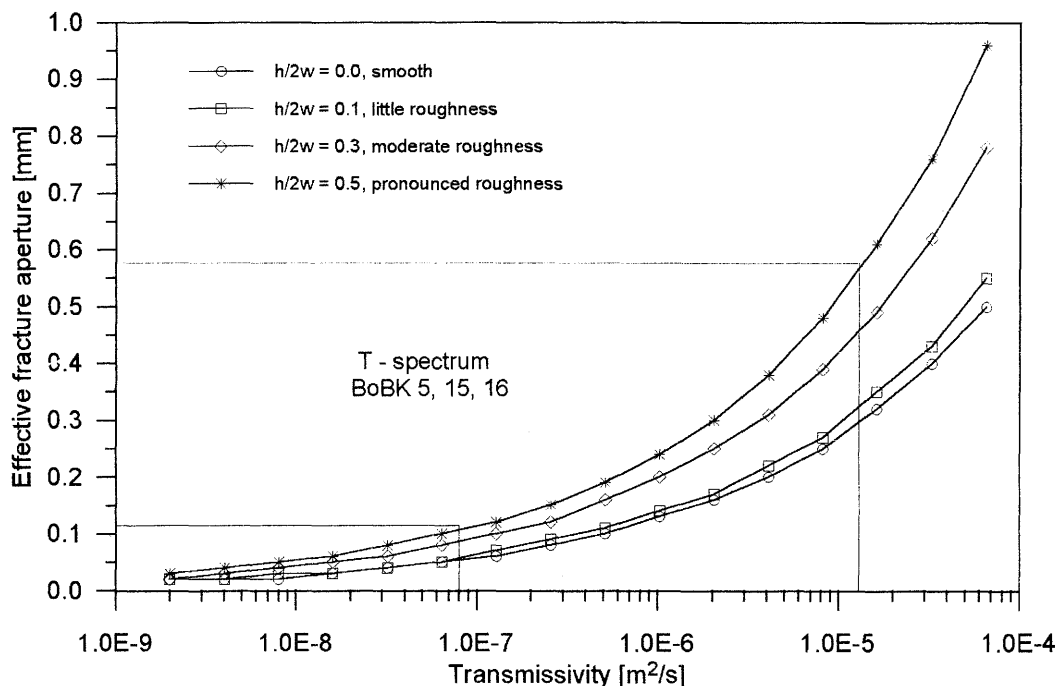


Figure 6.50: Effective fracture aperture as a function of transmissivity acc. to equation 6.3 for various degrees of relative roughness

For areas with low transmissivity ($< 10^{-7} \text{ m}^2/\text{s}$), relative roughness plays only a subordinate role. At higher hydraulic conductivity levels, however, the curves for smooth and rough walls do deviate considerably. For instance, if relative roughness is left out of consideration at a transmissivity of $10^{-5} \text{ m}^2/\text{s}$, the effective fracture aperture is underestimated by 50%. With the present figure of mean transmissivity of $4.9 \cdot 10^{-6} \text{ m}^2/\text{s}$, the resulting value for the effective fracture aperture is approx.

$$2w = 0.4 \text{ mm.}$$

Geological investigations have shown that the hydraulically relevant fracture apertures in the BK area range up to $2w = 10 \text{ mm}$.

6.3.4.2 Breakthrough Times

Figure 6.51 shows the beginning of the breakthrough curve for the salt tracer in the range from 0-8 h. The temporal derivation was also plotted, since sudden changes, even very small ones, are rendered particularly noticeable using this curve. According to the course of this curve, the arrival time of the brine tracer can be estimated at

3.66 h. To obtain the actual breakthrough time, the 5 min must be subtracted that the tracer requires to traverse the path from the injection basin to the borehole head and 5.7 and 3.6 min for the path inside the boreholes. This results in a breakthrough time of

$$tb_s = 3.4 \pm 0.1 \text{ h}$$

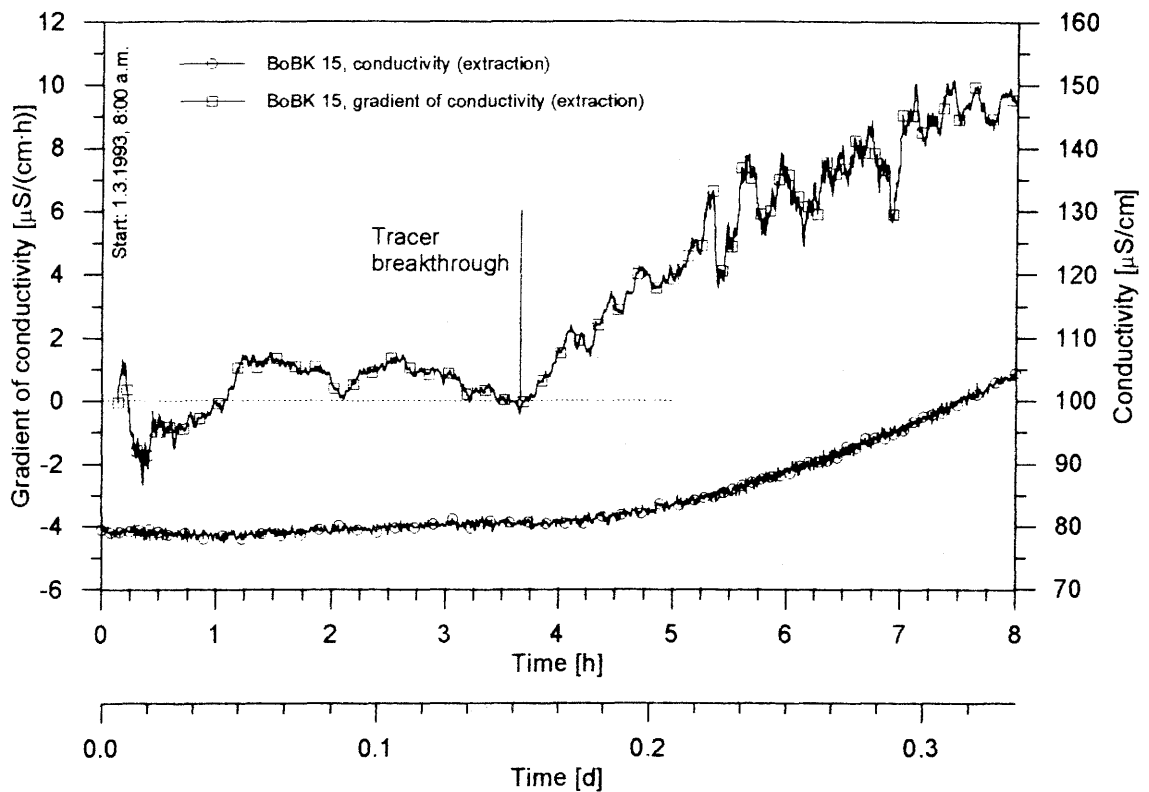


Figure 6.51: Beginning of breakthrough curve for salt tracer (scale on right) and its derivation (scale on left) for extraction borehole BoBK 15

The breakthrough time for the temperature tracer can be calculated in an analogous manner. Figure 6.52 shows the temperature curve within borehole BoBK 15 in the range from 225 h until the end of the test (scale on right). The temporal derivation is once again plotted above it, according to which the arrival time can be calculated as 338 ± 5 h. Approx. 45 min must be subtracted from this, which is the time the heat requires to reach the fracture depth in the injection borehole. This results in a thermal breakthrough time of

$$tb_\theta = 337 \pm 5 \text{ h}$$

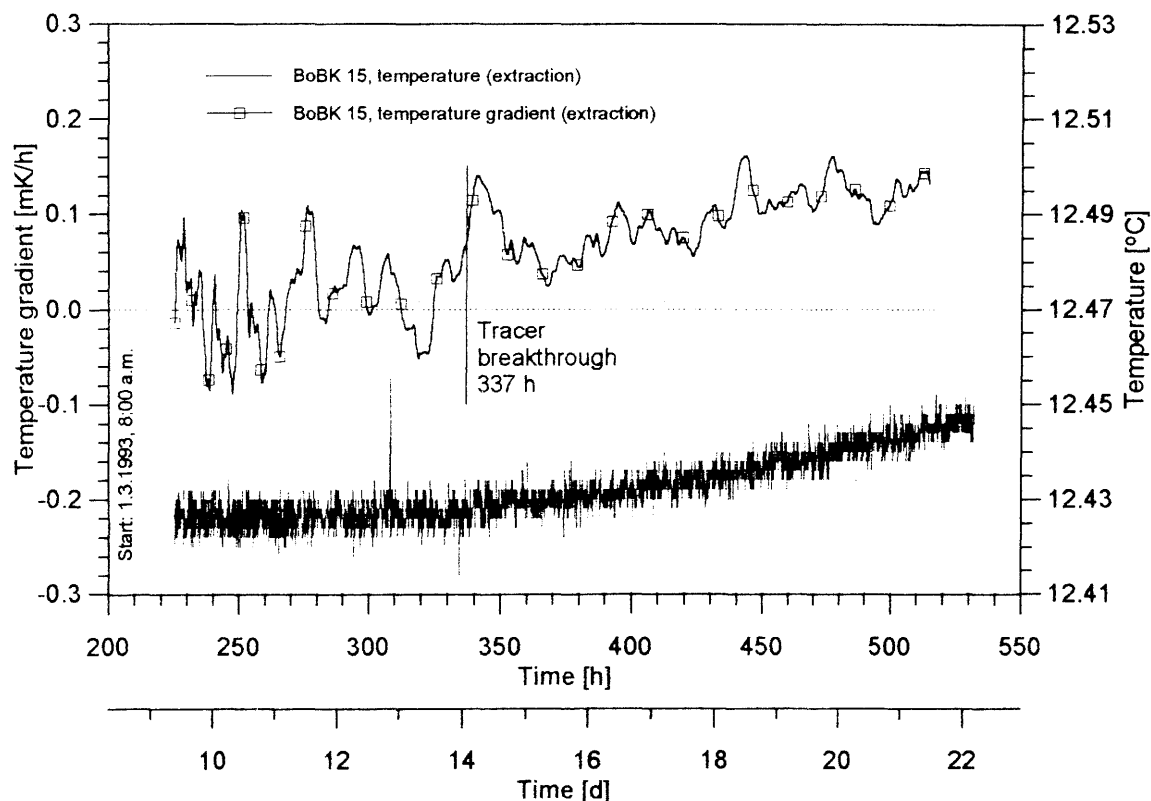


Figure 6.52: Temperature curve within extraction borehole BoBK 15 after 225 h (scale on right) and its derivation (scale on left)

6.3.4.3 Mass balance

A mass balance was determined to check how much of the injected amount of salt actually reached the borehole. Within a range of 0-2,000 $\mu\text{S}/\text{cm}$ there is a linear dependence between electrical conductivity and salt content calculated from equation 6.1 (see Section 6.2.2).

Thus if the flow rate is known the salt content can be calculated directly from the measured conductivity. Figure 6.53 shows the volume introduced during the injection period and the amount extracted from the target borehole during the entire test period in the form of a cumulative curve. Beyond approx. 400 h, this curve approximates an asymptotic value, i.e. no further appreciable amounts of salt are being extracted. All told, approx. 70% of the volume of salt injected is recovered from the target borehole by the end of the test, 30% thus remaining in the rock. Part of this amount was found at the leakages. The amount extracted there is also plotted in Figure 6.53 for purposes of comparison and comes to only about 2% due to the low flow rate. The dashed curve represents the sum from both extraction sites. Keeping in mind the fact that the extraction rate was twice as great as the injection rate, it is surprising that the

volume extraction curve appears to approximate a relatively low value asymptotically. A flow rate ratio of $q_{ex}/q_{in} > 1$ usually leads to a bundling effect on streamlines in the source-sink area, greatly increasing the probability of an even mass balance. The possibility cannot be excluded completely that the approximation to an asymptotic value is an illusion and that the curve would reach higher values in longer time periods. The authors strongly doubt this, however, since the extraction rate depended mainly on the natural groundwater stream, which certainly did bear large volumes of salt in the direction opposite to the desired tracer propagation direction, as seen in the amounts extracted at the leakages.

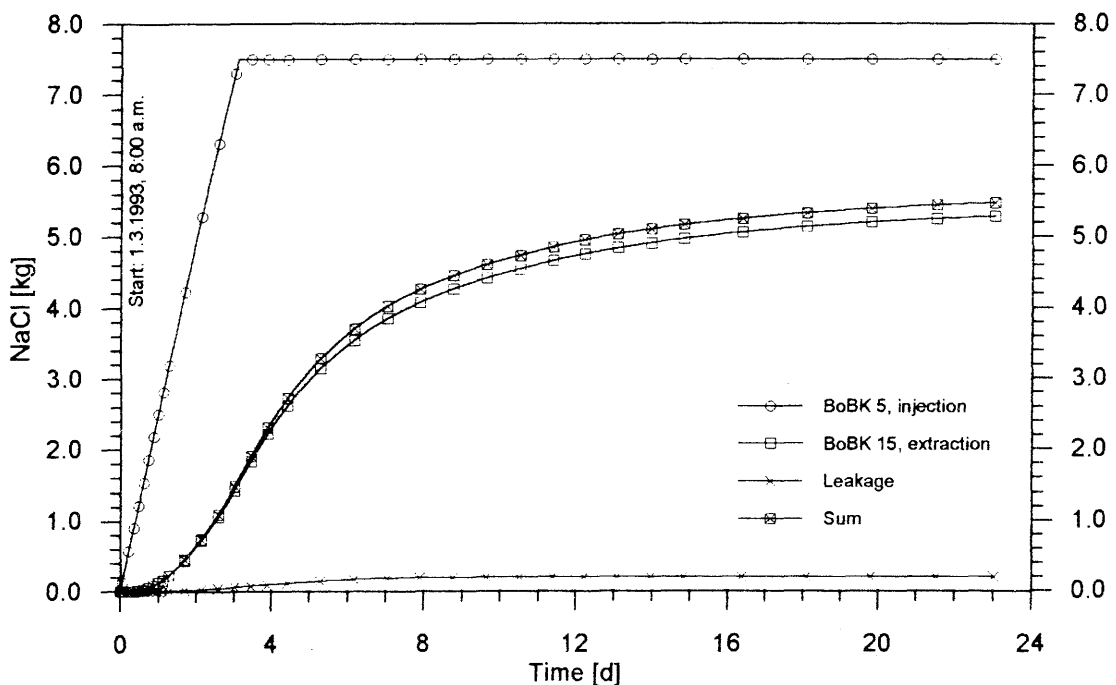


Figure 6.53: Mass balance - Amount introduced into borehole BoBK 5 and removed from extraction borehole and most important leakage as well as a cumulative curve of entire amount removed up to the end of the experiment

An energy balance was not done for thermal transport, since a really complete breakthrough curve was not obtained during the test and meaningful balancing was not possible.

6.3.4.4 Flow Velocity

Flow velocity of the tracer substance is a function of distance traversed and time required. The shortest distance (x) between source and sink is 7.35 m. The breakthrough time (tb_s) of the salt tracer was 3.4 ± 0.1 h, resulting in a flow velocity as follows:

$$v_a = x / t_{b_s} = 6.0 \cdot 10^{-4} \text{ m/s} = 3.6 \text{ cm/min}$$

This computation is a minimum estimation, since it is by no means certain that the water actually moves along the shortest direct (spatial) connection between source and sink. The value $v_a = 3.6 \text{ cm/min}$ is a borderline value to be seen as a minimum that must be reached in the corresponding model computations.

6.3.4.5 Thermal Conductivity

Thermal conductivity was measured in core samples taken directly adjacent to the flow fracture as a basis for modelling of heat dissipation from the heated water to the surrounding rock. Thermal conductivity data are available from ETH Zurich (KEUSEN et al. 1989), but they refer to a different rock area and cannot be considered representative for this test. Another factor is the hydrothermal decomposition of the rock often seen in the Grimsel massif, in particular in the extraction borehole BoBK 15 along the edge of the most important fracture.

During the process of hydrothermal alteration, certain minerals, mainly quartz, were dissolved in an initial phase and separated out in a later phase at a different location (STADLER 1964 and 1981). For example, the large rock crystal discoveries in the Grimsel area can be explained in this way. In general, however, more minerals are dissolved than recrystallise, so that the granite is frequently leached out. The increased porosity and leaching of quartz characteristic of this situation have a considerable effect on the thermal conductivity of the rock, the more so since quartz has the highest thermal conductivity of all minerals (SCHÖN 1983).

The decisive rock area for heat dissipation is the area in direct contact with the flowing fluid (where the highest temperature gradients are found). It therefore seemed logical to measure the thermal conductivity of core samples from this area.

Sampling began at the fracture and was carried out at 2 cm intervals. The cylindrical samples had a diameter of 50 mm and a height of 2 cm. They were measured with a BGR divided-bar apparatus under uniaxial pressure of 0.2 MPa, air-dry, i.e. with air as the pore filling, at various temperatures (Fig. 6.54). All eight samples showed a relatively uniform decrease in thermal conductivity with temperature.

The natural rock temperature in the fracture was approx. 12.5°C. When the value is taken from these curves at the corresponding temperature and the curves are plotted together with their distance from the fracture (Fig. 6.55a, lower curve), the influence of the hydrothermal decomposition zone on thermal conductivity becomes clear. Thermal conductivity is seen to increase greatly with distance from the fracture. Three of the samples are from rock outside the decomposed area and show similarly high values to those recorded by ETH Zurich in compact rock samples ($3.34 \pm 0.35 \text{ W/(m}\cdot\text{K)}$). Since, however, thermal conductivity depends not only on porosity but also on pore filling, one of the samples (9 cm from the fracture) was evacuated, wetted and

measured again. The thermal conductivity increased by 0.53 W/(m·K), i.e. by 19%. The values for the other samples from the decomposed area were determined by computation in accordance with this increase.

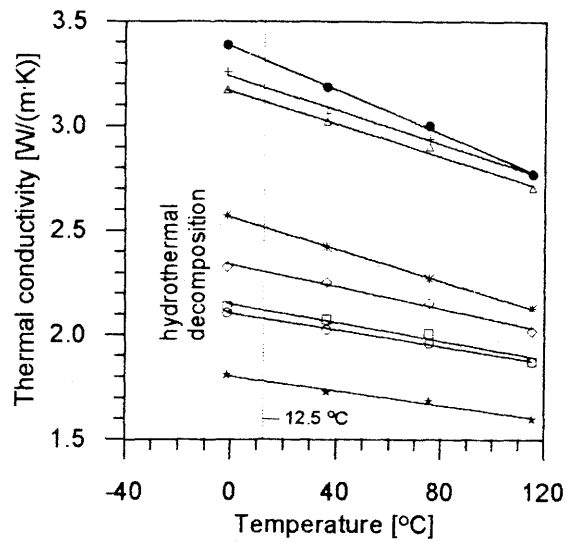


Figure 6.54: Thermal conductivity of core samples from borehole BoBK 15 taken near the most important fracture at a depth of 25 m as a function of temperature

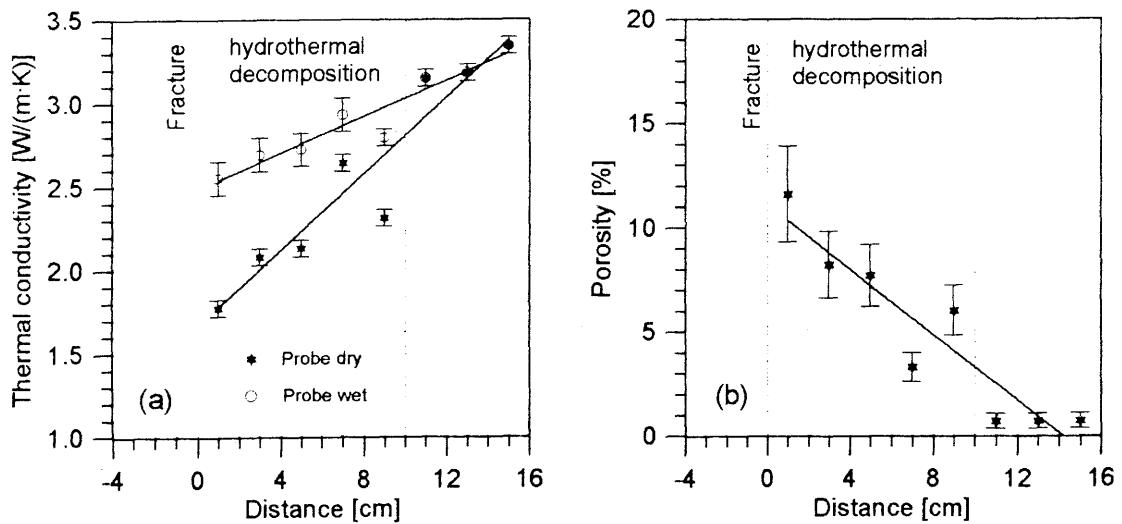


Figure 6.55: a) Thermal conductivity of core samples from borehole BoBK 15 as a function of distance from the fracture with air as pore filling (dry) and water as pore filling (wet) b) Effective porosity of the same core samples determined according to equation 6.5 as a function of distance from the fracture

The dependence of the effective thermal conductivity on porosity and pore filling can be described for crystalline rocks (porosities < 1%) after WALSH & DECKER (1969):

$$\lambda_e = \lambda_r \left[1 - \frac{\Phi(1 + 2\lambda_f / \lambda_r) \cdot (1 - \lambda_f / \lambda_r)}{\Phi(1 - \lambda_f / \lambda_r) + 3\lambda_f / \lambda_r} \right] \quad (\text{Eq. 6.4})$$

whereby λ_e [W/(m·K)] = Effective thermal conductivity
 λ_f [W/(m·K)] = Thermal conductivity of fluid
 λ_r [W/(m·K)] = Thermal conductivity of rock
 Φ [-] = Effective Porosity

and after WOODSIDE & MESSMER (1961) and SASS et al. (1971) as the geometric mean of a system with two components (porosities > 1%)

$$\lambda_e = \lambda_f^\Phi \cdot \lambda_r^{(1-\Phi)} \quad (\text{Eq. 6.5})$$

If measured data are available for the same sample with air and water as pore fillings, the two equations can be used, for example, to determine effective porosity by eliminating λ_e . Assuming that the thermal conductivity of the matrix is nearly identical, at least in the decomposed samples, the effective porosity and thermal conductivities can be estimated by way of computation.

The values determined in this way result in the upper curve in Figure 6.55a for water-saturated samples. This curve no longer climbs so dramatically, but thermal conductivity at the edge of the fracture is still about 20% below that of the non-decomposed material located farther away. Figure 6.55b shows the porosities as a function of the distance to the fracture. The values traverse a range of about 3 - 11% in the decomposed area. KEUSEN et al. (1989) calculated theoretical porosities based on unit weights with values up to 13%, so that agreement is good.

The greatly reduced thermal conductivities near the fracture are taken into account in the models.

6.3.5 Analytical Modelling

6.3.5.1 Fracture Model

Thermal behaviour of flow in a fracture can be described for simple hydraulic flow conditions by means of analytical solution. The dipole flow common in tracer tests can be treated within the framework of the potential theory. This approach goes back to MUSKAT (1937), who in his paper describes two-dimensional flow systems in saturated aquifers. GRINGARTEN & SAUTY (1975), RODEMANN (1979) and

SCHULZ (1987) expanded on this approach by introducing the factor of thermal transport as well. Figure 6.56 shows the corresponding model geometry.

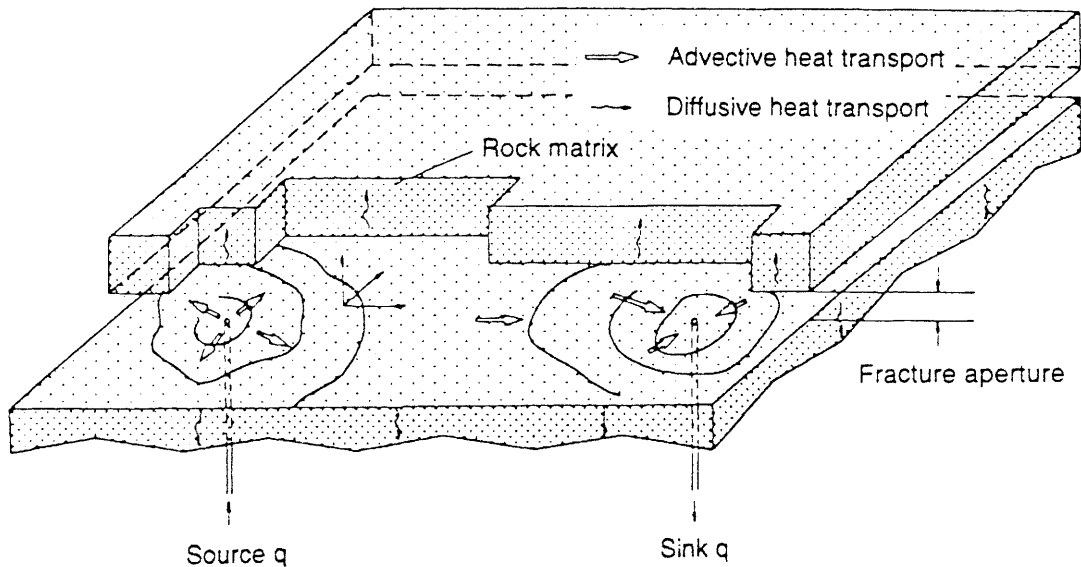


Figure 6.56: Model geometry of source-sink stream in a fracture

An infinitely extended fracture with an aperture of $2w$ is embedded in an impermeable rock matrix. Thermal transport is by means of 2-dimensional advection within the fracture as conditioned by the dipole flow system and 1-dimensional diffusion in the matrix orthogonal to the fracture. The pronounced temperature differences between the fluid in the fracture and the neighbouring rock essentially bring about a vertical orientation of the temperature gradients - and thus the heat flow - in relation to the fracture. Thus it can be seen that ignoring the heat diffusion in the matrix parallel to the fracture will not prevent a good approximation.

Using the coordinates $(x, y, z) = (-a, 0, 0)$ or $(x, y, z) = (a, 0, 0)$ for the source and sink of the dipole, the following equation applies to potential distribution (KOLDITZ & LEGE 1992):

$$h = -\frac{q \cdot \mu}{8 \cdot \pi \cdot k \cdot g \cdot \rho_w \cdot w} \ln \frac{(x+a)^2 + y^2}{(x-a)^2 + y^2} \tag{Eq. 6.6}$$

- whereby
- h [m] = Hydraulic head
 - q [m³/s] = Flow rate into entire fracture
 - μ [Pa·s] = Dynamic viscosity
 - k [m²] = Permeability of fracture
 - g [m/s²] = Gravity acceleration (9.81)
 - ρ_w [kg/m³] = Fluid density
 - w [m] = 1/2 fracture aperture

For the components of the velocity

$$v_x = \frac{q}{4 \cdot \pi \cdot w} \left(\frac{x+a}{(x+a)^2 + y^2} - \frac{x-a}{(x-a)^2 + y^2} \right) \quad (\text{Eq. 6.7})$$

$$v_y = \frac{q}{4 \cdot \pi \cdot w} \left(\frac{y}{(x+a)^2 + y^2} - \frac{y}{(x-a)^2 + y^2} \right) \quad (\text{Eq. 6.8})$$

and for the temperature

$$\Theta(t, h, z) = \delta[t-l(h)] \operatorname{erfc} \frac{1}{2\sqrt{t-l(h)}} \left(\frac{\sqrt{\lambda_r c_r \rho}}{c_w \rho_w w} \cdot l(h) + z \cdot \sqrt{\frac{c_r \rho}{\lambda_r}} \right) \quad (\text{Eq. 6.9})$$

whereby t [s] = Time
 δ [-] = Dirac function
 c_r [J/(kg·K)] = Specific thermal capacity of rock
 c_w [J/(kg·K)] = Specific thermal capacity of fluid
 ρ_r [kg/m³] = Density of rock

and with the geometry function acc. to equation 6.10/6.11

$$l(h) = \left[1 + 2 \cdot \cot \eta \cdot \arctan \left(\frac{\tan(\eta/2) \cdot (\tanh(\xi/2) - 1)}{1 + \tanh(\xi/2) \cdot \tan^2(\eta/2)} \right) - \frac{\sinh(\xi)}{\cosh(\xi) + \cos(\eta)} \right] \cdot \frac{4 \cdot \pi \cdot w \cdot a^2}{q} \cdot \sin^2(\eta) \quad \text{for } |\cos(\eta)| \neq 1 \quad (\text{Eq. 6.10})$$

$$l(h) = \left[1 - \frac{\sinh(\xi)}{\cosh(\xi) + \cos(\eta)} \cdot \left(1 + \frac{\cos(\eta)}{\cosh(\xi) + \cos(\eta)} \right) \right] \cdot \frac{4 \cdot \pi \cdot w \cdot a^2}{3 \cdot q} \quad \text{for } |\cos(\eta)| = 1 \quad (\text{Eq. 6.11})$$

$$\begin{aligned} \text{whereby } \xi &= \frac{1}{2} \cdot \ln \frac{(x-a)^2 + y^2}{(x+a)^2 + y^2} \\ &= \frac{4 \cdot \pi \cdot k \cdot g \cdot \rho_w \cdot w}{q \cdot \mu} \cdot h \quad (\text{potential function}) \end{aligned} \quad (\text{Eq. 6.12})$$

$$\text{and } \eta = \arctan \frac{2ay}{a^2 - x^2 - y^2} \quad (\text{stream function}) \quad (\text{Eq. 6.13})$$

Assuming a steady flow field, isotropy and constant physical parameters, this model can be used to investigate the following factors:

1. **Thermal breakthrough time:** Time at which the earliest change in temperature can be observed at the extraction borehole.
2. **Temperature buildup curve** in the extraction borehole following thermal breakthrough. (Not the entire breakthrough curve due to steady boundary conditions).
3. **Tracer breakthrough time:** Earliest time at which tracer, e.g. salt or uranine, can be observed in the extraction borehole. (Assuming a thermally isolated rock matrix ($\lambda = 0$) heat can be treated as a normal tracer until breakthrough time. Dispersion is, however, ignored in this case).
4. **Temperature distribution within** the fracture at random times (2D).
5. **Temperature distribution orthogonal** to the fracture at random location and times (2D).
6. **Flow velocities** within the fracture (2D).
7. **Potential distribution** within the fracture (2D).

This model also offers the possibility of determining the thermally relevant extent of the matrix area vertical to the fracture. This means one can calculate how far the temperature penetrates into the rock during the test. This is a factor of considerable significance for further numerical modelling. In this way, unnecessarily excessive model size of the matrix area is avoided, saving elements and computing time. At the same time, it is ensured that the extent is great enough so that temperature effects at the edge of the model do not unduly affect model results.

6.3.5.2 Model Computations

With this model, it is certainly not possible to simulate the tracer test with great precision, especially because varying injection and extraction rates cannot be selected. Modelling would, however, seem desirable to

- a) determine the above-mentioned thermally relevant, and thus minimum necessary, spatial extent of the numerical model vertical to the fracture.
- b) determine the influence of certain model parameters on the model results, in particular that of the breakthrough times.

The latter could possibly obviate, or at least reduce to a sensible minimum, time-consuming numerical sensitivity analyses of salt/heat transport.

Sensitivity analyses

The following considers the dependence of thermal breakthrough time on thermal conductivity λ , fracture aperture $2w$ and flow rate q by means of parameter variation under the boundary conditions of the test (Table 6.10).

Table 6.10: Model parameters used for the test and sensitivity analysis for λ , $2w$ and q

Symbol	Unit	Value	Designation
$2a$	m	7.40	Source-sink distance
Θ_{Ini}	°C	30.00	Fluid temperature
Θ_{Geb}	°C	12.40	Rock temperature
T	m^2/s	$5.0 \cdot 10^{-6}$	Transmissivity
m	$Pa \cdot s$	$1.6 \cdot 10^{-3}$	Dynamic viscosity
c_w	$J/(kg \cdot K)$	3,917	Specific thermal capacity of fluid
c_r	$J/(kg \cdot K)$	1,256	Specific thermal capacity of rock
r_w	kg/m^3	1,045	Fluid density
r_r	kg/m^3	2,660	Rock density

The fracture aperture is varied by two orders of magnitude in a range between 0.1 and 10.0 mm. This covers the range of fracture apertures found in the crystalline formations in the BK area. A variation of thermal conductivity over the entire range between 0 and 5 W/(m·K), typical for rock, allows a comparison between thermal breakthrough time and, for $\lambda = 0$, tracer breakthrough time. Figure 6.57 shows the thermal breakthrough time as dependent on λ for various fracture apertures.

The thermal conductivity of crystalline rock is within the range 1.5 - 4.5 W/(m·K) (CERMAK & RYBACH 1982). A variation of λ in this range results in differences in thermal breakthrough time of up to 150 h, whereas varying fracture aperture within a range of two orders of magnitude changes it by only approx. 1 h. This means that fracture aperture plays a secondary role in modelling of thermal breakthrough time as opposed to thermal conductivity. It is of particular importance to note that thermal breakthrough time changes only very little below fracture apertures of about 10 mm. KOLDITZ (1993) coined the term "**thermally relevant fracture aperture**" for this phenomenon in his study of thermal transport processes in a fractured medium.

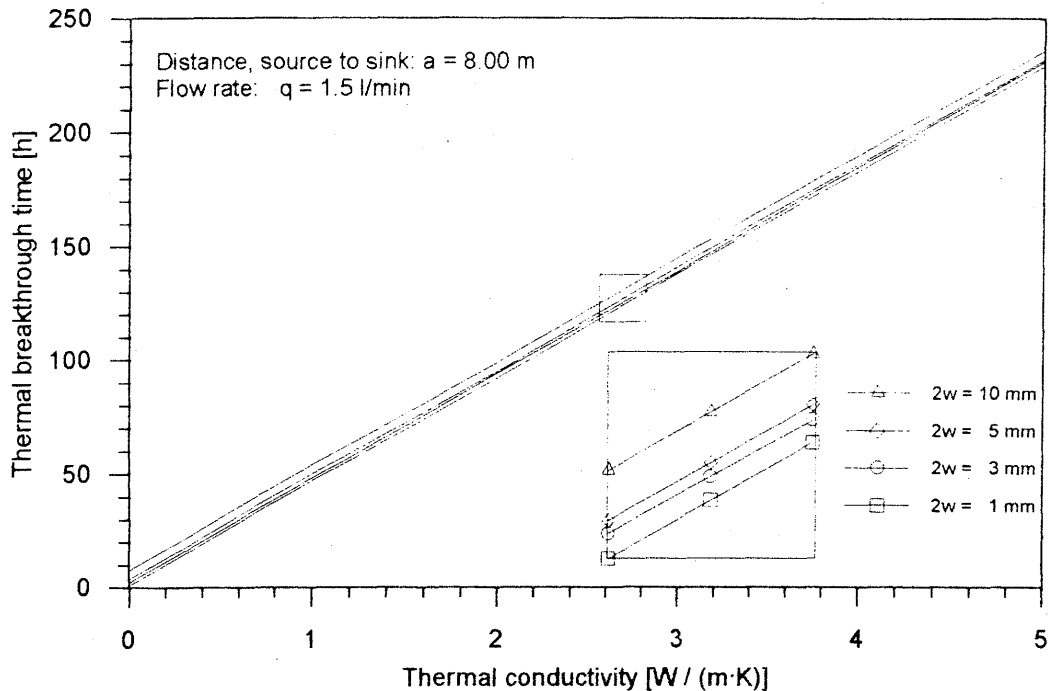


Figure 6.57: Thermal breakthrough time as a function of thermal conductivity for various fracture apertures ($q = 1.5$ l/min)

Hydraulic system behaviour reacts much more sensitively to any change in fracture aperture, since there is a direct quadratic relation (cubic law) between fracture aperture and fracture permeability. **Hydraulically** relevant fracture apertures are thus lower by 2-3 orders of magnitude. This difference can be explained physically by the fact that the thermal storage capacity of a water-saturated fracture is very low at below a certain fracture aperture. This means that heat dissipates into the rock very quickly, so that the thermal breakthrough time is hardly changed, even by increased advection.

This difference between hydraulically and thermally relevant fracture aperture is of considerable significance in numerical calculations. Small fracture apertures bring about high flow rates, which require in their turn (due to numerical stability conditions (Courant criterion)) a very fine time discretion for transport computation, so that long-term simulations are hardly feasible. Thermally relevant fracture apertures, on the other hand, afford much greater time increment widths without being the results falsified by numerical effects. The consistency between the numerical and the physical model is maintained.

In a second study, the flow rate q was varied within a range from 1 to 10 l/min, which is the order of magnitude for flow rates possible with the equipment in the BK area. The dependence of thermal breakthrough time on q is shown in Figure 6.58 for three different thermal conductivities. Above a flow rate of about 5 l/min, the thermal breakthrough time does not react very sensitively to increases in q or changes in λ . As flow

rate is reduced, the significance of thermal conductivity increases, since at the lower flow rate the water has more time to give off heat into the surrounding rock. If the flow rate drops to below about 2 l/min, the thermal breakthrough time increases dramatically. This means that the influence of flow rate is absolutely dominant in this case over the other factors. A reduction in q by a few tenths of litres per minute can mean a delay in thermal breakthrough of several days. If no data are available on the thermal conductivity of the rock matrix, the model design may be falsified, at least for flow rates below approximately 5 l/min.

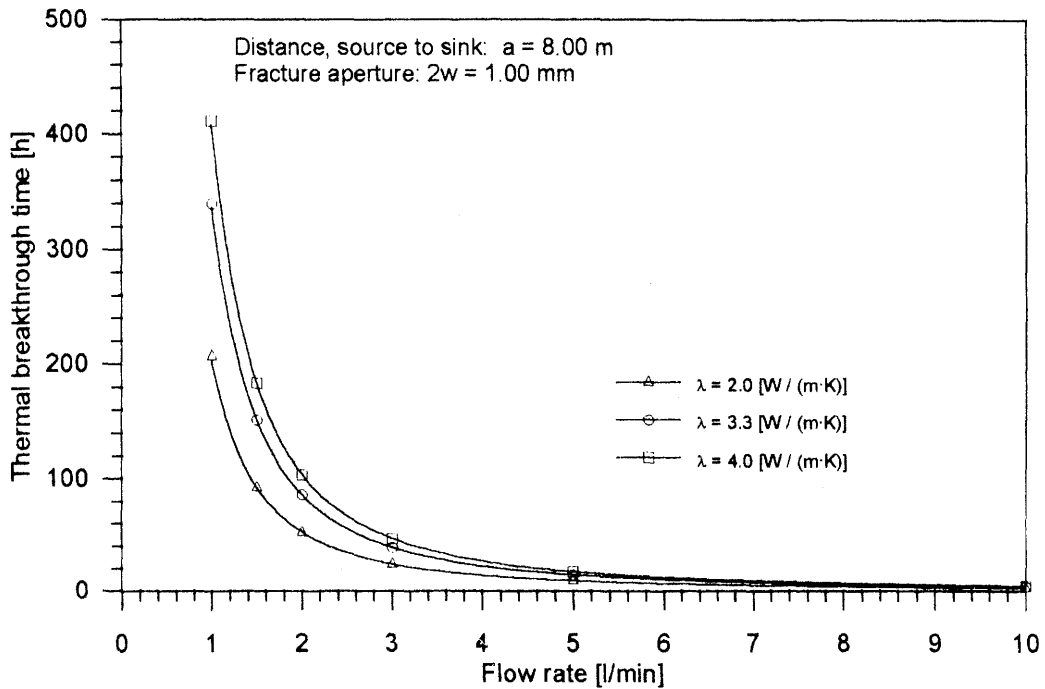


Figure 6.58: Thermal breakthrough time as a function of flow rate for various thermal conductivities

Breakthrough times

During the test, the extraction rate was double the injection rate (see Section 6.3.4.2). An attempt at even an approximate explanation of the measured breakthrough times on the basis of a mean flow rate $(q_{in} + q_{out})/2$ was doomed to failure. Even when the model parameters such as thermal conductivity or fracture aperture were selected very generously, the model breakthrough times were lower than the measured ones by several orders of magnitude. Reduction of the flow rate to the injection rate used in the test also failed to improve the situation markedly. It was not until the flow rate was halved to a value of 0.86 l/min that a model could be constructed that simulated the measured difference in hydraulic heads as well as the breakthrough times of heat and salt (without dispersion).

Table 6.11 lists the model parameters in a comparison with the test results. The injection rates ((θ) for temperature and (S) for salt) were obtained by taking the means during the time until each breakthrough.

Table 6.11: Comparison of test and model parameters

Designation	Unit	Test	Model
Source-sink distance	m	7.35	7.40
Effective fracture aperture	mm	0.40	3.3
Transmissivity	m ² /s	5.0·10 ⁻⁶	4.0·10 ⁻⁶
Thermal conductivity	W / (m·K)	3.3 (2.9)	2.9
Injection rate (S)	l/min	1.76	0.86
Injection rate (⊙)	l/min	1.45	0.86
Potential difference	m	52	51
Breakthrough time (S)	h	3.4 ± 0.2	3.5
Breakthrough time (⊙)	h	337 ± 5	340
Flow velocity	cm/min	3.6	4.3

Temperature distribution

The brine was injected into the fracture at a temperature of 30°C. The rock temperature was 12.5°C, so that the temperature disturbance introduced into the rock was $\Delta T = 17.5^\circ\text{C}$. Modelling of the breakthrough times resulted in a flow rate of 0.86 l/min. The resulting temperature distribution is shown in Figure 6.59 at three different times. Figures a1-a3 show propagation of temperature within the fracture and b1-b3 vertical to it along the shortest connection line between source and sink. In the case of purely advective transport in the fracture, the at first rapid progress of the temperature front is slowed noticeably with increasing distance. The heat exchange surface increases constantly, also increasing the amount of heat given off into the surrounding rock.

Assuming the 14-degree isotherm has travelled 2 m in 10 h (a1), this value will not double until 200 hours have passed (a2). Here the preferred direction of propagation of the temperature front is already in evidence. A further doubling, and thus reaching of the target borehole, will not be achieved until > 600 h (a3).

Figures b1-b3 show very clearly the dominance of advective heat transport in the fracture in the form of the characteristic deformation of the isolines with regard to the propagation rate as compared to purely conductive transport within the matrix. This means that advective transport is the sole decisive factor, even at this quite low flow rate, justifying the 1D, instead of 2D, computation of heat dissipation into the matrix.

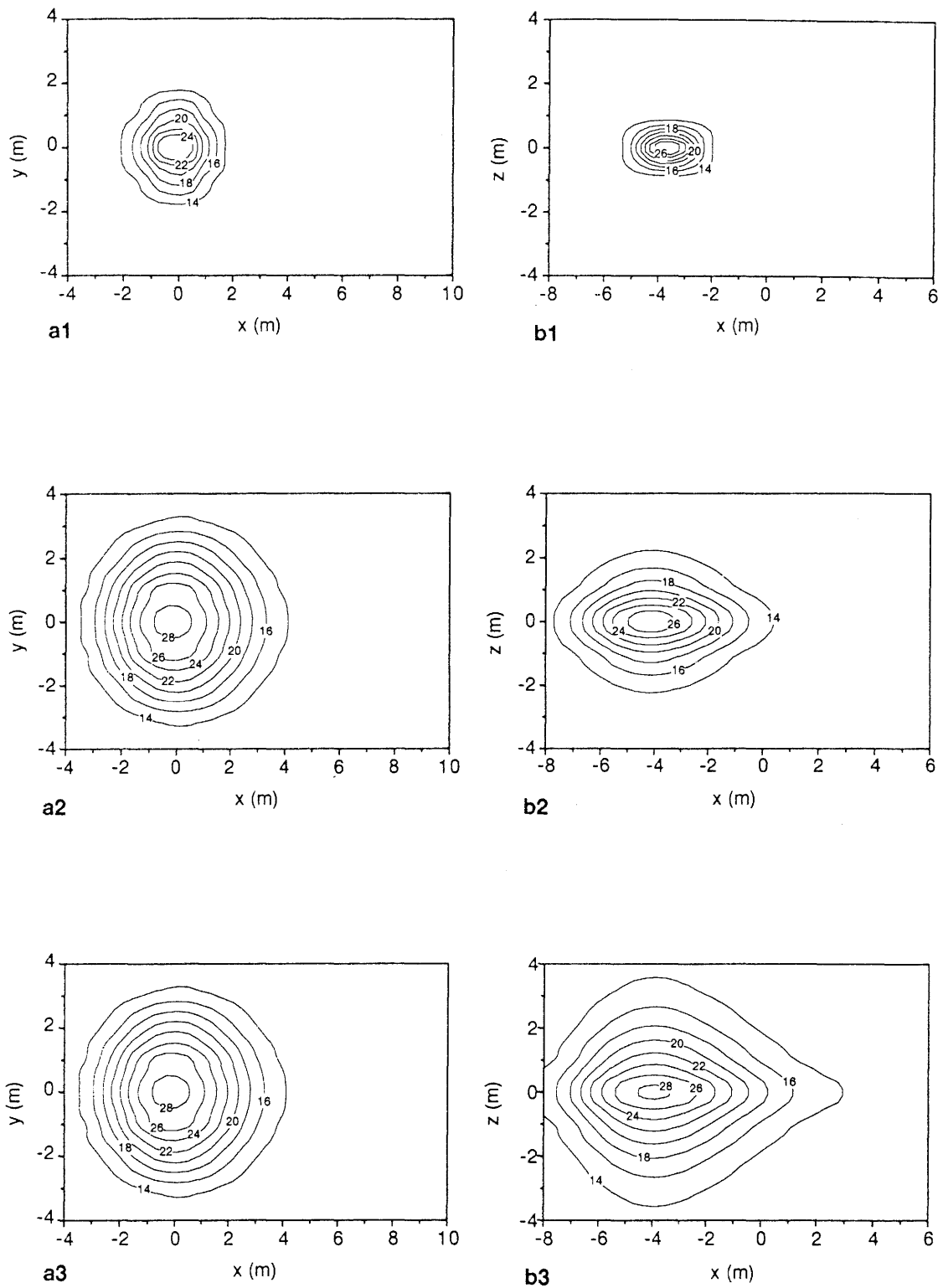


Figure 6.59: Temperature distribution within (a1-a3) and orthogonal (b1-b3) to the fracture at three different times (1 = 10 h, 2 = 200 h, 3 = 600 h; $q = 0.9$ l/min, $\lambda = 2.9$ W/(m·K), $2w = 3.3$ mm)

The penetration depth of the temperature, and thus the thermally relevant extent of the matrix for numerical modelling, is about 7 m. At that depth, the temperature increase up to the end of the test is less than 0.01 K with a thermal conductivity of 3.3 W/(m·K).

6.3.5.3 Discussion of Results

Modelling of the breakthrough times is apparently only possible if the flow rate is set lower than in the test. The breakthrough time of the salt could, it is true, also be modelled by increasing fracture aperture, but it would be impossible to fit the temperature breakthrough at the same time due to the existence of thermally relevant fracture apertures. In the numerical model, it might be possible to balance out this factor by introducing the element of dispersion, but this seems improbable due to the greatly reduced flow rates. There are thus many indications that the flow field is not defined by a purely source-sink stream. An additional natural groundwater stream, e.g. flowing in the direction opposite to the source-sink stream, could hinder tracer propagation and slow down breakthrough times accordingly. The same effect would be seen if the water did not take the direct path, but rather a "detour", e.g. through additional fractures, thus traversing a much longer pathway to reach the target borehole. Both effects were compensated for in the analytical model by the low flow rates.

Figure 6.60 shows how long such a "detour" might be. In this case, the distance between source and sink, beginning with the shortest distance of 7.40 m, was varied for three different flow rates until the breakthrough time was exceeded in each case. The flow rates selected were the mean injection rate, the mean extraction rate and the mean of the two. According to this investigation, the actual pathway traversed would be about 9.5 to 13.5 m long, depending on which flow rate was chosen.

6.3.6 Numerical Modelling

The numerical model computations for this test were carried out by the program system DURST (ROCKFLOW) (KRÖHN 1990 and WOLLRATH 1990). The program is used to calculate flow and transport processes in porous and fractured porous media. Verification of temperature transport was done by KOLDITZ & LEGE (1992) using the analytical 2D model presented in Section 6.4.5.

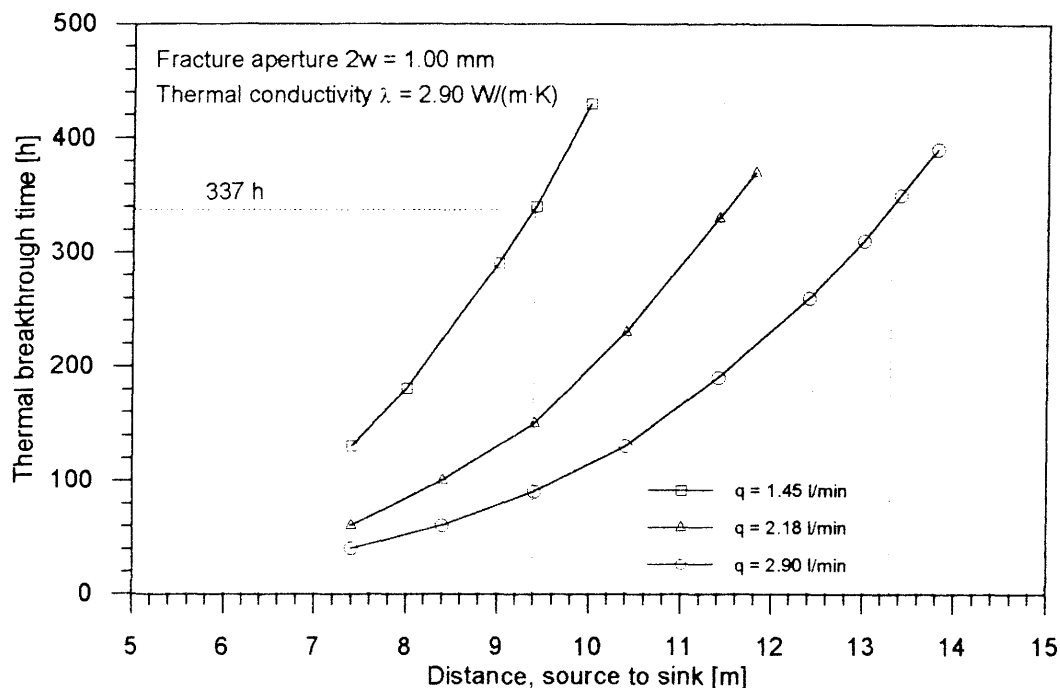


Figure 6.60: Thermal breakthrough time as a function of distance between source and sink for three different flow rates ($q = q_{inj} = q_{extr}$) ($\lambda = 2.9$ W/(m·K), $tb_{\infty} = 337$ Std)

6.3.6.1 Model Description

The results of the fluid logging test (Fig. 5.20) indicate a small band of fractures with a high mass flow level near a shear zone. The injection and extraction sites for the salt/heat tracer test were within this zone and may traverse the same fracture. The initial approximation was therefore based on a single fracture model. The spatial position of the model fracture within the BK area is shown in Figure 6.61 together with boreholes BoBK 5, 15, 16 and 9.

The model geometry was selected as in the analytical model, i.e. fracture discretisation with 2D hydraulically conductive elements and the matrix with 1D heat-conducting elements (Fig. 6.62). The actual element network for 2D discretisation is shown in Figure 6.63a and b. The strong gradient in the source-sink area was taken into account by means of doubling the network resolution in this area. The most significant leakage site was also integrated in the network with a correspondingly finer resolution to investigate the effects on the flow field and substance transport. The extent of the network is 66 x 59 m; it does not contact the lamprophyre zones in the BK area. The minimum characteristic element length was 0.33 m. All told, the model consists of 2,774 elements and 2,802 nodes.

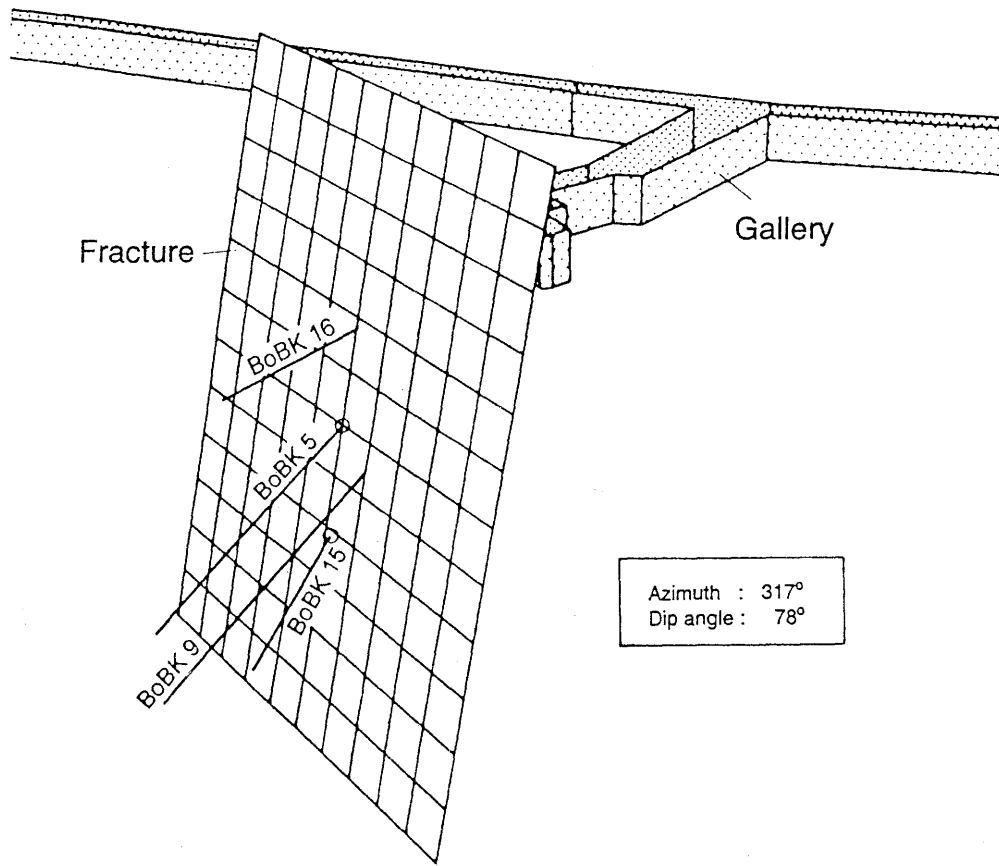


Figure 6.61: Position and extent of the modelled single fracture in the BK area

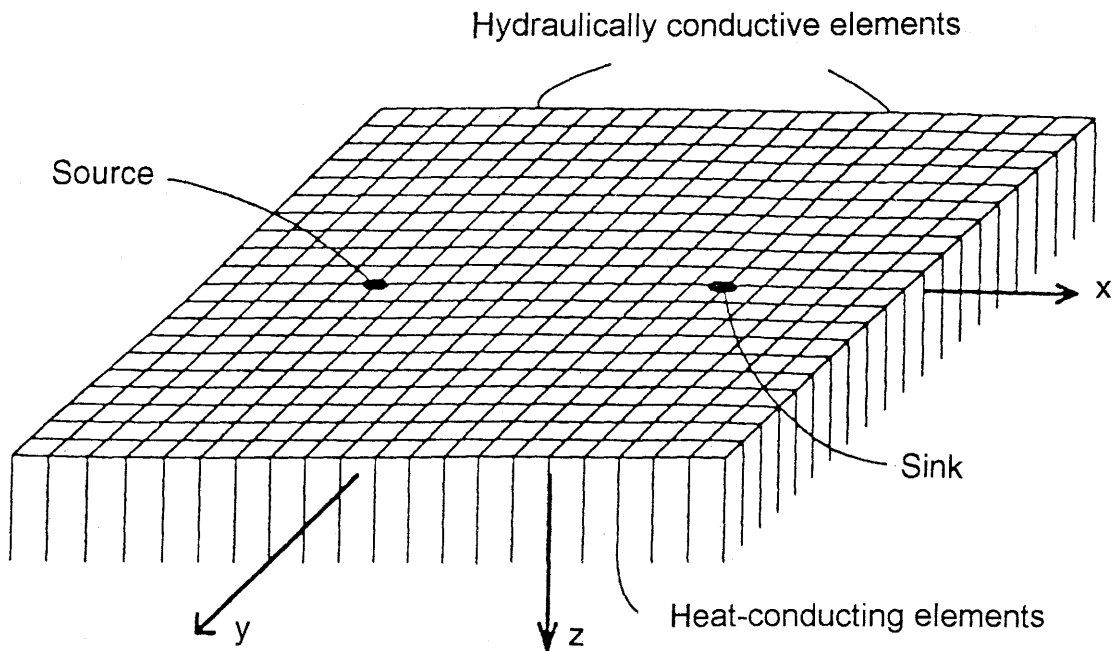


Figure 6.62: Spatial discretisation, representation of the coupling of 1D matrix elements and 2D fracture elements

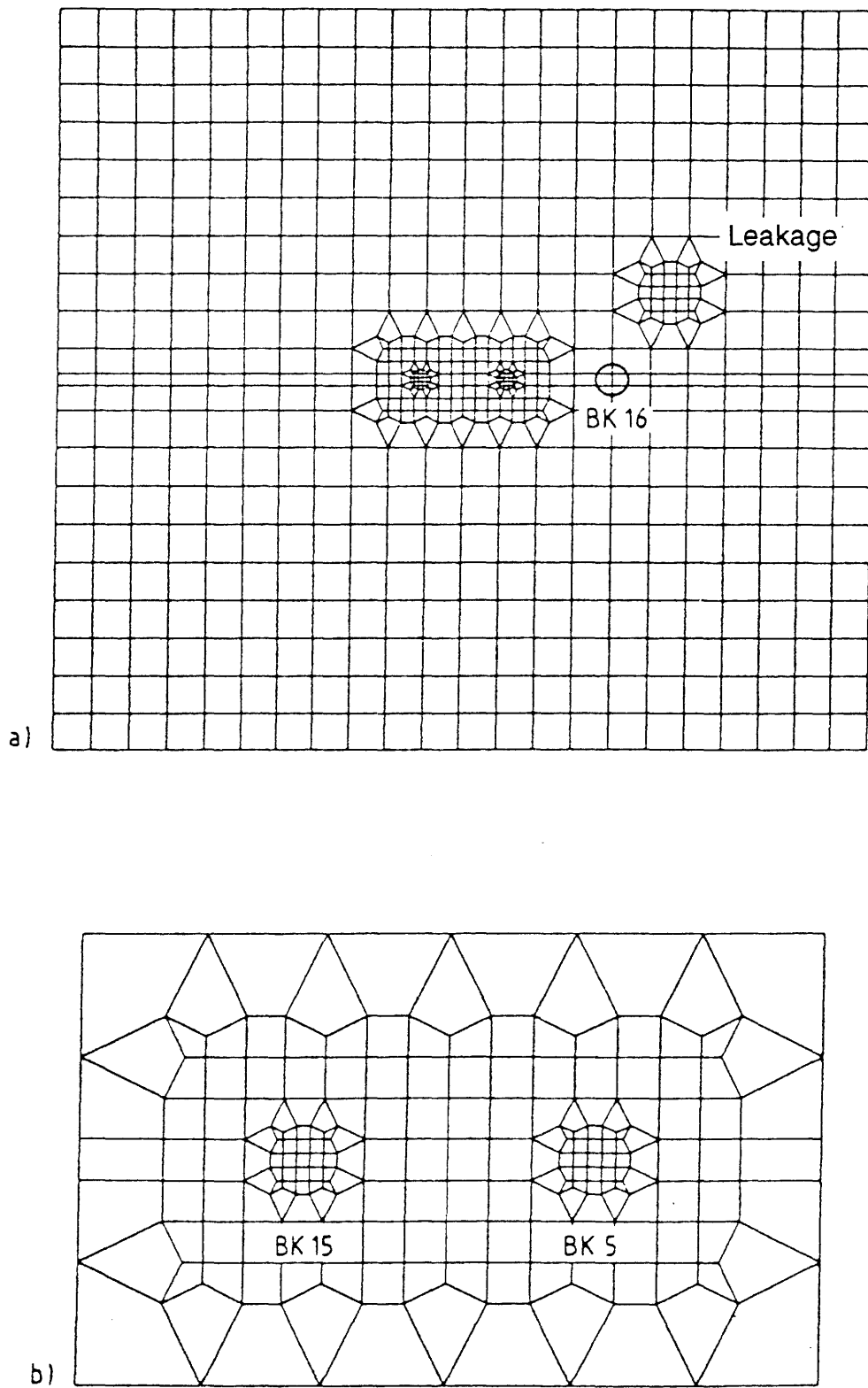


Figure 6.63: Spatial discretisation of hydraulically conductive elements
a) overall, b) source-sink area

6.3.6.2 Flow Conditions

The analytical model supports the assumption that the flow behaviour is not determined by the forced source-sink stream alone. The long breakthrough times are indicative of conditions or processes that inhibit the current flow between the source and the sink. For this reason, various flow models were assumed as a basis for the numerical modelling of substance transport:

- a) Pure source-sink stream
- b) Source-sink stream with impermeable barrier
- c) Source-sink stream with natural countercurrent

A steady flow field was assumed in the first approximation for all models.

a) Pure source-sink stream

The hydraulic system in this model is determined only by injection and extraction rates. In the test, the extraction rate was double the injection rate, leading to inflow from the model edges. The hydraulic head at the edges was assumed to be $h=0$, since flow processes are determined by pressure gradients and therefore absolute pressure is of no consequence in modelling. The piezometric pressure difference between injection and extraction site then adapts to the flow rates. Homogeneous isotropic hydraulic conductivity and constant specific storage coefficients (steady flow) were also assumed in the computations. The decisive model parameters hydraulic conductivity k_f and fracture aperture $2w$ were varied according to the relation $T=k_f \cdot 2w$ so that the transmissivities remained within the measured spread (see also Section 6.3.4.1). Figure 6.64 shows the distribution of the hydraulic heads and flow velocities. The potential funnel at the leakage site is very small relative to the sink, indicating that its influence on the flow field is minor and is not responsible for the long breakthrough times. The source-sink flow velocities are high relative to the surrounding areas; these, together with the flow directions of the water (Fig. 6.65), make it clear that the transport process involves essentially the source-sink axis.

The results of the transport simulation are shown in Figures 6.66 and 6.67, where the calculated breakthrough curves for salt and temperature are shown in a comparison with the measured values. In both cases, it proved impossible, using plausible parameters, to fit the model curve to the measured data. It is clear that the high source-sink flow velocities are instrumental in transport. One way to reduce these velocities would be to increase the fracture apertures in the model. However, even increasing them from 1 to 50 mm did not produce the desired result. The model curves shown were calculated at $2w = 50$ mm. This fracture aperture is, however, already outside the plausible range. The maximum fracture apertures measured in the geological fracture survey were 10 mm. It can surely be assumed that larger aperture widths apply in the local situation, but it would not make much sense to model the entire fracture with a fracture aperture of greater than 10 mm. Even a considerable increase in dispersion length from 1 m to 8 m (Fig. 6.66) did not produce a clear improvement.

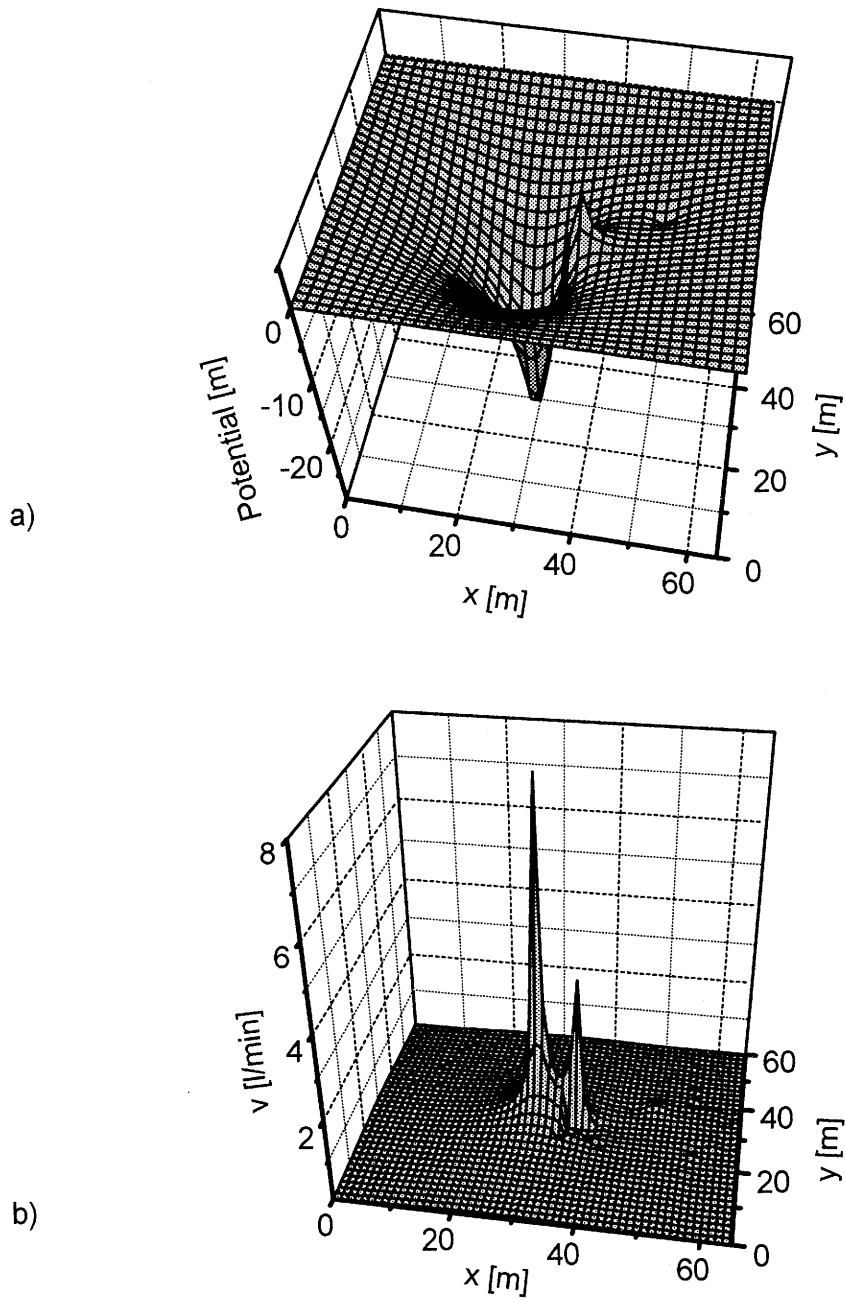


Figure 6.64: Hydraulic heads (a) and flow rates (b) as isosurfaces for a purely source-sink stream

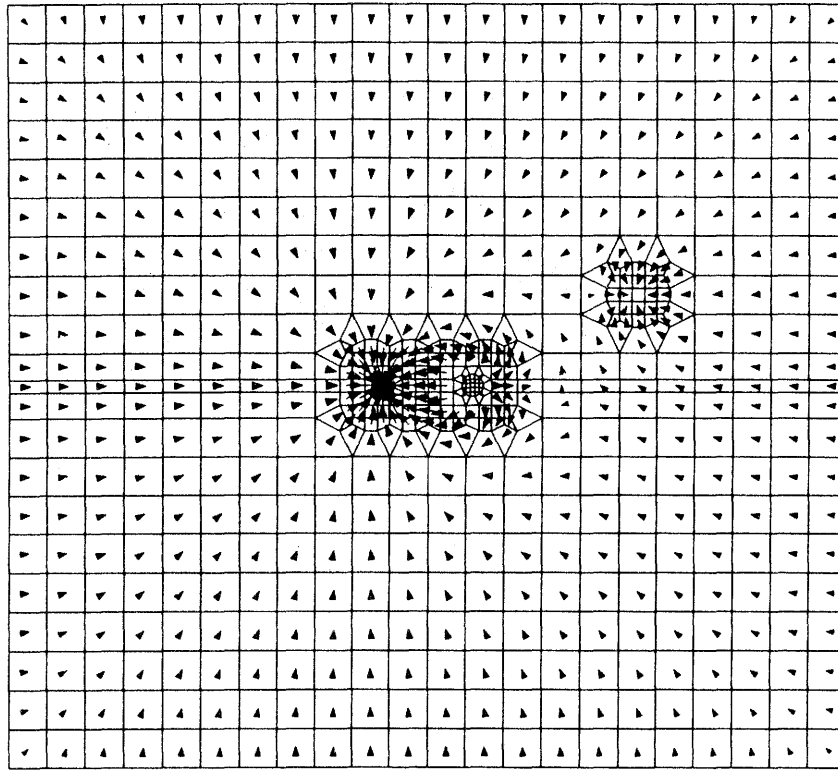


Figure 6.65: Flow field for a purely source-sink stream

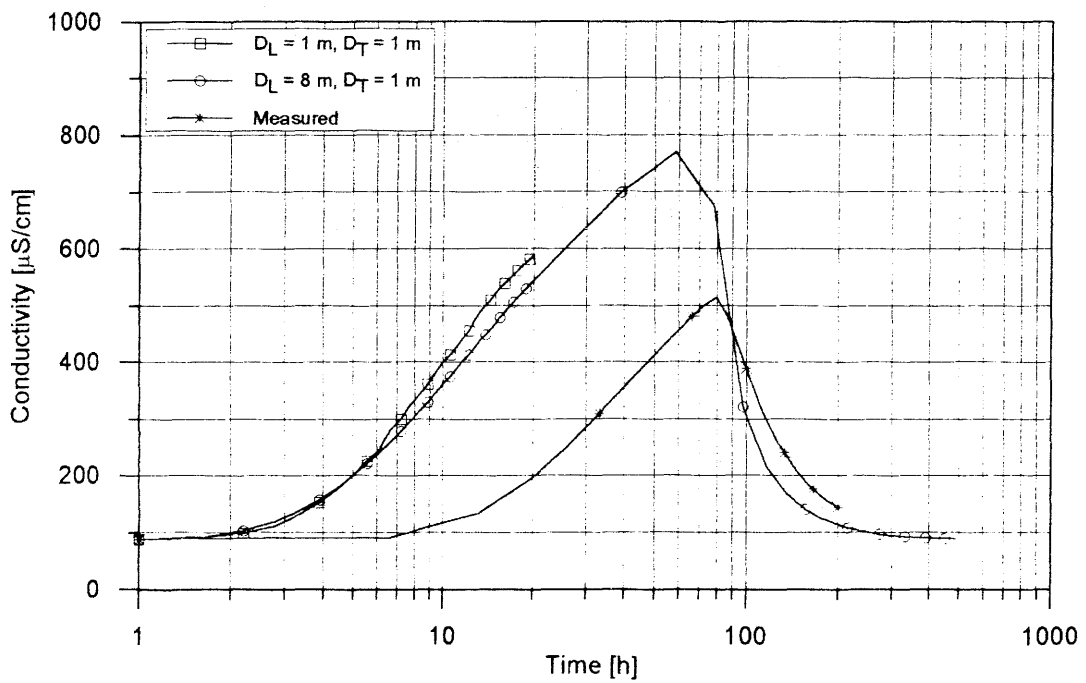


Figure 6.66: Comparison between modelled and measured breakthrough curve for salt tracer ($k_f = 2.5 \cdot 10^{-4}$ m/s, $2w = 50$ mm)

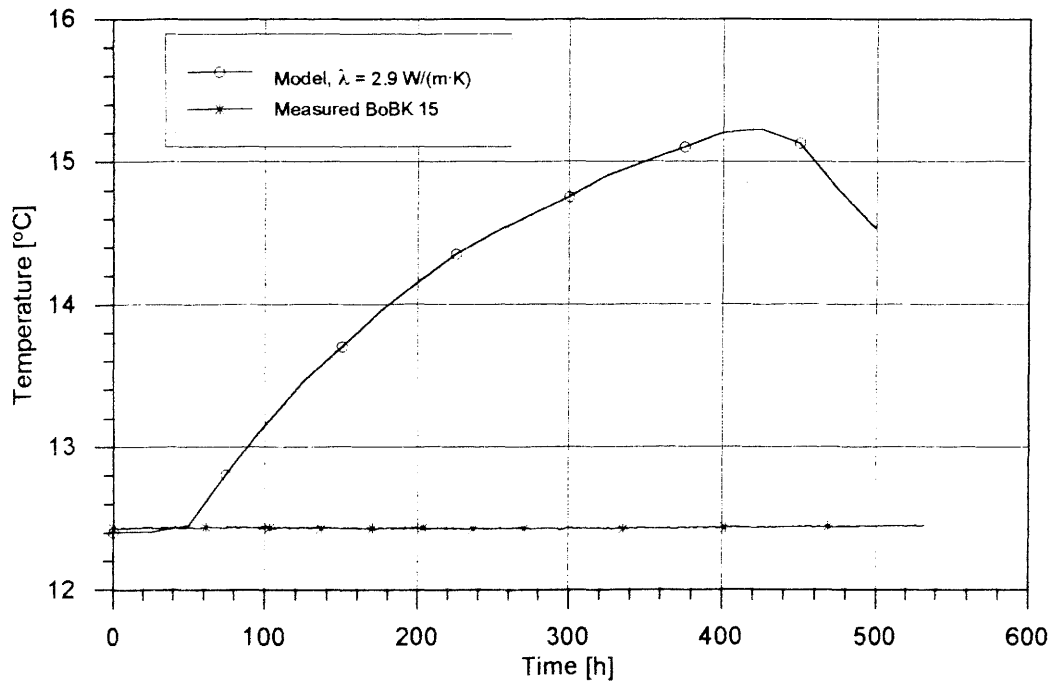


Figure 6.67: Comparison between modelled and measured breakthrough curve for temperature ($\lambda = 2.9 \text{ W}/(\text{m}\cdot\text{K})$)

Besides this, it is hardly possible to manipulate the temperature curve by varying the fracture aperture due to the existence of thermally relevant fracture apertures (see also Section 6.3.5.2). At the nodes representing borehole BoBK 16, no temperature reaction was observed and the salt tracer did not reach the leakage site. This last fact becomes plausible when the flow directions (Fig. 6.65) are taken into consideration. The result is that additional effects must be applied to fit the breakthrough curves for salt and temperature using the same model.

b) Source-sink stream with impermeable barrier

In this model, several hydraulically conductive elements between source and sink were considered impermeable, so that the water is forced to flow around this "barrier". The extent of the barrier was set so that the water would have to traverse a distance of about 12 m instead of 7.4 m. The path length 12 m was selected because the analytical model showed that, at a mean injection-extraction rate of 2.18 l/min, the measured thermal breakthrough time would be reproduced assuming this source-sink distance. Figure 6.68 shows the hydraulic heads and flow velocities and Figure 6.69 the corresponding flow field. The elements with no arrows in Figure 6.69 represent the impermeable barrier. Compared to the flow field without a barrier (Fig. 6.65), the streamlines are rendered much wider. There is also a clear current flow in the direction of the leakage site, which was not the case previously.

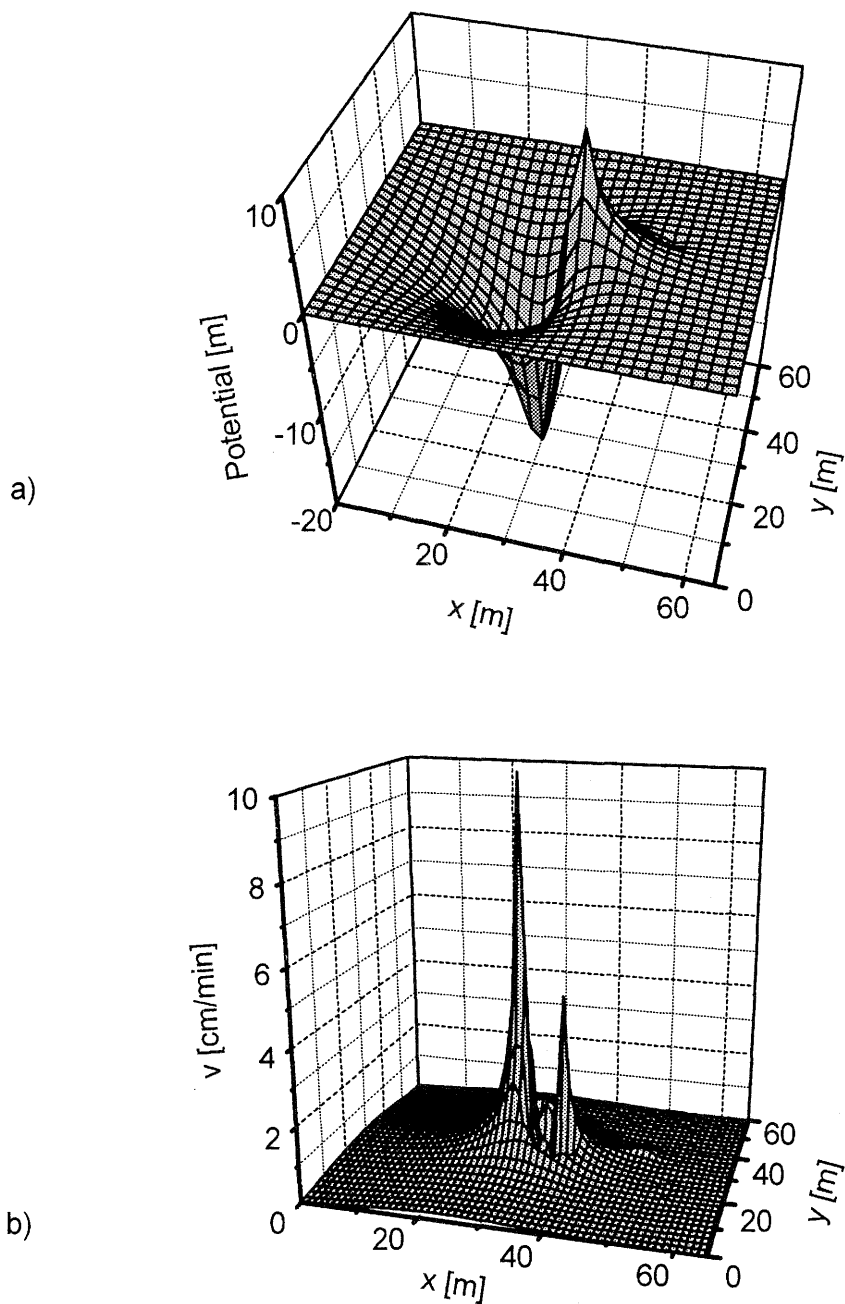


Figure 6.68: Hydraulic heads (a) and flow velocities (b) as isosurfaces in the presence of an impermeable barrier ($k_f = 1.5 \cdot 10^{-4}$ m/s, $2w = 10$ mm)

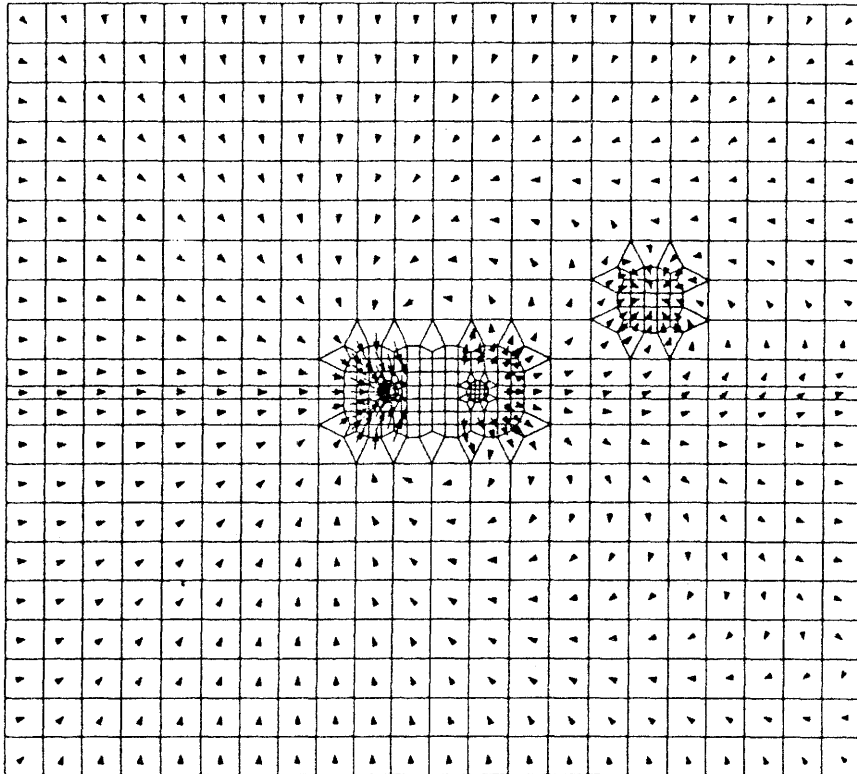


Figure 6.69: Flow field with impermeable barrier between source and sink

The corresponding transport simulation fittings were already useful. The salt tracer model (Fig. 6.70) estimated the breakthrough time and the peak arrival time quite well. The maximum and flank steepness are still somewhat too great. The thermal breakthrough time (Fig. 6.71) is also matched well by this model. A slight change in thermal conductivity optimises the fitting in this case. Figure 6.72 shows a temperature reaction at borehole BoBK 16 in the model that correlates with the measured values quite well. Figure 6.73 provides a summary view of the propagation of temperature in time, i.e. the distribution of temperature after 50, 150 and 500 h. The effect of the barrier forcing water, and thus temperature, to take a longer route to the sink is clearly seen.

It is also worthy of note that a fracture aperture of 10 mm is sufficient for this model. This value is at the upper limit of the fracture apertures found in the geological fracture survey. It remains questionable whether the entire distance between source and sink can be described by this still rather large fracture aperture figure, i.e. whether other factors might play a role as well.

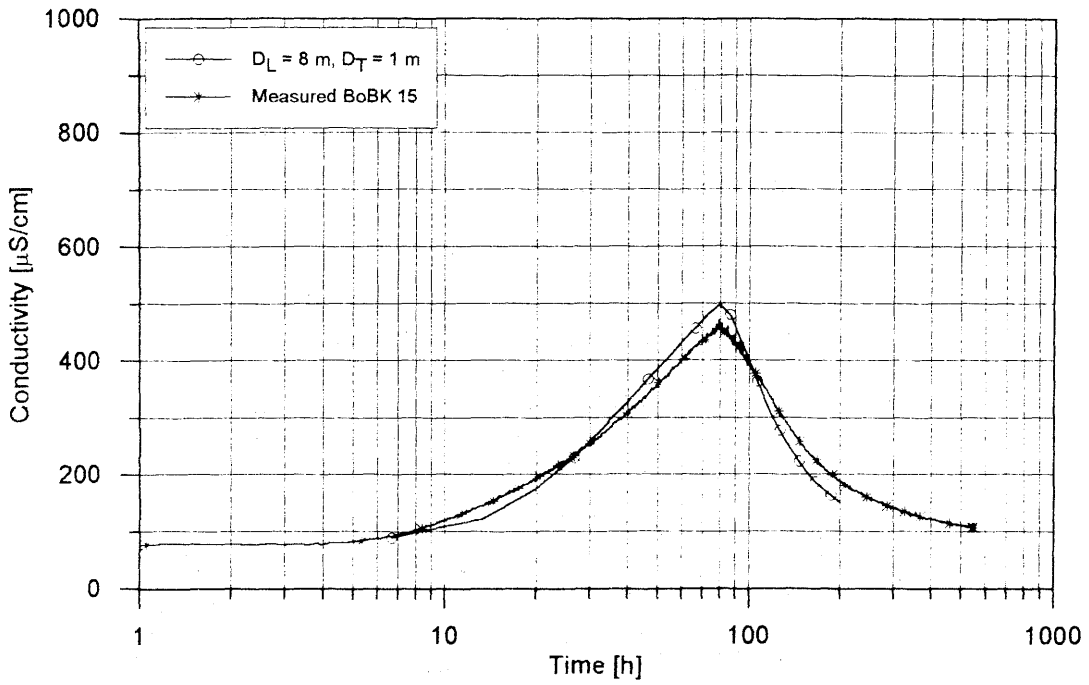


Figure 6.70: Comparison between modelled and measured breakthrough curve for salt tracer ($D_L = 8\text{m}$, $D_T = 1\text{m}$) for borehole BoBK 15

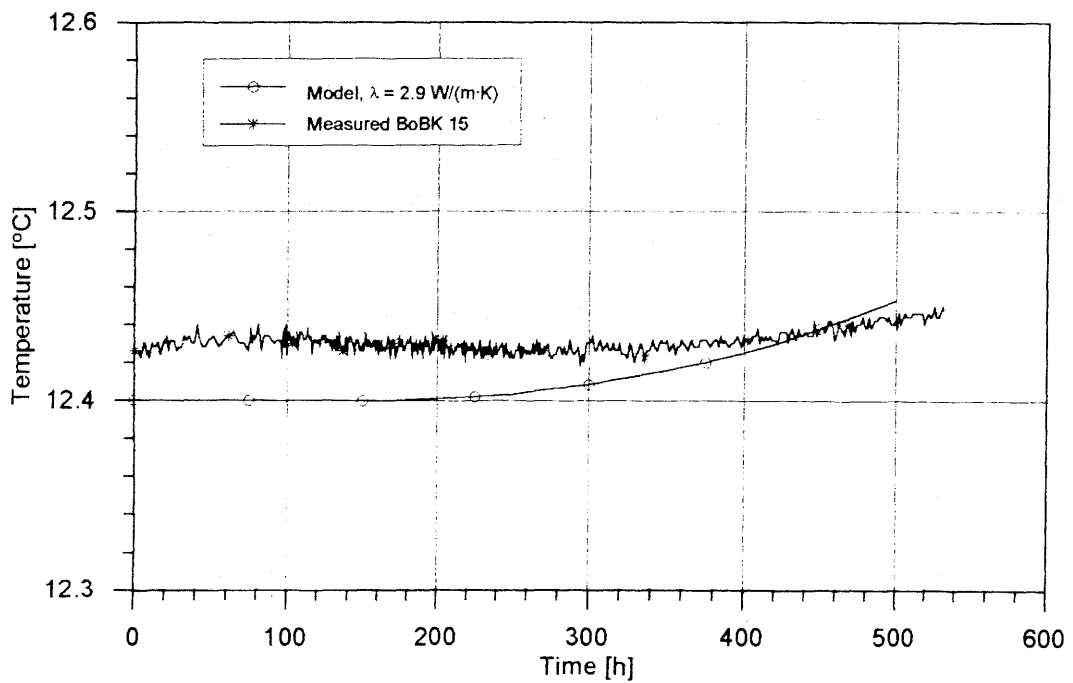


Figure 6.71: Comparison between modelled and measured breakthrough curve for temperature ($\lambda = 2.9\text{ W/(m}\cdot\text{K)}$) for borehole BoBK 15

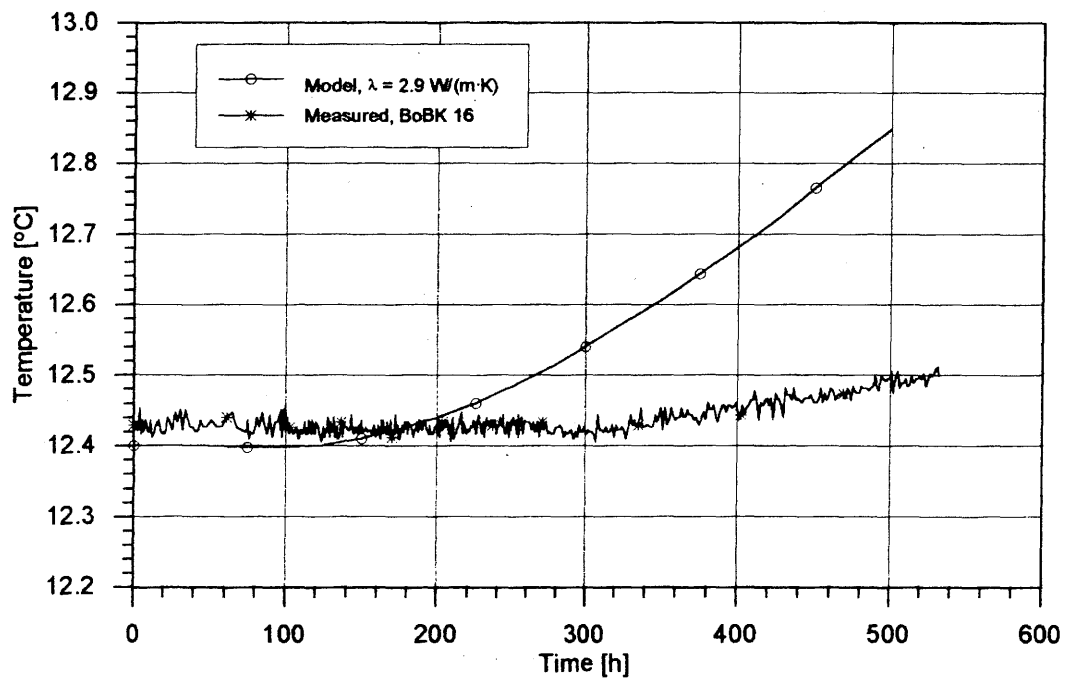


Figure 6.72: Comparison between modelled and measured temperature curve for borehole BoBK 16

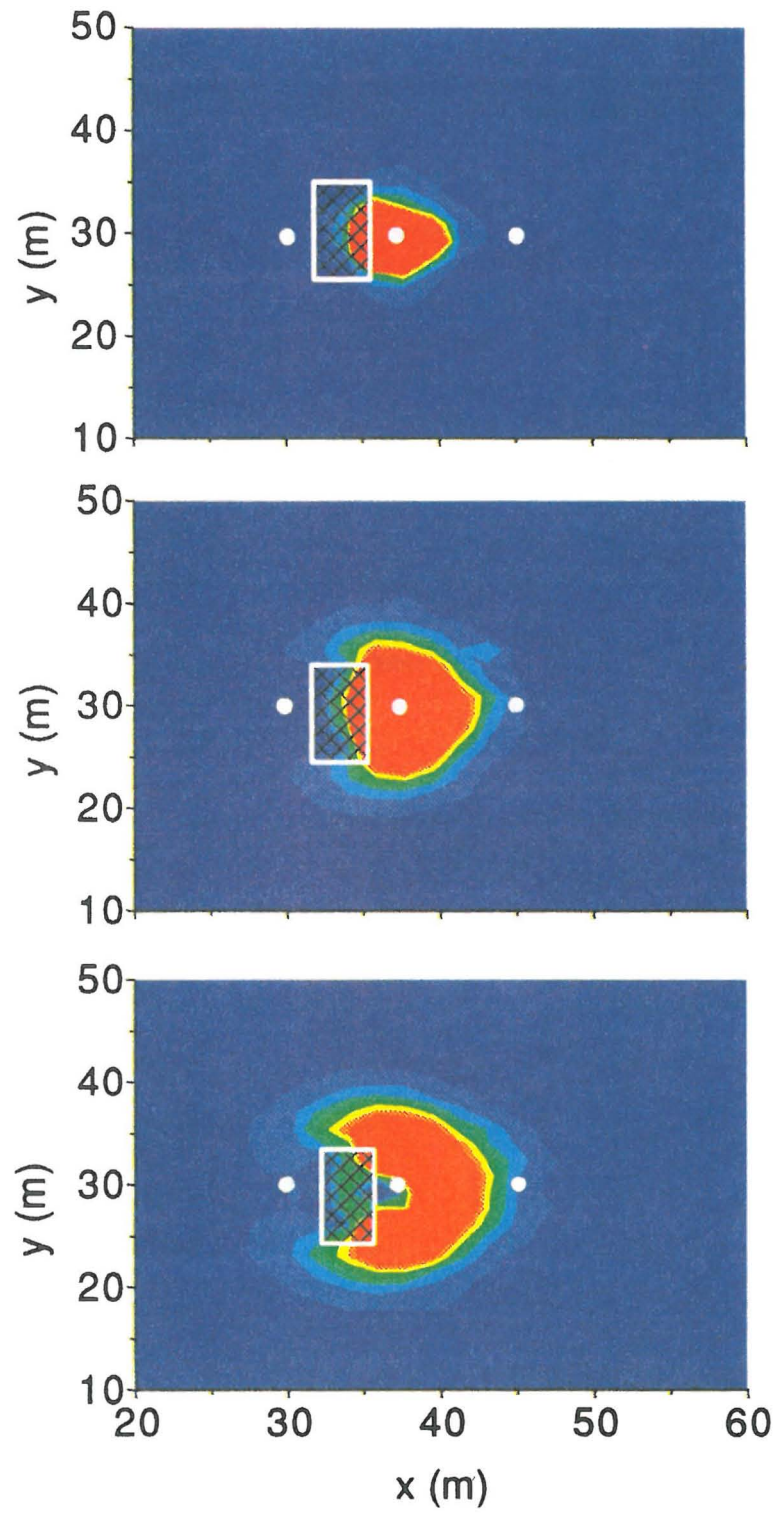


Figure 6.73: Temperature distribution at three different times (a = 50 h, b = 150 h, c = 500 h)

c) Source-sink stream with natural countercurrent

This model is used to investigate the extent to which the existing natural groundwater flow influences the artificially generated flow field - and whether this is the explanation for the long breakthrough times.

Previous flow tests demonstrated that a flow rate of approx. 2 l/min is established in the central BK area on a long-term basis, and then remains constant. This means the groundwater flow rate would be of the same order of magnitude as the injection rate, making a noticeable influence conceivable. A further preliminary test (VE 518) supplied indications of a possible countercurrent to the source-sink flow direction. For this test, borehole BoBK 15 was opened for one day. During this free flow period, a temperature increase of 0.03 K was registered by the temperature sensor installed at fracture level. Since temperature generally increases with depth, this supports the assumption that, in this test, mostly water from deeper regions in the fracture was drawn up. This would mean that the groundwater flow could be counter to the source-sink stream. In addition to this, in view of the general increase in pressure with increasing depth due to the steep incidence of the fracture (Fig. 6.61), a hydraulic gradient from the bottom to the top edge of the fracture is certainly to be assumed.

To model such a countercurrent, we began by shutting in the source and leakage and raising the hydraulic gradient, i.e. the boundary conditions of the model, until a flow rate of 2 l/min had been established at the nodes in borehole BoBK 15. The fracture aperture and k_f value were taken from the barrier model. A hydraulic gradient of 24 m from the bottom to the top edge was necessary to generate a flow of 2 l/min at the sink. The hydraulic heads and flow velocities shown in Figure 6.74 were derived from the boundary conditions determined in this way. Consideration of the flow field, shown in Figure 6.75, shows clearly that water flows to borehole BoBK 16 and the leakage site just as in the barrier model.

The transport model did not, however, produce the hoped-for results. The calculated breakthrough curve of the salt tracer developed a completely different shape to the measured curve (Fig. 6.76). The breakthrough time did increase, but not to the same extent as the measured values did. The curve also did not develop a pronounced peak, but rather gradually approached a saturation value, then fell off precipitously when salt injection ceased. The amount of tracer still in the rock following completion of injection, e.g. due to dispersion, is flushed away by the countercurrent, leading to this sharp drop. Models using other dispersion lengths and fracture apertures did not result in essential changes in the curve shape. Modelling of heat transport (Fig. 6.77) also produced a breakthrough time that was too short, in spite of the countercurrent. The temperature reaction in borehole BoBK 16 (Fig. 6.78) is much too strong, i.e. too much heat is being transported in this direction. This countercurrent model is not capable of explaining the measured values.

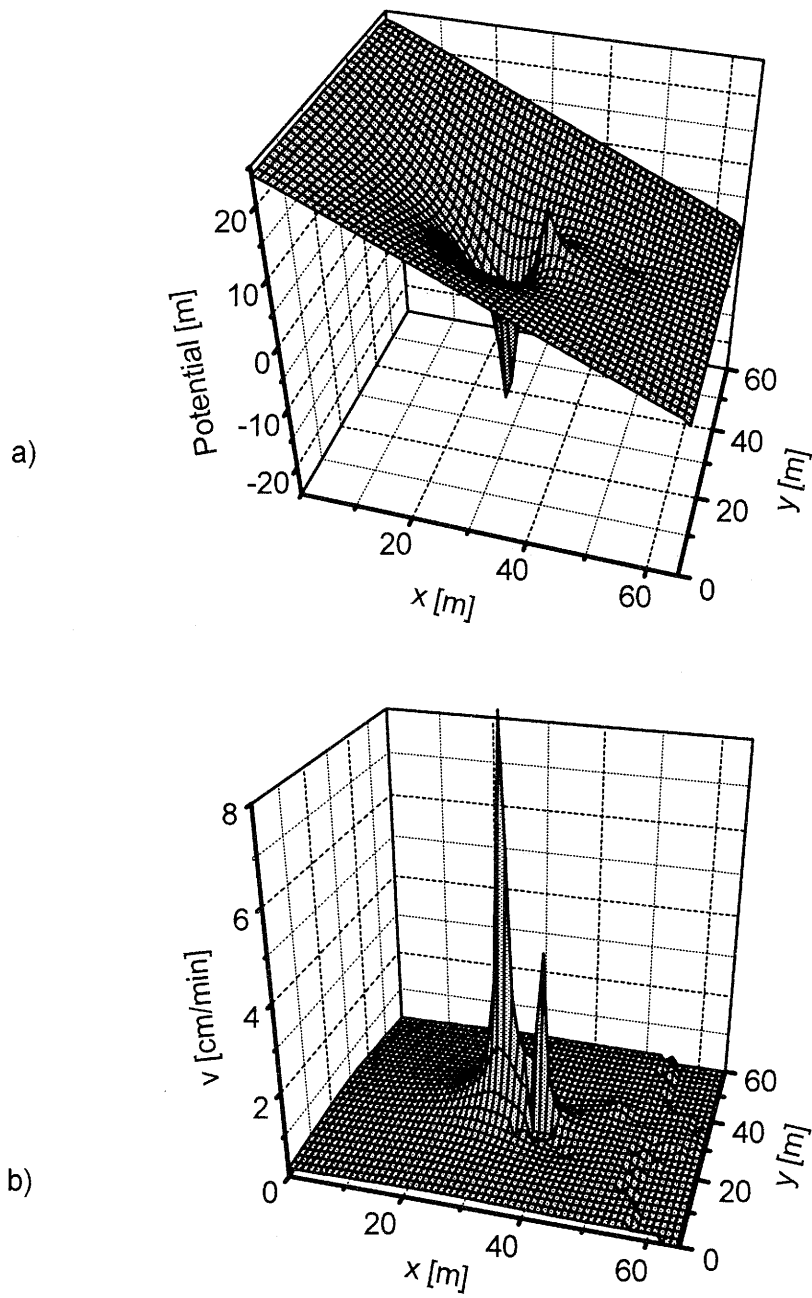


Figure 6.74: Hydraulic heads (a) and flow velocities (b) in the presence of a countercurrent ($k_f = 0.9 \cdot 10^{-4}$ m/s, $2w = 10$ mm)

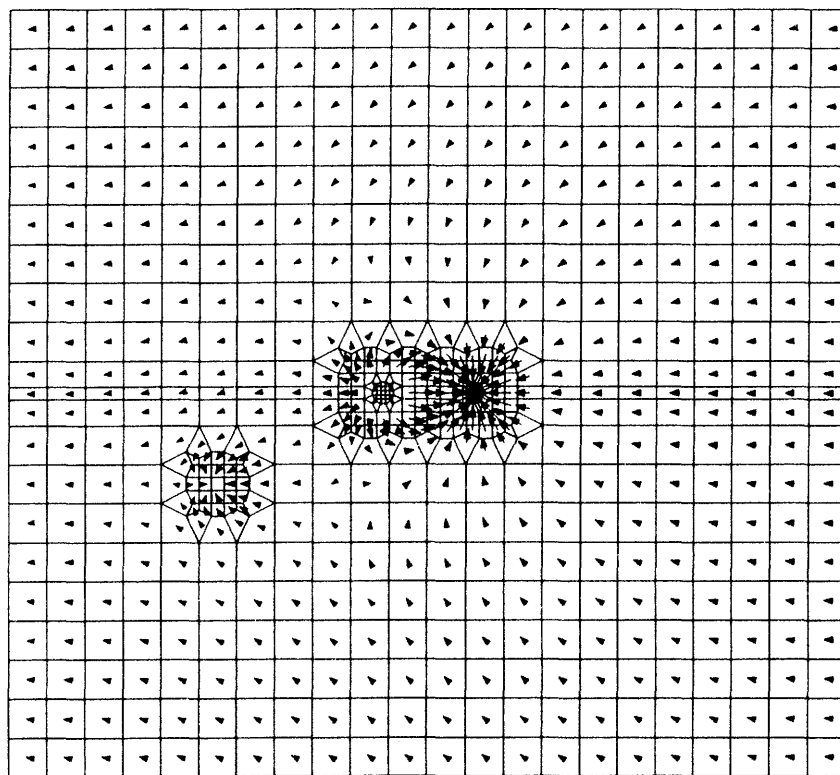


Figure 6.75: Flow field in the presence of a natural countercurrent

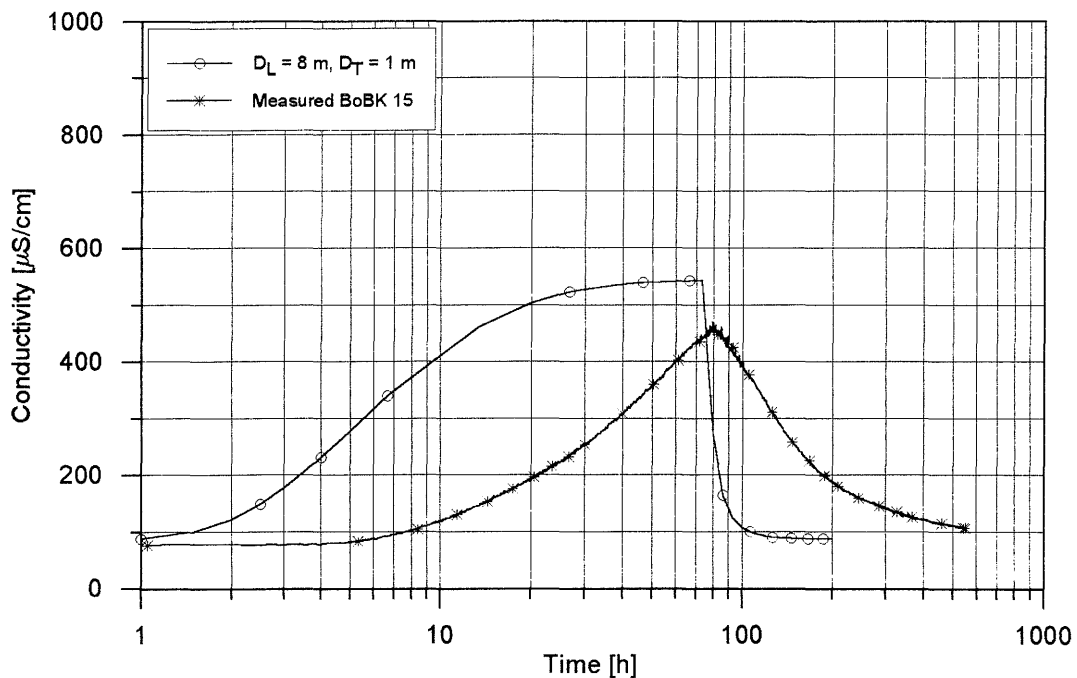


Figure 6.76: Comparison between modelled and measured breakthrough curve for salt tracer for borehole BoBK 15 in the presence of a countercurrent ($D_L = 8\text{ m}, D_T = 1\text{ m}$)

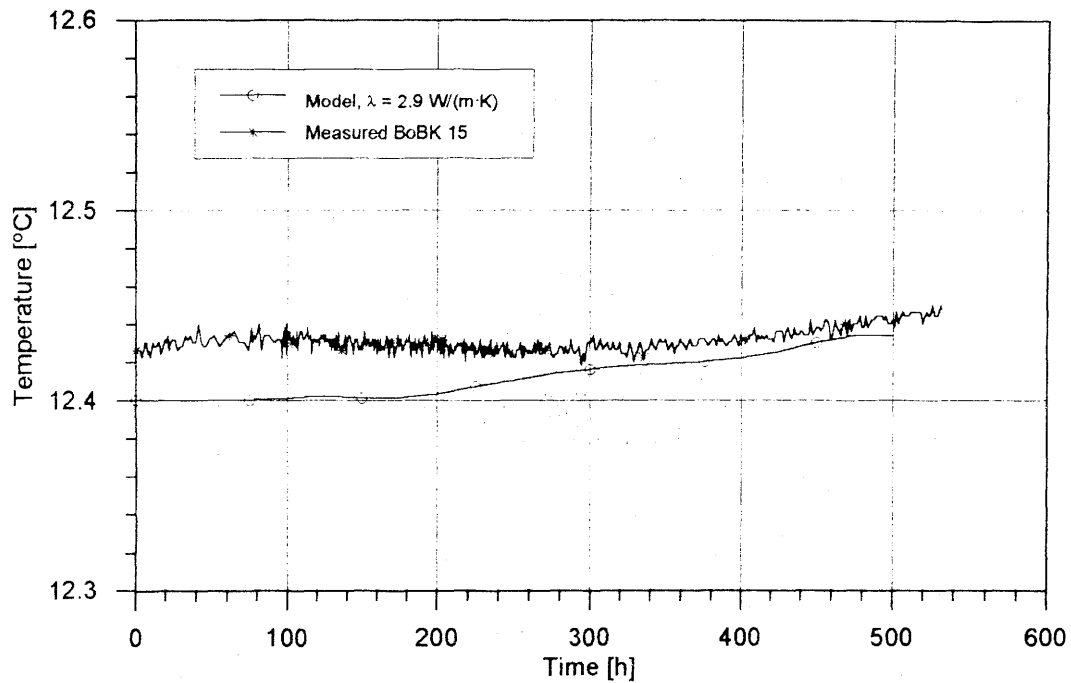


Figure 6.77: Comparison between modelled and measured thermal breakthrough curve ($\lambda = 2.9 \text{ W}/(\text{m}\cdot\text{K})$) for borehole BoBK 15 in the presence of a countercurrent

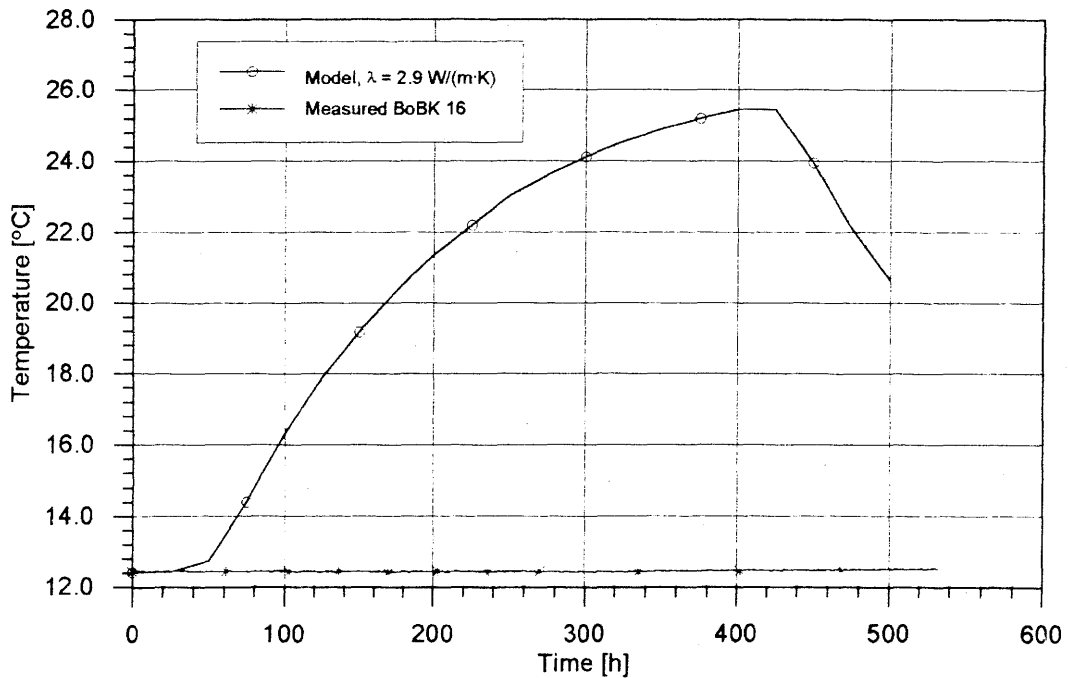


Figure 6.78: Comparison between modelled and measured thermal breakthrough curve ($\lambda = 2.9 \text{ W}/(\text{m}\cdot\text{K})$) for borehole BoBK 16 in the presence of a countercurrent

Temperature reaction in BoBK 9

To check whether the measured temperature increases in the two middle intervals of borehole BoBK 9 (see Section 6.3.3) are due to purely conductive heat transport via the matrix, the 2D hydraulically conductive elements were replaced by impermeable matrix elements with uniform thermal conductivity λ . λ was estimated (upper limit) at 3.5 W/(m·K). The distance between boreholes BoBK 5 and BoBK 9 is 5.0 m. Figure 6.79 shows the modelled breakthrough curve in a comparison with the measured values. The model curve indicates a temperature increase of only 0.03 K, whereas the measured values increased by 0.2/0.3 K. This means that, if the temperature reactions in borehole BoBK 9 are assumed to be based on purely conductive transport, they should be weaker by one order of magnitude. Bearing in mind that the maximum estimate is being made on the basis of a 2D model only - spatial heat dissipation not being considered - it can safely be assumed that the increase cannot have come about on a purely conductive basis.

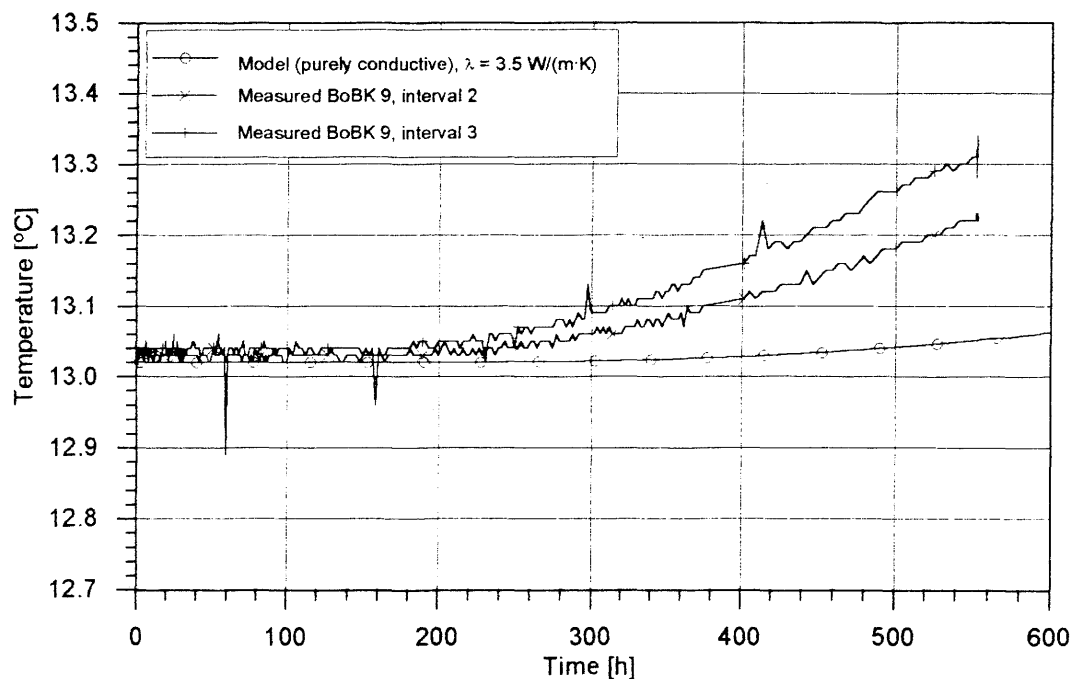


Figure 6.79: 2D, purely conductively modelled thermal breakthrough curve and measured temperatures in borehole BoBK 9 ($\lambda = 3.5$ W/(m·K)) in the presence of a countercurrent

6.3.6.3 Discussion of Results

A fitting to the measured curves proved impossible using plausible parameters in the model for the purely source-sink stream. Transport takes place for the most part between source and sink. The salt does not reach the leakage site, in accordance with the course of the streamlines, and no temperature increase is recorded in borehole BoBK 16. This confirms the results of the analytical model, which allows the assumption that the measured values, above all the long breakthrough times, cannot be explained on the basis of a purely source-sink stream. The introduction of a natural countercurrent, which is to be assumed on the basis of several pieces of evidence, lengthened the breakthrough times somewhat and brought the maximum into the same order of magnitude as the measured values, but it deformed the curve shape so severely that fitting to the measured curves was impossible. Among the main factors that made this model seem unrealistic were the sharp drop in the model curve when salt injection was stopped and the excessive temperature increase at borehole BoBK 16.

Only the barrier model, in which the water is forced to flow via a detour and cannot follow the direct route, provided a useful fitting. The breakthrough times and the peak arrival time of the salt tracer curve were both matched well. The flank steepness was, however, still a bit too extreme. Two explanations can be offered for this:

One possibility is that the concentration is increased too much at the edges of the barrier, leading to a slight channelling effect and thus to a steeper buildup and drop in concentration at the sink. This could be prevented by not using a barrier to lengthen the flow pathway, but instead, for example, two or more fractures that meet at a certain angle to produce a flow pathway of 12 m. Then the water could flow over into the next fracture along the entire width of the intersection and over-concentration would no longer occur.

The second possibility is to consider the flow field as nonsteady. A mean injection and extraction rate was used for the steady computations up till now. In fact, however, the flow rates slowly fall throughout the test. This decrease over time of the flow rates would reduce the ascent and descent of the breakthrough curve, and this effect would increase with passing time. This could conceivably improve the fitting of the model curve to the measured one.

7. Desk Study

7.1 Objectives of the Desk Study

The objective of the desk study is to summarise and compare evaluations of the GTS test projects

- in-situ tests carried out
- laboratory tests carried out
- results of the tests
- numerical methods and models

relevant to general aspects of hydraulic substance transport, since these phenomena play a central role in evaluation of a repository site. On the basis of the work done in the BK area, borehole tests and their results and theoretical simulations will receive the most attention. The projects fracture system flow test (BK), ventilation test (VE) and migration test (MI) will be points of concentration. Further projects such as the "Fracture Zone Investigation (FRI)" and "Hydraulic Modelling (MOD)" are being evaluated to see whether they are able to furnish answers to the above-mentioned problems and other matters of importance.

7.2 Various Projects at the Grimsel Test Site and their Objectives

Within the framework of the German-Swiss cooperation (Nagra, BGR and GSF) research work is being done on the following properties of crystalline rock formations, based on the example of the Aare granite:

- geological
- hydrogeological
- rock mechanical
- geophysical
- geochemical.

The objectives of setting up the Test Site were (NAGRA 1988):

- Analysis of foreign test results
- Realisation of own investigations
- Gaining know-how
- Development and testing of new measurement techniques.

In addition to projects within the framework of the German-Swiss cooperation, Nagra has carried out, and will continue to carry out, several projects involving cooperation with other foreign partners. All of the projects are intended to contribute to safety analysis relative to a potential repository site for radioactive wastes and to answering the following questions:

- What mechanisms influence the transport of radioactively contaminated liquids and gases in granite?
- What in-situ investigations and equipment are required to measure the relevant parameters?
- Do numerical models exist which are capable of simulating the physical processes measured in situ?

The projects carried out to date at the GTS are divided into four categories depending on the type of technique applied or material sampled:

Category A: Groundwater transport in rock

Fracture System Flow Test BK
Ventilation Test VE
Migration MI
Fracture Zone Investigation FRI

The projects in category A involve in-situ hydraulic tests. The objective is to describe the transport processes of water, and of substances dissolved in water, in rock.

The fracture system flow test attempts to characterise the hydraulic properties of fractures, while the ventilation test concentrates on the hydraulic properties of the compact rock matrix. The main emphasis of the migration test is the interaction between radionuclides and rock. The fracture zone investigation was concerned with the relation between seismic and hydrological parameters.

Category B: Hydraulic parameters and modelling

Hydraulic Potential Field HP
Hydraulic Parameters HPA
Hydrodynamic Modelling MOD
Near-Field Hydraulics NFH

In these projects, borehole hydraulics testing methods were developed and parameters defined for the groundwater model MOD. The verification of local MOD models was done in the test tunnels of the category A projects.

Category C: Tomographic investigations

Electromagnetic HF Measurements EM
Radar Reflection RR
Underground Radar UR
Underground Seismics US
Prediction Ahead of Tunnel Face SVP

Applicability of radar measurement techniques in granite was tested. Methods and equipment were developed for routine application of seismic methods in crystalline.

Category D: Rock mechanics**Rock Stresses GS****Excavation Effects AU****Heater Test WT****Tilt Meters NM**

Granite rock and its mechanical properties were the focus of these already concluded projects. Descriptions of granite, in particular geological fracture surveys and fracture statistics, were also performed in other projects. Geological mapping of the BK tunnel at the beginning of the fracture system flow test should be mentioned here.

7.3 In-situ Hydraulic Tests at the GTS

The first phase of research activities at the GTS within the framework of the German-Swiss cooperation included preparation for setting up the GTS (exploratory boreholes 1980, detailed facility planning, construction work on GTS) and execution of the first 12 investigative projects by 1987. In the second phase (1988-1990) the projects shared by Nagra, GSF and BGR were continued. Nagra also cooperated in projects with institutions from the US, Japan and France and carried out project work on its own. In the third phase, which was completed at the end of 1993, the main emphasis was on the three major projects ventilation, migration and fracture system flow test.

The GTS projects are guided by the principle of development of methods and systems that facilitate evaluation of the barrier qualities and effects of granite in terms of potential disposal of radioactive wastes. For this reason, development of methodological techniques is of prime importance. Thus the planning of in-situ tests is tightly bound up with development of measurement and testing techniques used to determine the relevant geological, hydraulic and chemical characteristics of the rock formation. In this field, the greatest development since numerical models has been due to advances in microelectronics and improved computer control of measurement and applications technology.

7.3.1 Testing Technology

The tests carried out in the category A projects were:

Fracture system flow test (BK):

- Fluid logging tests
- Pressure buildup and decay tests
- Injection and extraction tests
- Tracer tests with conservative tracers (salt)
- Tracer tests with non-conservative tracers (heat)

Ventilation (VE):

- Ventilation phases at constant temperature and testing of chamber air moisture content
- Measurement of water content and water potential in unsaturated granite
- Evaporation measurements

Migration (MI):

- Pressure decay tests
- Tracer dilution tests
- Tracer tests with sorbing tracers
- Tracer tests with non-sorbing tracers
- Analogue studies of uranium migration along tunnel wall
- Vacuum test along tunnel wall
- Miniventilation test along tunnel wall

7.3.2 Measurement Technology

Description of the measurement technology used in the category A projects:

Fracture system flow test (BK):

- Development of measuring tubes, probes and packers for use at high pressures (O-ring connections)
- Development of multifunctional probes, multiple-probe packer systems, including the possibility of activating and deactivating individual packers installed in a system
- Improvement in measuring technique employing A/D transformation in boreholes and controlled datalogging above-ground.

Ventilation (VE):

- TDR probes (water content)
- CAMI-TDR technology (water front movement)
- Thermocouple-psychrometer (water potential)
- Evaporation measurement via remote data transmission
- Infrared probe for measurement of temperature distribution along tunnel wall
- Pressure buildup and temperature measurement in parallel boreholes.

Migration (MI):

- Development of measurement chambers for vacuum test and miniventilation
- Laboratory equipment for exact determination of tracer concentrations in injection and extraction boreholes.

7.3.3 Methods of Hydraulic Test Interpretation

Standard methods of hydraulic test evaluation were applied in all projects as follows:

Table 7.1: Methods of hydraulic test evaluation

Test	Parameters	Parametric formulae	Method
Constant head	Injection rate as a function of time at constant injection pressure	$T = \frac{2.3}{4\pi} \cdot \frac{1}{s_w \beta'}$	JACOB & LOHMANN (1952)
Constant flow	Injection pressure as a function of time at constant injection rate	$T = \frac{2.3}{4\pi} \cdot \frac{Q}{\beta}$ $S = 2.25 \cdot T \cdot \frac{t_0}{r^2}$	COOPER & JACOB (1946)
Recovery	Pressure as a function of time following conclusion of constant head or constant flow tests	$T = \frac{2.3}{4\pi} \cdot \frac{Q}{M}$	HORNER (1951)
Steady State	Pressure and flow rate in steady state	$T = \frac{2.3}{4\pi} \cdot \frac{Q}{s_w} \cdot \log \frac{R}{r}$	LOHMANN (1972)

Key to symbols in Table 7.1:

- T [m²/s] = Transmissivity
 S [-] = Storage coefficient
 Q [m³/s] = Flow rate
 R [m] = Radius of influence
 r [m] = Borehole radius for single borehole tests
 = Distance between test borehole and observation borehole in dipol tests

s_w [m]	= Drawdown
M [m]	= Incidence of tangents to curve $s_w = f(\log(t_D))$
t_D [-]	= Normalised time $(t_c + \Delta t)/\Delta t$ (see 5.1)
t_c [s]	= Injection or extraction time (production time)
Δt [s]	= Time following end of injection or extraction (shut-in time)
t_o [s]	= Time at which the balancing straight line intercepts the x-axis (interception time)
β' [s/m ²]	= Incidence of tangents to curve $s_w/Q = f(\log(t_c/r^2))$
β [m]	= Incidence of tangents to curve $s_w = f(\log(t_c))$

It is assumed that flow to the observation borehole is radial and that the medium is homogeneous, porous and infinite in extent. This supposition is at best only approximated in the fractured granite in the Grimsel area. There follows an example of comparison of calculated transmissivities obtained from different methods in the migration area (HOEHN et al. 1990): Two boreholes, BoMI 86.004 and BoMI 87.009 were tested using all the methods in Table 7.1. It was seen that evaluation of the constant head tests provided the most stable data. The corresponding steady-state tests in most cases provided higher values and the recovery tests lower values.

7.4 Numerical Models for Simulation of Hydraulic Tests

In all three major projects (BK, VE, MI) at the GTS, numerical models were developed independently for the special requirements of the processes to be simulated in each case and verified in in-situ tests. Numerical methods were also developed in the now concluded fracture zone investigation (FRI). In these projects, in-situ hydraulic tests and their numerical simulation are of major interest. In the MOD project, development of a numerical model was the main objective. The natural data required to verify the model were provided, and are still being provided, by the other projects.

7.4.1 Fracture System Flow Test: DURST/ROCKFLOW

The program DURST, which was modified and further developed in the course of the fracture system flow test (commercially available under the name ROCKFLOW), is described in detail by PAHL et al. (1992). Section 4.2 describes in detail the work done during the reporting period. A detailed description is therefore unnecessary here.

The main advantages of the program system are its modular structure including flow and transport models and various pre-processors and post-processors (graphics module, network generator). The finite element modelling feature allows for computation in 1D, 2D and 3D models with any number of formed model elements, to simulate for example the fracture zones in an otherwise compact rock matrix. Various model elements can be made to meet at the nodes. Computation can be carried out on the basis of non-steady states. An apparently unlimited number of model variants require, however, a sensitive response to the spatial geometric situation and a model-

related concept of the course of physical events in nature. The computing runs simulating tracer test VE 298 (LEGE & ZIELKE 1993) show the abstractions required in the borehole area to obtain reasonable orders of magnitude for calculated flow velocities.

7.4.2 Ventilation

Model computations in this project are being carried out by the GSF together with the Institute for Deep Hole Technology and Mining of Petroleum and Natural Gas at the University of Clausthal and Golder Associates, Celle. The computing program ECLIPSE/ECL (KULL et al. 1989) is being used. "The simulation model must, first of all, test whether the amount of water outflow measured for a given fracture system with replenishment can come solely from the surrounding granite massif or if the water inflow requires the explanation that the fracture system outcrops above-ground" (BREWITZ et al. 1988).

The rock is simulated as a dual porosity medium with a fracture continuum (high permeability, low storage capacity) surrounded by a matrix continuum (low permeability, high storage capacity). In accordance with the defined objective, the model was dimensioned so that the water inflow into the tunnel could come from above-ground or from the rock matrix as an intermediate storage medium. The discretion is much finer in the near-tunnel area than near ground level, since the flow area to be modelled is a fracture system surrounding the tunnel, the water inflow from which into the tunnel is measured. This also facilitates comparison of the pressures in the boreholes running parallel to the tunnel with the model values.

The rock parameters (porosity, permeability (or hydraulic conductivity)) as determined in laboratory tests are prescribed in the simulation computations. The permeability of the fracture zone is introduced into the model computations as an unknown. In sensitivity analyses, the thickness and length of the fracture were varied as well. "Results to date tend to confirm the assumption that the fracture system is fed only from the granite massif and has no direct contact with the surface" (BREWITZ et al. 1988).

7.4.3 Migration

The programs used in this project were developed to provide an understanding of the physical phenomena of migration as observed in the experiments and to develop the ability to make predictions relevant to planned tests.

Acc. to HERZOG (1991), the migration model comprises the following components:

- Hydraulic model
- Fracture model
- Transport model

FRICK et al. (1992) provide a summary of hydraulic models and their uses. According to these authors, hydraulic models are used to

- determine borehole locations during a drilling campaign
- interpret in-situ tests
- determine input data for transport models (flow pathways and stream flow velocities)
- and contribute to tracer breakthrough tests.

The following models were used:

- PSI steady-state model (HERZOG 1989)
- LBL model (DAVEY et al. 1990)
- NAMMU code (WYSS 1990) and a
- 2D model (WYSS 1990).

In the PSI steady-state model, a coupled local and regional model with varying network densities are used. The fracture zone in the migration tunnel is considered as a two-dimensional, isotropic, heterogeneous, porous medium. The transmissivities are between $1.5 \cdot 10^{-6}$ and $1 \cdot 10^{-8}$ [m²/s].

In the LBL model, the aquifer is presented as a network of conductive elements (same hydraulic conductivity in all directions). The geological and geophysical field data are used to construct an initial basic model to simulate the water-bearing fractures and this model is then modified via inverse modelling, i.e. adding or taking away of so-called conductive elements, until optimum agreement is achieved in comparisons of model and natural values.

The model was tested under steady flow conditions. Since the measured data in the area of lower hydraulic conductivity between the two boreholes were not easily simulated, work was begun on expanding the model to include variable permeabilities as well (FRICK et al. 1992).

The NAMMU code (source: United Kingdom Atomic Energy Authority) was used to produce type curves of tests based on constant flow. Since the model calculated steady flow conditions, and the field conditions were found to be transient, the approach with a homogeneous continuum modelled with 2D elements was of no use.

WYSS (1990) described the development of a further 2D model with the familiar division into local and regional modelling. The poor correspondence between measurements and model met with in this case is ascribed to the high degree of heterogeneity in the fracture zone, which the model is unable to simulate properly.

7.4.4 Other Numerical Models

7.4.4.1 Rock Hydraulics

Within the framework of the MOD project, a groundwater model (finite element - FE) was developed for the Grimsel area (VOBORNY et al. 1991 and HUFSCHMIED & ADANK 1988). The name of the project is now used for the numerical model developed therein, even though other program modules are known under their own names (e.g. FEM301). The MOD program works with a hierarchically organised image of the rock formation in the form of a regional model (surface area approx. 30 km²), a local model (volume approx. 900-450-400 m³) and submodels embedded therein (individual test tunnel).

In the regional model, only the water-bearing main fracture system is modelled as 2D and 3D elements. The local model with its much smaller elements differentiates between shear zones (2D), lamprophyres (3D), artificial installations (3D) and boreholes.

Saturation is assumed at the open surface of the rock, i.e. that the terrain surface is also the groundwater level. The model edges are assumed to be impermeable. The program run consists of the three phases, namely pre-processing (provision of data material), computation (calculation) and post-processing. The result is a water potential for each node. Inflow and outflow are calculated for all nodes with a definitive water potential at the beginning of computation.

The regional model is calibrated on the basis of discharge measurements in three segments of the main GTS entrance tunnel. The local model uses boundary and initial conditions from the regional model and is calibrated using measurements from the BK, VE and MI projects. The problem in verifying the numerical model was determining the model elements and parameters (type and arrangement of elements, transmissivities, storage coefficients), so as to provide optimum agreement of model and natural data.

The main emphasis in the MOD project, besides greatest possible accuracy of the model data in relation to measured parameters, was on matters of method:

- Does a method exist that ensures a best discretisation of geometric structures (fractures, shear surfaces, boreholes)?
- How great need the detail be in the boundary and initial condition simulation?
- What levels are required, and possible, regarding calibration and validation of the model?

VOBORNY et al. (1991) arrive at the conclusion that the field observations and model values agree well using the MOD strategy for calibration and validation of the model.

7.4.4.2 Stress Propagation

PAHL et al. (1989) provide an example of stress propagation in rock using a finite element model developed for the purpose of checking in-situ measurements at the GTS and detecting any local disturbance zones.

The network used consists of 180 axially symmetric, isoparametric elements with a total of 646 nodes. The model was used to compute the temporal evolution of stresses and expansions during overcoring. The computations supported the measured detection of initial expansion processes followed by a contraction phase and subsequent renewed axial expansion of the pilot borehole.

7.4.4.3 Heat Propagation

A model for simulation of heat propagation in granite was developed within the framework of the WT project by the GSF. In a multi-stage heatup and cool-off test using two heater probes installed 2.20 m apart in boreholes, the temperature field surrounding the heater probes was monitored using a total of 127 thermometers. These measurements were converted for isoline imaging. The numerical model was designed as an axially symmetric FE model. Vertical convection in the borehole and rock matrix resulting from changing water density cannot be integrated using this model. SCHNEEFUSS et al. (1989) considered the accuracy of the results with this model sufficient with a view to the given limitations. The authors also mention that deviations between model and measurement may occur due to local structural disturbances and propose a systematic parametric study to facilitate selection of realistic thermal conductivities and thermal capacities.

7.5 Procedure for Development of a Repository in Granite

The procedure for evaluation of a potential repository in granite must address the central question of what mechanisms influence the transport of radioactively contaminated liquids and gases. Assuming leakage of radioactivity in the proposed repository, it must be possible, in accordance with recognised technical rules, to predict in which direction the radionuclides will move, what concentration they will retain thereby and whether they will enter the biosphere.

Numerical models will be employed to answer these questions. This presupposes that models exist that have been proved to integrate flow processes and transport of substances, heat and nuclides correctly.

The desk study has considered the question of whether the numerical models are capable of describing transport processes in fractured rock with sufficient accuracy. In all published cases, good agreement of model and measured values is obtainable within the areas of application under consideration. In some cases, numerical models

were also used successfully for trend exploration and were thus demonstrated to predict accurately.

As soon as the numerical models have reached maturity, it will become clear which geological, hydrological and geochemical parameters and boundary conditions are required, and at what level of density they are required. Then decisions can be made on which investigative methods should be applied in the proposed repository area to obtain the parametric data required by the numerical models. In principle, it is a question of technical and financial expenditure. It must also be considered to what extent destructive testing (e.g. boreholes) and non-destructive testing (e.g. seismic tests) should be used. Creation of new flow pathways by cutting into previously independent rock units so as to connect different fracture systems must be avoided. Figure 7.1 provides a rough schematic sketch of repository evaluation procedure.

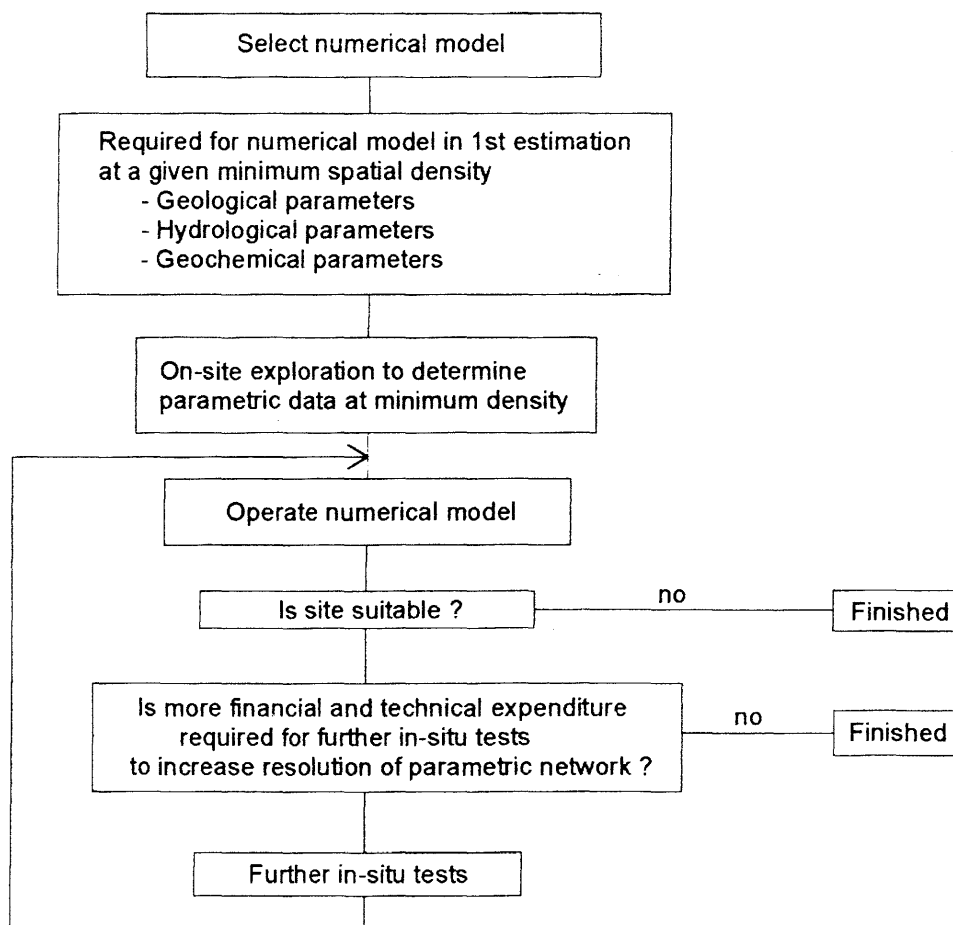


Figure 7.1: Repository evaluation procedure

8 Summary

8.1 Results of Phase III of the Fracture System Flow Test

Equipment developments for the flow test setup

The packer and probe systems proved dependable in tracer tests lasting several months with the exception of a few failures. Increased data acquisition equipment redundancy reduced data losses due to disturbances occurring during testing. The compressed air supply and packer distribution equipment was renewed and handling simplified. A pump aggregate for long-term injection was also purchased and tested.

The newly developed multipacker-multifunctional probe system was tested for the first time in water-saturated boreholes. The system consists of a bottom probe, several probe/packer combinations (injection probes) and a top packer with plug. The test intervals are connected to the injection line running through the probe segment via computer-controlled cutoff valves. All intervals can be opened and closed at will, facilitating a large number of injection and extraction procedures. The probe signals are digitised by the probe computer and transmitted to the acquisition equipment in the cavern without line losses or signal disturbance. The multipacker-multifunctional probe system is controlled by the MS-DOS program PC_MULI. The necessary data (test configuration, calibration data, channel occupancy) are entered in dialog mode by the operator and saved in files. The process status information and measured values are presented on-line on the screen. All special functions ("open interval", "shut in interval", "close packer") can be actuated during measurement from the menu.

Software development - program system DURST/ROCKFLOW

The modular program system DURST/ROCKFLOW was systematically expanded and tested on the basis of the requirements of the in-situ tests carried out. In the actual computation model, the transport module was expanded by addition of the feature of free selection of an initial boundary condition. This improves adaptation to complex structures of the area to be modelled. Preliminary tests have been carried out to estimate the influence of matrix diffusion and the existence of dominant flow pathways. The program system was expanded by addition of a new version of the gas model. Gas flow processes in a fracture network can be simulated using this partial program.

Multiphase flow processes

The simulation of multiphase flow processes with the numerical model DURST represents a new element in the BK work. Approximation of such processes in fractured porous media requires representation of the fluid phases in isolation and within the framework of their mutual influences dependent on the geological situation. Approaches taken from the literature were developed on a theoretical basis and integrated in a mathematical formulation reflecting, on the one hand, the relation between capillary pressure and saturation and, on the other hand, that between relative permeability and saturation for flow systems in fractures. The finite element program "GM2" is the result of this study.

Hydraulic tests in the BK area

The in-situ hydraulic tests in the BK area were once again the focus of work in Phase III of the fracture system flow test. The tests fell into two main groups: The tests on pressure-dependent hydraulic conductivity of the fractured rock were carried out in the peripheral area (BoBK 3 and BoUS 3) and did not indicate a significant degree of pressure-dependence of this parameter, although higher transmissivities had been expected under higher pressures and, thus, wider fracture apertures. Tracer tests (see below) and preliminary tests were carried out in the central BK cavern area. These included interference tests and fluid logging tests to detect inflow sites and any flow pathways. These tests served to determine material transport rates in fractured rock.

Tracer tests and their simulation

Developments in the tracer tests carried out went in the direction of longer-term tests over longer distances. The objective was simulation of flow and transport characteristics of such tests in numerical models. For this reason, it was very important that all boundary conditions, including the leakage sites and tracer concentrations there, be recorded with the greatest possible accuracy.

In tracer test VE 483, covering a distance of approx. 25 m, brine with 1,000 $\mu\text{S}/\text{cm}$ was injected for a period of 13 days. In tracer test VE 493, covering approx. 70 m, the flow pathway traversed three intersecting fracture systems. The tracer material used in this test was brine with a conductivity of 10,000 $\mu\text{S}/\text{cm}$, injected for 24 h.

Salt/heat tracer test VE 520 used two different tracer substances (conservative and non-conservative). The use of temperature was particularly successful, since its transport mechanism differs clearly from that of salt. Development of a consistent model that explains the measured curves obtained for both tracers requires precise analysis of the local situation and reduces the chances of fitting to the measured curve on the basis of non-physical parameters valid for one curve only.

Analytical modelling provided valuable information on the design of numerical models and selection of parameters. Numerical modelling based on a single fracture did lead to a plausible explanation for both transport processes, but left several questions unanswered that could be solved by means of specific tracer experiments employing variable test setups.

Integration of fracture networks and/or non-steady flow processes in the modelling procedure could lead to a broader understanding, above all in the form of phenomenological studies.

All three tests were rechecked by computation with the program system DURST/Rockflow in extensive simulation runs with systematic parameter variation. A mass balance was worked out for the tracer tests to verify the flow pathways in the rock.

The measuring and computation results show, as had been assumed previously, that active pathways certainly can be detected in a fracture system over greater distances. The spatial distribution of the tracer substances would, however, tend to indicate a hydraulic interconnection of fracture systems.

Desk study

Work on a desk study was begun in the second half of Phase III of the fracture system flow test. The study provides a summary and comparative evaluation of the in-situ experiments, the accompanying laboratory analyses, the knowledge gained thereby and the numerical methods and models used to simulate the in-situ studies carried out at the GTS. The study focuses on the three projects "fracture system flow test", "ventilation test" and "migration test" because of their relevance to the field of hydraulic substance transport.

8.2 Planned Future Investigations

Studies within the framework of the German-Swiss cooperation are to be continued in a future Phase IV at the Grimsel Test Site. Based on the work done in previous projects, which focused on detection of significant flow pathways and the flow velocities within them, including possibilities of numerical modelling, future studies will be concerned with large and small-scale transport mechanisms.

A tracer test with a flow distance of over 400 m is planned to address the question of large-scale substance transport. According to our present knowledge concerning the size and extent of the main fracture zones, this is the longest feasible flow distance for a tracer test in the BK area of the Grimsel Test Site.

On small-scale, tests are planned with the transport media water and gas and combinations of the two phases. Preliminary work in this direction has already been done in the form of formulation of a theoretical basis of multiphase flow processes, providing a basis for carrying out specific in-situ tests to check the numerical methods.

Since accident scenarios for potential repositories cannot exclude the possibility of escape of contaminated gases, the phenomenon of gas diffusion in fractured rock is to be investigated independently of the transport processes involved in two-phase flow.

The planned flow and transport studies with gas and water, above all on the small-scale, will require development of new equipment, e.g. based on multifunctional probes. Use of a new process control computer to acquire and store the data is planned, the objective being to improve the speed and accuracy of the measuring process, above all in short-term trials.

9. References

- BREWITZ, W., BRASSER, Th., KULL, H. & HUFSCHMIED, P. 1988: Ventilationstest. In: Nagra informiert. 10. Jahrgang, Vol. 1/2, NAGRA, Baden, Switzerland.
- BURDINE, N.T. 1953: Relative Permeability Calculations from Pore Size Distribution Data. Trans. Am. Inst. Min. Metall. Pet. Eng., Vol. 198, 71-77.
- BROOKS, R.H. & COREY, A.T. 1964: Hydraulic Properties of Porous Media. Hydrol. Paper 3, Colorado State Univ., Fort Collins, CO.
- CERMAK, V. & RYBACH, L. 1982: Wärmeleitfähigkeit und Wärmekapazität der Minerale und Gesteine. In: Landolt-Börnstein Vol. V1a.
- COOPER, H.H.jr. & JACOB, C.E. 1946: A Generalized Graphical Method for Evaluating Formation Constants and Summarizing Well-Field History. Am. Geophys. Union Trans., Vol. 27(4), 526-534.
- DAVEY, A., KARASAKI, K., LONG, J.C.S., LANDSFELD, M., MENSCH, A. & MARTEL, S.J. 1990: Analysis of Hydraulic Data from the MI Fracture Zone at the Grimsel Rock Laboratory, Switzerland. NAGRA-DOE Cooperative Project Report NDC-15/LBL-27864.
- FABIG, U. 1992: Numerische Experimente zur Untersuchung von Zwei-Phasenströmungen in Kluftsystemen. Techn. Report Institute for Flow Mechanics and Electronic Calculation, University of Hannover.
- FATT, I. & KLIKOFF, W.A. 1959: Effect of Fractional Wettability on Multiphase Flow Through Porous Media. Trans AIME, Vol. 216, 426-432.
- FRICK, U., Alexander, W.R., BAEYENS, B., BOSSART, P., BRADBURY, M.H., BÜHLER, Ch., EIKENBERG, J., FIERZ, Th., HEER, W., HOEHN, E., MCKINLEY, I.G. & SMITH, P.A. 1992: The Radionuclide Migration Experiment - Overview of Investigations 1985 - 1990. Nagra Technical Report 91-04, NAGRA, Wettingen, Switzerland.
- GATES, J.I. & TEMPELAAR-LIETZ, W. 1972: Relative Permeabilities of California Cores by the Capillary Pressure Method. Presented at the API Meeting, Los Angeles, Calif..
- GOURNAY, L.S., BURDINE, N.T. & REICHERTZ, P.P. 1950: Pore Size Distribution of Petroleum Rocks. Trans. AIME, Vol. 189-195.
- GRANT, M.A. 1977: Permeability Reduction Factors at Wairakei. Presented at the AIChE-ASME Heat Transfer Conference, Salt Lake City, Utah, 15.-17. August.

- GRINGARTEN, A.C. & SAUTY, J.P. 1975: A Theoretical Study of Heat Extraction from Aquifers with Uniform Regional Flow. *Journal of Geophysical Research*, Vol. 80, 4956-4962.
- GUYONNET, D. & LAVANCHY, J.M. 1992: Analysis of Single and Crosshole Tests at the BK-Site, Grimsel Test Site. Nagra Technical Report 91-09, NAGRA, Wettingen, Switzerland.
- HARRINGTON, J.D. 1949: A Correlation of the Measurements of Capillary Pressure and Relative Permeability on Small Core Samples. Ph. D. Thesis, Univ. of Oklahoma.
- HELMIG, R. & ZIELKE, W. 1991: Mehrphasenprozesse in geklüftet-porösen Medien - Stand der Forschung. Techn. Report Institute for Flow Mechanics and Electronic Calculation, University of Hannover.
- HELMIG, R. & MORITZ, L. 1993: Aufbereitung der empirischen Ansätze zur Beschreibung des Kapillardruck-Sättigungs- und des Relative-Permeabilitäts-Sättigungs-Verhaltens in geklüftet-porösen Medien. Techn. Report Institute for Flow Mechanics and Electronic Calculation, University of Hannover.
- HELMIG, R. 1993: Theorie und Numerik der Mehrphasenströmungen in geklüftet-porösen Medien, Report Nr. 34, Institute for Flow Mechanics and Electronic Calculation, University of Hannover.
- HERZOG, F. 1989: Hydrologic Modelling of the Migration Site at the Grimsel Test Site - The Steady State. Nagra Technical Report 89-16, NAGRA, Baden, Switzerland.
- HERZOG, F. 1991: A Simple Transport Model for the Grimsel Migration Experiments. NAGRA Technical Report 91-31, NAGRA, Wettingen, Switzerland.
- HOEHN, E., FIERZ, Th. & THORNE, P. 1990: Hydrogeological Characterisation of the Migration Experimental Area at the Grimsel Test Site. Nagra Technical Report 89-15, NAGRA, Baden, Switzerland.
- HORNER, D.R. 1951: Pressure Build-up in Wells. *Proc. 3rd World Petrol. Congr., The Hague*, Vol. 2, 503-521.
- HUFSCHMIED, P. & ADANK, P. 1988: Modellierung der Gebirgswasserströmung im Gebirgskörper um das Felslabor Grimsel. in: *Nagra informiert*. 10. Jahrgang, Vol. 1/2, NAGRA, Baden, Switzerland.
- HUYAKORN, P.S. & PINDER, G.F. 1978: A new Finite Element Technique for the Solution of Two-Phase Flow through Porous Media. *Water Resources Research* 1(5).

- JACOB, C.E. & LOHMANN, S.W. 1952: Nonsteady Flow to a Well of a Constant Drawdown in an Extensive Aquifer. Am. Geophys. Union Trans., Vol. 33, 559-569.
- JUNG, R. 1986: Erzeugung eines großflächigen künstlichen Risses im Falkenberger Granit durch hydraulisches Spalten und Untersuchung seiner mechanischen und hydraulischen Eigenschaften. Report Institute of Geophysics, Ruhr-Universität Bochum, Series A, Nr. 20, Thesis paper.
- KEUSEN, H.R., GANGUIN, J., SCHULER, P. & BULETTI, M. 1989: Geology, Grimsel Test Site. Nagra Technical Report 87-14E, NAGRA, Baden, Switzerland.
- KOLDITZ, O. & LEGE, T. 1992: Verifizierung des Programmsystems "ROCKFLOW" hinsichtlich des Wärmetransports in Kluft-Matrix-Systemen. NLFB-Report, Archiv-No. 109603, Hannover.
- KOLDITZ, O. 1993: 3-D Modellierung von Wärmetransportprozessen im geklüfteten Medium (Effekt der räumlichen Wärmediffusion). NLFB-Report, Archiv-No. 110238, Hannover.
- KRÖHN, K.P. 1990: Simulation von Transportvorgängen im klüftigen Gestein mit der Methode der Finiten Elemente. University of Hannover, Institute for Flow Mechanics and Electronic Calculation, Thesis paper.
- KULL, H., LEITENBAUER, J., SIEBERT, R. & WEBER, R. 1989: Simulation of Groundwater Flow in Crystalline Formations with Use of Three-Dimensional, Dual-Porosity-Modell. Proc. ENVIROTECH Vienna 20.-23.2.1989.
- KULL, H., BREWITZ, W. & KLARR, K. 1993: Ventilationstest - In-Situ-Verfahren zur Permeabilitätsbestimmung im Kristallin. Nagra Technical Report 91-02, NAGRA, Wettingen, Switzerland.
- LAUWERIER, H.A. 1955: The Transport of Heat in an Oil Layer Caused by the Injection of Hot Fluid. Appl. Sci. Res., Vol. A5, 145-150.
- LEGE, T. & ZIELKE, W. 1993: Simulation von Tracerversuchen im Felslabor Grimsel mit dem Programmsystem Rockflow. Techn. Report Institute for Flow Mechanics and Electronic Calculation, University of Hannover.
- LEVERETT, M.C. 1941: Capillary Behaviour in Porous Solids. Trans. AIME, Vol. 142, 152 - 169.
- LIEDTKE, L. & ZUIDEMA, P. 1988: Der Bohrlochkranzversuch. In: Nagra informiert. 10. Jahrgang, Vol. 1/2, NAGRA, Baden, Switzerland.

- LIEDTKE, L., NAUJOKS, A. & SIEMERING, W. 1992: Bohrlochkranzversuch - Fracture System Flow Test - Felslabor Grimsel, Annual Report 1991. BGR-Hannover, Archiv-No. 109284.
- LIEDTKE, L. & PAHL, A. 1993: Geohydraulische Modelluntersuchungen für Schadstoffausbreitung im geklüfteten Fels. Proc. Geotechnica, Köln.
- LOHMANN, S.W. 1972: Groundwater Hydraulics. U.S. Geol. Survey Prof. Paper 708, U.S. Government Print Office, Washington.
- MARSCHALL, P. & JOHNS, R. 1993: Spectral Analysis of Hydraulic Crosshole Tests. Unpublished Nagra Int. Rep., NAGRA, Wettingen, Switzerland.
- MUSKAT, M. 1937: The Flow of Homogeneous Fluids Through Porous Media. McGraw-Hill Book Company.
- NAGRA 1988: Nagra informiert. 10. Jahrgang, Vol. 1/2, NAGRA, Baden, Switzerland.
- PAHL, A., HEUSERMANN, S., BRÄUER, V. & GLÖGGLER, W. 1989: Grimsel Test Site - Rock Stress Investigations. Nagra Technical Report 88-39E, NAGRA, Baden, Switzerland.
- PAHL, A., LIEDTKE, L., NAUJOKS, A. & BRÄUER, V. 1992: Bohrlochkranzversuch - Durchströmung von geklüftetem Fels. Nagra Technical Report 91-01, NAGRA, Wettingen, Switzerland.
- PAHL, A. & LIEDTKE, L. 1993: Geotechnical Site Investigations to Prove the Rock Stability of Large Cavities and the Barrier Efficiency of the Rock Mass. Engineering Geology, Vol. 35, Elsevier, Amsterdam (in press).
- PERSOFF, P., PRUESS, K. & MYER, L. 1991: Two-Phase Flow Visualization and Relative Permeability Measurement in Transparent Replicas of Rough-Walled Rock Fractures. Technical Report, University of California.
- PRUESS, K. 1987: TOUGH User's Guide. Lawrence Berkeley Laboratory, Univ. of California.
- PRUESS, K. & TSANG, Y.W. 1990: On Two-Phase Relative Permeability Capillary Pressure of Rough-Walled Rock Fractures. Water Resources Research, Vol. 10.
- PRUESS, K., COX, B.L. & PERSOFF, P. 1990: A Casting and Imaging Technique for Determining Void Geometry and Relative Permeability Behaviour of a Single Fracture. Lawrence Berkeley Laboratory, University of California.
- RODEMANN, H. 1979: Modellrechnungen zum Wärmeaustausch in einem Frac. NLfB-Report, Archiv-No. 81990, Hannover.

- ROMM, E.S. 1966: Fluid Flow in Fractured Rocks. Moscow (translated by W.R. Blake, Bartlesville, OK).
- SASS, J.H., LACHENBRUCH, A.H. & MUNROE, R.J. 1971: Thermal Conductivity of Rocks from Measurements on Fragments and its Application to Heat-Flow Determinations. *Journal of Geophysical Research*, Vol. 76, 3391-3401.
- SCHEIDEGGER, A.E. 1961: General Theory of Dispersion in Porous Media. *Journal of Geophysical Research*, Vol. 66, No. 10, 3273-3278.
- SCHNEEFUSS, J., GLÄSS, F., GOMMLICH, G. & SCHMIDT, M. 1989: Grimsel Test Site - Heater Test. Nagra Technical Report 88-40E, NAGRA, Baden, Switzerland.
- SCHÖN, J. 1983: Petrophysik - Physikalische Eigenschaften von Gesteinen und Mineralien. Enke-Verlag, Stuttgart.
- SCHULZ, R. 1987: Analytical Model Calculations for Heat Exchange in a Confined Aquifer. *Journal of Geophysics*, Vol. 61, 12-20.
- SNELL, R.W. 1962: Three-Phase Relative Permeability in an Unconsolidated Sand. *J. Inst. Petr.*, Vol. 48, 80-88.
- STADLER, H. 1964: Petrographische und mineralogische Untersuchungen im Grimselgebiet. SMPM 44, 187-398, NAGRA, Baden, Switzerland.
- STADLER, H. 1981: Sondierbohrungen Juchlistock-Grimsel: Mineralogische Untersuchungen. Unpubl. Nagra Internal Report, NAGRA, Baden, Switzerland.
- STONE, H.L. 1970: Probability Model for estimating Three-Phase Relative Permeability. *Trans. SPE of AIME*, Vol. 249, 214-218.
- TANIGUCHI, T. 1992: Automatic Mesh Generation for FEM. Morikita Publishing Co. Ltd. (in Japanese, English Version i. p.).
- THEIS, C.V. 1935: Relation Between the Lowering of the Piezometric Surface and the Rate and Duration of Discharge of a Well Using Ground-Water Storage. *Am. Geophys. Union Trans.*, Vol. 16.
- THIEM, A. 1870: Die Ergiebigkeit artesischer Bohrlöcher, Schachtbrunnen und Filtergalerien. *Jour. für Gasbeleuchtung und Wasserversorgung*, No. 14, 450-467.
- VAN GENUCHTEN, M. Th. 1980: A Closed-Form Equation for Predicting the Hydraulic Conductivity of Unsaturated Soils. *Soil Sci. Soc. Am. J.*, Vol. 44, 892 - 898.

- VOBORNY, O., ADANK, P., HÜRLIMANN, W., VOMVORIS, S. & MISHRA, S. 1991: Modelling of the Groundwater Flow in the Rock Body Surrounding the Underground Laboratory. Nagra Technical Report 91-03, NAGRA, Wettingen, Switzerland.
- VOMVORIS, S., FRIEG, B., BOSSART, P., GMÜNDER, C., HEINIGER, P., JAQUET, O. & WATANABE, K. 1992: Overview of Nagra Field and Modelling Activities in the Ventilation Drift (1988-1990). Nagra Technical Report 91-34, NAGRA, Wettingen, Switzerland.
- WALSH, J.B. & DECKER, E.R. 1969: Effect of Pressure and Saturating Fluid on the Thermal Conductivity of Compact Rock. *Journal of Geophysical Research*, Vol. 71, No. 12, 3053-3061.
- WANG, J.S.Y. & NARASIMHAN, T.N. 1985: Hydrologic Mechanisms Governing Fluid Flow in a Partially Saturated, Fractured, Porous Medium. *Water Resources Research*, Vol. 21, 1861-1874.
- WOLLRATH, J. 1990: Ein Strömungs- und Transportmodell für klüftiges Gestein und Untersuchungen zu homogenen Ersatzsystemen. University of Hannover, Institute for Flow Mechanics and Electronic Calculation, Thesis paper.
- WOODSIDE, W. & MESSMER, J.H. 1961: Thermal Conductivity of Porous Media. *Journal of Applied Physics*, Vol. 32, No. 9, 1688-1699.
- WYSS, E 1989: Felslabor Grimsel: Hydrogeologische Untersuchungen zur Bestimmung hydraulischer Potentiale. Nagra Technical Report 89-01, NAGRA, Baden, Switzerland.
- WYSS, E 1990: Felslabor Grimsel Migrationstest: Drei Beispiele für das weitere Verständnis des hydraulischen Verhaltens. Unpubl. Nagra Internal Report, NAGRA, Baden, Switzerland.
- ZIELKE, W., HELMIG, R. & MORITZ, L. 1993: Aufbereitung der empirischen Ansätze zur Beschreibung des Kapillardruck-Sättigungs- und des Relative-Permeabilitäts-Sättigungsverhaltens in geklüftet-porösen Medien. Unpubl. Report, Institute for Flow Mechanics and Electronic Calculation, University of Hannover.